Microscopic Imaging Techniques for Molecular Assemblies: Electron, Atomic Force, and Confocal Microscopies

Kubota, Ryou; Tanaka, Wataru; Hamachi, Itaru

Kubota, Ryou ...[et al]. Microscopic Imaging Techniques for Molecular Assemblies: Electron, Atomic Force, and Confocal Microscopies. Chemical Reviews 2021, 121(22): 14281-14347

2021-11-24

http://hdl.handle.net/2433/269544

Chemical Reviews: special edition for molecular self-assembly

Microscopic Imaging Techniques for Molecular Assemblies: Electron, Atomic Force, and Confocal Microscopies

Ryou Kubota[1†], Wataru Tanaka[1†#], Itaru Hamachi[1,2*]

[1]Department of Synthetic Chemistry and Biological Chemistry, Graduate School of Engineering, Kyoto University, Katsura, Nishikyo-ku, Kyoto 615-8510, Japan

[2]JST-ERATO, Hamachi Innovative Molecular Technology for Neuroscience, Kyoto University, Katsura, Nishikyo-ku, Kyoto, 615-8530, Japan

†Contributed equally to this work

#Present address: Department of Applied Chemistry, Graduate School of Engineering, The University of Tokyo, 7-3-1 Hongo, Bunkyo-ku, Tokyo 113-8656, Japan

*Correspondence: ihamachi@sbchem.kyoto-u.ac.jp

Abstract

Self-assembly is promising for construction of a wide variety of supramolecular assemblies, whose 1D/2D/3D structures are typically relevant to their functions. In-depth understanding of their structure-function relationships is essential for rational design and development of functional molecular assemblies. Microscopic imaging have been used as powerful tools to elucidate structures of individual molecular assemblies with sub-nanometer to millimeter resolution, which is complementary to conventional spectroscopic techniques that provide the ensemble structural information. In this review, we highlight the representative examples of visualization of molecular assemblies by use of electron microscopy, atomic force microscopy, confocal microscopy, and super-resolution microscopy. This review comprehensively describes imaging of supramolecular nanofibers/gels, micelles/vesicles, coacervate droplets, polymer assemblies, and protein/DNA assemblies. Advanced imaging techniques that can address key challenges like evaluation of dynamics of molecular assemblies, multicomponent self-assembly, and self-assembly/disassembly in complex cellular milieu, are also discussed. We believe this review would provide guidelines for deeper structural analyses of molecular assemblies to develop the next-generation materials.

Contents

1. Introduction

Both natural and synthetic molecular assembly produced by non-covalent interactions provide a variety of unique 1D/2D/3D structures such as sphere, rod, fiber, tape, grid, sheet, helix, and others with a variety of sizes, which cannot be constructed by use of only covalent bond linkage. Owing to reversible connections through noncovalent bonds, these structures are dynamic and transform each other, which may be tightly associated with their functions in many cases. These self-assembled molecules/materials are expected as promising soft-materials in the next generation where the sustainability will be highlighted. For rational design of functional molecular assembly, it is crucial to decipher a valuable relationship between the structure and the function in details. Structural analyses of such molecular assembly so far have been mostly carried out with X-ray crystallography and various spectroscopies including UV-visible, fluorescence, circular dichroism (CD), and NMR. The crystallographic analysis can give precise information of the assembly on the molecular packing in atomic resolution, while these are static in the crystal state. Small angle X-ray/neutron scattering technique has also been becoming useful to elucidate sizes and shapes of molecular assemblies in solution. Indeed useful, the spectroscopic data in either solution or solid state give only ensemble information of the assembly. Structural study of molecular assembly using microscopy such as TEM (transmission electron microscopy), SEM (scanning electron microscopy), AFM (atomic force microscopy) and CLSM (confocal laser scanning microscopy) should be complementary to these conventional analytical methods. These approaches allow to address the individual structures/dynamics of molecular assembly, rather than averaged ones, by imaging the individual self-assembled objectives with their corresponding spatial and temporal resolutions.

In this review, we summarize representative imaging techniques, electron microscopy (EM), AFM, and CLSM, for molecular assemblies such as micelles/vesicles, supramolecular/covalent polymers, coacervate droplets, DNA/protein assemblies, and others. As shown in Table 1,[1] each imaging modality has (dis)advantages over others in terms of spatial and temporal resolutions, sample preparation protocols, imaging conditions, and the contaminated artifacts. It is thus keenly needed to select appropriate imaging techniques for samples of interest. For example, EM realizes a near atomic-level resolution but it is difficult to evaluate the dynamic processes due to its requirement of drying or freezing in the sample preparation. AFM enables to examine the dynamic aspects of molecular assemblies at nm resolution, but interactions between sample-tip and sample-substrate should be carefully considered. Although the lower spatial resolution, CLSM and recently developed super-resolution techniques allows *in situ* multicolor imaging at a wide range of frame rates (s~h/frame) through selective fluorescent staining. Here, we introduce the imaging techniques and their application examples for various kinds of artificial/natural molecular assemblies and discuss advantages and limitations of each imaging modality.

Table 1. Comparison of imaging techniques for organic molecular assemblies. Modified from ref 1.

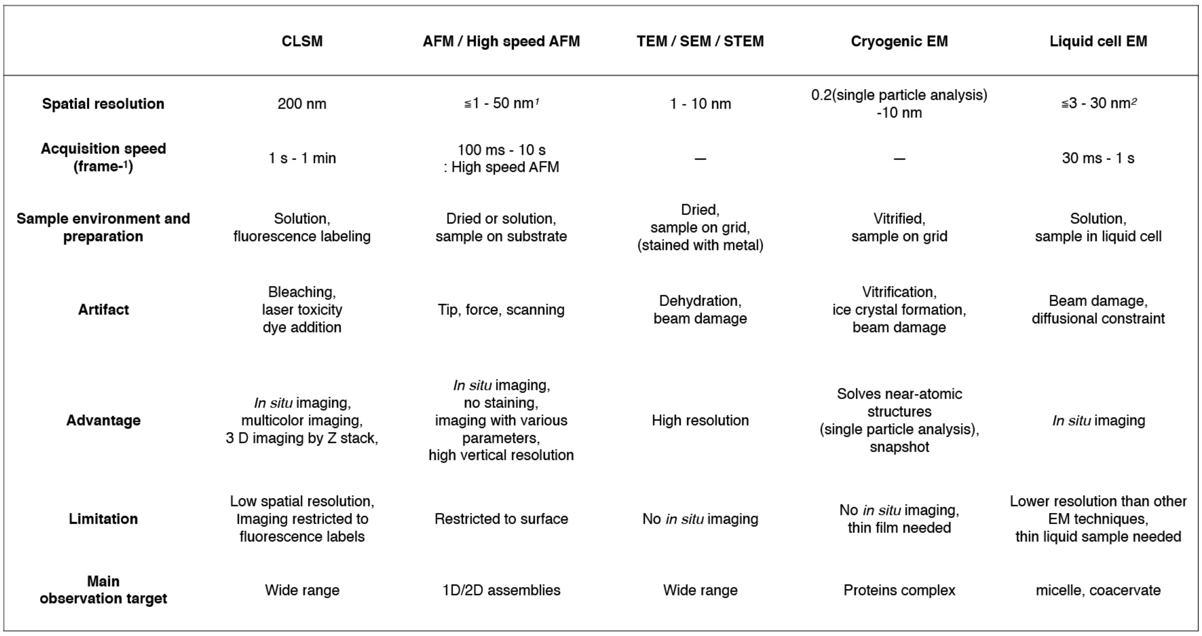

	CLSM	**AFM / High speed AFM**	**TEM / SEM / STEM**	**Cryogenic EM**	**Liquid cell EM**
Spatial resolution	200 nm	≦1 - 50 nm[1]	1 - 10 nm	0.2(single particle analysis) -10 nm	≦3 - 30 nm[2]
Acquisition speed (frame-1)	1 s - 1 min	100 ms - 10 s : High speed AFM	―	―	30 ms - 1 s
Sample environment and preparation	Solution, fluorescence labeling	Dried or solution, sample on substrate	Dried, sample on grid, (stained with metal)	Vitrified, sample on grid	Solution, sample in liquid cell
Artifact	Bleaching, laser toxicity dye addition	Tip, force, scanning	Dehydration, beam damage	Vitrification, ice crystal formation, beam damage	Beam damage, diffusional constraint
Advantage	*In situ* imaging, multicolor imaging, 3 D imaging by Z stack,	*In situ* imaging, no staining, imaging with various parameters, high vertical resolution	High resolution	Solves near-atomic structures (single particle analysis), snapshot	*In situ* imaging
Limitation	Low spatial resolution, Imaging restricted to fluorescence labels	Restricted to surface	No *in situ* imaging	No *in situ* imaging, thin film needed	Lower resolution than other EM techniques, thin liquid sample needed
Main observation target	Wide range	1D/2D assemblies	Wide range	Proteins complex	micelle, coacervate

[1]: On membrane proteins, resolution ≤1 nm can be achieved, on mammalian cells ~50 nm and on microbial cells ~10 nm.

[2]: Resolution ≲3 nm can be achieved when specimen contains heavy metal

2. Imaging modality

EM, AFM, and CLSM are most major methods for imaging the structures of molecular self-assemblies. These techniques have been greatly improved in recent years in a few of critical aspects including frame rate, spatial resolution, and sample preparation/conditions. More recently, cryogenic electron microscopy (cryo-EM) has enabled us to investigate the detailed packing structure of molecular assemblies in near-atomic resolution.[2–6] Liquid cell electron microscopy (LC-EM)[7–9] and high speed atomic force microscopy (HS-AFM)[10–12] are available to capture dynamics of molecular assemblies in nm resolution. A great progress in several super-resolution fluorescence microscopies such as stimulated emission depletion microscopy (STED), single molecule localization microscopy (SMLM), and structured illumination microscopy (SIM) allows *in situ* multicolor imaging of molecular assemblies at a higher resolution than conventional CLSM. Herein, we comprehensively describe examples for imaging of organic molecular assembly with EM (chapter 3), AFM (chapter 4), and CLSM (chapter 5).

3. Electron microscopy

TEM, SEM, and scanning transmission electron microscopy (STEM) are most representative methods for imaging various inorganic/organic objectives including molecular self-assemblies. Although SEM/TEM/STEM have the nanometer spatial resolution with good signal to noise ratio, there are concerns in artifacts due to drying and metal shadowing in the sample preparation process and electron-beam damage while imaging. Cryo-EM using rapid freezing sample can reduce such artifacts and is advantageous in time-resolved snapshot imaging.[13–15] Very recently, a few of atomic level 3D reconstructions of artificial or small molecular assemblies by single particle analysis have been reported.[4–6] LC-EM is recently developed as another powerful technique, which allows direct observation of liquid specimens in real time, and has now begun to be applied to follow the dynamics of organic molecular assemblies.[7–9] In this chapter, we mainly focus on recent advances in imaging molecular self-assemblies using cryo-EM and LC-EM.

3.1. TEM/SEM/STEM

Since the 1970s, TEM/SEM/STEM have been actively used for imaging molecular self-assemblies formed by biopolymers such as proteins and polysaccharides.[16–22] As an early example, Trelstad *et al.* imaged self-assembly of collagen by TEM with phosphotungstic acid negative staining.[18] TEM image of a sample of freshly prepared collagen solutions showed non-structural images. After 5 minutes incubation at 37 °C, the thin fibrous aggregates with a diameter of 5 nm appeared. Further incubations provided their entangled 18 nm thick fibers. These results indicated that self-assembly process of collagen fibers contained multiple steps with distinct stages. TEM/SEM/STEM had been similarly applied for imaging artificial molecular self-assemblies.[23–29] In 1993, Gulik-Krzywicki *et al*. reported TEM images of supramolecular liquid crystalline polymers formed by 1:1 mixture of complementary molecules which contained L-, D-tartaric acid in center and pyridine derivatives or uracil at edges (LP_2, LU_2, DP_2, DU_2).[26] The right- and left- handled helical nanostructures were clearly observed in the mixture of LP_2/LU_2 and DP_2/DU_2, respectively, indicating that the chirality of small molecules was translated into their supramolecular helicities.

Energy dispersive X-ray spectroscopic (EDX) analysis allows elemental mapping of molecular assemblies and is valuable to confirm the colocalization of self-assembled molecules and other molecules.[30–32] The spatial resolution of the EDX analysis for thin specimens is 2–100 nm. In 2006, Wang *et al*. prepared a catalytic supramolecular hydrogel by co-assembly of two amino acid derivatives and hemin in water (Figure 1A).[30] The authors compared the catalytic activity of hemin using the oxidation reaction of pyrogallol in the presence of H_2O_2. The activity of the hemin-modified supramolecular hydrogel (Gel II) is higher than that of free hemin, hemin in a polymer hydrogel, or the hemin-unmodified supramolecular hydrogel (Gel I). TEM image of Gel I showed only dense nanofibers with a diameter of *ca.* 20 nm (Figure 1B), whereas the nanofibers of Gel II were surrounded by a loose layer (Figure 1C). The EDX analysis indicated that the surrounded area had 2.23 wt% Fe and there was no Fe signal in the blank area (Figure 1D, E, F). From the UV/Vis analysis, it was clear that presence of the supramolecular hydrogel inhibited dimerization of hemin. These results suggested that hemin molecules adsorbed on the supramolecular nanofibers without dimerization and were efficiently exposed to the outside, resulting in the higher catalytic activity. In 2009, Komatsu *et al*. reported Ca^{2+} ions responsive hydrogelation of a phospholipid mimic hydrogelator.[31] The STEM-EDX line profile of the resulting hydrogel showed that C and P signal of the phospholipid colocalized well on the Ca signal, indicating that formation of Ca^{2+}-phosphate complex stabilized the nanofiber to induce the sol-gel transition. EDX analysis was also utilized for elucidating the formation of self-assembly block nanostructures.[33,34] In 2011, Zhang *et al*. developed a semiconducting supramolecular block-nanotube.[34] The nanotubes were formed by the following stepwise processes: (i) self-assembly of single molecule (HBC 1) into a homo-nanotube formation; (ii) inhibition of the monomer exchanges by construction of Cu^{2+}-coordination network; (iii) sonication to provide dispersed seeds; (iv) seeds-driven self-assembly of the other molecule (HBC 2) to fabricate the block nanotube (Figure 1G). STEM visualized the nanotubes composed of two segments with different contrasts (Figure 1H) and the Cu signal in the EDX analysis was detected only along the bright segment (Figure 1I, J, K). These observations clearly demonstrated the formation of a supramolecular block-nanotube.

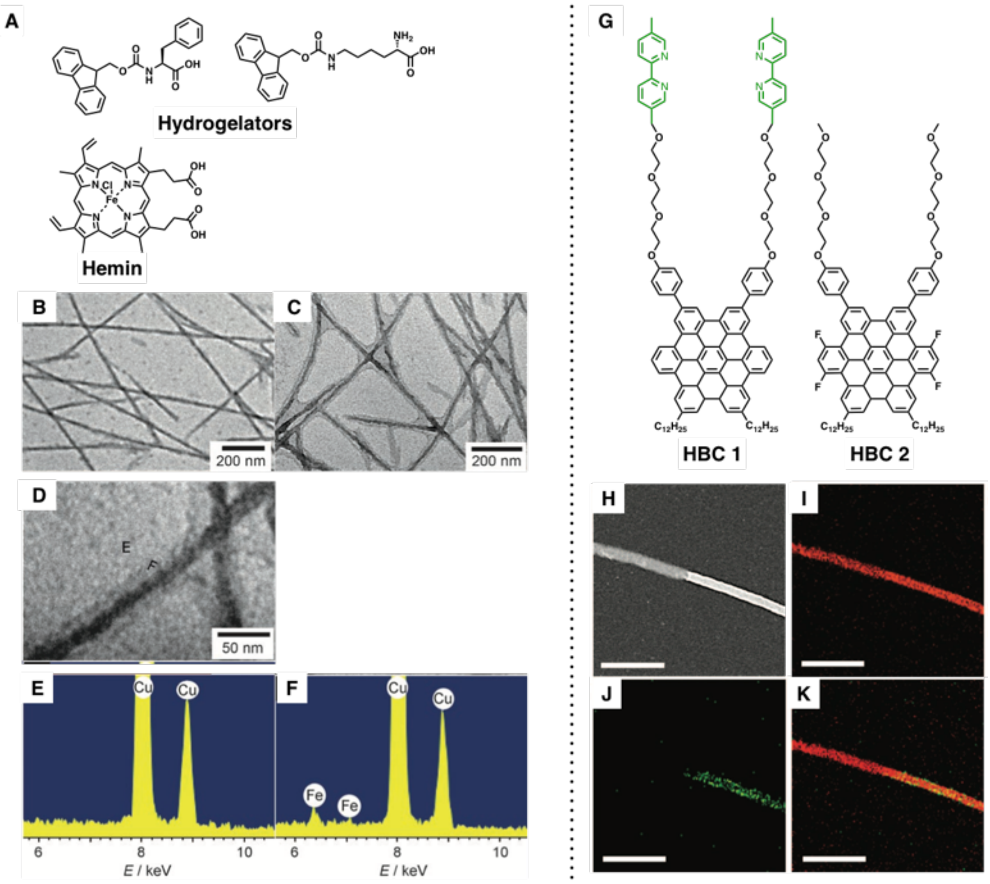

Figure 1. EDX analysis of small molecular assemblies. (**A**) Chemical structures of hydrogelators and hemin. (**B**, **C**) TEM images of (**B**) hemin-unmodified supramolecular hydrogel (Gel I) and (**C**) hemin-modified supramolecular hydrogel (Gel II). (**D**) High resolution TEM image of Gel II. (**E**, **F**) EDX analysis of selected area in (**D**). Reproduced

with permission from ref 30. Copyright 2007 Wiley-VCH. **(G)** Chemical structures of monomers for tubular assembly. **(H)** STEM image of the block nanotube. **(I, J, K)** STEM-EDX map of **(I)** carbon, **(J)** copper, and **(K)** their merge. Scale bars: 50 nm. Reproduced with permission from ref 34. Copyright 2011 AAAS.

3.2. Cryo-EM

Conventional EM imaging requires sample drying, which might cause morphological change of molecular assemblies to give unfavorable artifacts.[35] In contrast, cryo-EM technique, the samples of which are prepared by rapid freezing in a cryogenic environment, was developed to minimize such artifacts coming from the sample dryness.[36–40] However, the blotting process in preparation of thin film specimens may lead to structural changes. Mears *et al.* indeed demonstrated by small angle neutron scattering analysis that the cryo-TEM imaging greatly suppressed the artifacts in the self-assembly structure of low molecular weight gelators compared to the SEM/AFM imaging after drying.[13] As an early example of cryo-TEM imaging of artificial molecular assemblies, Won *et al.* observed poly(ethylene oxide)-poly(butadiene) (PEO-PB) diblock copolymer in vitrified water,[41] revealing that PEO-PB formed worm-like micelles with PB cores. Cryo-EM is also utilized for imaging nanometer scale orthogonal self-assemblies.[42–44] van Esch and coworkers observed that a low molecular weight gelator and a surfactant orthogonally self-assembled to form nanofibers and vesicles, respectively.[42,43] Following their works, Majumder *et al.* observed orthogonal self-assemblies of vesicles and peptide nanofibers by cryo-EM. They utilized these orthogonal assemblies to simultaneously control the release rate of a small molecule and a protein drug, resulting in effective induction of cancer cells death.[44]

In cryo-EM imaging, the specimens are quickly vitrified at a certain timing. Hence, cryo-EM is applicable for imaging time-dependent morphological change of molecular assemblies,[14,15] especially at seconds to several minute ranges. Danino *et al.* observed guanosine triphosphate (GTP)-induced structural change of a tubular complex comprising proline rich domain-lacking dynamin (ΔPRD dynamin) and phosphatidylserine (PS) by the cryo-EM snapshot imaging.[45] Dynamin, a large GTPase, plays an important role in endocytosis by fission of vesicles from membranes.[46] The complex of ΔPRD dynamin and PS formed tubular structures with diameter of 50 nm before treatment of GTP (Figure 2A, left). The constricted tubular structures with diameter of 40 nm and dynamin-free liposomes were observed 210 s after addition of excess GTP and the intermediate state containing both the non-constricted and the constricted tubes could be seen at 5 s after addition of GTP (Figure 2A. right). Importantly, the GTP treated structures visualized by conventional TEM were different from that by cryo-EM, probably because of artifacts during sample preparation of conventional TEM. Small molecular self-assembly behaviors were also evaluated by cryo-EM snapshot.[47–51] In 2010, Pashuck and Stupp used cryo-EM snapshot to observe molecular assembly of a peptide amphiphile (PA), a short peptide that has a hydrophobic alkyl chain at N-terminus.[47] The cryo-EM snapshot visualized the morphological change from short twisted ribbons to long helical ribbons over 1 month. In 2019, Yuan *et al.* imaged supramolecular polymerization processes of amphiphilic amino acid derivatives, Fmoc-Ala/His and Z-FF.[51] The samples were prepared by mixing alkaline or DMSO solution of the amino acid derivatives and an aqueous solution in the presence or absence of $AgNO_3$. In all cases, kinetic liquid-liquid phase separation was observed at initial stage followed by nucleation and growth of the thermodynamically stable nanofibers from the solute rich droplets after lag-time (Figure 2B, C). Combination of the cryo-EM images with other analyses suggested that the liquid-liquid phase separation was crucial for decreasing the nucleation barriers to form the supramolecular nanofibers. Cryo-EM method can visualize organic self-assembly materials which reversibly interact with guest molecules. In 2019, Li *et al.* succeeded in imaging a metal-organic framework (MOF) of zeolite imidazolate framework (ZIF-8) and the CO_2-adsorbed MOF by use of cryo-TEM, where the cryogenic condition stabilized the ZIF-8 structure and inhibited desorption of CO_2.[52] The cryo-TEM images of empty and CO_2-filled ZIF-8 showed that insertion of CO_2 induced structural change of ZIF-8.

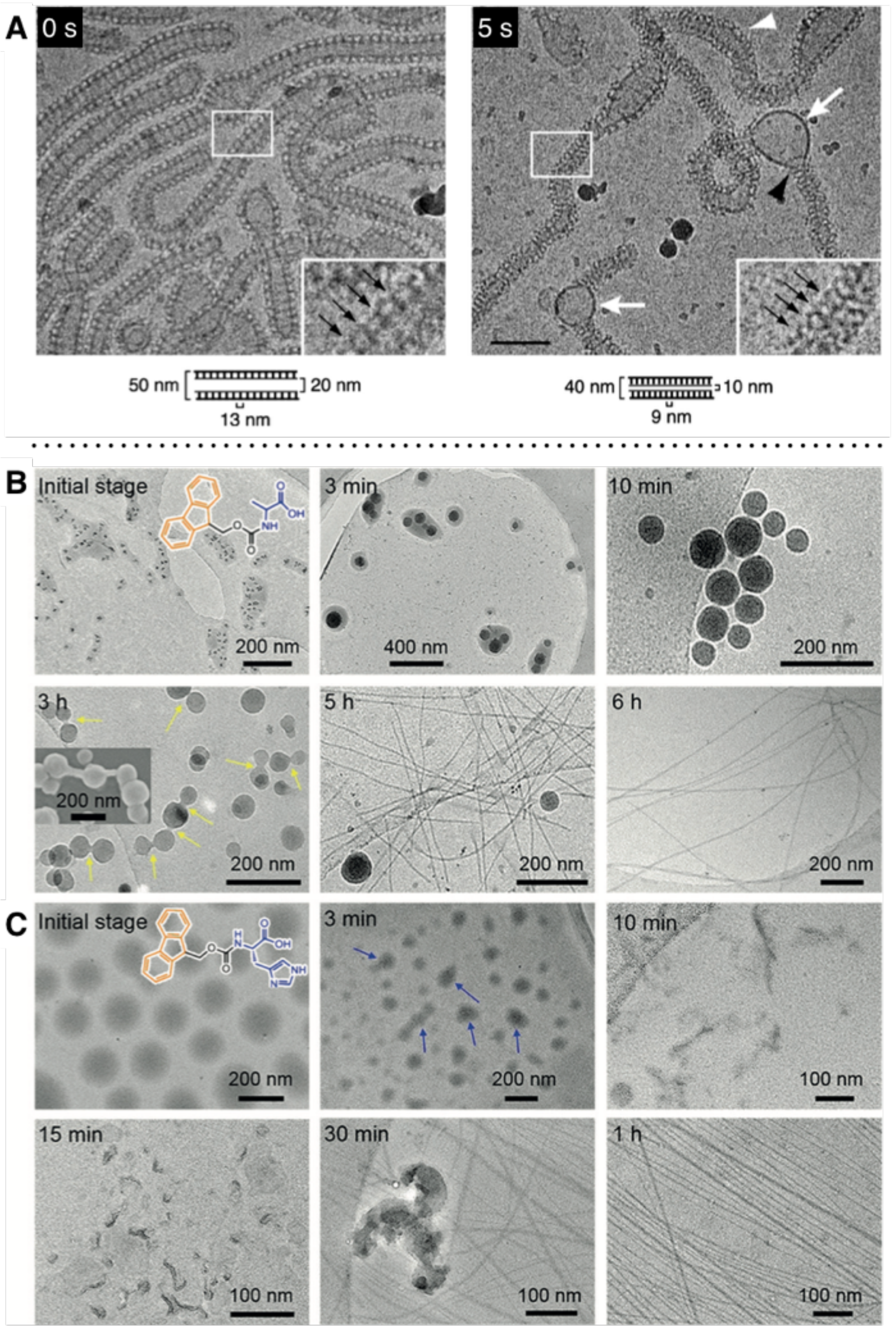

Figure 2. (**A**) Cryo-TEM images of ΔPRD dynamin / PS tubular complex before and 5 s after addition of GTP. Scale bar: 100 nm. Reproduced with permission from ref 45. Copyright 2004 Elsevier. (**B**, **C**) Cryo-TEM time-dependent images of formation processes of (**B**) Fmoc-Ala and (**C**) Fmoc-His nanofibers in presence of Ag^+ ions. Reproduced with permission from ref 51. Copyright 2019 Wiley-VCH.

Thanks to the recent advances in direct electron detectors and image processing systems, cryo-EM is now available to analyze 3D structures of proteins in near-atomic to nm resolution using single particle analysis[2,53–56] and cryo-electron tomography.[57,58] These techniques are now applied for resolving the structures of protein self-assemblies such as microtubules.[59,60] Microtubules, ubiquitous cytoskeletal filaments, are well known to play a vital role in multiple cellular functions.[61] Heterodimer of α- and β-tubulin self-assembly into protofilament, that associate laterally to afford a microtubule. It is conceivable that the formation and collapse of microtubules are highly dynamic, which depend on GTP and other binding molecules. Supramolecular polymerization of the tubulin dimer gives polarity, in which the fast and slow growth end are called plus and minus end, respectively. In 2014, Alushin *et al*. utilized cryo-EM single particle analysis to construct high resolution microtubule structures (4.7–5.6 Å) in presence of GTP-like GMPCPP (a slowly hydrolyzing analog of GTP), guanosine diphosphate (GDP), or GDP/Taxol (Figure 3A).[3] N and E sites are GTP binding domains located at plus end direction of α- and β-tubulin, respectively. Comparison of the GMPCPP-bound and the GDP-bound state structures indicated that GTP hydrolysis induced the compaction of the E site into generation of strain at the dimer interface, which resulted in deformation of microtubules (Figure 3B). In addition, it was revealed that taxol allosterically inhibited most of these changes. After this report, many researchers provided high resolution microtubule structures in presence of microtubule binding molecules by cryo-EM.[60,62–65]

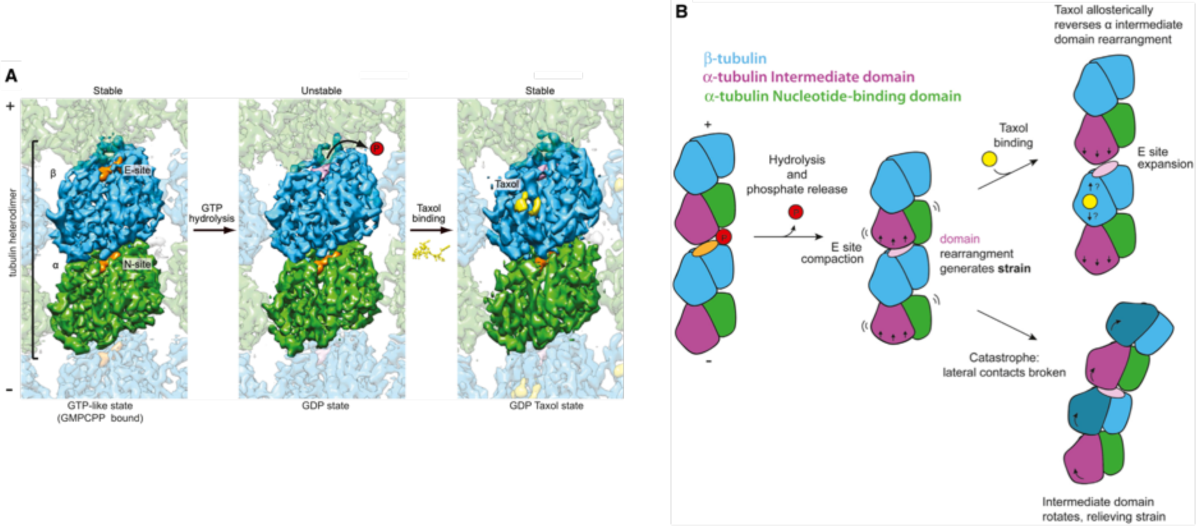

Figure 3. (**A**) Single particle cryo-EM structures of microtubule in GTP-like, GDP, and GDP/Taxol states. (**B**) Proposed model of microtubule stabilization and destabilization. Reproduced with permission from ref 3. Copyright 2014 Elsevier.

In the past few years, cryo-electron tomography and single particle analysis have extended to artificial (small molecular) assemblies.[4–6,66] In 2016, the inner structure of a sub-50 nm homopolymer nanoparticle derived from a poly-ionic liquid (Figure 4A) was evaluated by cryo-electron tomography.[66] According to the 2D cryo-EM images, the nanoparticle seemed to form an onion-like layered structure with 5 nm domain spacing (Figure 4B). However, the 3D reconstruction image of cryo-electron tomography revealed that the inner structure was more complicated than the simple layered structure (Figure 4C). In 2016, Yang *et al*. reported a construction of a well-ordered protein microtubule mimic composed of a tetrameric soybean agglutinin and a rhodamine-conjugated sugar (Figure 4D).[4] The designer microtubular 3D structure at a resolution of 7.9 Å were determined by single particle cryo-EM analysis. In 2018, Guenther *et al*. performed single particle cryo-EM to determine the molecular packing structure of DLIIKGISVHI derived from an amyloid protein, TAR DNA-binding protein 43.[5] The 3D reconstruction structure at a resolution of 3.7 Å revealed that the 11 amino acid peptide represented several distinct conformations in the amyloid fibril (Figure 4E). These pioneering works predicted that cryo-electron tomography and single particle cryo-EM would be widely applied for in-depth structure analysis of artificial and small molecular self-assemblies in the near future. In addition to the imaging-based techniques, microcrystal electron diffraction (MicroED) with cryo-EM is also powerful to elucidate the atomic level conformation of crystalline self-assemblies.[5,67–72]

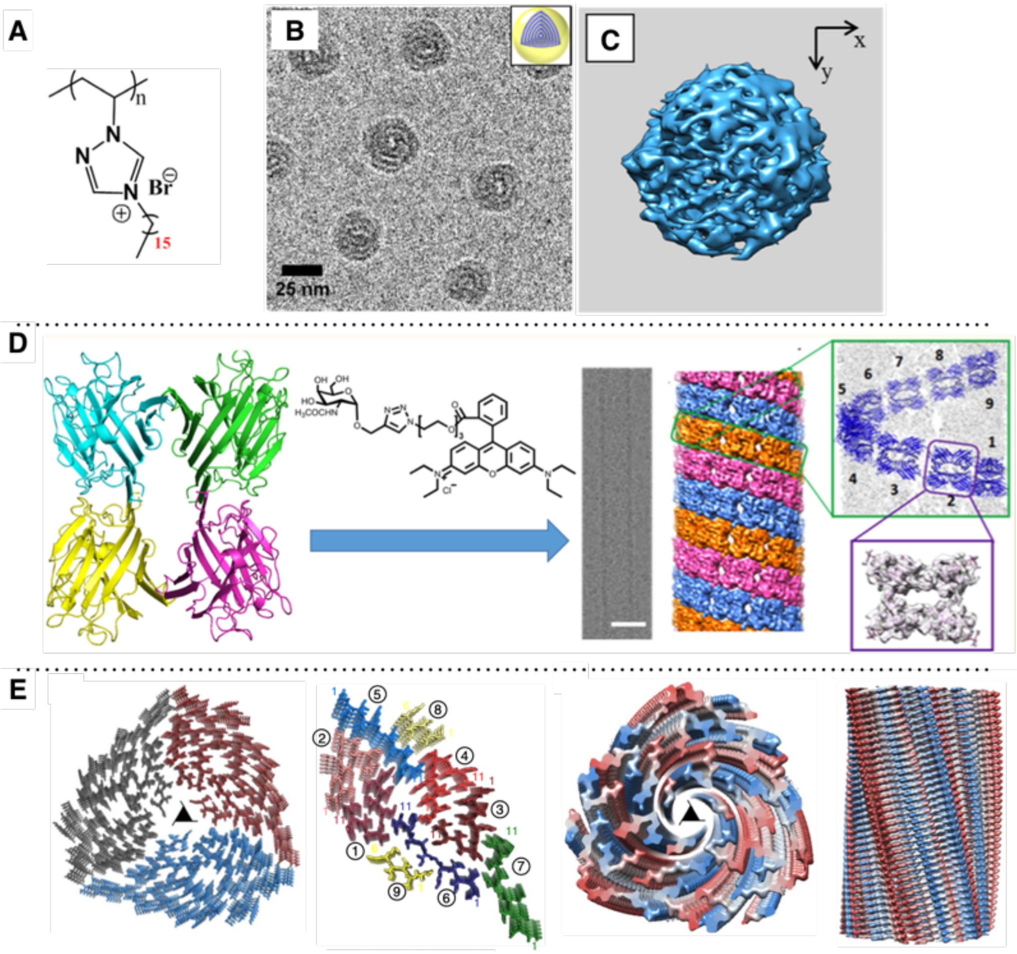

Figure 4. (**A**) Chemical structure of a poly(ionic liquid). (**B**) Cryo-TEM image of the homopolymer nanoparticles. (**C**) 3D structure of the homopolymer nanoparticle reconstructed by cryo-electron tomography. Reproduced with permission from ref 66. Copyright 2016 American Chemical Society. (**D**) Single particle cryo-EM structure of the artificial microtubule composed of a tetrameric soybean agglutinin and a rhodamine-conjugated sugar. Scale bar: 25 nm. Reproduced with permission from ref 4. Copyright 2016 American Chemical Society. (**E**) Single particle cryo-EM structure of DLIIKGISVHI fibril. Reproduced with permission from ref 5. Copyright 2018 Springer Nature.

3.3. Liquid cell electron microscopy

In spite of the great progress in cryo-EM, it is yet challenging to image wet samples in real time because the extremely high vacuum environment is necessary in EM. To sidestep the obstacle, LC-EM technique, where liquid samples are placed in a small space between two thin, tough and highly transmittance membranes, has been developed (Figure 5).[7,73–75] LC-EM allows *in situ* time-lapse imaging of wet samples at nanometer resolution with sub-second time scale. In the past two decade, LC-EM was widely used for imaging inorganic nanowires/nanoparticles[76–79] and cellular proteins labeled by gold nanoparticles/quantum dots.[80,81] Furthermore, dynamics analysis of organic self-assembly by LC-EM was launched.[8,9,82–90]

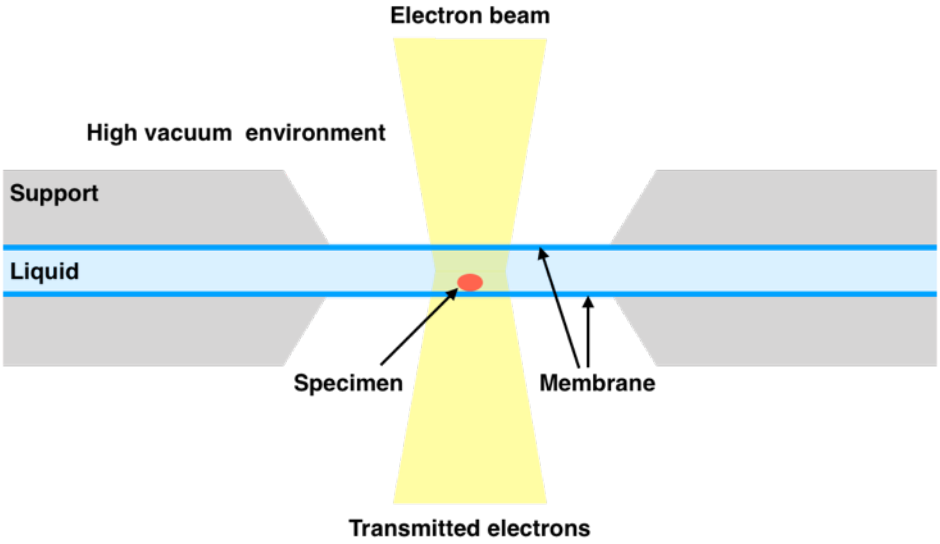

Figure 5. Schematic illustration of a liquid cell and a liquid specimen for LC-TEM imaging.

In 2014, Gianneschi and coworkers used LC-TEM to observe the dynamics of organic micellar nanoparticles in real time for the first time.[82] A norbornene based amphiphilic block copolymer was modified with Pt(II)-complex unit in order to facilitates good contrast for LC-TEM. The time-lapse images with a maximum time frame rate of 25 frames/s successfully captured the motion of the nanoparticles with a diameters of *ca.* 100 nm. In 2017, the same group followed the motion of amphiphilic block copolymer micelles without metal-loading by LC-TEM (Figure 6A–L).[83] They successfully conducted to directly visualize nanoscale dynamic events such as micelle-micelle fusion (Figure 6H–L), non-fusion collisions, micelle growth by unimer incorporation. It is noted that the inner structure of the fused micelle could not be characterized by LC-TEM (Figure 6C) unlike by cryo-TEM (Figure 6G) that has the higher spatial resolution, clearly implying that the combination use of LC-EM and cryo-EM is important to accurately evaluate behaviors of nanoscale soft materials. LC-EM is suitable to study the dynamic process of MOF,[91] since the incorporation of metal is appropriate for low electron beam LC-EM imaging with high contrast.[74] In 2015, Patterson *et al*. observed ZIF-8 in real time by LC-TEM.[92] The LC-TEM movie over 11 min showed the nucleation and growth process of ZIF-8 nanoparticle without the coalescence. Importantly, the formation kinetics and structures were consistent to that obtained in bulk without liquid cell and electron beam radiation.

LC-EM is powerful to visualize nanoscale dynamic events of a solute-rich liquid droplet, called coacervate, formed by liquid-liquid phase separation.[84,85] In 2019, Ianiro *et al*. directly examined the vesicle formation process of amphiphilic artificial molecules through liquid-liquid phase separation by use of LC-TEM.[84] They selected poly(ethylene oxide)-block-poly(caprolactone) (PEO-*b*-PCL) as a model for *in situ* imaging study because this polymer was determined by theoretical prediction to be appropriate in solvent switch induced vesicle formation through liquid-liquid phase separation. They continuously obtained the images for 900 s with an interval of 1 s, capturing the formation process of the vesicles with a final diameter of *ca*. 150 nm (Figure 6M–O). At 46 s after starting observation, a low contrast homogeneous coacervate could be imaged. Subsequently, LC-TEM visualized the gradual formation of some distinct spherical structures (130, 242 s) which then coalesced to form a continuous membrane at the edge of the coacervate (912 s). These observations indicated that the PEO-*b*-PCL initially formed a coacervate that acted as a precursor of micelles, which further transformed into a vesicle (Figure 6P).

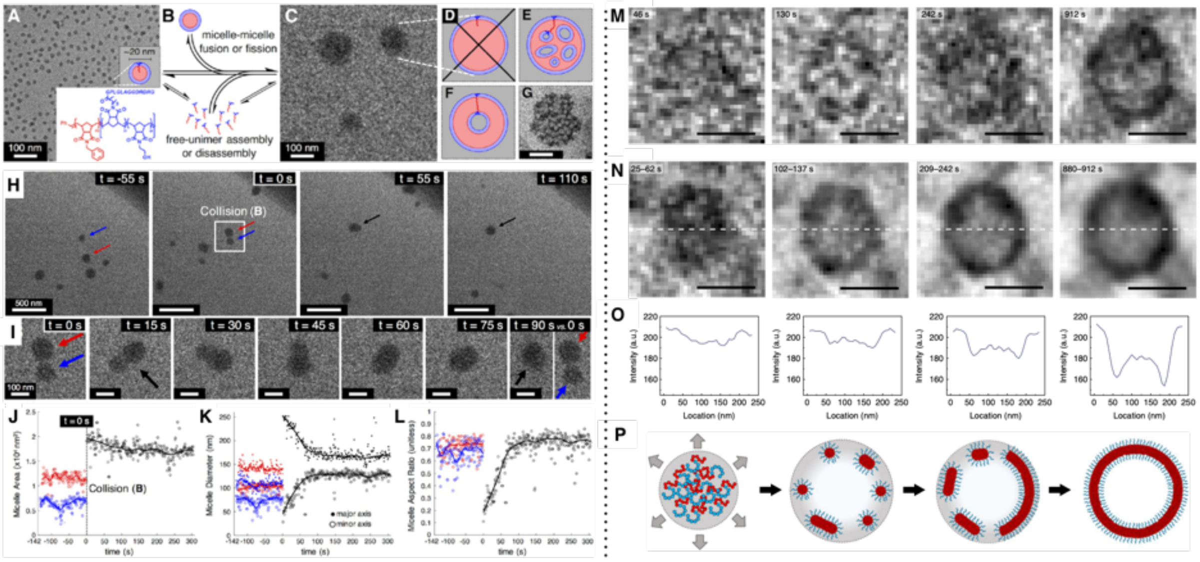

Figure 6. LC-EM imaging of organic molecular assemblies. (**A**–**G**) Evolution of micelles in solution. (**A**) Cryo-TEM image of the initial small micelles. (**B**) Schematic illustration of the size evolution process. (**C**) LC-TEM image of the large micelles. (**D**, **E**, **F**) Potential internal structures supposed by LC-TEM image (**D** is not possible for the unimer). (**G**) Cryo-TEM image of the large micelles. Scale bar: 100 nm. (**H**–**L**) Micelle fusion in solution. (**H**) LC-TEM time-lapse images of fusion process of two micelles. (**I**) Enlarged images of white square in (**H**). (**J**) Micelle area plot. (**K**) Micelle width plot. (**L**) Micelle aspect ratio plot. Reproduced with permission from ref 83. Copyright 2017 American Chemical Society. (**M**–**P**) Coacervate mediated vesicle formation from PEO-*b*-PCL. Scale bars: 100 nm. (**M**) LC-TEM images of the formation process of the vesicle. (**N**) 30 frame average time series images of (**M**). (**O**) Line plot intensity profiles along the white dashed line in (**N**). (**P**) Schematic illustration of formation process of the vesicle. Reproduced with permission from ref 84. Copyright 2019 Springer Nature.

For time-resolved imaging of organic molecules by LC-EM, influences of the electron beam damage should be carefully considered. Touve *et al.* imaged stimuli-induced self-assembly of a cyclic peptide by LC-TEM.[86] They evaluated whether the electron beams affected the final chemical structure of specimens using matrix assisted laser desorption ionization imaging mass spectroscopy (MALDI-IMS) for the first time. The experiments were conducted in three steps (Figure 7). First, the peptide in a liquid cell is continuously imaged by LC-TEM with and without stimulus. Second, the liquid cell is separated into two silicon nitride membranes and the sample on the membranes is dried. Third, the MALDI-IMS imaging with a 50 μm laser probe diameter is performed after spraying a matrix. After they obtained the MALDI-IMS spectra under the various conditions with varying electron beam flux (0.11 ± 0.07 to 27.8 ± 5.7 $\text{e}^{-}\ \text{Å}^{-2}\ \text{s}^{-1}$) and the time length (10 min to 1 h), the most feasible conditions were determined for imaging the peptide without electron-induced damage.

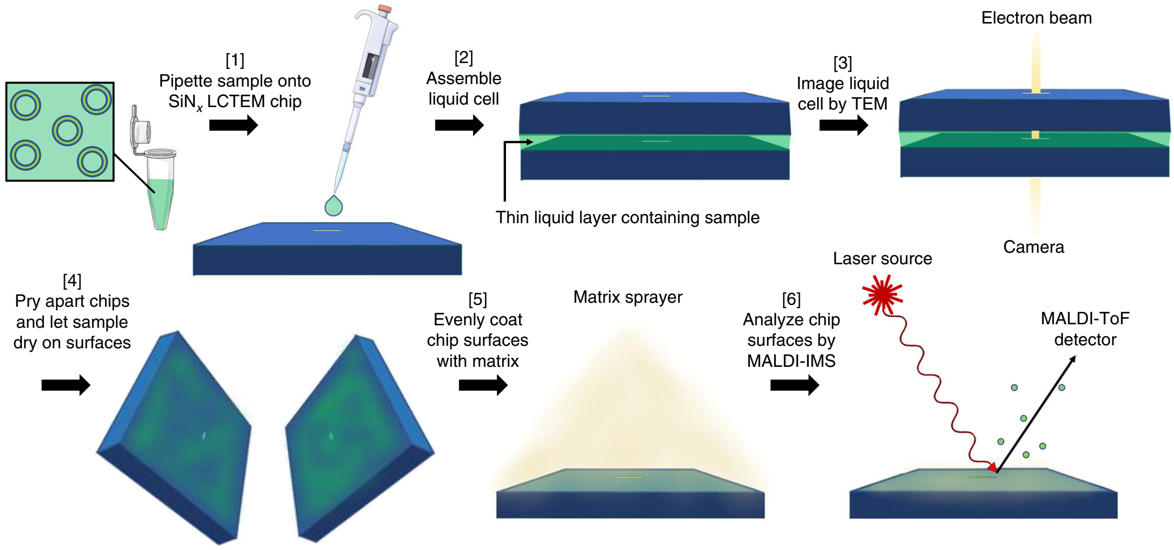

Figure 7. Schematic illustration of LC-TEM imaging with MALDI-IMS post-mortem analysis. Reproduced with permission from ref 86. Copyright 2019 Springer Nature.

Therefore, LC-EM is a valuable technique for capturing motion of nanoscale molecular assemblies formed by very weak interactions in real time. This should be an important advantage of LC-EM compared with the below-mentioned high speed AFM that inevitably requires mechanical invasions. LC-EM could greatly contribute to determine formation mechanisms of a variety of molecular soft-assemblies.

4. Atomic force microscopy

AFM, a scanning microscopy which detects the atomic force between the tip and sample surface, was developed in 1986.[93] AFM has been a promising tool for tracking motion of native cells and proteins because it can image objects in water at nm resolution.[1,94–98] It turned out that AFM is also important for imaging many of natural and artificial molecular self-assemblies.[99–101] One of the unique features of AFM represents its ability to image objects with various physical and chemical parameters.[1,102,103] In molecular self-assemblies, for example, mechanical strength of the nanostructures were investigated by AFM. In recent years, high speed AFM (HS-AFM) that has both high spatial- and temporal-resolutions has been actively utilized to monitor the dynamics of a variety of specimens including supramolecular polymers.[10–12,104,105] In this chapter, we initially focus on imaging artificial molecular assemblies by conventional AFM, followed by introduction of dynamics analysis of molecular assemblies with HS-AFM.

4.1. Dried sample imaging

There are two methods in AFM imaging: (1) imaging pre-dried samples on substrate surface; (2) imaging wet samples without dryness (*in situ* AFM). We here started to describe imaging of dried samples.

In the late 1980s, AFM imaging of nanostructures of various biomolecular assemblies launched, such as actin filaments and DNA double strands.[106–108] AFM was subsequently applied for imaging artificial molecular assemblies. As an early example, Kohori *et al.* observed thermally responsive block copolymer micelles by AFM.[109] The block copolymer was composed of poly(*N*-isopropylacrylamide) (PNIPAM) and poly(DL-lactide). PNIPAM is well known to aggregate in water above lower critical solution temperature (LCST) (32 °C) due to dehydration.[110] The AFM image of the copolymer after drying on mica at 4 °C showed the well-dispersed individual micelles. In contrast, the AFM images after drying at 40 °C clearly visualized the aggregates of the micelles that were seen on a limited part of the mica substrate. In the early 2000s, supramolecular polymers were visualized by AFM.[111–113] Schenning *et al.* applied AFM for imaging a supramolecular polymer that was formed by co-assembly of an oligo(*p*-phenylenevinylene) (OPV) derivative and a perylene bisimide (PBI) derivative.[111] UV/Vis, fluorescence, and CD experiments in methylcyclohexane (MCH) clearly suggested that the OPV and PBI derivatives co-assembled at 2:1 ratio by hydrogen boding and π-π interactions into formation of J-aggregates with helical screw sense. AFM images of the dried sample on the glass substrate showed 7 nm width helical nanofibers and their entangled bundles. The 7 nm width agreed well with the length of the one OPV-PBI-OPV derivatives complex. Based on the combined results of spectroscopic analyses with AFM imaging, the authors were able to present a possible molecular arrangement model of the supramolecular polymer. AFM is now in common use for imaging supramolecular polymers. As one of the most recent examples, Yagai and coworkers imaged various unique nanostructures of artificial supramolecular polymers after deposited/dried on substrate surface.[114] They constructed polycatenanes comprising supramolecular polymer toroids and succeeded in their direct imaging with AFM.[115] The monomer that has a barbiturate head, an aromatic linker and a nonpolar tail initially forms six-membered macrocycles through hydrogen bonding of barbiturate moieties (Figure 8A). Then, the macrocycles vertically stack by π-π interaction between aromatic linkers into construction of supramolecular polymers with various morphologies including toroids, helicoids, and random coils. Spectroscopic analysis showed that the toroids greatly promoted the supramolecular polymerization, and molecular simulation experiments revealed that the toroid surface had strong affinity to the trimer of six-membered macrocycles to act as secondary nucleation sites for the formation of new toroids. The authors performed ten-portion injection experiments in order to afford polycatenanes (Figure 8B). The AFM imaging clearly showed construction of polycatenanes, among which the longest polycatenanes were 22-members one (Figure 8C).

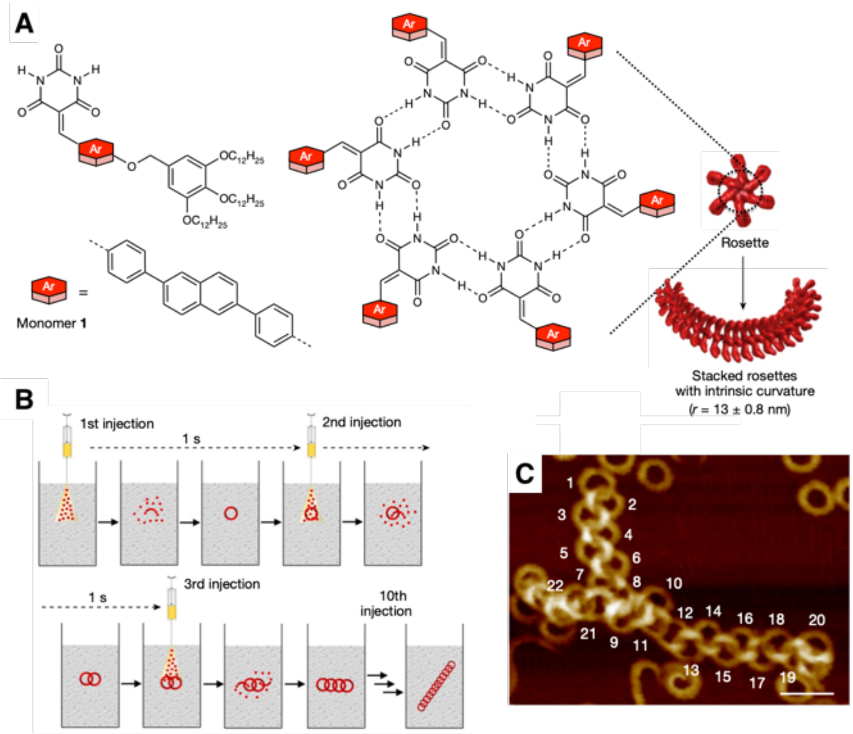

Figure 8. Self-assembled polycatenane from supramolecular toroids. (**A**) Chemical structure of a monomer and schematic illustration of formation of a supramolecular nanostructure with intrinsic curvature via six-membered rosette. (**B**) Schematic illustration of 10-portion injections method to efficiently construct polycatenanes. (**C**) AFM image of the polycatenane. Scale bar: 50 nm. Reproduced with permission from ref 115. Copyright 2020 Springer Nature.

Imaging with various chemical and physical parameters is available by AFM.[1,102,103] Force distance curve AFM (FD-AFM) has been performed to measure Young's modulus of supramolecular nanostructures.[116–121] In FD-AFM, the AFM tip initially approaches to and subsequently retracts from objectives at an arbitrary *xy* point (Figure 9A).[1] In 2005, Kol *et al.* measured a mechanical property of supramolecular nanotubes made of diphenylalanine (Phe-Phe), a well-known β-sheet forming peptide.[117] The sample was prepared by diluting the peptide stock solution in an organic solvent with ultrapure water followed by drying on a mica surface. By AFM imaging, the diameters of the nanotubes were determined to be 80 to 300 nm (Figure 9B). FD-AFM experiments were performed at the center of the single nanotubes to determine that the averaged Young's modulus of the nanotubes was 19 GPa

(Figure 9C). This value is much higher than that of most biological nanostructures such as microtubules.[116] In 2019, Bera *et al*. measured Young's modulus of Pro-Phe-Phe that was selected by computationally analysis to be the most aggregation-prone tripeptide of 8000 candidates.[121,122] CD spectrum of Pro-Phe-Phe in a phosphate buffer at pH 7.4 exhibited negative peaks at 210 nm and 224 nm and a positive peak at 198 nm, indicating that Pro-Phe-Phe self-assembled to form a helical structure unlike Phe-Phe. Single crystal X-ray analysis revealed that the tripeptide indeed formed a helical sheet which was stabilized by hydrophobic interactions of Phe residues. FD-AFM measurement determined the Young's modulus of the nanofiber to be 44 GPa (Figure 9D). The substitution of Pro residue to hydroxyproline (Hyp-Phe-Phe) increased the Young's module to be 108 GPa due to an additional hydrogen bonding with negligible conformational change (Figure 9E). These results demonstrated that the helix-like peptide conformation achieved one of the stiffest nanostructures in biological molecular assemblies (Figure 9F).

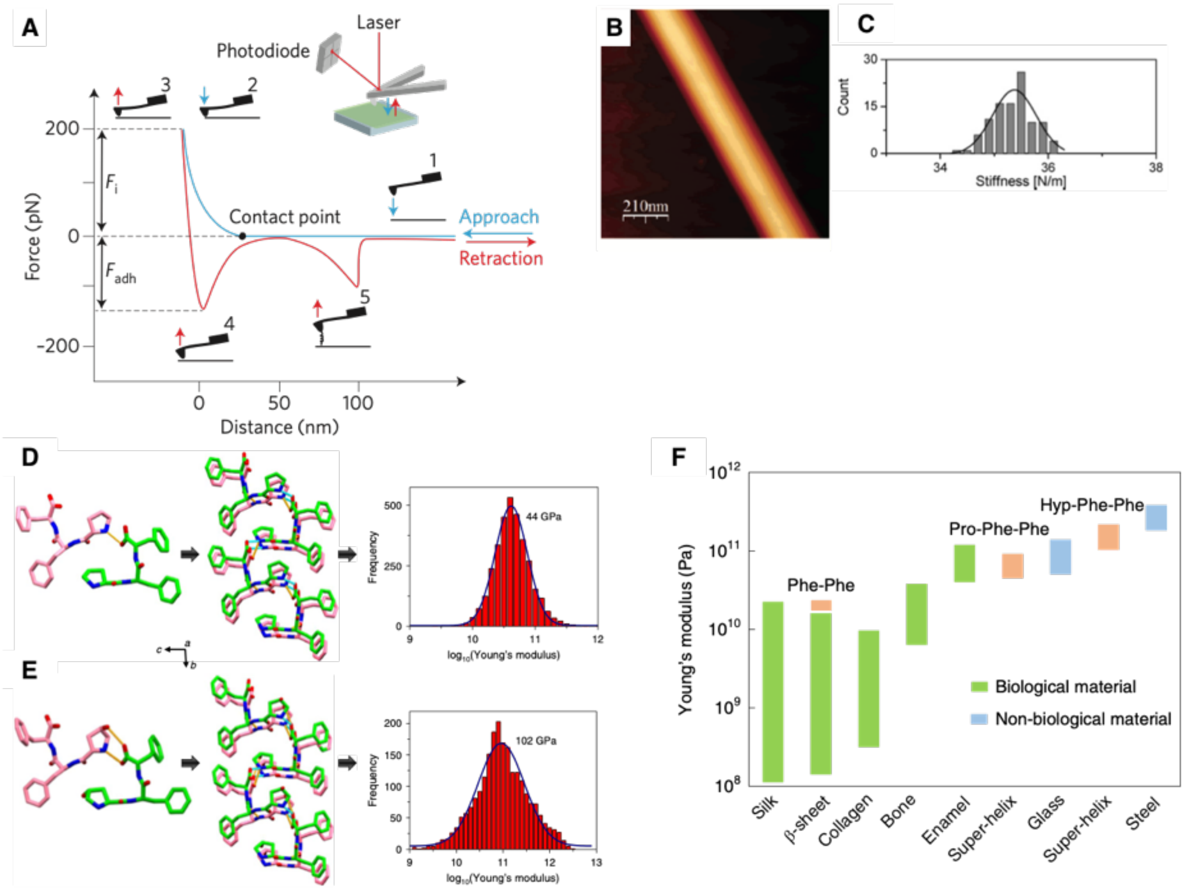

Figure 9. (**A**) Schematic illustration of FD-AFM. Reproduced with permission from ref 1. Copyright 2017 Springer Nature. (**B**) AFM image of a Phe-Phe nanotube. (**C**) 100 Phe-Phe nanotubes spring constants measured by FD-AFM. Reproduced with permission from ref 117. Copyright 2005 American Chemical Society. (**D**, **E**) Packing structures and Young's moduli of (**D**) Pro-Phe-Phe and (**E**) Hyp-Phe-Phe. Yellow lines indicate hydrogen bonds. (**F**) Comparison of Young's moduli of materials. Reproduced with permission from ref 121. Copyright 2019 Springer Nature.

4.2. *In situ* imaging

In situ AFM allows direct observation of specimens without drying and thus is suitable for capturing self-assembly processes in real time. As a pioneering example, Manne and coworkers started to use *in situ* AFM for imaging surfactant self-assemblies at solid-liquid interfaces.[123–125] In 1995, this group reported the AFM imaging of cationic surfactant assemblies on various substrates in aqueous solution.[124] AFM images showed that the cationic surfactant, tetradecyl trimethyl ammonium bromide (C14TAB), self-assembled into three different structures, half cylinders, full cylinders, and spherical aggregates, the morphologies of which depended on the substrates, highlighting that the substrate surfaces could affect the morphologies and formation kinetics of molecular assemblies in AFM imaging.

In addition, one should be careful that the tip-sample interactions sometimes cause sample damages in AFM observation in general. On the other hand, some of the researchers actively applied this relatively strong mechanical force to break molecular assemblies.[126–129] In 2008, Yang *et al*. reported the mechanical-force-induced supramolecular polymerization of a 16 residue peptide, EAK16-II (Figure 10A).[127] The EAK16-II peptide nanofiber deposited on a negatively charged mica surface (Figure 10B) was broken into fragments by AFM tip in water. AFM images thereafter clearly showed the seeded growth of many nanofibers from the fragments (Figure 10C, D, E, F). This is the first report to use AFM mechanical manipulation for growth of peptide nanofibers. In 2016, Jin *et al*. used *in situ* AFM to visualize lipid membrane mimetic 2D materials of self-assembled amphiphilic peptoids which are oligo-glycine analogues with *N*-substituents (Figure 10G).[129] Simple crystallization induced by evaporation constructed a stable, free standing, and lipid bilayer-like 2D peptoid membrane as shown by AFM. Also, the authors monitored by the time-dependent *in situ* AFM images that the peptoid self-assembled on mica into a non-defect single layer membrane over 25 min in water (Figure 10H, I, J). Finally, self-repairing event of the peptoid membrane after generation of defects with AFM tip was visually confirmed by *in situ* AFM (Figure 10K, L, M). In 2017, Ma *et al.* also used *in situ* AFM to elucidate the crystallization pathways of peptoids.[130] Their careful AFM height imaging demonstrated that the peptoid self-assembly on substrate surface was a two-step process and the slight substitution of the peptoid sequence altered the pathway to a simple single step process.

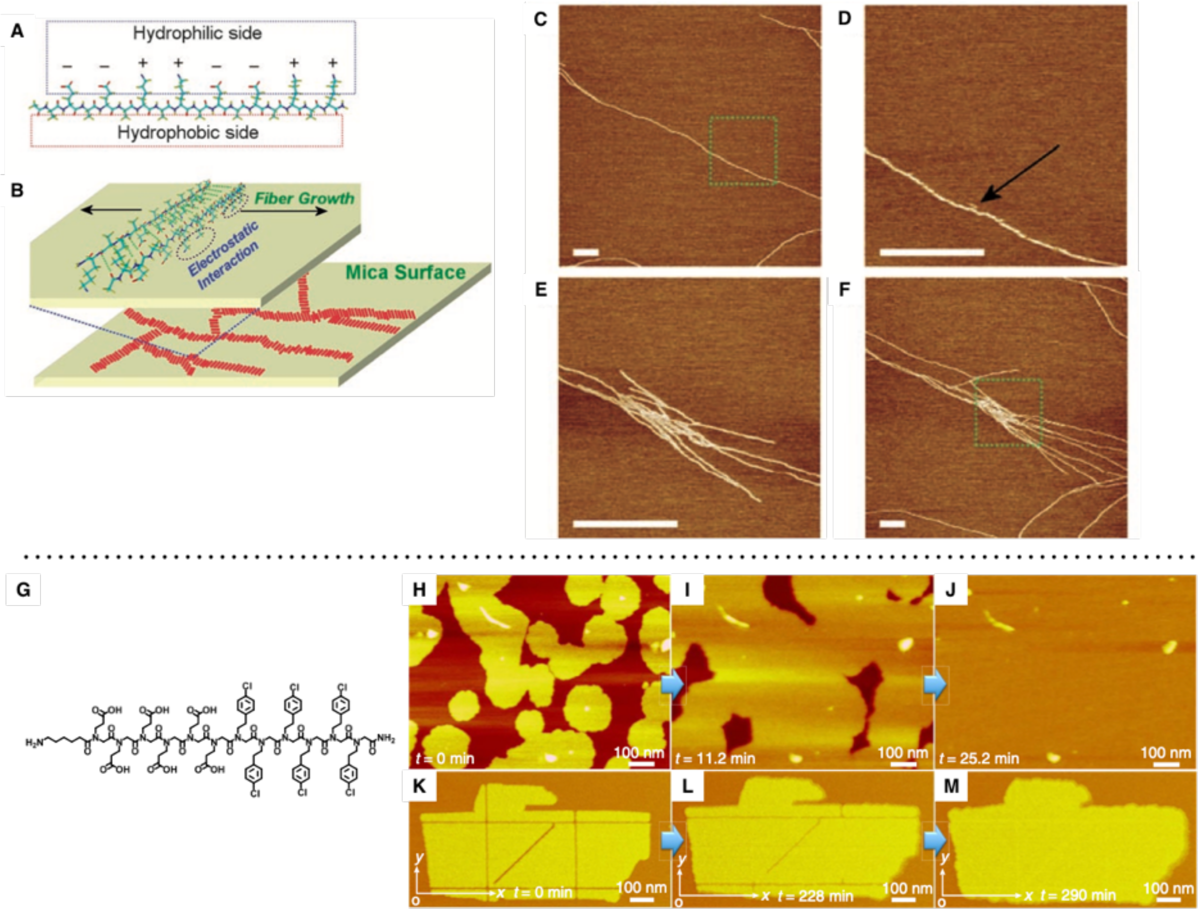

Figure 10. *In situ* AFM imaging with mechanical manipulation. (**A**) Molecular structure of EAK16-II. (**B**) Schematic illustration of interaction between EAK16-II fibers and a mica surface. (**C**) AFM image of EAK16-II fibers on mica. (**D**) Enlarged image of a green square

in (**C**). Black arrow indicates a fragment fiber produced by tip-fiber interaction while imaging. (**E**) AFM image after three times scan at the same location as (**D**) showing many growing fibers. (**F**) Lower magnification AFM image after the manipulation. Scale bars: 200 nm. Reproduced with permission from ref 127. Copyright 2008 Wiley-VCH. (**G**) Chemical structure of a peptoid. (**H**, **I**, **J**) *In situ* AFM images of formation process of a single layer peptoid membrane on mica. (**K**, **L**, **M**) *In situ* AFM imaging of self-repairing process of peptoid membrane on mica after producing defects. Reproduced with permission from ref 129. Copyright 2016 Springer Nature.

AFM is powerful to visualize 2D DNA origami structure in solution. DNA origami is well-ordered designer 2D or 3D nanoarchitectures formed by self-assembly of a long single stranded DNA (scaffold strand) and numerous short DNA oligonucleotides (staple strands).[131–133] In 2006, Rothemund first proposed a rational design strategy of DNA origami.[134] *In situ* AFM allowed to observe the designer six shapes of 100 nm-sized DNA origami such as a star and a disk with three holes. In addition, various words and pictures decorated on the DNA origami by mixing unusual staple strands were clearly visualized by AFM with the extremely high vertical resolution. DNA origami is expected to be an invaluable template to arrange functional molecules with intended positions and distances regulated by a variety of molecular interactions such as aptamer-protein interactions, DNA/RNA hybridizations, or protein-ligand interactions.[135–144] Such hybrids have been applied to detect biomolecules and construct spatially-confined chemical/enzymatic reaction systems. In 2008, Ke *et al.* reported DNA origami-based label free sensing of RNA (Figure 11A).[138] The authors constructed DNA origami tiles, each of which had a different topographic index at one side and six RNA-targeted probes in a line at the other side (Figure 11B, top). Owing to the barcoded index, the DNA tiles were clearly distinguishable by AFM imaging (Figure 11B, middle). An equimolar mixture of the four DNA origami that included three RNA-targeted tiles and a control tile without RNA adsorption ability were used for RNA detection experiment, and high specific RNA detections were confirmed by AFM imaging (Figure 11B, bottom). The specific RNA detection was not inhibited in the presence of 2 mg/mL cellular RNA. Furthermore, the titration experiment revealed that the hybridization efficiency of target RNA and probes are approximately 100% even when the concentration of DNA tile was only 200 pM. In 2010, Voigt *et al.* reported site specific single-molecules chemical reactions on DNA origami and their imaging with AFM.[141] On a DNA origami template, 12 biotin molecules were placed at predefined positions via three distinct linkers, that is linker A was not cleavable, linker B and C contained reduction-triggered and single oxygen-triggered cleavage sites, respectively. The AFM image clearly visualized well-ordered 12 streptavidin molecules on the single DNA origami after incubation with an excess of streptavidin (Figure 11C, left). Addition of DTT (dithiothreitol, a reducing agent) showed the disappearance of four streptavidin at the positions corresponding to linker B (Figure 11C, center). The selective removals of streptavidin attached thorough linker C were observed by AFM with white light irradiation in the presence of singlet oxygen photosensitizer eosin (Figure 11C, right). The authors also demonstrated that Cu(I) click chemistry and a condensation reaction followed by streptavidin binding took place on the designer DNA origami surface, which can be monitored by AFM at a single molecule level (Figure 11D). The reactions with biotinylated *N*-hydroxysuccinimide (NHS) or biotinylated azide/alkyne with Cu(I) catalyst followed by incubation with streptavidin accomplished 84–90 % yields and non-specific streptavidin presentation was not observed in more than 600 origami investigations. These results demonstrated that post-assembly chemical reaction is a reliable strategy for selective and efficient manipulation of functional molecules on DNA nanostructures.

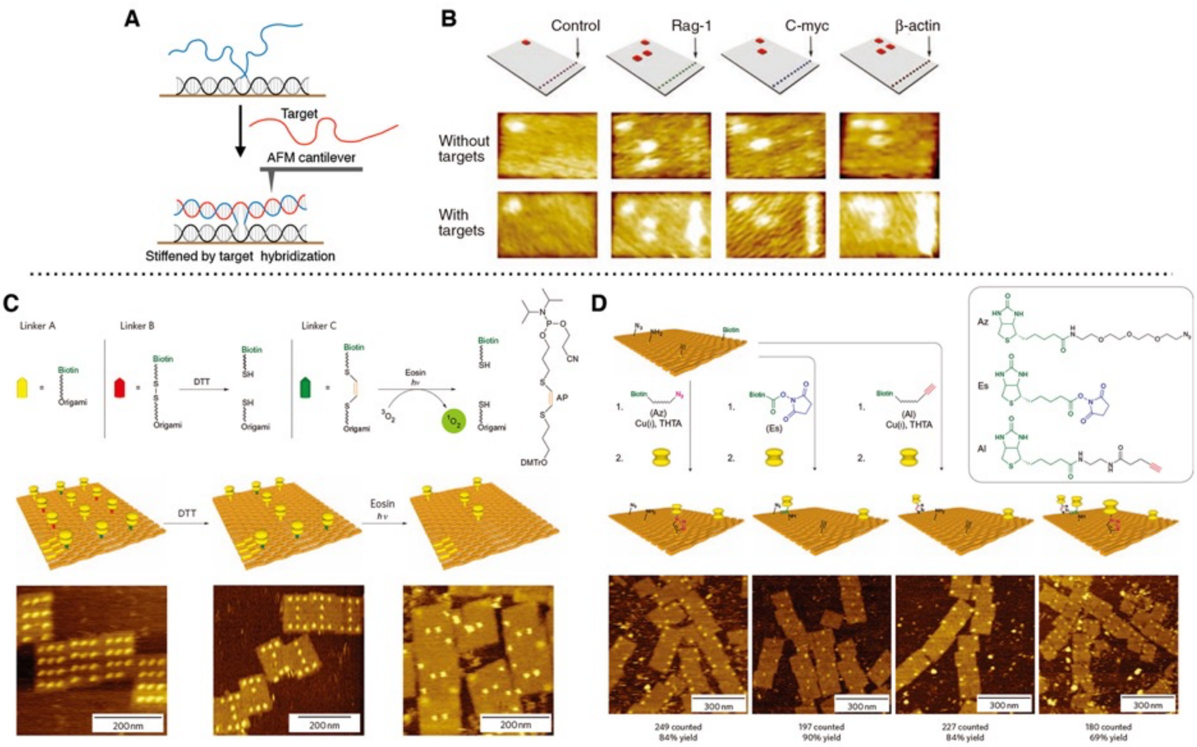

Figure 11. (**A**, **B**) DNA origami based RNA sensor. (**A**) Schematic illustration of target DNA detection by AFM imaging. (**B**) AFM images of DNA origami sensors with and without treatment of target DNA. Reproduced with permission from ref 138. Copyright 2008 AAAS. (**C**, **D**) (**C**) Removal and (**D**) presentation of streptavidin molecules on intended locations in a DNA origami by using single molecule chemical reactions. Reproduced with permission from ref 141. Copyright 2010 Springer Nature.

Dynamic self-assembly/disassembly of DNA origami have been also visualized in the same field of view of AFM with continuous temperature change. In 2012, Song *et al.* directly observed the collapse process of a rectangular DNA origami by *in situ* AFM with stepwise elevation of temperature.[145] The height profiles of images showed that the disassembly was initiated at 55 °C and completed at 75 °C. They also attempted to capture the reassembly process of the DNA origami by temperature decrease in the presence of excess staple strands. During a cyclic temperature change with heating to 72 °C and subsequently cooling to room temperature, the AFM images captured the process of partial disassembly followed by complete recovery of the DNA origami structure (Figure 12). This is the first report to image formation process of DNA origami *in situ.*

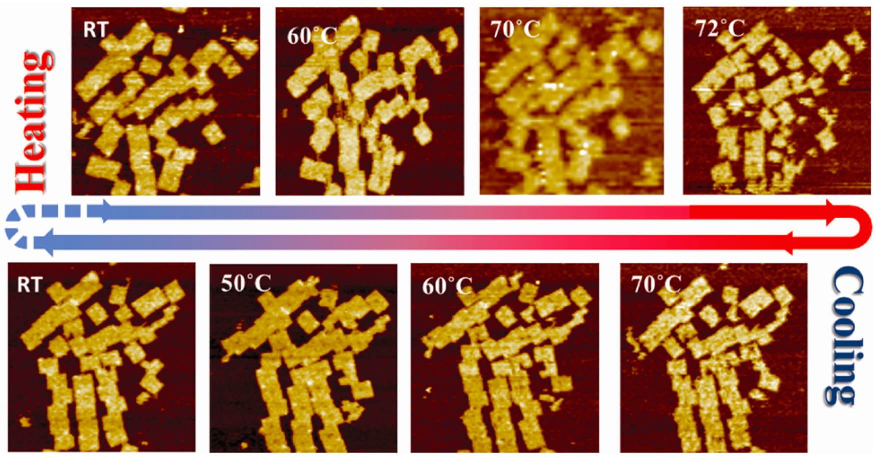

Figure 12. *In situ* AFM imaging of thermal response of DNA origamis. Reproduced with permission from ref 145. Copyright 2012 American Chemical Society.

AFM enabled to image the surface morphology of hydrogels in water.[146–149] In 1996, Suzuki *et al.* first reported direct observation of hydrogel surfaces using *in situ* AFM.[146] The authors investigated impact of cross-linking density on the surface structure of a polyacrylamide (PAAm) hydrogel. The AFM images of the standard PAAm hydrogel surfaces showed 10 nm sized sponge-like domains, while the sponge-like domains became less clear by increasing the cross-linking density (4-fold). The temperature effect on a PNIPAM hydrogel was also evaluated by *in situ* AFM. At 25 °C, AFM study of the PNIPAM hydrogel surface visualized many of sponge-like structures with larger size than that of PAAm gels. By increasing the temperature to 38 °C, the sponge-like domain became more clear because of the aggregation of PNIPAM. In 2019, de Almeida *et al.* observed the surface of a fully-synthetic hydrogel consisted of stress-responsive hydrogel network of polyisocyanide (PIC) and thermo-responsive linear chain of PNIPAM by *in situ* AFM (Figure 13).[149] The hybrid hydrogel showed the heat-induced stiffness change around LCST of PNIPAM without contraction. In particular, the hybrid hydrogel composed of 17 mg/mL PIC and 1 mg/mL PNIPAM exhibited the 51-fold increase of the storage modulus by only a 5 °C increase and the stiffness change of the hydrogels was completely reversible. AFM images of the hydrogel at 25 °C showed the smooth surface, while the roughness of the surface significantly increased due to the clustering of PNIPAM by the temperature increase to 40 °C. Such heat-induced surface roughness change was not observed in a PIC hydrogel.

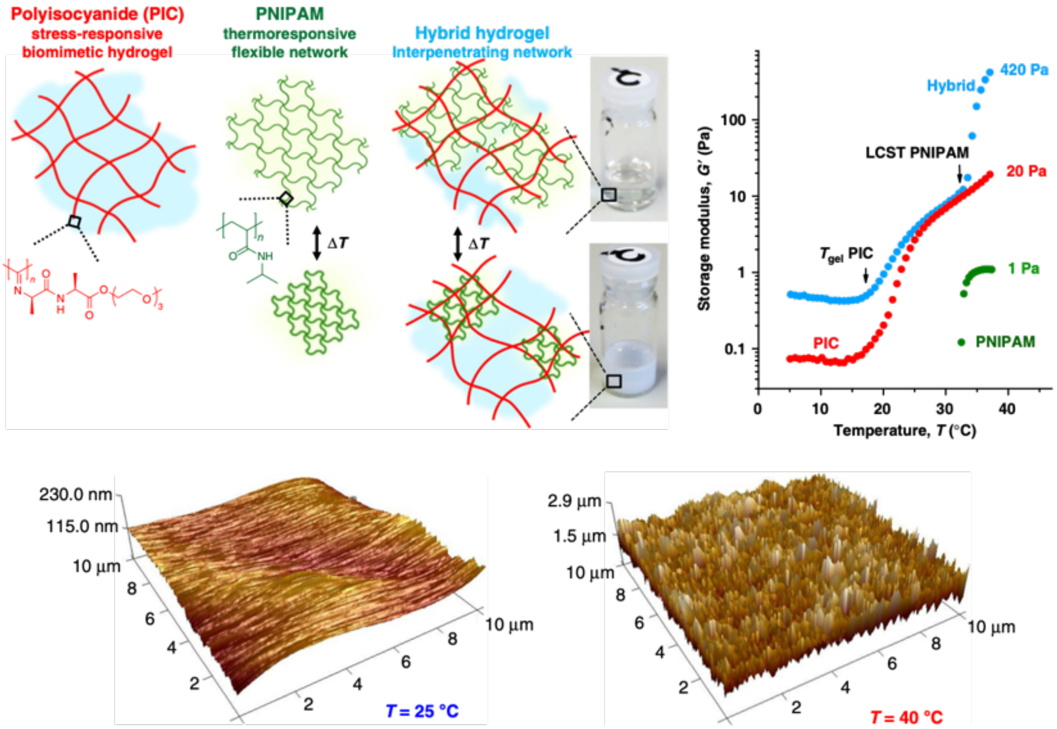

Figure 13. Temperature dependent changes of rheological property and surface roughness of PIC-PNIPAM hybrid hydrogel. Reproduced with permission from ref 149. Copyright 2019 Springer Nature.

AFM measurement is able to provide mechanical maps of hydrogel surfaces.[150–156] In 2011, Ouasti *et al.* reported µm-sized mechanical maps of hybrid hydrogels derived from thiolated hyaluronic acid and polyethylene glycol (PEG) diacrylate.[152] After preparation by photo-radical polymerization, the hydrogels were swollen in phosphate buffered saline (PBS) and applied to Young's modulus measurements by AFM. The force maps of the hydrogels showed that the surface Young's modulus was decreased by increasing the hyaluronic acid concentration and the molecular weight. Furthermore, the trend was consistent with storage modulus of the bulk hydrogels determined by oscillatory rheology experiments. Importantly, the Young's modulus in each hydrogel was mostly homogeneous in 10 µm × 10 µm square, ensuring that the hydrogels could be considered as mechanically homogeneous materials in the further cell experiments. In 2017, Aziz *et al.* provided mechanical maps of two-layered hydrogels, in which each layer had distinct mechanical properties due to the difference of monomer concentrations.[154] First, the single layer hydrogels were fabricated by thiol-ene photo-polymerization of 10 wt% (hydrogel I) or 25 wt% (hydrogel IV) 8-arm PEG-norbornene monomer and 4-fold molar PEG-dithiol crosslinker in water containing 0.05 % photo initiator. The average Young's moduli of the individual hydrogels surface were determined to be 78 kPa (hydrogel I) and 244 kPa (hydrogel IV) by AFM (Figure 14C). The two-layer hydrogel was fabricated by a step-wise protocol. The hydrogel IV was initially formed and then the precursor solution of hydrogel I was carefully deposited on the hydrogel IV followed by photo-polymerization, resulting in formation of the two-layer hydrogel (Figure 14A, B). The AFM mechanical map demonstrated that the Young's modulus of the layered hydrogel gradually altered from stiff (hydrogel IV) to soft (hydrogel I) layer without discontinuous mechanical transitions (Figure 14D).

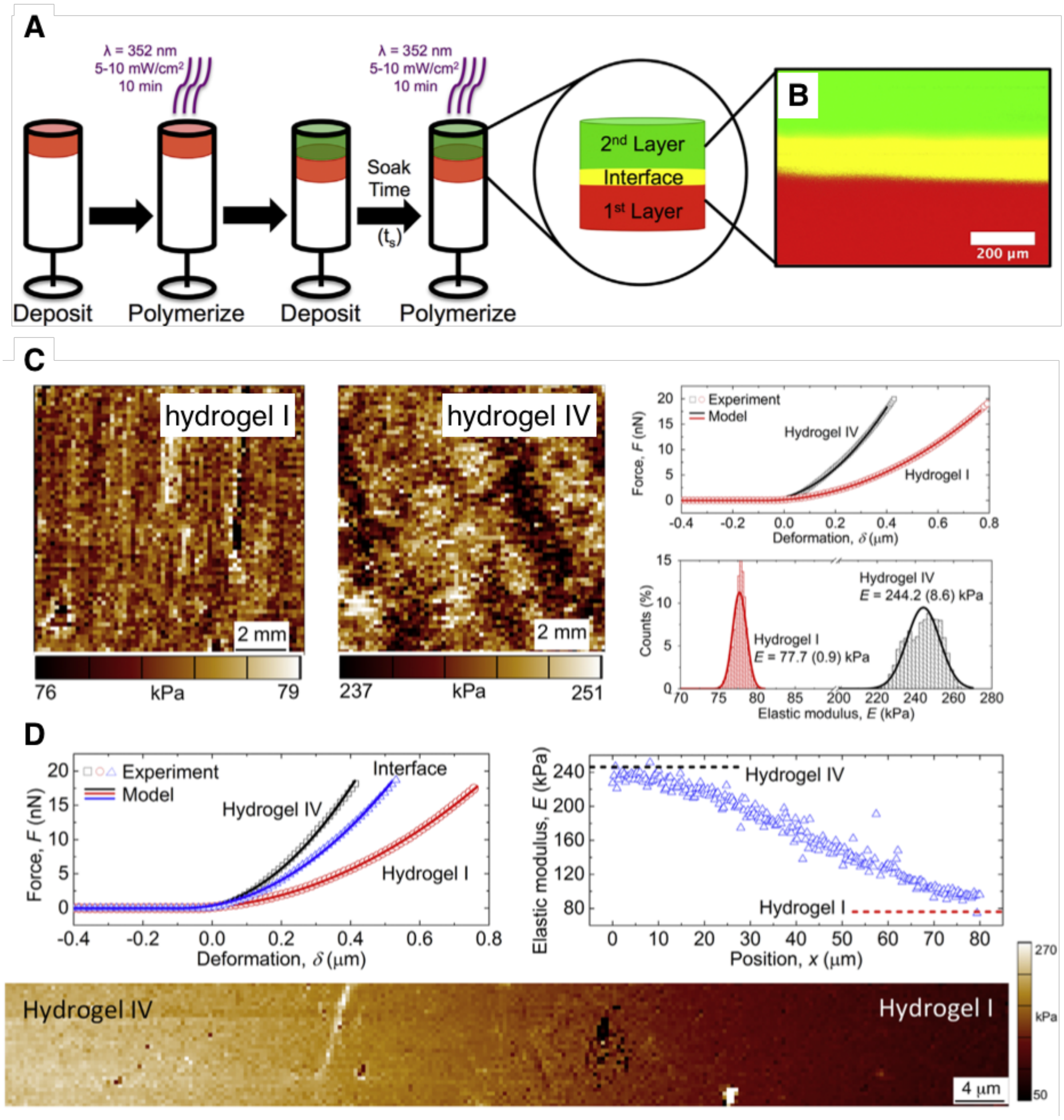

Figure 14. (**A**) Schematic illustration of preparation of the two-layered hydrogel by sequential photo-polymerization. (**B**) CLSM image of the two-layered hydrogel. (**C**) AFM mechanical map of hydrogel I and hydrogel IV. (**D**) AFM mechanical map of the two-layered hydrogel. Reproduced with permission from ref 154. Copyright 2017 Elsevier.

4.3. HS-AFM imaging

HS-AFM that allows imaging of wet specimens with nanometer resolution at an interval time of 100 ms was developed in 2008.[157,158] HS-AFM is now an invaluable technique to capture the fast motion of native proteins at molecular level. In the past decade, HS-AFM has greatly contributed to unveil dynamics of a wide variety of biomolecular systems.[159–164] For more details on HS-AFM imaging of protein complex, excellent reviews were previously reported.[10–12] In this section, we focus on HS-AFM imaging of dynamic assembly/disassembly process of proteins complexes and other synthetic supramolecules.

The dynamic 2D assembly process of Annexin V on surface of lipid bilayers was investigated by HS-AFM.[165–167] Annexins, abundant cytoplasmic proteins, bind to negatively charged lipid membranes in response to Ca^{2+} ions, which is involved in many membrane-related cellular functions.[168] In 2016, Miyagi *et al.* succeeded in tracking assembly and disassembly of annexin V 2D lattice with HS-AFM by real-time bidirectional control of effective Ca^{2+} ions concentration.[165] In the pumping system, the flow rate of solutions in the fluid cells can be altered at a range of 0.01 to 1 μL/s, allowing fine control of buffer components such as Ca^{2+} ions and ethylenediaminetetraacetic acid (EDTA) (Figure 15A). Also, the pulsed laser system can trigger the local release of Ca^{2+} ions from the caged Ca^{2+} with high spatiotemporal resolution. The AFM image showed the appearance of well-ordered annexin lattices in the presence of 2 mM $CaCl_2$, which was completely collapsed by injection of 40 mM EDTA (Figure 15B). The local UV irradiation for the Ca^{2+} ions release resulted in partial reconstruction of the lattice in the photo-irradiation field, and following incubation without UV laser induced disassembly of the lattice again. The dynamic process could repeatedly be observed several times. Self-assembly/disassembly processes of 2D DNA origami were also imaged by HS-AFM.[169–171] Suzuki *et al.* used HS-AFM to observe self-assembly of DNA origami on lipid-bilayer supported mica (Figure 15C).[170] The cross shaped DNA origami was designed to have four blunt ends for linkage. In addition, self-assembly of the DNA origami on lipid-coating mica was assisted by appropriately moderate electrostatic interactions in the presence of magnesium ions. HS-AFM of the DNA origami successfully visualized the formation process of large and high-ordered lattices, unveiling there are several steps including fusion of smaller lattices, reorganization by association and dissociation coupling, and defect filling by monomers association (Figure 15D).

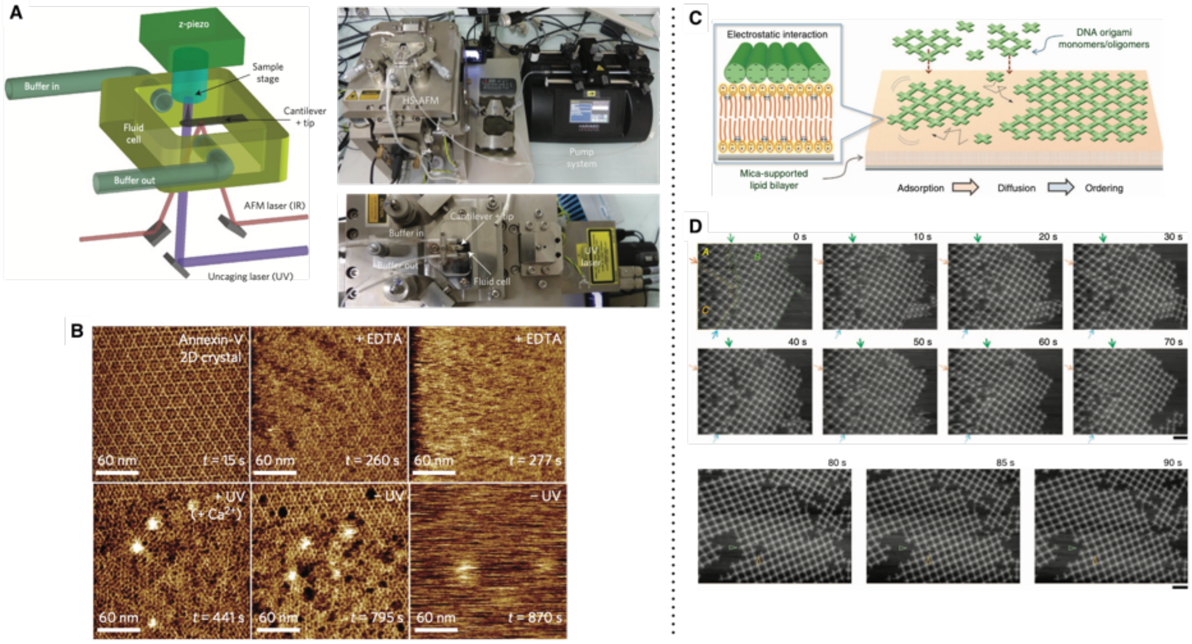

Figure 15. (**A**) Schematic illustration and photos of HS-AFM with a pump system and a UV laser system. (**B**) HS-AFM images of dynamic assembly/disassembly of Annexin-V 2D crystal. Reproduced with permission from ref 165. Copyright 2016 Springer Nature. (**C**) Schematic illustration of DNA origami assembly on lipid-coating mica. (**D**) Time-lapse HS-AFM images of large DNA origami lattices formation. Scale bars: 200 nm. Reproduced with permission from ref 170. Copyright 2015 Springer Nature.

Many researchers sought to monitor the dynamics of protein-based supramolecular nanofibers such as cytoskeletons and amyloid fibrils using HS-AFM.[172–178] As an early example, Yamamoto *et al.* directly imaged actin polymerization by HS-AFM at a frame rate of 0.25 s in 2009 (Figure 16A).[172] Actin filament is well known to have structural polarity and the two ends exhibit different polymerization kinetics.[179] The authors broke an actin filament by increasing the contact force to produce both plus and minus ends of actin filament in the field of HS-AFM view. The filament growth occurred at one end, while the growth did not occur at the other end, clearly indicating that the former and the latter end were plus and minus end, respectively. The growth rate of plus end was determined to be 0.11 μm/min by HS-AFM observation, which was in good agreement with the value previously reported by use of total internal reflection fluorescence microscopic (TIRFM) study.[180,181] In

2016, Watanabe-Nakayama *et al.* reported HS-AFM imaging of nanofiber formation of amyloid $\beta_{1\text{-}42}$ on mica.[175] They separated the amyloid $\beta_{1\text{-}42}$ samples by size exclusion chromatography into two fractions, low molecular weight (LMW) and high molecular weight (HMW) fractions. The LMW fraction contained monomers and low-order oligomers, while the HMW fraction contained higher-order oligomers. The HS-AFM time-lapse images of the sample of the LMW fraction captured the formation process of straight fibrils (Figure 16C) and spiral fibrils with a pitch length of 100 nm (Figure 16B). Interestingly, the authors observed switching of the two distinct growth modes and the resulting hybrid fibrils (Figure 16D). HS-AFM of the HMW fraction under the same conditions gave images of spherical aggregates as main components, although the formation of small amounts of fibrils similar to the structures seen in the LMW sample was also observed, indicating that a major fraction of the HMW peptide was off-pathway aggregate. They also performed HS-AFM imaging of the LMW peptide by addition of 100 mM KCl instead of NaCl. Potassium ion is known to reduce the interaction of proteins with mica surface relative to sodium ion.[182] The replacement of salt from NaCl to KCl resulted in changing the ratio of spiral, straight, and hybrid fibrils, where the main component was altered from spiral to hybrid (Figure 16E, F, G). The modest environmental change can affect the morphogenesis of amyloid β fibril, which was clearly distinguished by HS-AFM.

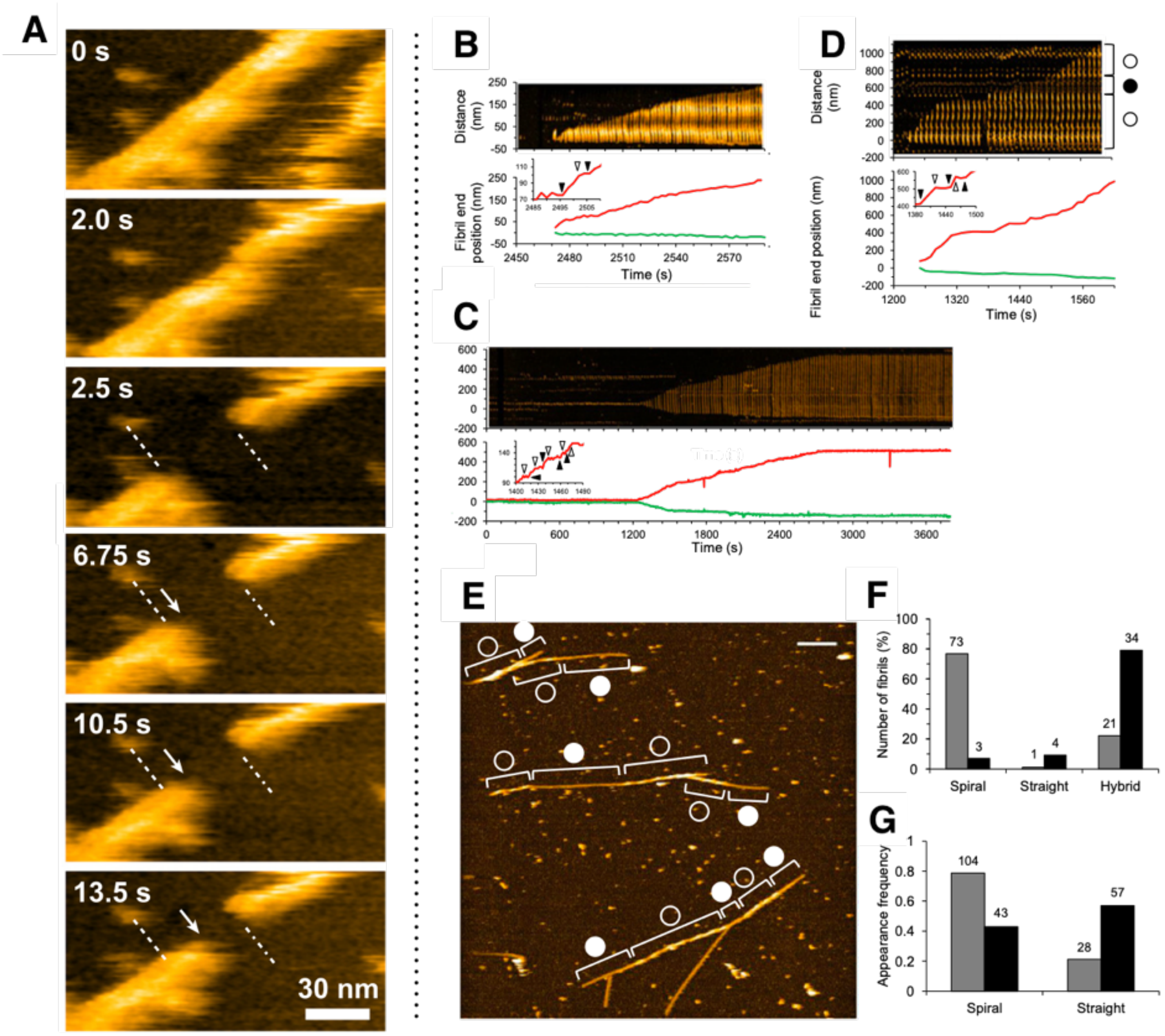

Figure 16. (**A**) HS-AFM images of an actin filament. To produce two-types of the ends, contact force was increased at initial stage (2–2.5 s) of the imaging. Reproduced with permission from ref 172. Copyright 2009 Elsevier. (**B**, **C**, **D**) HS-AFM kymographs of three kinds of fibril formation from the LMW amyloid $\beta_{1\text{-}42}$ fraction in presence of 100 mM NaCl. (**B**) Spiral fibril. (**C**) Straight fibril. (**D**) Hybrid fibril. (**E**) AFM image of LMW amyloid $\beta_{1\text{-}42}$ fibrils in presence of 100 mM KCl (Scale bar, 200 nm. Z scale, 15 nm.). Open- and filled-circles indicate spiral- and straight-fibril growth modes, respectively. (**F**) Percentage of the number of spiral, straight, and hybrid fibrils from the LMW amyloid $\beta_{1\text{-}42}$ in presence of 100 mM NaCl (gray) or KCl (black). (**G**) Appearance frequency of spiral and straight fibril growth modes from LMW amyloid $\beta_{1\text{-}42}$ in presence of 100 mM NaCl (gray) or KCl (black). Reproduced with permission from ref 175. Copyright 2016 National Academy of Sciences.

Very recently, HS-AFM was applied to imaging of artificial supramolecular polymers.[104,105] In 2018, Fukui *et al.* observed the polymerization process of an artificial supramolecular nanofiber using HS-AFM for the first time.[104] The authors employed a porphyrin derivative (porphyrin 1) that forms a thermodynamically stable nanofiber through a kinetically trapped nanoparticle, an off-pathway intermediate, after lag time (Figure 17A, B).[183] For HS-AFM imaging of the seeded growth of this porphyrin derivative, the short nanofibers seeds in MCH were spread on highly ordered pyrolytic graphite (HOPG). The kinetically trapped nanoparticle in MCH was then added to initiate the nanofiber growth. The time-lapse HS-AFM images at an interval of 100 ms clearly visualized the seeded polymerization of the single nanofiber with the average growth rate of 12.4 nm/s which corresponded to 35 molecules/s (Figure 17C). The images also captured the sudden break of the elongated nanofiber, probably due to the tip-nanofiber contact during imaging. The authors also constructed a supramolecular diblock copolymer using HS-AFM manipulation. The center part of the long nanofiber was broken by contact force between tip and the nanofiber, followed by compensation of the defect with another porphyrin derivative (porphyrin 2) (Figure 17A). In 2020, Maity *et al.* examined the self-assembly mechanism of a self-replicator driven by nanofiber formation using real-time HS-AFM imaging.[105] The peptide-based monomer containing two thiol units formed into various ring-size of macrocycles which transformed each other by disulfide bond exchange (Figure 17D). The authors previously revealed that the monomer initially oligomerized to cyclic trimer and tetramer, followed by construction of hexamer, a self-replicator that formed into long nanofibers under mechanical agitation (Figure 17E).[184,185] HS-AFM visualized the growth of the hexamer-based nanofiber on the mica surface coated with negatively charged lipid by addition of precursors containing monomer, trimer, and tetramer. Time-dependent AFM images with an interval of 30 min revealed that the attachment of precursors aggregates near the nanofiber ends significantly promoted the fiber growth. In contrast, adsorption of the aggregates on the middle or no adsorption yielded in limited or negligible growth of nanofibers, respectively. These indicated that both the formation of precursors aggregates and their adsorption on the nanofiber ends were critical for the nanofiber growth. They then performed *in situ* HS-AFM imaging over 1930 s at an interval of 500 ms (Figure 17G, H, I). The HS-AFM imaging of the nanofiber that adsorbed the precursor aggregates at the end visualized the five step processes of the fiber extension: (i) rapid fiber growth phase; (ii) slow fiber growth phase; (iii) stagnant phase with emerging new aggregates at the middle of fiber; (iv) slow fiber growth phase; (v) rapid fiber growth phase, where the newly emerged aggregate became smaller. Remarkably, HS-AFM captured that the new emerged aggregates initially moved to the fiber ends direction (phase iii) and then stopped (phase iv), followed by acting as reservoir of monomers required for fiber growth (phase v). Such observations let the authors hypothesize that aggregates or free precursors attached to the fiber surfaces into construction of reservoir which have propensity to diffuse to the fiber ends, resulting in accelerating fiber extension (Figure 17F). The hypothesis was supported by *ex situ* AFM images and molecular dynamics simulations, highlighting that real-time HS-AFM imaging is a promising tool for investigating formation mechanisms of molecular assemblies in molecular scale.

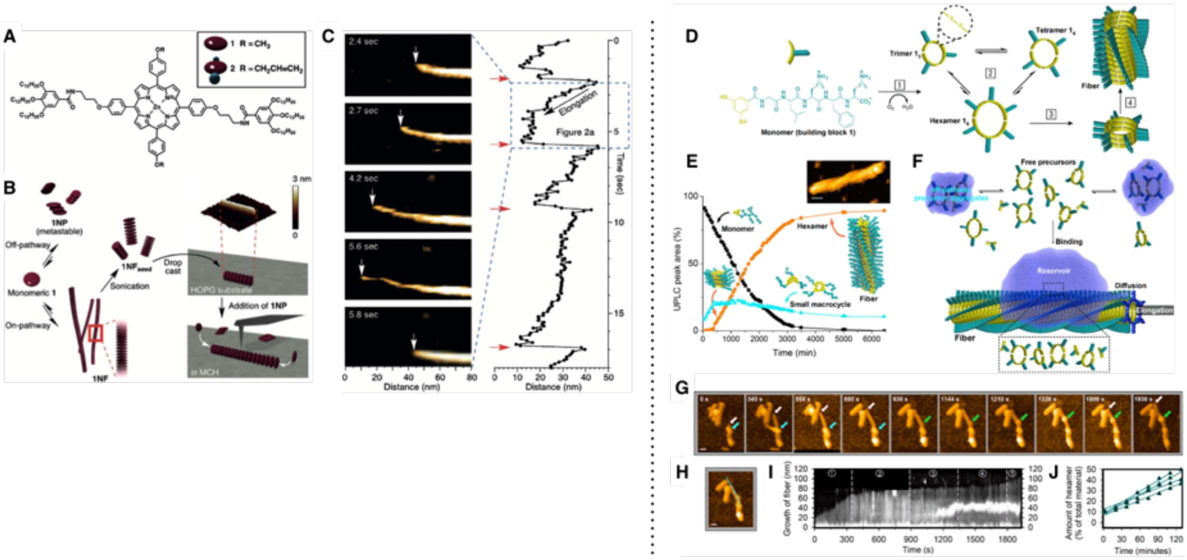

Figure 17. HS-AFM imaging of artificial supramolecular polymers. (**A**) Chemical structures of porphyrin 1 and 2. (**B**) Schematic illustration of seeded growth of porphyrin 1 fiber and their HS-AFM imaging. (**C**) HS-AFM images of growth and sudden break of the porphyrin 1 supramolecular polymer. Reproduced with permission from ref 104. Copyright 2018

Wiley-VCH. (**D**) Schematic illustration of formation process of a cyclic hexamer and their stacked nanofiber from monomer 1. (**E**) Time-dependent population change of monomer, small macrocycle, and cyclic hexamer under stirred conditions. (**F**) Proposed model of the nanofiber elongation from a seeded fiber. (**G**) HS-AFM images of nanofiber growth. Scale bars: 20 nm. (**I**) Kymographic analysis of the nanofiber growth along the line in (**H**). (**J**) Hexamer evolution rate in solution determined by ultra-performance liquid chromatography (UPLC). Reproduced with permission from ref 105. Copyright 2020 American Chemical Society.

Like cryo-EM techniques, HS-AFM was actively applied to biological samples such as DNA/RNA and proteins, which has already made great contributions to molecular biology and biophysics. It is clear that HS-AFM would have tremendous potential to provide new insights in the field of synthetic molecular assembly/supramolecular chemistry, although its application to synthetic molecular assembly has just launched. It is envisioned that HS-AFM studies of molecular assemblies will increase dramatically, leading to new finding of molecular mechanisms and construction of new generation synthetic materials.

5. Confocal laser scanning microscopy

CLSM is one of the powerful tools to visualize fluorescent signals from specimens. CLSM has higher spatial resolution than conventional wide-field fluorescent microscopy due to reduction of the fluorescent signals from a non-focal plane with a pinhole in the front of a detector. As demonstrated in cell biology studies, confocal imaging has several advantages to observe supramolecular assemblies over EM and AFM. First, drying/freezing processes are not necessary for sample preparation. Second, a three-dimensional image can be reconstructed from multiple two-dimensional *z*-stacked images. Third, *in situ* dynamic processes (for example, formation and degradation processes) can be observed by time-lapse imaging. Fourth, multiple molecular species can be distinguished when the selective fluorescent staining is available. Fifth, the use of various objective lens with different magnification (and image tiling with a precise motorized stage) allows for imaging specimens from a wide range of fields of views (sub μm ~ cm). One of the drawbacks is its lower spatial resolution than EM and AFM, while the recently-developed super-resolution techniques (STED microscopy,[186–188] SMLM,[189–192] and SIM[193–195]) enable to acquire images at the higher resolution than the Abbe's diffraction limit (typically, less than 100 nm). In this section, the early examples about confocal imaging of molecular assemblies are introduced, then representative advanced techniques are also described. For the detailed mechanisms of confocal imaging, please refer to other excellent reviews.[196–198] In this review, we excluded examples of confocal imaging of liposomes.

5.1. Design of fluorescent probes

To observe molecular assemblies by confocal and SR microscopies, staining of them by fluorescent probes is required. Design strategies of appropriate fluorescent probes are categorized into three types: (i) use of fluorescently-modified monomers, (ii) use of fluorescent dyes that interacted with molecular assemblies, (iii) use of fluorescent probes that possess the self-assembled moiety almost identical with the monomers (Figure 18). As an example of strategy (i), Xu and coworkers often employed peptide-type hydrogelators covalently modified with an environmental-responsive fluorescent dye, such as NBD. This strategy enables to directly visualize the molecular assemblies in the complex milieu like living cells. Perylene bisimide derivatives are widely used as building blocks for both self-assembled and fluorescent moieties. One of the drawbacks of this strategy is that the fluorescent dye moiety often affect properties of molecular assemblies. In the cases of strategy (ii) and (iii), fluorescent probes are added to non-fluorescent monomers/assemblies. In these methods, a small amount of fluorescent dyes and probes is sufficient for visualization of molecular assemblies (typically, 0.01–0.1 mol%), which can reduce unfavorable impacts on structures and properties of molecular assemblies. As an example of strategy (ii), fluorescent probes with a guanidium group was employed to detect supramolecular nanofibers comprising a peptide-type hydrogelator that has a carboxylate group at the C-terminus. As the strategy (iii), the van Esch group prepared a fluorescent probe that has an FITC group at the terminus of the hydrogelator backbone. Hamachi and coworkers demonstrated that the strategy (iii) is powerful to selectively stain self-sorting supramolecular nanofibers. Besides, fluorescent dyes should be carefully selected. Their excitation wavelengths should be fitted with the laser wavelength of the microscopy. High photostability is required for time-lapse imaging. Their chemical properties (hydrophobicity, hydrophilicity, and charges) should also be considered to achieve efficient and selective fluorescent staining.

Despite powerful, CLSM and SR techniques sometimes produce artifacts that may lead to misunderstandings. First, interactions among molecular assemblies and fluorescent probes may change the assemblies structure. Second, too strong fluorescent crosstalk could confuse the understanding of images when multicolor imaging is conducted. Third, laser irradiation may lead to photobleaching of the fluorescent dyes and increment of local temperature. Fourth, the deconvolution process in SR imaging often make noise. To correctly interpret CLSM and SR imaging results, many of appropriate control experiments (*e.g.* dependence of probe concentration and optimal laser intensity, confirmation of staining selectivity, *etc*) should be conducted.

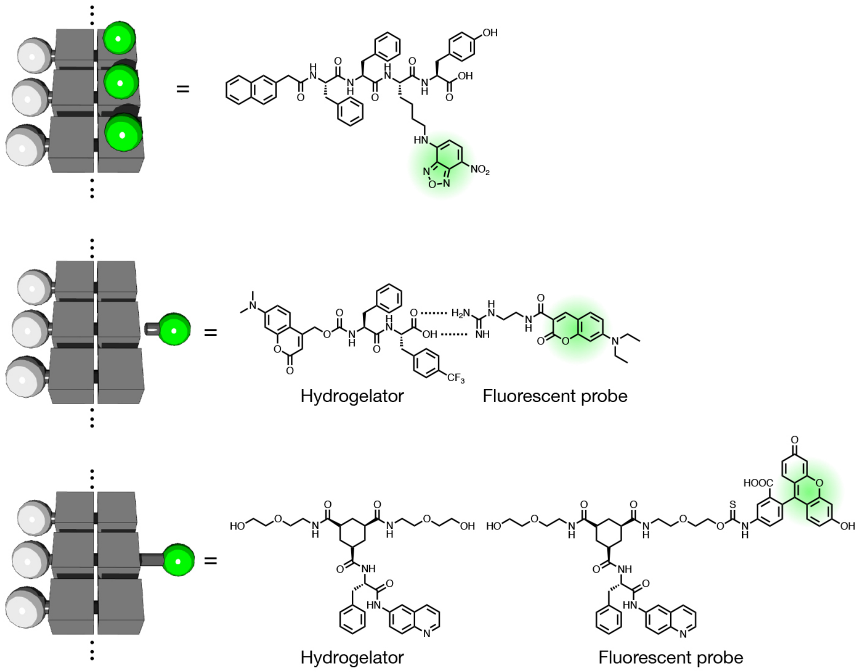

Figure 18. Design of fluorescent probes: (top) Fluorescently-modified monomers, (middle) fluorescent probes that is interacted with a monomer, (bottom) fluorescent probes that have the same self-assembled moiety as monomers.

5.2. Early examples of CLSM imaging

In 1998, Donath *et al.* firstly reported confocal imaging of polyelectrolyte shells composed of poly(sodium styrenesulfonate) (PSS) and poly(allylamine hydrochloride) (PAH) on colloids with thickness of a few to tens nanometers (Figure 19A).[199] The shells were characterized by SEM, TEM, and AFM. They also showed the confocal image of the shell composed of nine layers with a diameter of 8 μm, which was consistent with other microscopic analyses. In 2000, Ilhan *et al.* reported confocal imaging of polymer vesicles formed through self-assembly of two distinct random copolymers possessing a complementary hydrogen bonding pair (Figure 19B).[200] The vesicles were obtained by mixing an equal amount of polymers in $CHCl_3$ in the presence of a flavin functionalized polymer. CLSM imaging showed that the vesicles were composed of a bright membrane structure with less fluorescent central regions. CLSM also visualized unique morphologies of the vesicles like a vesicle-in-vesicle structure and fused vesicles. Bellomo *et al.* reported CLSM imaging of vesicles composed of an amphiphilic diblock copolypeptide ($K^P{}_{100}L_{20}$) [K^P: poly(N_ε-2-(2-(2-methoxyethoxy)ethoxy)acetyl-L-lysine, L: poly(L-leucine)].[201] CLSM imaging after staining with $DiOC_{18}$ clearly visualized the spherical unilamellar giant vesicle of 5–10 μm diameter. Both CLSM imaging and small angle neutron scattering analysis indicated a polymeric bilayer assembly, which is similar to the lipid bilayer structure.

CLSM imaging also allows to visualize the network structure of physically- and chemically-crosslinked polymer hydrogels.[202–208] In 1999, Hirokawa *et al.* reported direct observation of the network structure in PNIPAM chemical gels by reflection CLSM imaging, for the first time (Figure 19C).[202] Their CLSM imaging showed the sea-island pattern consisting of dark and bright areas. CLSM imaging after staining with ANSA which emits stronger fluorescence in a hydrophobic environment, visualized that ANSA fluorescence could be detected only from the bright region of the reflection CLSM image, suggesting that the hydrophobic isopropyl groups of NIPAM formed the dense domains in the polymer network. The sea-island pattern was changed depending on the gel preparation temperature, which well corresponded with the opacity of the hydrogel. The authors also succeeded in visualization of a 3D network composed of a bicontinuous domain structure by reconstruction from a series of the *z*-sliced CLSM images (Figure 19D). In 2002, Nowak *et al.* reported CLSM imaging of a physical hydrogel composed of self-assembling polypeptide amphiphiles (Figure 19E).[209] The authors synthesized diblock copeptide, $K_{160}L_{40}$, which self-assembled in water through formation of rod-like α-helices of poly(L-leucine) to form a hydrogel. CLSM imaging after staining the hydrophobic region of the polypeptide gel with lipophilic $DiOC_{18}$ showed the sea-island like network structure. In the same year, Schneider and coworkers reported *in situ* CLSM imaging of the hydrogel composed of intramolecularly-folded β-hairpin peptide consisting of 20 amino acid residues (Figure 19F).[210] The self-assembled structure of this peptide was determined to be the sea-island pattern, which resembles to the PNIPAM gel as previously described.

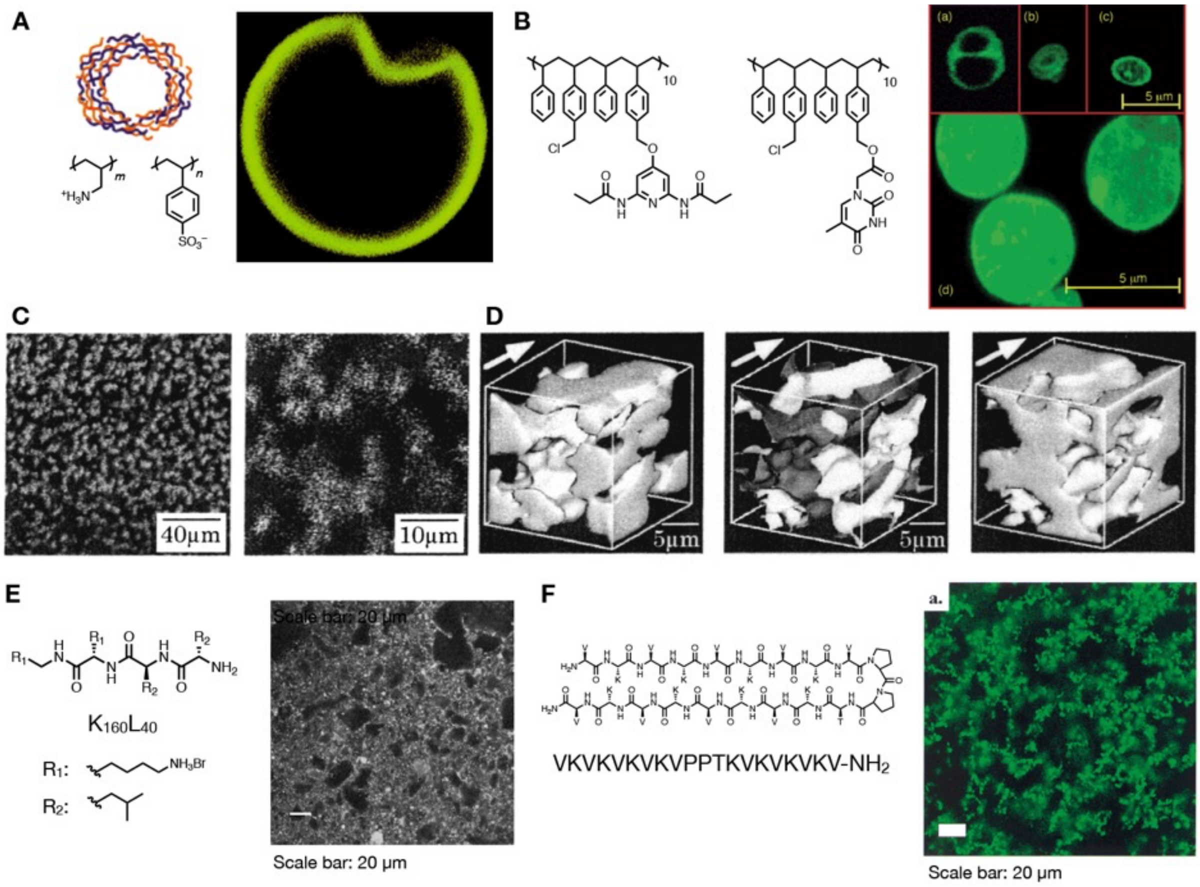

Figure 19. (**A**) Confocal image of a hollow polyelectrolyte shell with a diameter of 8 µm. Adapted with permission from ref 199. Copyright 1998 Wiley-VCH. (**B**) Polymer vesicles composed of diaminopyridine- and thymine-based polymers. Reproduced with permission

from ref 200. Copyright 2000 American Chemical Society. (**C**) 2D and (**D**) 3D confocal microscopic images of a PNIPAM gel. Reproduced with permission from ref 202. Copyright 1999 American Chemical Society. (**E**) Confocal image of 1 wt% $K_{160}L_{40}$ gel. Reproduced with permission from ref 209. Copyright 2002 Springer Nature. (**F**) Chemical structure and CLSM image of self-assembled peptide. Reproduced with permission from ref 210. Copyright 2002 American Chemical Society.

CLSM is also powerful to elucidate the self-assembled structures of small organic or inorganic molecules such as low-molecular-weight hydrogelators (molecular weight < 1,000).[31,43,51,121,207,208,211–323] In 2002, Kiyonaka *et al.* firstly demonstrated CLSM imaging of the self-assembled fibrous structure of the low-molecular-weight hydrogelator (Figure 20A).[211] They synthesized artificial amphiphilic glycolipid hydrogelators and found that these self-assembled into the fibrous structure in water and an aqueous buffer. CLSM imaging after staining by an environmental fluorescent dye, HANBD, showed the 3D network structure composed of bundled nanofibers with a diameter of 0.2–0.6 μm. Frusawa *et al.* successfully showed alignment of a single-lipid nanotube on a glass plate by microextrusion with monitoring by CLSM in real time.[213] They employed a microinjection system containing a dispersion of the glycolipid nanotubes. Upon touching a microneedle on a substrate, a small amount of the nanotube dispersion was dropped, and then water evaporated due to the light irradiation. Using this technique, the authors succeeded to write the word “tube” with single nanotubes. In 2004, Sugiyasu *et al.* reported CLSM imaging of an organogel composed of cholesterol-based perylene derivatives (Figure 20B).[216] The gelator formed an organogel in a mixed solvent of alcohol and *p*-xylene with a critical gelation concentration of 0.5 wt%. CLSM imaging of the gel showed a network structure composed of fibrous aggregates. In 2005, Del Guerzo *et al.* reported an organogel formed through coassembly of the didecyl derivative of anthracene doped with 2% of a tetracene derivative possessing two decyl chains (DDOT) (Figure 20C).[220] CLSM imaging of this organogel showed that DDOT fluorescence could be detected throughout the self-assembled nanofibers, suggesting that the doped DDOT was homogeneously distributed to achieve efficient energy transfer.

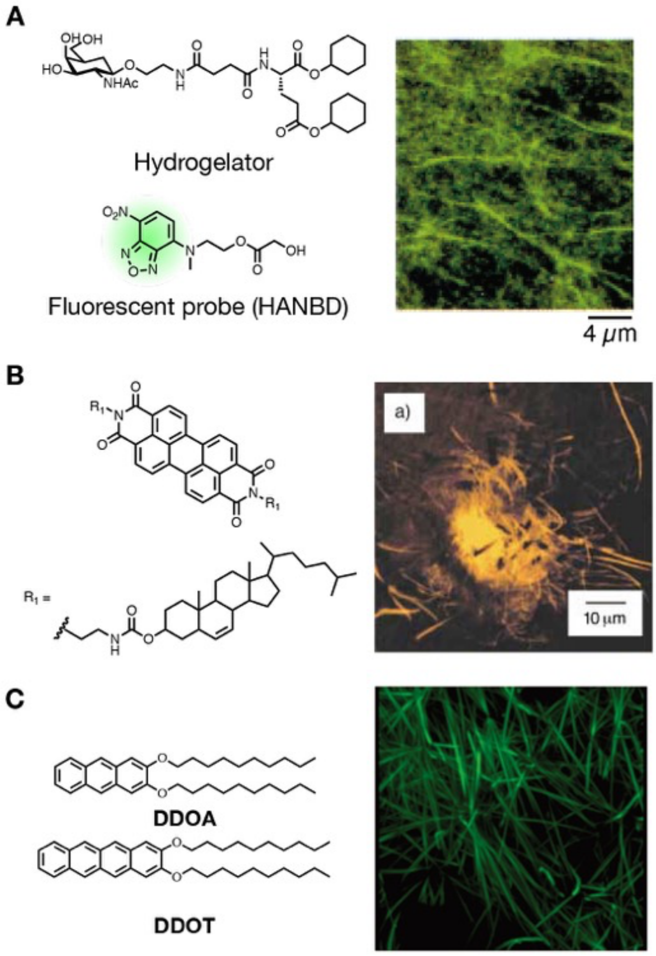

Figure 20. (**A**) Confocal image of a supramolecular hydrogel composed of an amphiphilic gelator. Reproduced with permission from ref 211. Copyright 2002 American Chemical Society. (**B**) Supramolecular organogel consisting of a perylenebisimide derivative. Reproduced with permission from ref 216. Copyright 2004 Wiley-VCH. (**C**) CLSM image (50×50 μm^2) of an organogel composed of a mixture of DDOA and 2 mol% DDOT. Reproduced with permission from ref 220. Copyright 2005 American Chemical Society.

5.3. Super-resolution microscopy

Super-resolution (SR) microscopy including STED, SMLM [photoactivated localization microscopy (PALM), stochastic optical reconstruction microscopy (STORM)], and SIM have emerged as powerful tools to elucidate the more precise structures of molecular self-assemblies (lateral resolution: 20–100 nm) than conventional CLSM imaging. Table 2 describes characteristics of conventional CLSM and SR imaging techniques. Despite their higher spatial resolution, SR microscopy shows disadvantages such as reconstruction artifacts and requirement of special fluorescent dyes and buffers. Recently, confocal-based SR imaging techniques without limited dye choice (*e.g.* Airyscan[324,325] and Lightning: lateral resolution: ~120 nm) have been developed. SR imaging techniques are useful for the detailed structural evaluation of multicomponent supramolecular systems such as self-sorting supramolecular nanofibers, which is extremely difficult by use of other microscopic imaging techniques. In this section, the early and/or representative examples of SR imaging of supramolecular assemblies are briefly described.

Table 2. Characteristics of conventional confocal and super-resolution microscopies[191]

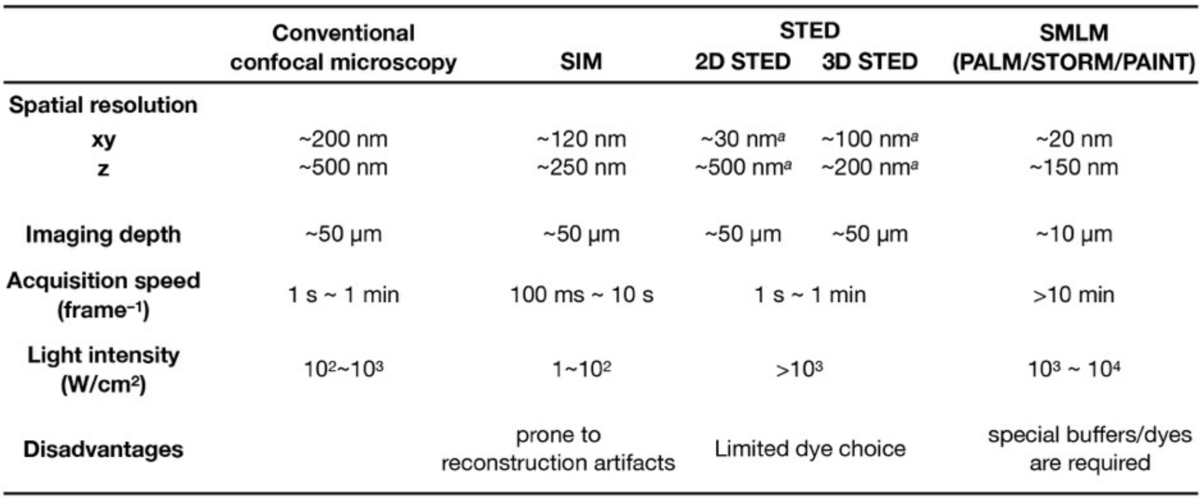

	Conventional confocal microscopy	SIM	STED		SMLM (PALM/STORM/PAINT)
			2D STED	3D STED	
Spatial resolution					
xy	~200 nm	~120 nm	~30 nm^a	~100 nm^a	~20 nm
z	~500 nm	~250 nm	~500 nm^a	~200 nm^a	~150 nm
Imaging depth	~50 μm	~50 μm	~50 μm	~50 μm	~10 μm
Acquisition speed (frame^{-1})	1 s ~ 1 min	100 ms ~ 10 s	1 s ~ 1 min		>10 min
Light intensity (W/cm^2)	10^2~10^3	1~10^2	>10^3		10^3 ~ 10^4
Disadvantages		prone to reconstruction artifacts	Limited dye choice		special buffers/dyes are required

a: depends on intensity of a depletion laser.

5.3.1. Structured illumination microscopy

Structured illumination microscopy (SIM) is based on a wide-field fluorescent microscopy with a laser-based patterned illumination (*e.g.* stripe or lattice patterns) as a light source.[193–195] Super-resolution images are acquired through reconstruction of multiple images obtained at different orientations of the patterned illumination by calculating the Moiré fringes. Despite the spatial resolution lower than other SR techniques (SIM: ~120 nm, STED: ~50 nm, SMLM: ~20 nm), SIM has several advantages, that is, no requirement of special fluorescent dyes (*e.g.* photoactivatable/photoswitchable) and buffers, multiple staining available, and faster imaging acquisition than STED and SMLM. One of the drawbacks is prone to produce artifacts during image reconstruction.

Qiu *et al.* reported SIM imaging of uniform, monodisperse rectangular platelet micelles composed of crystalline polymer brends.[326] The low-polydispersity rectangular platelet micelles ($A_w/A_n < 1.01$) were synthesized through living crystallization-driven self-assembly of a blend of PFS_{36}-*b*-$P2VP_{502}$ and PFS_{20} unimers with PFS_{28}-*b*-$PDMS_{560}$ seeds in a 1:3 hexane/iPrOH mixture [PFS: poly(ferrocenyldimethylsilane), P2VP: poly(2-vinylpyridine), PDMS: polydimethylsiloxane]. TEM and AFM analyses revealed that the length, width, area, and aspect ratio of the platelet micelle can be controlled by the unimer-to-seed ratio and the length of the cylindrical seeds. Furthermore, CLSM and SIM imaging visualized that the living crystallization-driven self-assembly in the presence of fluorescently-labeled PFS-*b*-PDMS with different fluorescent dyes yielded a series of fluorescent rectangular platelet block comicelles exhibiting multiple and variable fluorescence (Figure 21A).

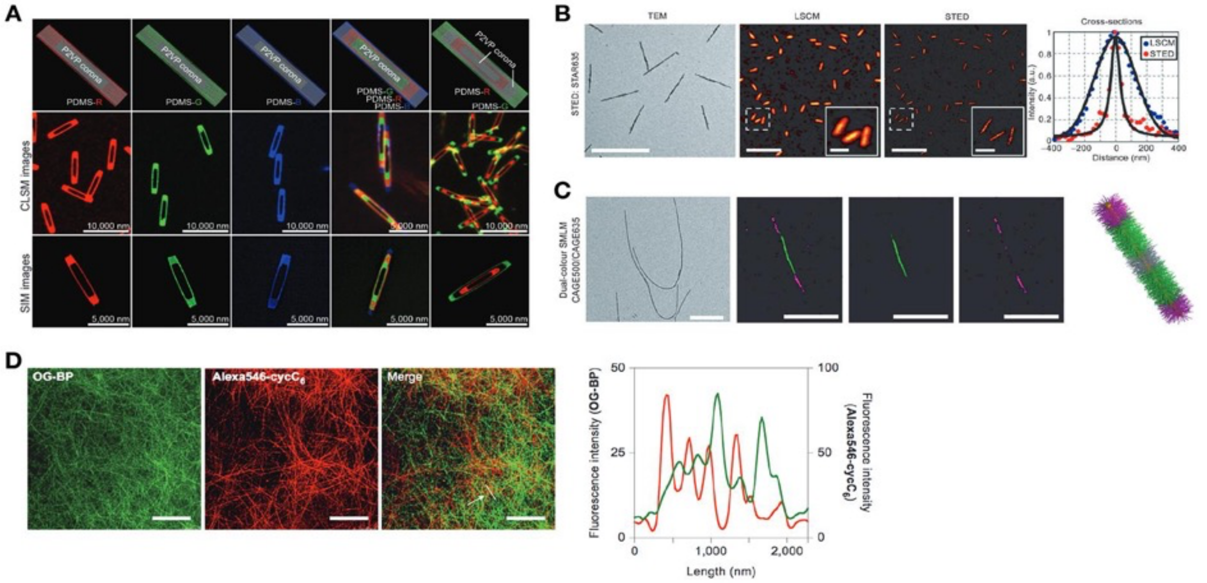

Figure 21. (**A**) CLSM and SIM images of rectangular platelet micelles of a blend of PFS_{36}-*b*-$P2VP_{502}$ and PFS_{20} unimers with PFS_{28}-*b*-$PDMS_{560}$ seeds. Reproduced with permission from ref 326. Copyright 2016 AAAS. (**B**) STED and (**C**) SMLM images of cylindrical micelles composed of PFS_{56}-*b*-($PDMS_{775}/DYE_{20}$). Scale bars: 2 μm (**B**, TEM), 5 μm (**B**, LSCM and STED), 1 μm (**B**, inset), 1 μm (**C**, TEM), 2 μm (**C**, SMLM). Reproduced

with permission from ref 327. Copyright 2015 Wiley-VCH. (**D**) (Left) STED images of self-sorting supramolecular nanofibers comprising (green) peptide- and (red) lipid-type hydrogelators. (Right) Fluorescent intensity profile along a white line shown in the STED image. Scale bar: 5 μm. Reproduced with permission from ref 260. Copyright 2016 Springer Nature.

5.3.2. Stimulated emission depletion microscopy

STED microscopy enables super-resolution (30–80 nm) beyond the diffraction limit by deactivating fluorescence around the center of the focal volume with a donut-shaped depletion laser.[323] Despite high spatial resolution, the limited fluorophores can be used because high photostability and appropriate excitation/emission wavelengths are strictly required for the depletion laser.

In 2015, Boott *et al.* reported super-resolution imaging (STED, SMLM) of block copolymer self-assembly in organic solvents.[327] For STED and SMLM imaging, they selected rhodamine-based fluorescent dyes (STAR635 and CAGE635 for STED; CAGE635 and CAGE552 for SMLM) with which a cylindrical micelle was covalently modified to obtain PFS_{56}-*b*-($PDMS_{775}/DYE_{20}$). STED imaging showed the rod-like self-assembled structure with full-width half-maximum of 77 nm (Figure 21B). Also, the authors succeeded in dual-color SMLM imaging of triblock comicelles in which the middle segment was labelled with CAGE500 and the two outer segments were modified with CAGE635 (Figure 21C). The lengths measured by STED and SMLM imaging were in good agreement with those estimated by TEM.

In 2016, Onogi *et al.* demonstrated two color STED imaging of two distinct self-sorted supramolecular nanofibers.[260] Their peptide- and lipid-type hydrogelators self-assemble without mixing with each other (namely, self-sorting phenomena) to form a supramolecular double network hydrogel. By selective staining with appropriate fluorescent probes possessing the self-assembled moieties identical with each hydrogelator, these peptide- and lipid-type nanofibers can be discriminated by fluorescent colors, which enable real-time imaging of self-sorting events of the supramolecular nanofibers *in situ*. STED imaging clearly visualized that two distinct supramolecular nanofibers were well entangled but not overlapped with each other (Figure 21D).

5.3.3. Single-molecule localization microscopy

Single-molecule localization microscopy (SMLM) enables to obtain super-resolution images by acquiring the accurate position of individual fluorophores.[189,190,328,329] SMLM needs the ON/OFF state of the fluorophores that can be controlled by use of photoswitching or spontaneously-blinking dyes. The overall super-resolution image is constructed by combining several (tens) thousands of different frames. The spatial resolution of SMLM is estimated as $\lambda/\sqrt{N}$, where λ is emission wavelength and N is the photon number, and the typical spatial resolution is *ca.* 20 nm. Based on the technique to switch the ON/OFF state of the fluorophore, SMLM is subdivided into photoactivated localization microscopy (PALM), (direct) stochastic optical reconstruction microscopy (STORM, dSTORM), and point accumulation for imaging in nanoscale topography (PAINT).

In 2012, Aoki *et al.* reported the conformational analysis of a single polymer chain by PALM for the first time.[330] They analyzed poly(butyl methacrylate) labeled by a rhodamine spiroamide derivative which shows equilibrium of open and closed conformations. PALM imaging enabled to visualize the conformation of a single polymer chain with a spatial resolution of 15 nm (Figure 22A–E). This direct observation revealed that the polymer took a random coil conformation in a film. Recently, several groups developed a series of fluorescent dyes applicable to PALM imaging, such as spiropyrans and diarylethene derivatives.[331,332] For example, Yan and coworkers reported PALM imaging of block copolymer micelles composed of polystryrene-*b*-poly(ethylene oxide) by staining with spiropyrans. Spiropyrans show reversible fluorescent switching by alternate irradiation of UV and visible light. PALM imaging visualized cylindrical micelle structures with a resolution of 49 nm, which was improved by 6-fold than conventional fluorescent imaging.

In 2014, the Meijer group demonstrated the first example of STORM imaging of supramolecular polymers.[251] They employed 1,3,5-benzenetricarboxamide (BTA) monomer, which self-assembled into 1D nanofibrous structure, and the fluorescently-labeled variants, BTA-Cy3 and BTA-Cy5. STORM imaging showed the supramolecular polymers with a spatial resolution of 25 nm (Figure 22F, G), and they succeeded to evaluate the monomer exchange rate by time-lapse STORM imaging (see below).

Very recently, Albertazzi and coworkers succeeded in visualization of the fibrous assemblies of a widely-used diphenylalanine peptide hydrogelator, Fmoc-FF, by iPAINT technique, which employs a fluorescent dye that reversibly binds to supramolecular nanofibers (Figure 22H–J).[263,312] In this study, they used Cy5-modified diphenylalanine as a PAINT probe as it had been reported to reversibly bind to nanofibers. Using this probe, PAINT imaging enabled to improve the spatial resolution enough to visualize the thinner nanofibers with a diameter of *ca.* 50 nm and entangled or bundled nanofibrous structures. Moreover, PAINT imaging allowed to estimate the distribution of the mesh size of the hydrogel. The current limitation of this method is to observe the bulk gel in depth and small accessible areas due to the limited diffusion of the fluorescent probes, Cy5-FF.

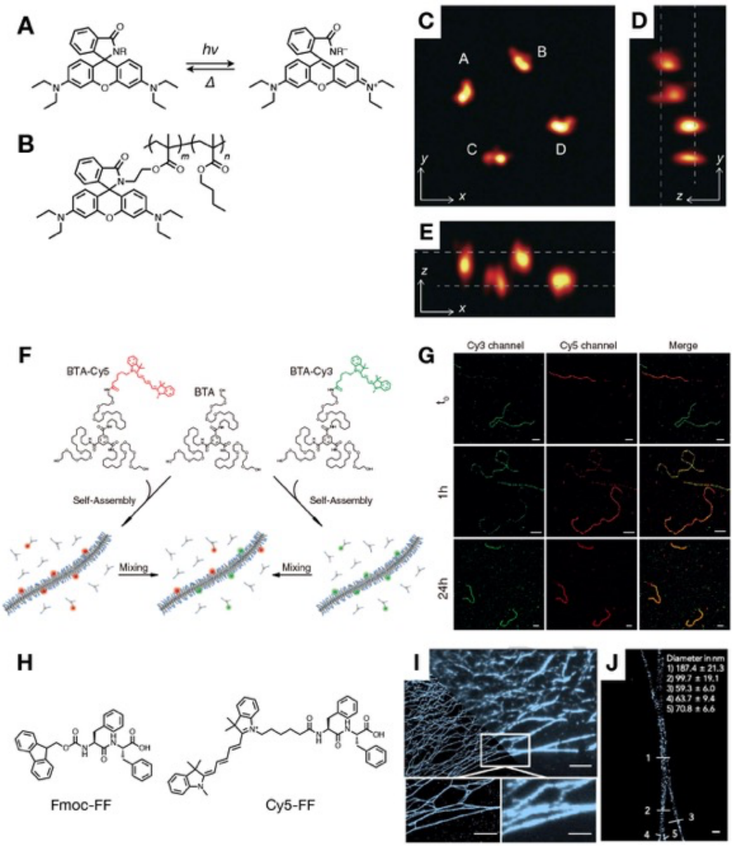

Figure 22. (**A**) ON-OFF switching of a tetraethylrhodamine derivative. (**B**) Molecular structure and (**C**–**E**) 3D PALM images of a fluorescently-modified polymer (the image size: 1250 × 1250 × 600 nm^3). Reproduced with permission from ref 330. Copyright 2012 Royal Society of Chemistry. (**F**) Molecular structures of a monomer and fluorescent probes and schematic illustration of the monomer exchange between the supramolecular polymers. (**G**) Time-dependent STORM imaging of the polymers. Scale bar: 1 μm. Reproduced with permission from ref 251. Copyright 2014 AAAS. (**H**) Molecular structures of a peptide-type hydrogelator, Fmoc-FF, and its fluorescent probe, Cy5-FF. (**I**, **J**) PAINT images of the Fmoc-FF gel with spatial resolution of *ca.* 50 nm. Scale bars: 2.5 μm (**I**), 200 nm (**J**). Reproduced with permission from ref 312. Copyright 2020 Wiley-VCH.

5.4. Advanced applications of CLSM imaging

5.4.1. Time-lapse imaging: dynamic aspects of self-assembly

One of the fascinating characteristics of CLSM is to be able to observe the dynamic aspects of molecular self-assembly (*e.g.* formation, collapse, and monomer exchange) by *in situ* time-lapse imaging. We here summarizes representative examples of real-time CLSM imaging to evaluate the dynamics of molecular self-assembly.

5.4.1.1. Fluidity determination by fluorescence recovery after photobleaching

Fluorescence recovery after photobleaching (FRAP) measurements are one of the widely-used methods to estimate diffusion coefficients of fluorescently-labeled monomers in molecular assemblies (Figure 23A). In FRAP experiments, the fluorescent molecules in the limited area are bleached by the intense laser, and then the recovery rate of the fluorescent intensity is monitored by time-lapse CLSM imaging, which gives us the diffusion coefficients by the fitting analysis.

In 2002, as an early example, Gao *et al.* employed FRAP analysis to examine the state of fluorescein isothiocyanate (FITC)-modified dextran (molecular weight: 77 kDa) encapsulated in the polyelectrolyte capsules composed of PSS and PAH.[333] The authors found that water-soluble substances like dextran show spontaneous deposition into the capsule through interaction with PSS/melamine formaldehyde (MF) complex (MF was used as a template for PSS/PAH membrane formation). FRAP analysis revealed that the fluorescent intensity of FITC-dextran never recovered after photobleaching, indicating that no dextran exchange took place within the capsule (Figure 23B). However, fluorescent intensity of the FITC-dextran in another capsule showed substantial recovery, suggesting that this capsule had larger holes in its walls.

FRAP analysis can be applicable to investigation of the fluidity of supramolecular assemblies.[222,229,260,284,294,334–345] For example, Tamaru *et al.* analyzed the fluidity of glycolipid-based supramolecular nanofibers with a fluorescently-labeled monomer analogue as a probe. FRAP analysis showed that immediate recovery of the fluorescent intensity and the diffusion coefficient was determined to be 0.12 ± 0.03 $\mu m^2 s^{-1}$ (Figure 23C).[229] Using the fluidity of the glycolipid nanofibers, the authors demonstrated the controlled directional motion of proteins and nanobeads along the nanofibers by use of CLSM. Furthermore, Onogi *et al.* showed that such determination of the diffusion coefficient was useful to identify the individual nanofibers in self-sorting hydrogels.[260] The authors compared the fluidities of peptide- and lipid-type nanofibers in single-component and self-sorting double-network hydrogels. FRAP analysis demonstrated that the diffusion coefficient of the lipid-type nanofibers in the single-component and self-sorting hydrogels are almost identical [$(9.1 \pm 1.1) \times 10^{-3}$ and $(8.0 \pm 0.2) \times 10^{-3}$ $\mu m^2 s^{-1}$] (Figure 23D). In contrast, no fluorescent recovery of the peptide-type nanofibers was observed, indicating that the distinct fluidity of the peptide- and lipid-type nanofibers remains intact even in the self-sorting state. In 2018, Roberts *et al.* measured the internal mobility of the network consisting of partially ordered polypeptides of disordered elastin-like polypeptides and the structurally stable polyalanine helices.[342] FRAP measurements of the Alexa Fluor 488 labeled network showed the minimal recovery was observed and the immobile fraction was high (86%), suggesting that the network was kinetically stable due to physical crosslinking from helical bundling within the network. FRAP analysis is also applicable to liquid condensates. In 2019, Alshareedah *et al.* investigated the diffusion of fluorescently-labeled peptides in the liquid condensates consisting of $[KGKGG]_5$/$[RGRGG]_5$ peptides and polyU/polyA RNAs by FRAP experiments.[343] FRAP analysis demonstrated that the peptide diffusion within $[KGKGG]_5$/polyA droplets had considerable degree of mobility (diffusion coefficient was determined to be 0.11 ± 0.02 $\mu m^2 s^{-1}$), whereas the diffusion was nearly arrested within $[RGRGG]_5$/polyA droplets. Combined with other experimental results such as droplet fusion controlled by optical tweezers, the authors concluded that the peptide mobility at the nanoscale was partially dependent on the intermolecular short-range interactions (*e.g.* cation-π interaction) between RNAs and peptides.

FRAP analysis is useful for determination of the diffusion coefficient and dynamics (*e.g.* kinetic constant of association and dissociation behaviors) of not only monomers but also encapsulated fluorescent molecules within the molecular assemblies.[346–351] DeForest and Tirrell evaluated the diffusion coefficient for fluorescein-modified bovine serum albumin (BSA) within a four-armed PEG gel by use of FRAP analysis.[352] The obtained diffusion coefficient ($\sim 1.8 \times 10^{-11}$ $m^2 s^{-1}$) was roughly quarter of that of BSA in water. In 2018, Deng *et al.* conducted FRAP analysis of enhanced green fluorescent protein (EGFP) encapsulated in a *E. Coli* lipid liposome containing cell lysates and nucleoid DNA (Figure 23E).[353] At concentration of 60 g/L, the fluorescence recovered within 1 s in the liposome. In contrast, after shrinking by hypertonic shock (concentration: *ca.* 260 g/L), the fluorescence recovery took more than 40 s, demonstrating the crowded interior of the liposome.

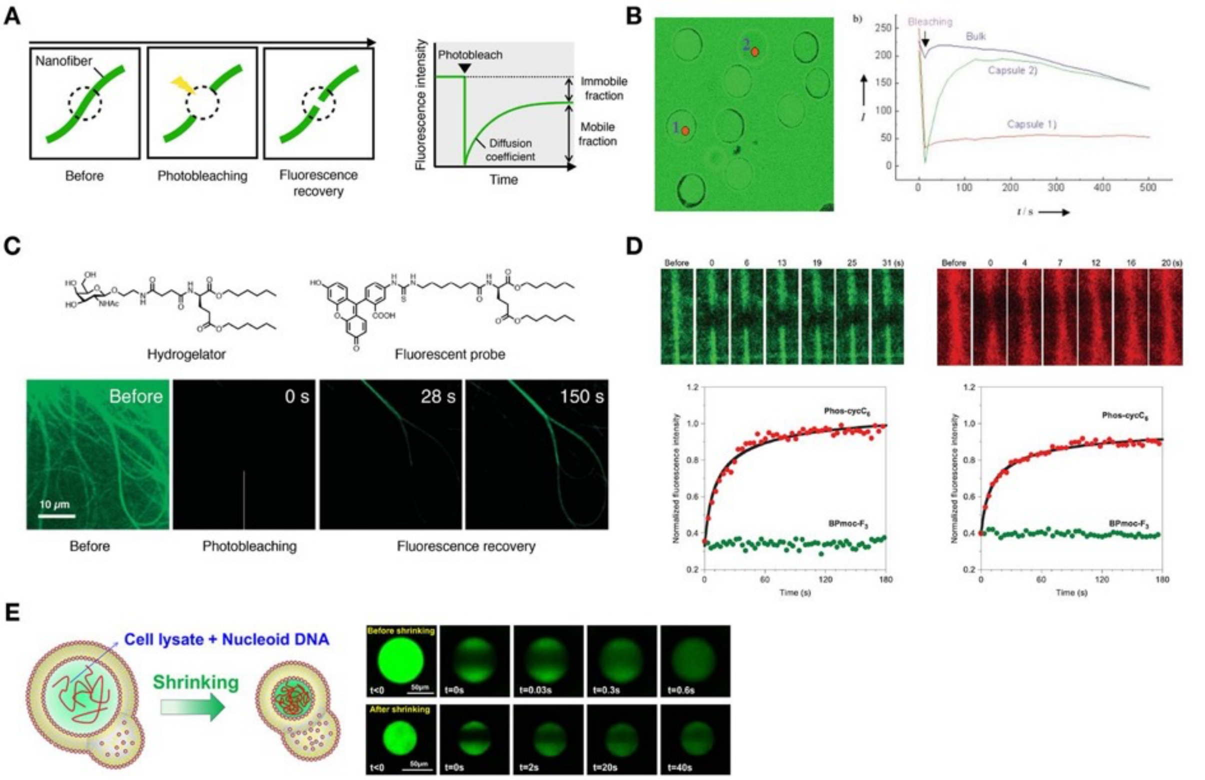

Figure 23. (**A**) Schematic illustration of FRAP experiments. Reproduced with permission from ref 307. Copyright 2020 Wiley-VCH. (**B**) FRAP analysis to determine the permeability of FITC-dextran through the polyelectrolyte shell. Reproduced with permission from ref 333. Copyright 2002 Wiley-VCH. (**C**) FRAP analysis of lipid-type supramolecular nanofibers. Reproduced with permission from ref 229. Copyright 2010 Springer Nature. (**D**) (Top) Time-lapse CLSM images of (left) peptide- and (right) lipid-type nanofibers in the self-sorting supramolecular hydrogel before and after photobleaching. (Bottom) Time-dependent changes of the fluorescent intensity of the (green) peptide- and (red) lipid-type nanofibers in (left) the single-component and (right) self-sorting hydrogels. Reproduced with permission from ref 260. Copyright 2016 Springer Nature. (**E**) FRAP analysis of the interior of the liposome (top) before and (bottom) after hypertonic-induced shrinking. Reproduced with permission from ref 353. Copyright 2018 American Chemical Society.

5.4.1.2. Determination of persistence lengths

The persistence length is one of the mechanical properties of supramolecular nanofibers about the bending stiffness. The persistence length can be estimated by use of time-lapse CLSM imaging at a high scan rate.[262,308,354,355] For example, Yamamoto *et al.* determined the persistence length of phospholipid nanotubes by direct observation using fluorescent microscopy (Figure 24A, B).[354] The phospholipid nanotubes were made from 1,2-dioleoyl-*sn*-glycero-3-phosphocholine (DOPC) and rhodamine-red-DPPE (DPPE: 1,2-dipalmitoyl-*sn*-glycero-3-phosphoethanolamine) by the hydration and subsequent pipetting method. Sequential images acquired at 31.93 frames/s showed translational and intrachain Brownian motions of the nanotubes. From the observed Brownian motion, the persistence length of the nanotube was determined to be 2–8 μm, which varied depending on the nanotubes. In 2020, Kubota *et al.* also estimated by time-lapse CLSM imaging obtained at 33 frames/s the persistence length of artificial Zn^{2+}-induced tripeptide-based supramolecular nanofibers to be 25 ± 2 μm, which is comparable to that of actin filaments (18 μm)[356] (Figure 24C).[308]

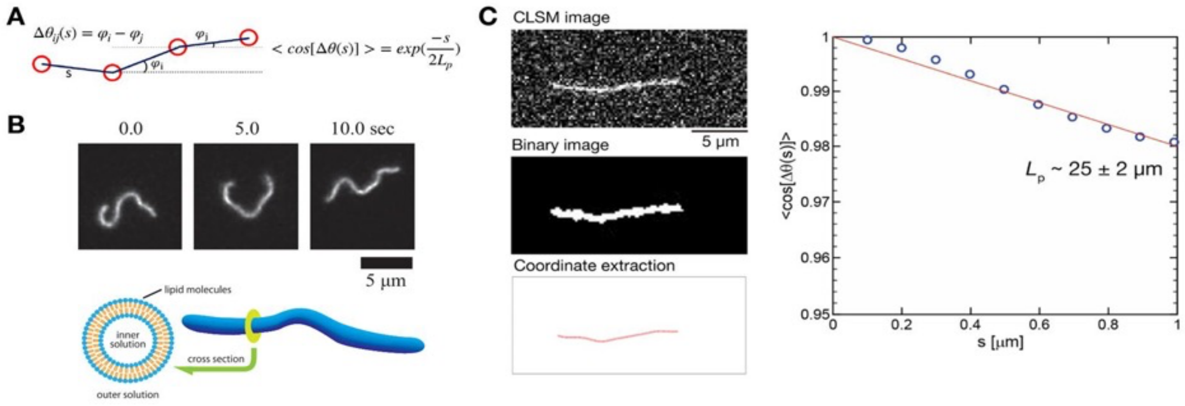

Figure 24. (**A**) Schematic illustration of determination of persistence lengths (L_p: persistence length). Reproduced with permission from ref 308. Copyright 2020 Springer Nature. (**B**) Time-lapse images of a lipid-based nanofiber. Reproduced with permission from ref 354. Copyright 2012 American Physical Society. (**C**) Determination of the persistence length of peptide-type supramolecular nanofibers by CLSM. Reproduced with permission from ref 308. Copyright 2020 Springer Nature.

5.4.1.3. Mesh size estimation from Brownian motion of nanobeads

Imaging of Brownian motions of nano-/micrometer-sized fluorescent beads gives us a valuable method to estimate the mesh size of hydrogels.[223,248,284,357] For example, Shigemitsu *et al.* demonstrated a change of mesh sizes of an aqueous sol/gel composed of a lipid-type hydrogelator bearing a phosphate head group (Phos-cycC$_6$) before/after treatment of phosphatase.[284] Upon treatment of phosphatase, the solution of Phos-cycC$_6$ became the gel state through partial hydrolysis of the phosphate group, resulting in the macroscopic sol–gel transition. Time-lapse CLSM imaging showed that 300 nm beads moved freely in a solution of Phos-cycC$_6$, while almost stopped after addition of phosphatase (Figure 25A). The critical beads size that show the Brownian motion on and off was shifted from 500–800 nm to 200–300 nm, suggesting that a dense cross-linked network was formed by phosphatase treatment (Figure 25B).

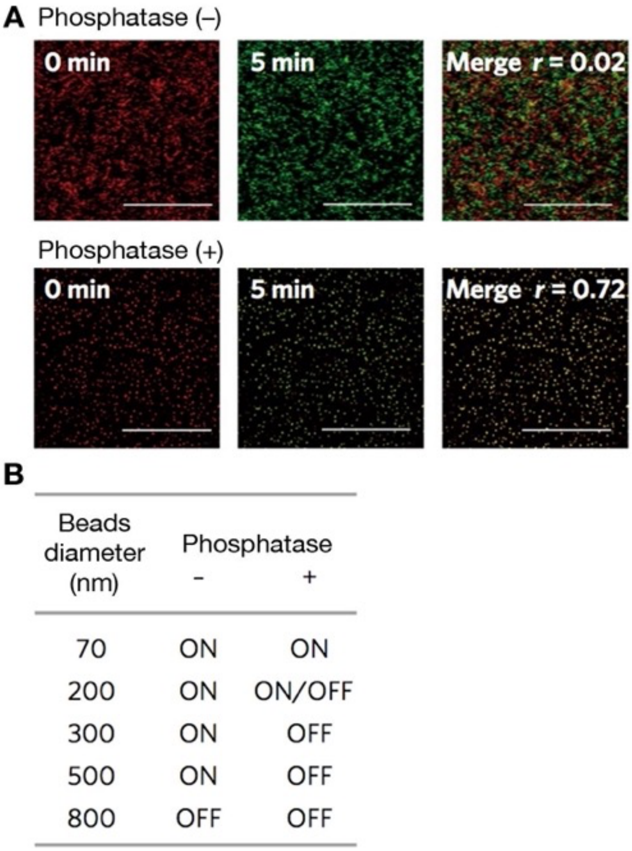

Beads diameter (nm)	Phosphatase –	Phosphatase +
70	ON	ON
200	ON	ON/OFF
300	ON	OFF
500	ON	OFF
800	OFF	OFF

Figure 25. (**A**) Time-lapse CLSM imaging of the Brownian motion of nanobeads (diameter: 300 nm) in (top) a Phos-cycC$_6$ solution and (bottom) a hydrogel after addition of phosphatase. Left: 0 min, middle: 5 min, right: overlay images. (**B**) Brownian motions of beads with different diameters before and after addition of phosphatase. Scale bar: 25 µm. Reproduced

with permission from ref 284. Copyright 2018 Springer Nature.

5.4.1.4. Kinetics of monomer exchange

In situ time-lapse imaging can provide valuable information about the kinetics and pathway of monomer exchange.[251,261,273,277] In 2014, Albertazzi *et al.* successfully evaluated the exchange kinetics of fluorescently-labeled monomers between supramolecular polymers by time-lapse STORM imaging.[251] They mixed two distinct supramolecular polymers, each of which was stained with Cy3- or Cy5-modified monomers. Time-lapse STORM imaging visualized that exchange of fluorescent monomers gradually proceeded and reached in the equilibrium state within 24 h (Figure 22F, G). From the quantitative analysis, the monomer exchange should take place on the mechanism of homogenous exchange along the polymer backbone. The suggested mechanism is different from that of cytoskeletons, where monomer exchange proceeds on "polymerization-depolymerization at the end" and/or "fragmentation-recombination" mechanisms. Similarly, de Silva *et al.* estimated molecular exchange kinetics and mechanisms of a different type of supramolecular nanofiber composed of peptide amphiphiles.[261] In this case, time-lapse STORM images showed that labelled monomers were inserted over the entire length of the nanofibers, which can be explained by neither polymerization-depolymerization at the end, nor fragmentation-recombination mechanisms. Quantitative analysis suggested that the monomer exchange proceeds via a mechanism of the transfer of monomers and small clusters. Furthermore, *in situ* imaging visualized the coexistence of fully dynamic and kinetically inactive domains, suggesting the structural diversity of the supramolecular nanofibers.

5.4.1.5. Real-time observation of unique formation and degradation processes

Time-lapse CLSM imaging is also powerful to elucidate the formation processes of molecular assemblies. In 2016, Onogi *et al.* succeeded in *in situ* observation of the formation process of the peptide-type nanofibers in the absence and presence of seeds.[260] Temperature-dependent CD spectra predicted that the peptide-based supramolecular nanofibers are formed through the cooperative nucleation-elongation mechanism. Time-lapse CLSM imaging of a hot solution of the peptide monomer revealed that the nanofibers gradually and stochastically form with an induction time of 5 min in a heat-cool preparation protocol (Figure 26A, bottom). Interestingly, in the presence of the seeds, the peptide-type nanofibers immediately generated and grew from the surface of the seeds and the resultant nanofibers seemed much thicker than the nanofibers without any seeds (Figure 26A, middle), which gave direct evidence on the nucleation-elongation mechanism. Such differences cannot be assessed by conventional spectroscopic analyses, which provide ensemble structural information. Very recently, Kubota *et al.* found that a formation process of a pH-responsive self-assembling peptide-grafted polymer (PeP) hydrogel is remarkably different from that of small-molecule peptide-type hydrogelators (Figure 26B, top).[358] Time-lapse CLSM imaging after addition of glucono-δ-lactone to a solution of the PeP gelator showed that spherical aggregates with a diameter of 400–500 nm appeared homogeneously and then immediately connected with each other to form the 3D sea-island network structure during the gradual pH decrease (Figure 26B, middle), while small-molecule peptide-type hydrogelators constructed the nanofibrous network structure through the formation process based on the nucleation-elongation mechanism as described above (Figure 26B, bottom). Thus, CLSM imaging demonstrated that grafting on polymers dramatically modulates the self-assembled structure and the process of the triphenylalanine-based hydrogelator.

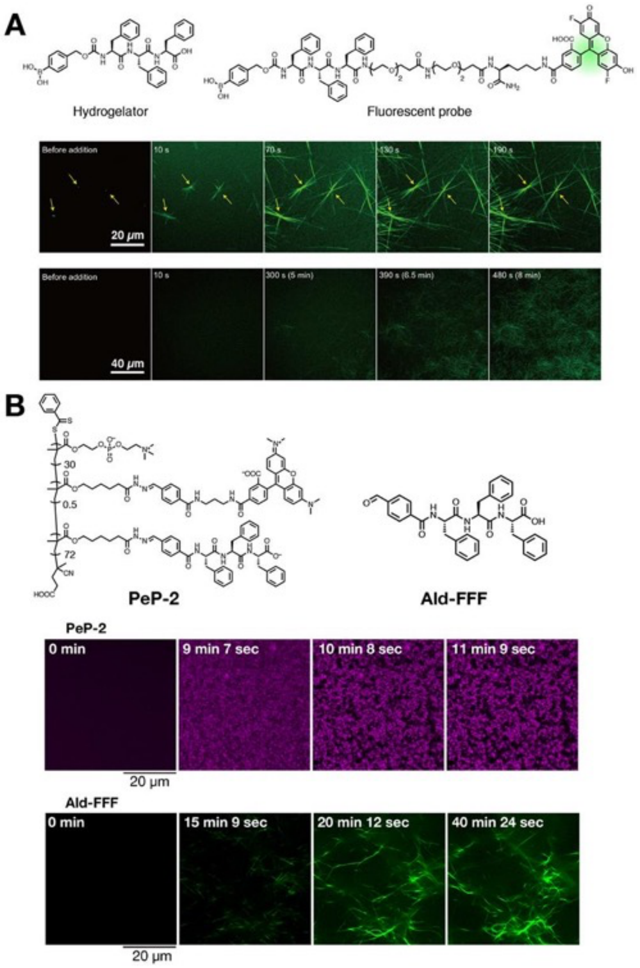

Figure 26. (**A**) (Top) Molecular structures of a hydrogelator and a fluorescent probe. Time-lapse CLSM images of formation of supramolecular nanofibers in the (middle) presence and (bottom) absence of seeds. Reproduced with permission from ref 260. Copyright 2016 Springer Nature. (**B**) (Top) Molecular structures of a self-assembling peptide-grafted polymer and a small-molecule-type hydrogelator. Time-lapse imaging of formation processes of (middle) PeP-2 and (bottom) Ald-FFF upon pH decrease. Reproduced with permission from ref 358. Copyright 2020 Chemical Society of Japan.

Leira-Iglesias *et al.* successfully visualized a spatially-propagated seeded growth of supramolecular colloids.[359] They used a perylene diimide (PDI) derivative that forms supramolecular polymers in an aqueous buffer (Figure 27A, left). A solution of the PDI monomer was poured into a handmade glass slide chamber (spaced by 1 mm), and then the preorganized seeds of PDI assemblies were added on one side of the chamber. CLSM imaging showed that formation of supramolecular colloids propagated with a velocity of 0.26 ± 0.01 mm/min, which was 20 times faster than molecular diffusion of the PDI monomer (Figure 27A, right). The velocity of the propagating front gradually decreased probably because of the reduction of the density difference, which leads to convective instabilities.

In 2016, Aliprandi *et al.* demonstrated time-dependent molecular packing changes by the spectral CLSM imaging technique that allows measurement of the fluorescence spectrum at each pixel.[265] They synthesized a luminescent neutral Pt(II) complex, which self-assembles through π-π stacking and Pt–Pt interactions (Figure 27B, top). The Pt(II) complex formed two kinetic species, a spherical aggregate (a) and a ribbon-like intermediate (b), and one thermodynamically stable fiber (c). The emission properties of these assemblies are different due to distinct packing structures and Pt–Pt distances, which can be used as a molecular fingerprint. Time-lapse spectral imaging successfully uncovered complex dynamics of the assembly evolution (Figure 27B, bottom). After formation of spherical aggregates (a), intermediates (b) anisotropically appeared by consuming the neighboring aggregates (a), and then intermediates (b) slowly interconverted into the thermodynamic fibrous structures (c). Real-time imaging revealed that all the self-assemblies formed in dynamic equilibrium with monomers, which is similar to biological infection processes.

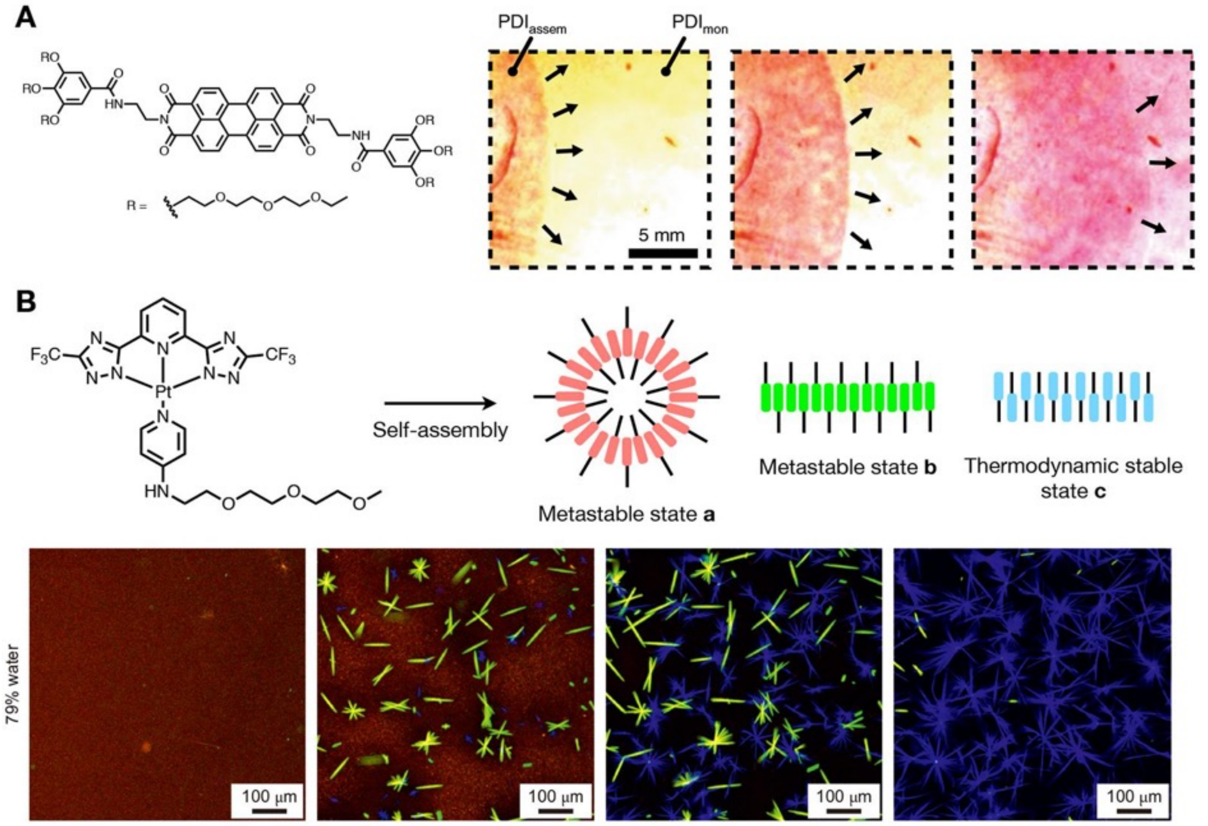

Figure 27. (**A**) Time-lapse imaging of a traveling front of supramolecular aggregates initiated by seed addition. Reproduced with permission from ref 359. Copyright 2018 Springer Nature. (**B**) (Top) Schematic illustration of self-assembly of a neutral Pt(II) complex. (Bottom) Real-time spectral CLSM imaging of self-assembled structures of the neutral Pt(II) complex. Reproduced with permission from ref 265. Copyright 2016 Springer Nature.

Real-time CLSM can also visualize unique formation processes of synthetic polymers and lipid vesicles.[360–389] In 2009, Howse *et al.* observed the controlled formation process of unilamellar giant polymer vesicles from a self-assembled surface in real time.[364] A block copolymer, poly(ethylene oxide)$_{16}$-*co*-poly(butylene oxide)$_{22}$ (PEO$_{16}$-PBO$_{22}$) forms hexagonal packed rods through microphase separation by partial hydration (less than 10% water), and further hydration leads to formation of lamellae. After deposition of the polymer on the photopatterned surface (which gives the hydrophilic surface: 19 × 19 μm or 5.3 × 5.3 μm), the substrate was immersed into water. Real-time CLSM imaging showed the vesicles formation through the hydration and expansion of the upper surface layers at a rate of *ca.* 2 ×

10^3 vesicles $\mathrm{cm}^{-2}\,\mathrm{s}^{-1}$ (Figure 28A). The uniform fluorescent intensity from different vesicles was observed, suggesting that the resultant vesicles should have a uniform membrane thickness. The observed vesicle diameter correlated with a mesh size of the photopatterned surface and has an upper limit, which is comparable to theoretical upper limit ($d = 2^{1/2}L$) where polymer formed a hemisphere on the hydrophilic surface. Furthermore, the size distribution of the obtained vesicles was narrower than those obtained by conventional rehydration and electroformation, indicating that this method is powerful for spontaneous formation of unilamellar vesicles with a narrow size distribution.

In 2015, Hardy *et al.* reported unique vesicle growth through continuous formation of phospholipid by membrane-bound self-reproducing catalyst.[374] They employed Cu^+-catalyzed azide-alkyne cycloaddition (CuAAC) with oligotriazole ligands, which could reproduce themselves through CuAAC from 1-azidedodecane and tripropargylamine. The resultant Cu^+-oligotriazole catalysts also produced triazole phospholipids from 1-azidedodecane and alkyne-lysolipid. Indeed, the formation kinetics of the oligotriazole from 1-azidedodecane and tripropargylamine revealed a sigmoidal-shaped curve consisting of an induction period and a subsequent rapid rise, suggesting the desired autocatalytic reaction process. Moreover, the half-times depends on the initial concentration of the ligand (1.94 and 0.81 h for 5 and 35 μM, respectively). Time-lapse fluorescent imaging visualized the gradual membrane growth from <1 μm to up to 5 μm over 10 h. The authors succeeded to observe the morphological change due to formation of multilameller vesicles. More recently, the same group demonstrated *de novo* formation and division of the vesicles through *in situ* generation of phospholipids based on adenylate chemistry catalyzed by a soluble fatty acyl adenylate ligase FatD10 (Figure 28B, top).[381] FadD10 converts long-chain saturated fatty acids into corresponding fatty acyl adenylates in the presence of adenosine triphosphate (ATP) and Mg^{2+} ions, which reacted with amine-functionalized lysolipids to produce the amidophospholipids. Real-time optical microscopic imaging after mixing an amine-functionalized lysolipid, dodecanoic acid, and FadD10 revealed that small vesicles formed within 30 min and gradually transformed into larger vesicles with various sizes and lamellarities. Spinning disk confocal microscopy images showed that Alexa Fluor

488-labeled FadD10 was colocalized with a fluorescent membrane probe, Texas Red DHPE, suggesting that FadD10 interacted with the membrane through electrostatic interaction. Furthermore, time-lapse fluorescence microscopic imaging captured drastic morphological transformations when continuously supplying reactive precursors by a microfluidic device (Figure 28B, bottom). Some vesicles showed membrane growth followed by division into small vesicles, which resembles the division process of L-form bacteria.

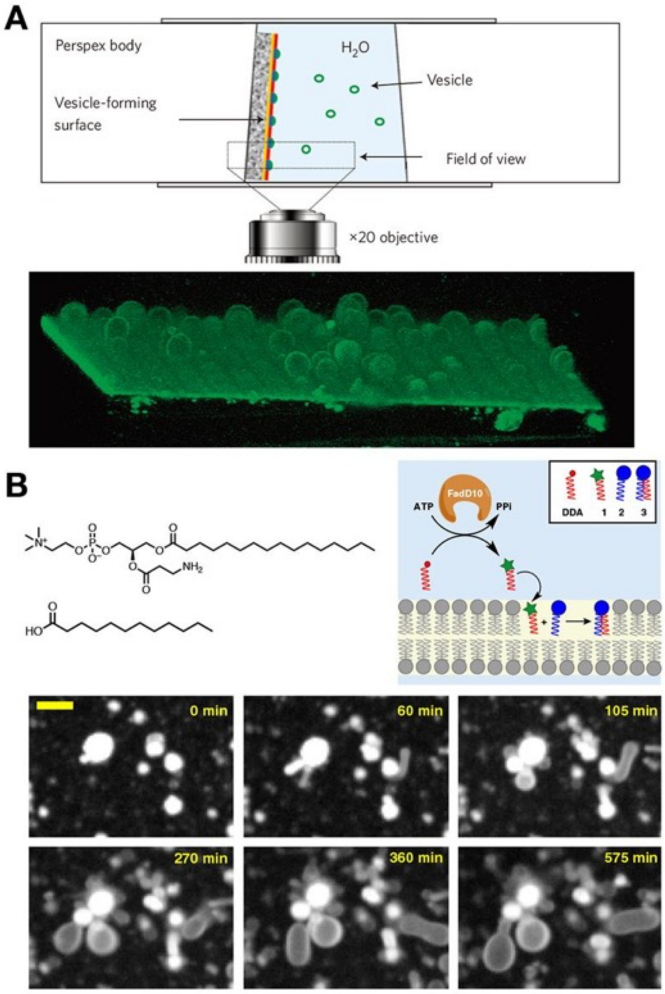

Figure 28. (**A**) CLSM image of vesicle formation from the patterned surface. Reproduced with permission from ref 364. Copyright 2009 Springer Nature. (**B**) (Top) Molecular structures of phospholipid precursors and schematic illustration of *in situ* generation of phospholipids by FatD10. (Bottom) Time-lapse imaging of *de novo* formation of giant vesicles through *in situ* generation of phospholipids. Scale bar: 10 µm. Reproduced with permission from ref 381. Copyright 2019 Springer Nature.

In situ CLSM imaging is also applicable to coacervate droplets that are actively studied as a scaffold for protocell models.[336,340,343–345,348,349,353,390–448] In 2016, real-time CLSM imaging of enzyme-mediated decomposition and formation of complex coacervates was reported by Aumiller *et al.*[410] The coacervates were prepared from polyuridylic acid RNA (polyU, M_w = 600–1000 kDa) as polyanion and a cationic peptide, RRASLRRASL as confirmed by turbidity test, differential interference contrast (DIC) and fluorescent imaging. Importantly, single phosphorylation of serine residues inhibited coacervation due to insufficient positive charge density on the peptide backbone. To observe the formation process of the complex coacervate, the authors conducted DIC and CLSM imaging of a mixture of polyU/doubly-phosphorylated peptide in the presence of lambda protein phosphatase (LPP) (Figure 29A). At the initial stage, the solution was transparent. After 12.3 min, the coacervate started to form in solution and at the same time began to fall to the coverslip surface. They also succeeded in dissolution of the complex coacervate by addition of protein kinase A (Figure 29B). Initially, the droplets mainly existed on the surface of coverslip. After 12.5 min, the droplets began to be smaller, and almost all coacervates disappeared. During this process, the droplets remained a spherical morphology on the coverslip surface and did not show coalescence as much as LPP-induced coacervates.

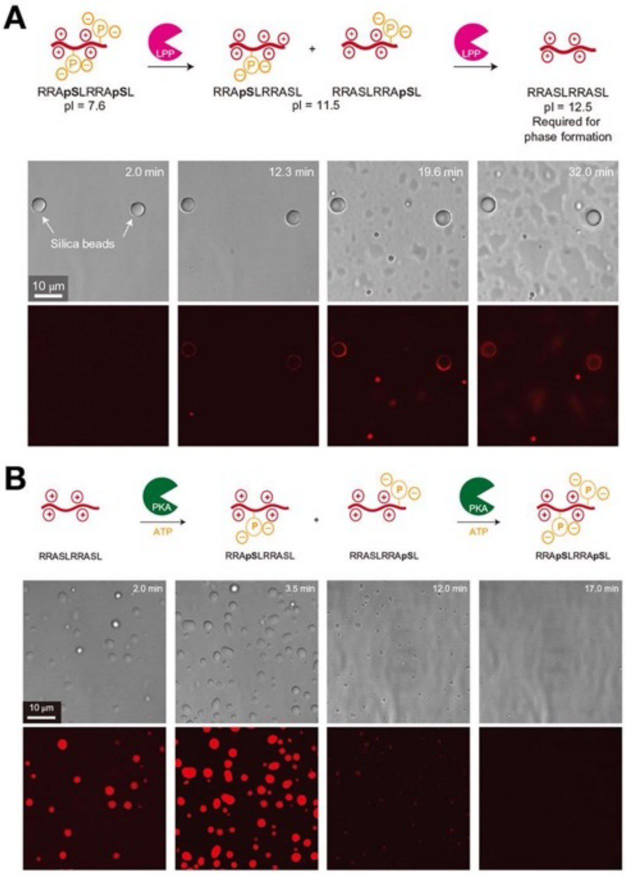

Figure 29. CLSM images of (**A**) formation and (**B**) collapse of coacervates by phosphatase and kinase, respectively. Reproduced with permission from ref 410. Copyright 2016 Springer Nature.

5.4.1.6. Fuel-driven dissipative self-assembly

Inspired by living cells and animals, it is now considered that fuel-driven dissipative self-assembly has become a key for construction of active, autonomous, and adaptive soft materials. Time-lapse CLSM imaging is powerful to address the unique dynamic behaviors of dissipative self-assembly that cannot be elucidate conventional, ensemble spectroscopic measurements.[253,270,308,313,318,323,359,386,449–459] In 2015, Boekhoven *et al.* succeeded in visualization of simultaneous growth and shrinkage of supramolecular nanofibers in proximity.[253] They realized transient formation of supramolecular nanofibers on treatment of a methylating reagent, dimethyl sulfate (DMS), to a hydrogelator precursor possessing carboxylate groups (Figure 30A). Upon methylation of the carboxylate group, the resultant methyl ester derivative behaves as a hydrogelator to form supramolecular hydrogel (nanofibers), and the subsequent ester hydrolysis leads to decomposition of the hydrogel (nanofibers). Real-time CLSM imaging visualized that the nanofibers stochastically collapsed from their tips with velocities of 15 μm/min (Figure 30B). Interestingly, both the elongation and collapse of the nanofibers were simultaneously observed in the same field of view. This indicated spatially-heterogeneous, non-synchronized formation and degradation of the nanofibers, which is similar to the nonlinear dynamics and dynamic instability of microtubule filaments in live cells.

Tena-Solsona *et al.* developed a self-erasable supramolecular ink by use of dissipative molecular self-assembly.[270] They synthesized Fmoc-protected amino acids and tripeptides that possess D or E at the C-terminus. Upon addition of 1-ethyl-3-(3-dimethylaminopropyl)carbodiimide (EDC), amino acids/peptides form hydrophobic acid anhydride, resulting in transient self-assembly into spherulites and colloids until hydrolysis of acid anhydride as characterized by CLSM imaging (Figure 30C, D). Moreover, they demonstrated the applicability of transient turbidity of Fmoc-D spherulites as a self-erasing ink (Figure 30E). After immobilization of Fmoc-D on a polyacrylamide polymer hydrogel, EDC solution was applied. Time-lapse photography and imaging analysis revealed that the print immediately appeared within 2 min and then the visibility of the print was gradually decreased over 600 min. The lifetime of the visibility could be tuned by the concentration of fuel.

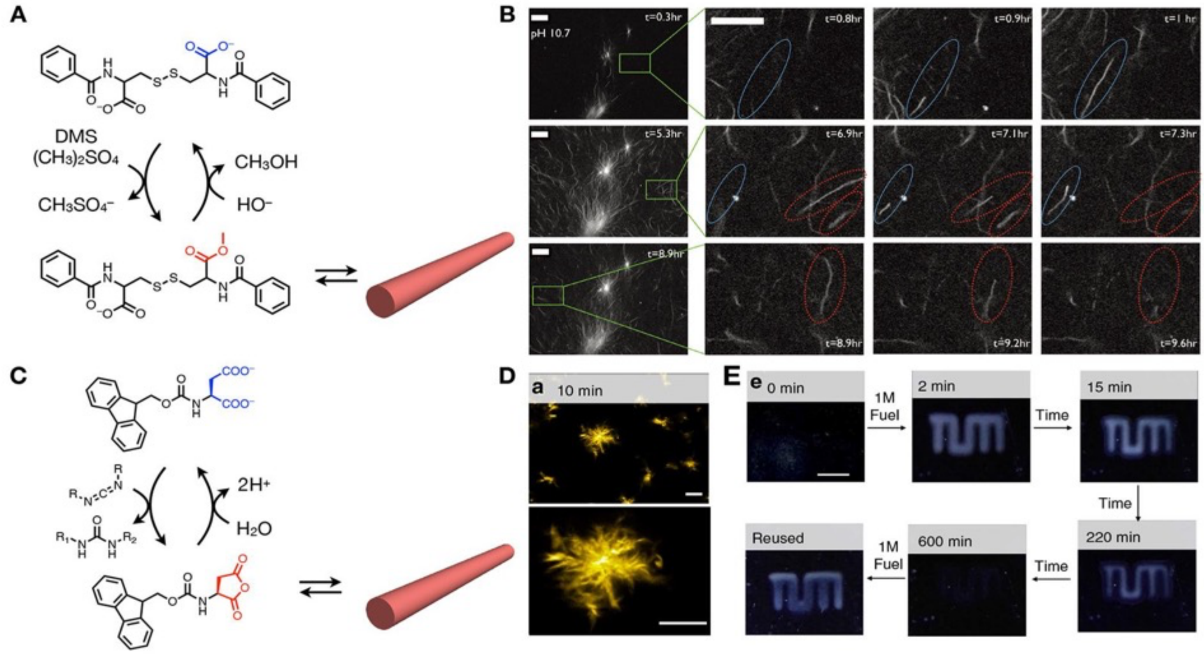

Figure 30. (**A**, **C**) Reaction cycles for fuel-driven dissipative self-assembly. The monomers activated by (**A**) DMS and (**C**) EDC self-assemble into fibrous structures. (**B**) Time-lapse CLSM images displaying growth and shrinking of supramolecular nanofibers. Scale bar: 10 µm. Reproduced with permission from ref 253. Copyright 2015 AAAS. (**D**) CLSM images 10 min after EDC to a solution of Fmoc-D. Scale bar: 10 µm. (**E**) Time-dependent photographs of a self-erasing medium composed of a 30% acrylamide hydrogel containing Fmoc-D. Scale bar: 1 cm. Reproduced with permission from ref 270. Copyright 2017 Springer Nature.

Time-lapse CLSM imaging also enables to elucidate dissipative self-assembly systems of vesicles and liquid droplets.[386,449,451,453,455–458,460] In 2016, Maiti *et al.* reported transient formation of vesicular reactors through stabilization with metal complexation between surfactants and ATP, which works as chemical fuel. In this system, they employed the surfactants with C_{16} chain and Zn^{2+}-TACN head group (C_{16}TACN-Zn^{2+}, TACN: 1,4,7-triazacyclononane). Upon addition of ATP, the surfactants showed structural transformation from the micelle to the vesicular structure through complexation of Zn^{2+}-TACN and a triphosphate group of ATP. To realize dissipative self-assembly, potato apyrase was introduced to degrade ATP to adenosine monophosphate (AMP) and phosphate ions. This system enabled to transiently form the vesicles, whose lifetime could be determined by the hydrolysis rate of ATP. By use of real-time CLSM imaging after fluorescent staining, the number of spherical objects was quantified. Immediately after addition of ATP, the number of particles increased and then gradually decreased over 300 sec.

Dynamic spatiotemporal patterns, such as waves and spirals, play essential roles in living cells. Rational design for artificial spatiotemporal patterns has remained a challenge for synthetic (supramolecular) chemists. In 2020, Kubota *et al.* realized a dynamic out-of-equilibrium pattern, a propagating wave, comprising of spatiotemporally-coupled formation and degradation of supramolecular nanofibers.[308] Inspired by actin waves in lamellipodia, a reaction network was designed to precisely control the fiber formation and degradation by two distinct chemically orthogonal stimuli (Figure 31A). A monomer, BPmoc-F_3, has two different reactive groups to trigger formation and degradation of supramolecular nanofibers: carboxylate and boronobenzyl groups at the C- and N-termini, respectively. In an aqueous buffer, BPmoc-F_3 forms supramolecular nanofibers upon addition of Zn^{2+} ions mainly due to bridging BPmoc-F_3 monomers and/or suppression of electrostatic repulsion. The resultant nanofibers were decomposed by addition of glucose oxidase (GOx)/glucose pair through H_2O_2-triggered 1,6-elimination reaction of the boronobenzyl group. Real-time CLSM imaging after addition of a mixture of Zn^{2+} ion and glucose at the edge of a droplet of BPmoc-F_3 and GOx clearly visualized the propagating wave with a travelling distance and velocity of 340 ± 40 μm and 54 ± 8 μm/min, respectively (Figure 30B). Numerical simulation suggested that concentration gradient of the degradation stimulus and the smaller diffusion coefficient are essential for the propagating wave emergence. Furthermore, the force generated by the supramolecular propagating wave was quantified to be 0.005 pN by the fluorescent beads displacement assay monitored with CLSM imaging (Figure 31C, D).

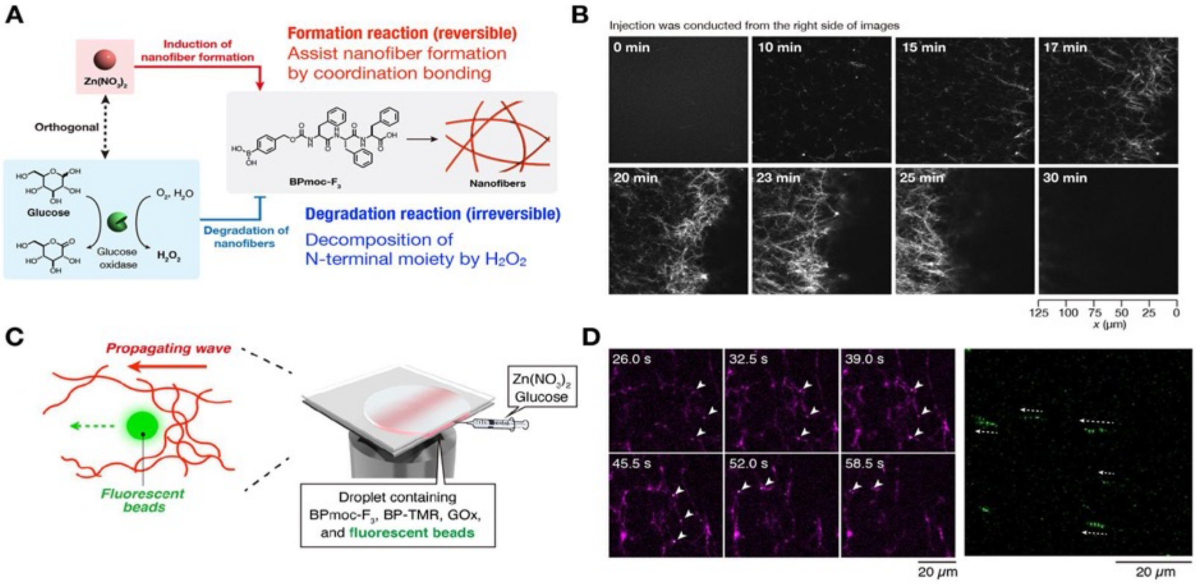

Figure 31. (**A**) A reaction network for a supramolecular propagating wave. (**B**) Time-lapse CLSM imaging of the propagating wave. (**C**) Schematic illustration of force generation by the wave. (**D**) (left) Time-lapse images and (right) maximum intensity projection of the beads displacement. Green: fluorescently-modified beads, magenta: supramolecular fibers. Reproduced with permission from ref 308. Copyright 2020 Springer Nature.

5.4.2. Multicolor imaging: multicomponent self-assembly

One of the fascinating characteristics of CLSM represents a capability to discriminate between different types and domains of molecular assemblies by selective fluorescent staining. In this section, representative examples to visualize supramolecular assemblies with multiple distinct domains (*e.g.* supramolecular block copolymers) and multicomponent supramolecular assemblies are described.

5.4.2.1. Multi-domain observation in a molecular assembly

Self-assembly of block copolymers provides a promising way to rationally fabricate complex compartmentalized soft matters with well-defined hierarchical nanostructures. The Manners group pioneered living crystallization-driven self-assembly (CDSA) in the preparation of multicompartment block co-micelles, such as one-dimensional cylinder micelles and two-dimensional platelet co-micelles, of controlled length/size and narrow distribution.[326,327,461–475] In 2014, Hudson *et al.* demonstrated *in situ* visualization of multiblock cylinder co-micelles formed through the crystallization-driven living self-assembly of fluorescent block copolymers, PFS$_{62}$-*b*-(PDMS$_{605}$-*r*-PMVS$_{21}$), with a series of fluorophores that exhibit blue, green, and red fluorescence [PMVS: poly(methylvinylsiloxane)] (Figure 32A).[462] CDSA allowed preparation of 11-block co-micelles from the sequential addition of fluorescent unimers to a solution of non-fluorescent seeds with additional non-fluorescent spacers to increase optical resolution. CLSM imaging clearly visualized centrosymmetric cylindrical nanostructure with a length of *ca.* 5 μm that consists of spatially segregated red, green, and blue fluorescence (Figure 32B, C). Moreover, Manners and coworkers succeeded in *in situ* CLSM observation of 2D concentric lenticular micelles, cross-shaped supermicelles, rectangular platelet micelles, semiconducting or heterojunction segmented nanowires prepared by the CDSA approach.

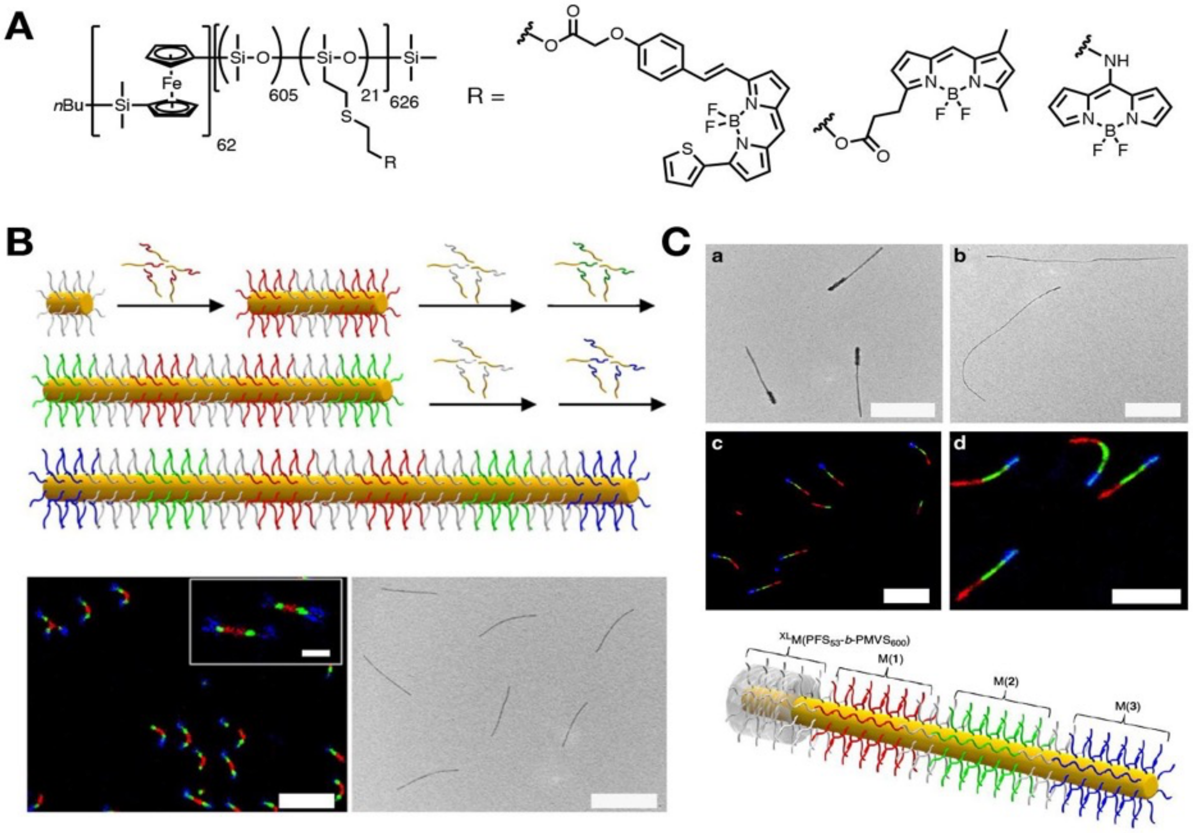

Figure 32. (**A**) Molecular structures of (PFS$_{53}$-*b*-PMVS$_{626}$) and fluorescently-labeled derivatives. (**B**) (left) CLSM and (right) TEM images of fluorescent 11-block polymer micelles. Scale bar: 5 μm (CLSM), 3 μm (TEM). (**C**) (top) TEM and (middle) CLSM images

of 7-block non-centrosymmetric RGB micelles. Scale bar: 500 nm (TEM, left), 2 μm (TEM, right), 10 μm (CLSM, left), 5 μm (CLSM, right). Reproduced with permission from ref 462. Copyright 2014 Springer Nature.

CLSM and SR imaging also enable visualization of supramolecular block copolymers.[288,289,319,320,476] In 2018, Adelizzi *et al.* demonstrated that the super-resolution technique, interfacial point accumulation for imaging in nanoscale tomography (iPAINT), can be applied to observation of supramolecular block copolymers.[288,289] The supramolecular block copolymer was prepared under thermodynamic control by mixing two types of preorganized supramolecular homopolymers stained with photoactivatable fluorescent dyes (Cage-635 and Cage-552) through physisorption (Figure 33A, B). iPAINT imaging clearly revealed the existence of supramolecular di- and triblock copolymers, where red and green fluorescence was alternately aligned. These results correspond well to the formation of supramolecular block copolymers supported by CD spectroscopy.

Sarker *et al.* recently reported the cooperative supramolecular block copolymerization of fluorescent monomers under thermodynamic control, which enabled energy migration and light-harvesting across the interfaces of linearly connected segments (Figure 33C).[319,320] In this study, the naphthalene diimide derivatives modified with ethoxy or pentanethiol (SS-diOEt or SS-dithiol, respectively) showing distinct green and red fluorescence, respectively, were employed. On the basis of temperature-dependent self-assembly behaviors of these monomers, the A-B-A-like supramolecular block copolymers could be constructed through fast nucleation of SS-dithiol and the subsequent elongation of SS-diOEt under precise temperature control. SIM imaging revealed that coassembled nanofibers contained alternate green and red emitting nanofibers as expected by spectroscopic studies (Figure 33D). The green nanofibers, corresponding SS-diOEt, over several micrometers were elongated from short red segments with a length of *ca.* 1 μm. The resultant segmented arrangements of donor (SS-diOEt) and acceptor (SS-dithiol) would work as organic coaxial-heterostructures. Spectrally-resolved fluorescence imaging showed the significantly enhanced emission from the acceptors, which was an unambiguous indicator of excitation energy transfer (Figure 33E).

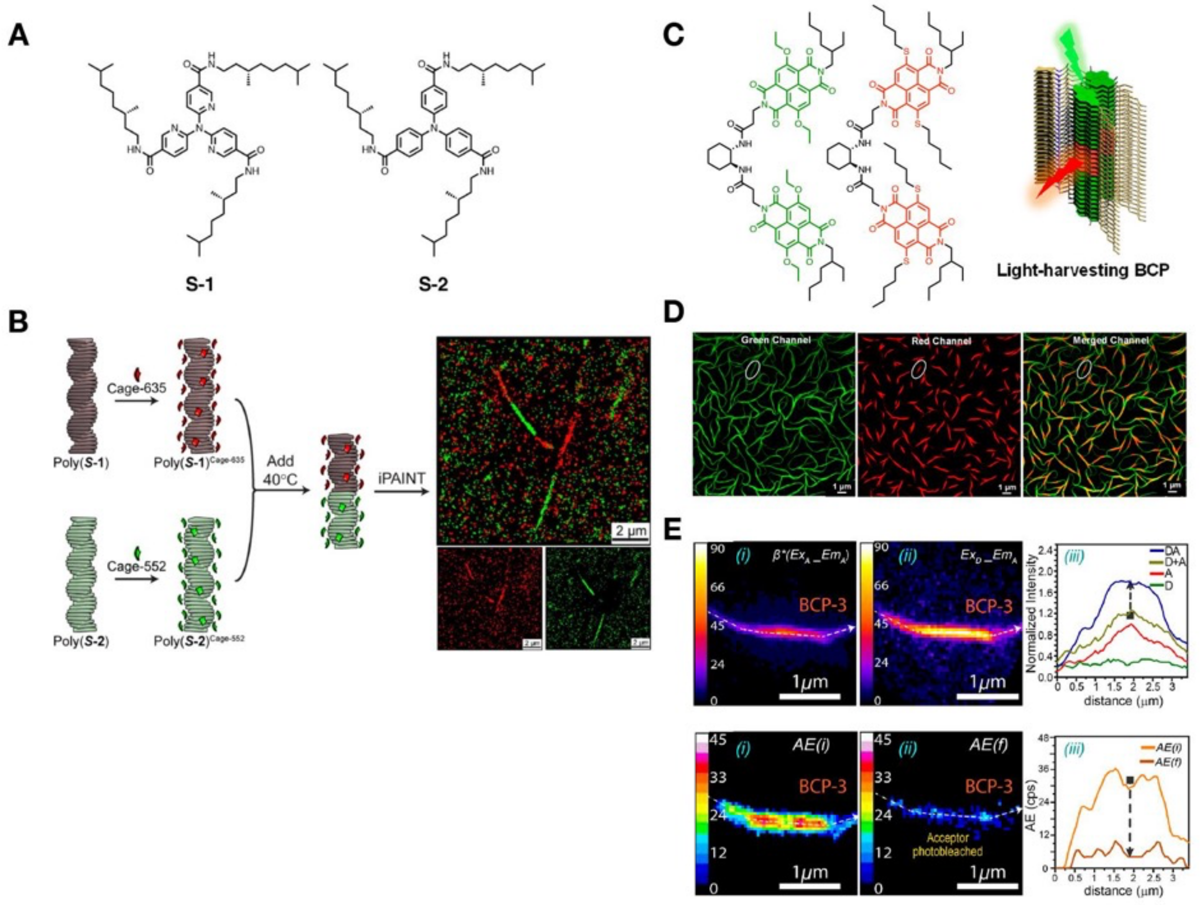

Figure 33. (**A**) Molecular structures of monomers. (**B**) STORM images of supramolecular block copolymers stained by iPAINT. Reproduced with permission from ref 288. Copyright 2018 American Chemical Society. (**C**) Molecular structure of naphthalene diimide derivatives. (**D**) SIM images and (**E**) spectrally-resolved fluorescent imaging of block copolymers. Reproduced with permission from ref 320. Copyright 2020 American Chemical Society.

The domain structure formed on lipid/polymer vesicles can also be elucidated by CLSM.[346,397,477–490] In 2009, Christian *et al.* reported ligand-induced domain formation of polymer amphiphile vesicles.[337] A relatively symmetric poly(acrylic acid)-poly(butadiene) copolymer (AB1) formed polymersomes and micelles depending on pH and salt concentration, whereas nonionic poly(ethylene oxide)-poly(butadiene) copolymer (OB18) yields coexisting cylinders and vesicles independent of pH and salt concentration. CLSM imaging showed that Ca^{2+}-induced domains were clearly formed in all of the vesicles or cylinder micelles composed of a mixture of AB1 and rhodamine-labelled OB18. Such spotted vesicles were stable under tension applied by aspiration. Systematic CLSM study revealed that responsive Janus structures were highly dependent on pH and Ca^{2+} concentration that are centered near the characteristic binding constants for polyacid interactions.

In 2016, Takeuchi and coworkers reported CLSM-based study on a lipid dynamics in asymmetric vesicles formed by a microfluidic jet flow.[491] By applying a jet flow to an asymmetric planar lipid bilayer, vesicles with a diameter of 3–20 µm were obtained (Figure 34A). To investigate flip-flop dynamics in the asymmetric vesicles, interaction between 1,2-dioleoyl-*sn*-glycero-3-phospho-L-serine **(**DOPS) and fluorescent-modified annexin V that selectively binds to PS in the presence of Ca^{2+} ions. CLSM imaging showed the fluorescence of annexin V could be observed only on the vesicles prepared with DOPS/DOPC outer leaflet. The time-dependent CLSM imaging revealed that the fluorescent intensity profile from the vesicle surface was gradually decreased, suggesting a flip-flop dynamics of DOPS, and the half time was determined to be 5–6 hours similar to that of apoptotic cells (Figure 34B). They also demonstrated the flip-flop dynamics of PS could be promoted by addition of cinnamycin, which is a specific binder to PE and promotes the exposure of PE from outer to inner leaflet (Figure 34C, D).

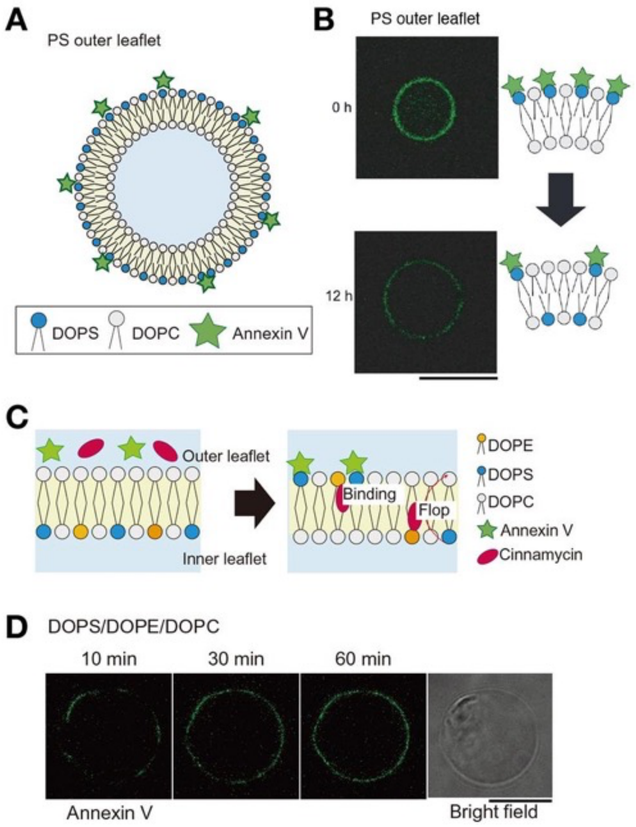

Figure 34. (**A**) Schematic illustration of DOPS detection by fluorescently-labeled annexin V in an asymmetric vesicle. (**B**) Time-dependent CLSM images of the annexin V-treated vesicle. (**C**) Cinnamycin-enhanced membrane dynamics of asymmetric vesicles. (**D**) Time-dependent CLSM images of the asymmetric vesicles in the presence of cinnamycin. Reproduced with permission from ref 491. Copyright 2016 Springer Nature.

5.4.2.2. Multicomponent self-assembly

Eukaryotic cells exhibit intricate functions based on elegant interplay among a myriad of biomolecules and molecular assemblies such as cytoskeletons and spatially isolated and distributed various organelles. Multicomponent supramolecular systems containing chemically-distinct nanometer- or micrometer-sized domains are promising for imitation of cell-like sophisticated functions such as multiple stimuli response and biosensing. We summarize here the representative examples about multicomponent supramolecular systems characterized with *in situ* CLSM imaging.[203,207,208,227,233,240,260,267,269,282,284,285,294–296,299,306,309,316,340,349,350,353,395,396,399,401,423,433,436,437,440–445,492–497]

Encapsulation of (inorganic) porous materials in supramolecular hydrogels enables to construct multicomponent supramolecular hydrogels possessing distinct nano/micro-sized environments. Such multicomponent supramolecular hydrogels have been shown to be useful for wet-based sensing devices and controlled drug release matrices. Wada *et al.* in 2009 developed polyanion-selective sensing materials composed of a glycolipid-type supramolecular hydrogel, phosphatase, MCM-41 type mesoporous silica nanoparticles (NH_2-MCM), and fluorescent probes (Figure 35A).[227] This multicomponent hydrogel has three distinct domains: hydrophobic environment of the interior of the glycolipid nanofibers, cationic inner surface of NH_2-MCM, and water layer containing phosphatase. The anionic fluorescent probe, P-Coum, which initially installed inside the NH_2-MCM through electrostatic interaction, was released to the water phase upon addition of polyanion (Figure 35B). After hydrolysis by phosphatase, the hydrolyzed probe (Coum) translocated to the hydrophobic domain of the supramolecular nanofibers. FRET was induced from Coum to a BODIPY-based probe embedded in the nanofibers, leading to polyanion detection by fluorescent color change. CLSM imaging clearly demonstrated that the spherical fluorescence of P-Coum in NH_2-MCM and the fiber-like fluorescence of the BODIPY-type probe in the supramolecular nanofibers (Figure 35C). Addition of polyanion induced translocation of the fluorescence of Coum to BODIPY-stained supramolecular nanofibers as confirmed by *in situ* CLSM imaging. Ikeda *et al.* expanded this concept and constructed a fluorocolorimetric sensor for polyamine with a hybrid of a supramolecular hydrogel and montmorillonite (MMT) (Figure 35D, E).[233] The surface of MMT, a layered clay, has high anionic charge density to facilitate aggregation of cationic diethylaminocoumarin probes (G-Coum). Upon addition of polyamines (*e.g.* spermine and spermidine), a greenish excimer emission of the probe converted to an intensified blue monomer emission through cation exchange in MMT and subsequent translocation to the supramolecular nanofibers. *In situ* CLSM imaging showed that the coumarin fluorescence was observed as spherical spots with a diameter of 1–10 μm and not completely overlapped with a BODIPY fluorescence of the supramolecular fibers, suggesting that the coumarin probe selectively bound to MMT (Figure 35F, left). 30 min after addition of spermine, the coumarin fluorescence could also be detected from the supramolecular nanofibers (Figure 35F, right). With this multicomponent hydrogel system, polyamines such as spermine and spermidine can be detected in a concentration-dependent manner by fluorescent color change at the bulk state (Figure 35G).

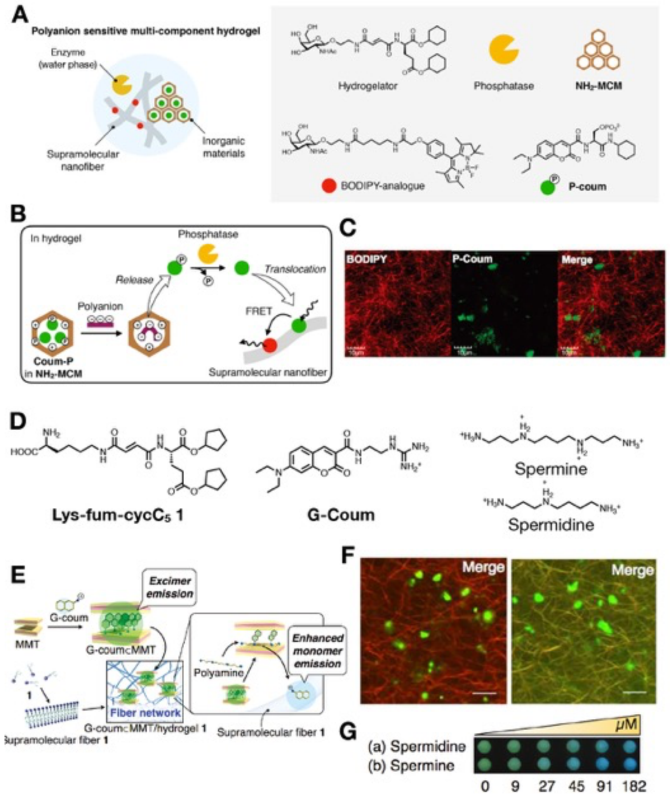

Figure 35. (**A**) Schematic illustration of a polyanion sensor based on a multicomponent supramolecular hydrogel containing phosphatase and NH_2-MCM. (**B**) FRET-based sensing mechanism of the polyanion sensor. Reproduced with permission from ref 301. Copyright 2020 Wiley-VCH. (**C**) CLSM imaging the polyanion sensor. Reproduced with permission from ref 227. Copyright 2009 American Chemical Society. (**D**) Molecular structures used for a polyamine sensor. (**E**) Schematic illustration of the polyamine sensing mechanism. (**F**) CLSM imaging of the multicomponent hydrogel containing (red) supramolecular nanofibers, (green) G-Coum, and MMT (left) before and (right) after addition of sperimine. Scale bar: 5 μm. (**G**) Detection of spermidine and spermine by a hydrogel droplet chip. Reproduced with permission from ref 233. Copyright 2011 American Chemical Society.

In 2012, Boekhoven *et al.* reported a drug delivery/release platform with tunable release rate by combination of an enzyme-responsive supramolecular hydrogel and enzyme-loaded liposomes (Figure 36A, B).[240,309] Upon heating above the phase transition temperature of the liposome, the encapsulated chymotrypsin was diffused to the gel matrix, followed by hydrolysis of a fluorophore-modified gelator, resulting in the release of the fluorescent molecules. To evaluate the structure of the multicomponent hydrogel, the supramolecular fibers and liposomes were stained with the fluorescently-labeled monomers, 1-FITC and NBD-PE, respectively, and RITC-chymotrypsin was employed. *In situ* CLSM imaging of this multicomponent hydrogel showed that the fluorescence of supramolecular fibers and liposomes were not overlapped with each other and the fluorescence of RITC-chymotrypsin was detected from the interior of the liposome, indicating the orthogonal self-assembly of supramolecular nanofibers and liposomes without any leakage of the enzyme (Figure 36C).

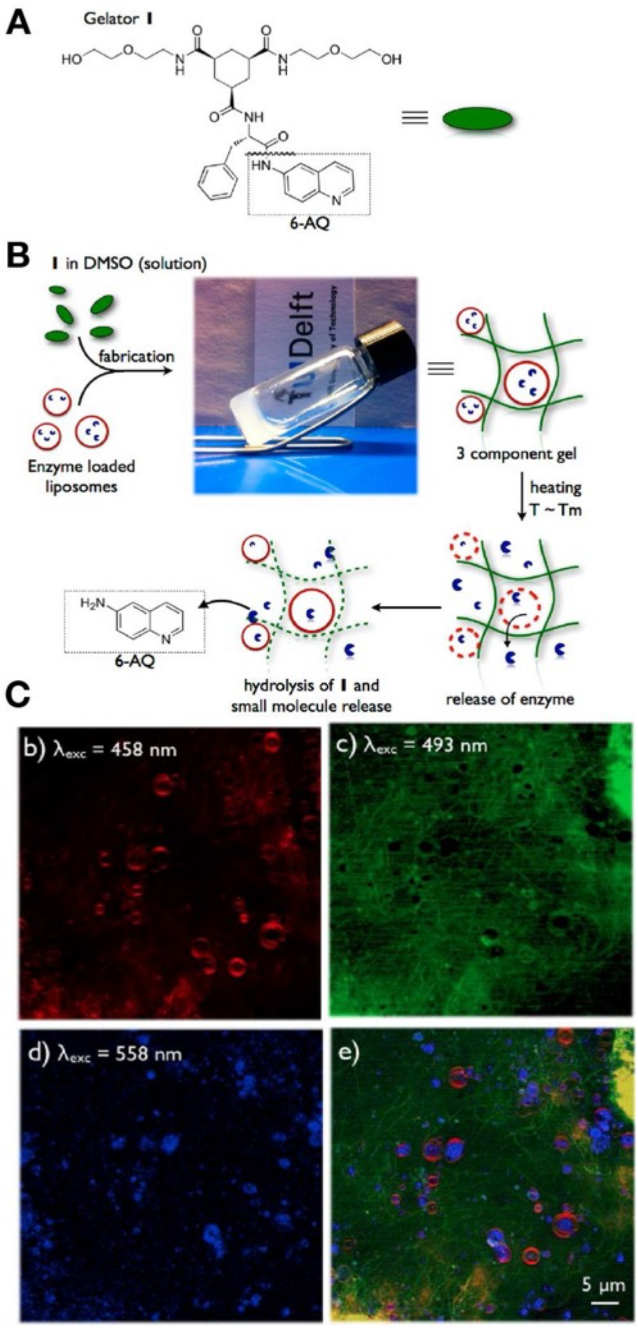

Figure 36. (**A**) Chemical structure of a gelator. (**B**) Schematic illustration of controlled release from the gel network with embedded liposomes. (**C**) CLSM imaging of the multicomponent hydrogel. Red: liposomes stained with a lipid probe, green: the gel network, blue: fluorescently-labeled chymotrypsin. Reproduced with permission from ref 240. Copyright 2012 American Chemical Society.

CLSM imaging after selective fluorescent staining is powerful to characterize self-sorting supramolecular nanofibers, whose characterization is extremely difficult by TEM, SEM, and AFM.[260,267,284,285,294,299,306,316] Onogi *et al*. reported super-resolution microscopic imaging of self-sorting nanofibers composed of peptide- and lipid-type hydrogelators with STED and Airyscan CLSM (Figure 37A). They designed two distinct fluorescent probes that possess the corresponding same self-assembled motif same as each hydrogelator (Figure 37B). Super-resolution STED imaging of the hydrogel consisting of two hydrogelators and two fluorescent probes visualized an orthogonal self-sorting network, in which the peptide- and lipid-type nanofibers were well entangled but not overlapped with each other (Figure 37C). By use of 3D Airyscan CLSM imaging, the self-sorting network was formed in the depth direction (Figure 37D). Real-time imaging immediately after dissolving the hydrogelators and probes showed distinct kinetics of nanofiber formation; formation of the lipid-type nanofibers already completed but the peptide-type nanofibers gradually generated with an induction time of 15 min (Figure 37E, F). It suggested that distinct formation kinetics should be important for self-sorting phenomena. To obtain an implication about rules of the self-sorting of supramolecular fibers in molecular design, Kubota *et al.* investigated self-assembly properties of a focused library of the peptide- and lipid-type hydrogelators about distinct hydrophobicity and net charge (Figure 38).[285] The imaging-based assay revealed that the same charge of peptide- and lipid-type hydrogelators and moderate hydrophobicity of the peptide-type hydrogelator would be required to achieve the self-sorting.

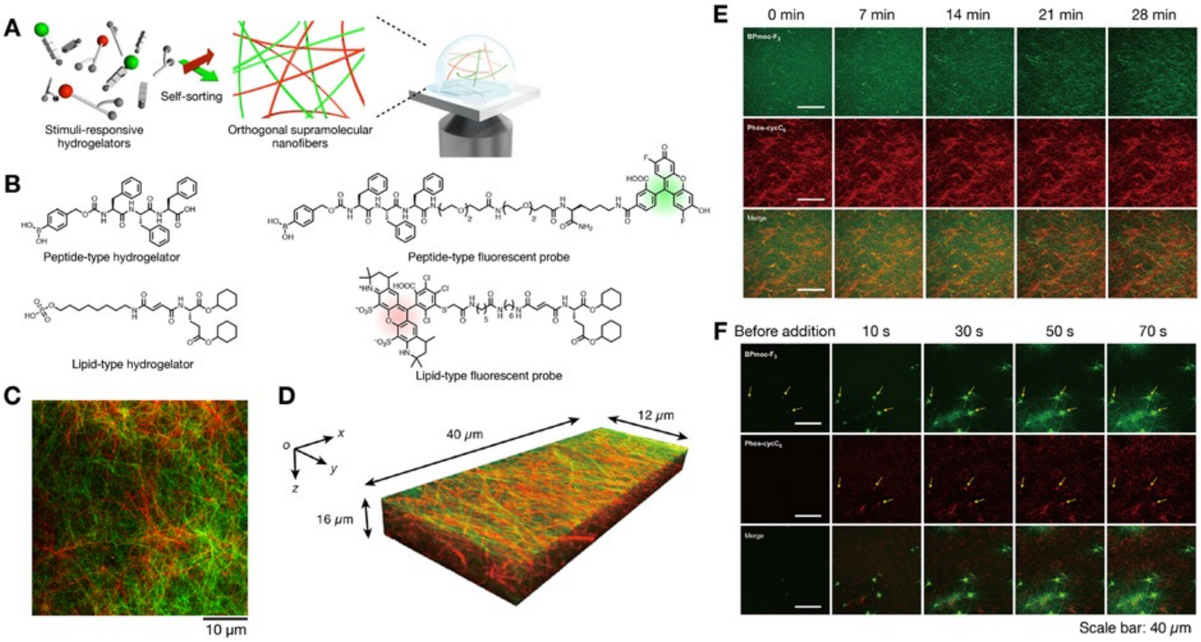

Figure 37. (**A**) Schematic illustration of orthogonal formation of distinct supramolecular nanofibers through self-sorting phenomena. (**B**) Chemical structures of hydrogelators and their selective fluorescent probes. (**C**) STED and (**D**) 3D Airyscan CLSM images of orthogonal supramolecular nanofibers. (**E**, **F**) Time-lapse CLSM imaging of the formation process in the (**E**) absence and (**F**) presence of peptide-type seeds. Green: peptide-type nanofibers, red: lipid-type nanofibers. Reproduced with permission from ref 260. Copyright 2016 Springer Nature.

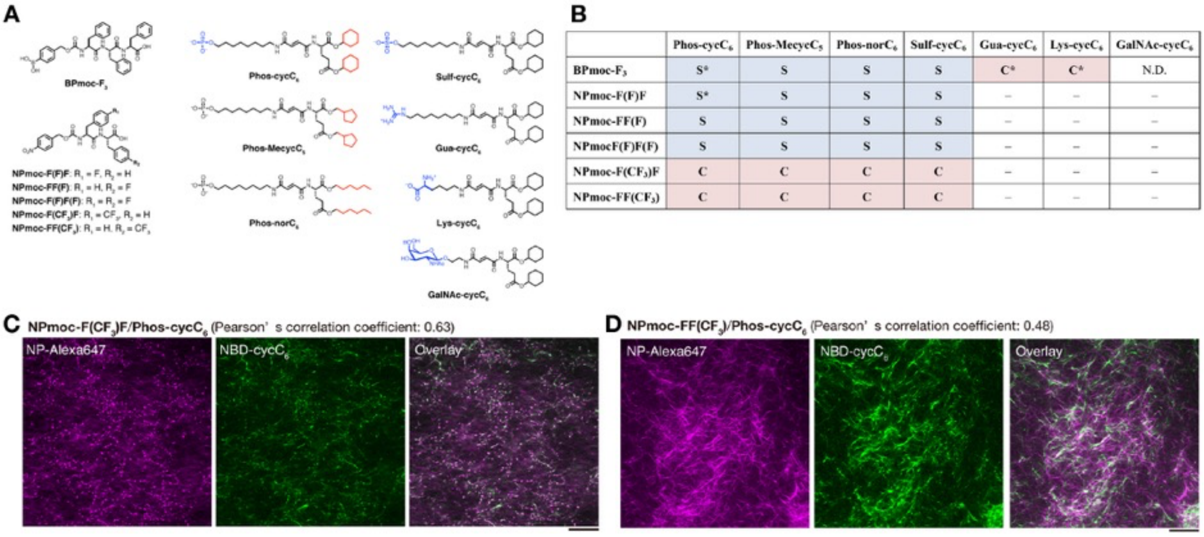

	Phos-cycC$_6$	Phos-MecycC$_5$	Phos-norC$_6$	Sulf-cycC$_6$	Gua-cycC$_6$	Lys-cycC$_6$	GalNAc-cycC$_6$
BPmoc-F$_3$	S*	S	S	S	C*	C*	N.D.
NPmoc-F(F)F	S*	S	S	S	–	–	–
NPmoc-FF(F)	S	S	S	S	–	–	–
NPmocF(F)F(F)	S	S	S	S	–	–	–
NPmoc-F(CF$_3$)F	C	C	C	C	–	–	–
NPmoc-FF(CF$_3$)	C	C	C	C	–	–	–

Figure 38. (**A**) Chemical structures of peptide- and lipid-type hydrogelators. (**B**) Table for self-sorting behaviors among various kinds of peptide- and lipid-type hydrogelators. S: self-sorting, C: coassembly. (**C**, **D**) Representative examples of coassembled structures. Magenta: peptide-type nanofibes, green: lipid-type nanofibers. Scale bar: 20 μm. Reproduced with permission from ref 285. Copyright 2018 American Chemical Society.

In 2020, the same group succeeded in construction of two distinct self-sorting network patterns, interpenetrated and parallel, by using oxime formation and exchange reactions (Figure 39A).[306] In this study, a benzaldehyde-tethered peptide-type hydrogelator was newly synthesized to control the self-assembly ability through oxime bond formation with a hydroxylamine compound. Airyscan CLSM imaging revealed that the interpenetrated self-sorting network (peptide- and lipid-type nanofibers were entangled but not overlapped) was formed upon addition of benzylhydroxylamine to a mixture of a peptide-type hydrogelator precursor and lipid-type nanofibers (Figure 39B, left). Interestingly, real-time imaging of visualized two different formation mechanisms; seed formation on the surface of the lipid-type nanofibers and subsequently at the interstitial water layer. On the basis of this observation, the authors succeeded to construct the parallel self-sorting network through controlling of selective seed formation on the surface of the lipid-type nanofibers (Figure 39B, right, 39C), where the peptide- and lipid-type nanofibers were oriented in parallel but slightly misaligned, by decelerating the generation kinetics of the peptide-type nanofibers using oxime exchange reaction.

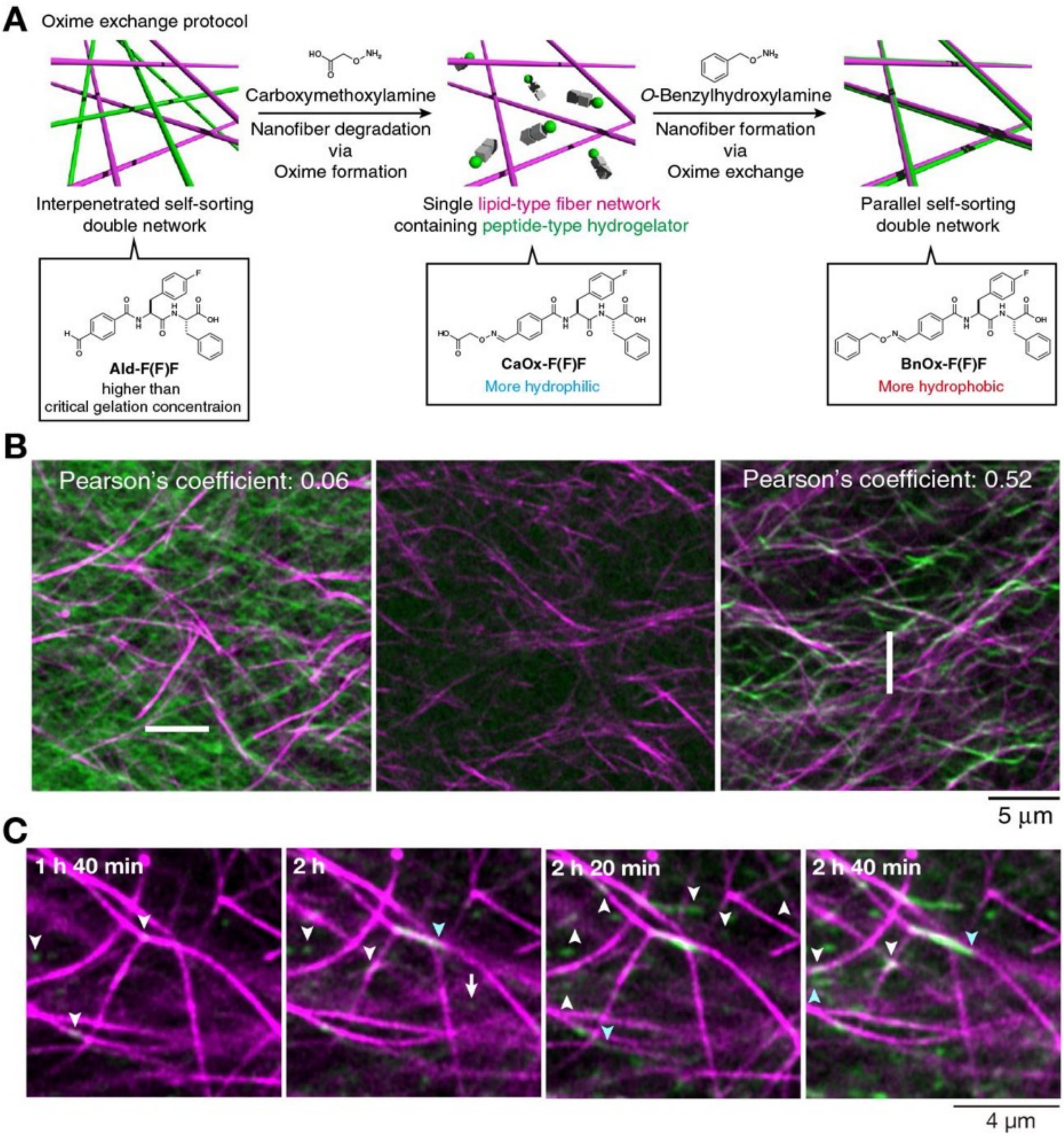

Figure 39. (**A**) Construction of the parallel self-sorting network from the interpenetrated self-sorting network through oxime-exchange reaction. (**B**) Airyscan CLSM images of (left) the interpenetrated self-sorting network, (middle) the lipid-type single network, (right) the parallel self-sorting network. (**C**) Time-lapse imaging of the formation process of the parallel self-sorting network. Green: peptide-type nanofibers, magenta: lipid-type nanofibers. Reproduced with permission from ref 306. Copyright 2020 Springer Nature.

Composite materials of supramolecular and polymer gels have recently emerged as novel soft matters that combine advantages of two components, such as flexible designability in functions and mechanical stiffness. As in the case of supramolecular double-network gels, CLSM imaging is powerful to elucidate the gel network structure. In 2012, Kiriya *et al.* reported meter-long, robust supramolecular strands encapsulated in polymer hydrogel jackets by use of microfluidic techniques (Figure 40A).[203] They employed a supramolecular lipid-type hydrogelator with a phosphate head group and calcium alginate as a polymer gel. In a microfluidic device, a fluid of lipid-type hydrogelators and a sheath fluid of sodium alginate, lipid-type fluorescent dyes and fluorescent beads were introduced in different inlets, and this flow was surrounded by a solution of $CaCl_2$ introduced from the third inlet. CLSM imaging of the resultant strands showed supramolecular nanofibers, which aligned along one-dimensional direction, were encapsulated by the alginate gel jacket with a width of *ca.* 50 μm (Figure 40B). The jacketed supramolecular strands were mechanically robust enough to form macroscopic patterns, and could work as a template for conductive polyaniline synthesis.

In 2017, Lovrak *et al.* reported generation of free-standing composite hydrogel objects with control over size, shape, and functionality based on a reaction-diffusion mechanism (Figure 40C).[207] In the polymer gel matrix (*e.g.* agar and alginate gels), they synthesized supramolecular hydrogelators through hydrazone bond formation of hydrazide and aldehyde precursors followed by self-assembly. CLSM imaging of the resultant hydrogel object revealed that localization of supramolecular nanofibers and the alginate network were well overlapped, suggesting that the alginate network may work as a scaffold of supramolecular nanofibers (Figure 40D). Moreover, using CLSM imaging, they demonstrated controlled functionalization over the location and density profile of multiple functional molecules (fluorescent dyes and proteins) in the hydrogels.

Shigemitsu *et al.* recently succeeded in visualization of a segregated structure of supramolecular nanofibers and physically-crosslinked polymer network in a composite hydrogel by CLSM imaging (Figure 40E).[208] The composite hydrogel is composed of an enzyme-sensitive peptide-type supramolecular gel and an agarose. The supramolecular nanofibers were stained with a TMR-guanidium probe and fluorescein-modified agarose was employed (Figure 40F). Airyscan CLSM imaging of the composite hydrogel revealed the segregated structure of supramolecular nanofibers and the sea-island network made of agarose (Figure 40G). Interestingly, supramolecular nanofibers located mainly at the darker void region of the agarose network, which were also supported by the line plot analysis. The orthogonality of supramolecular nanofibers and agarose was also supported by CD spectroscopy and temperature-dependent rheological analysis. It was also confirmed that stimulus-response of supramolecular nanofibers retained in the composite hydrogel, where supramolecular nanofibers and agarose played distinct roles in controlled protein release, protein entrapment and mechanical stiffness, respectively.

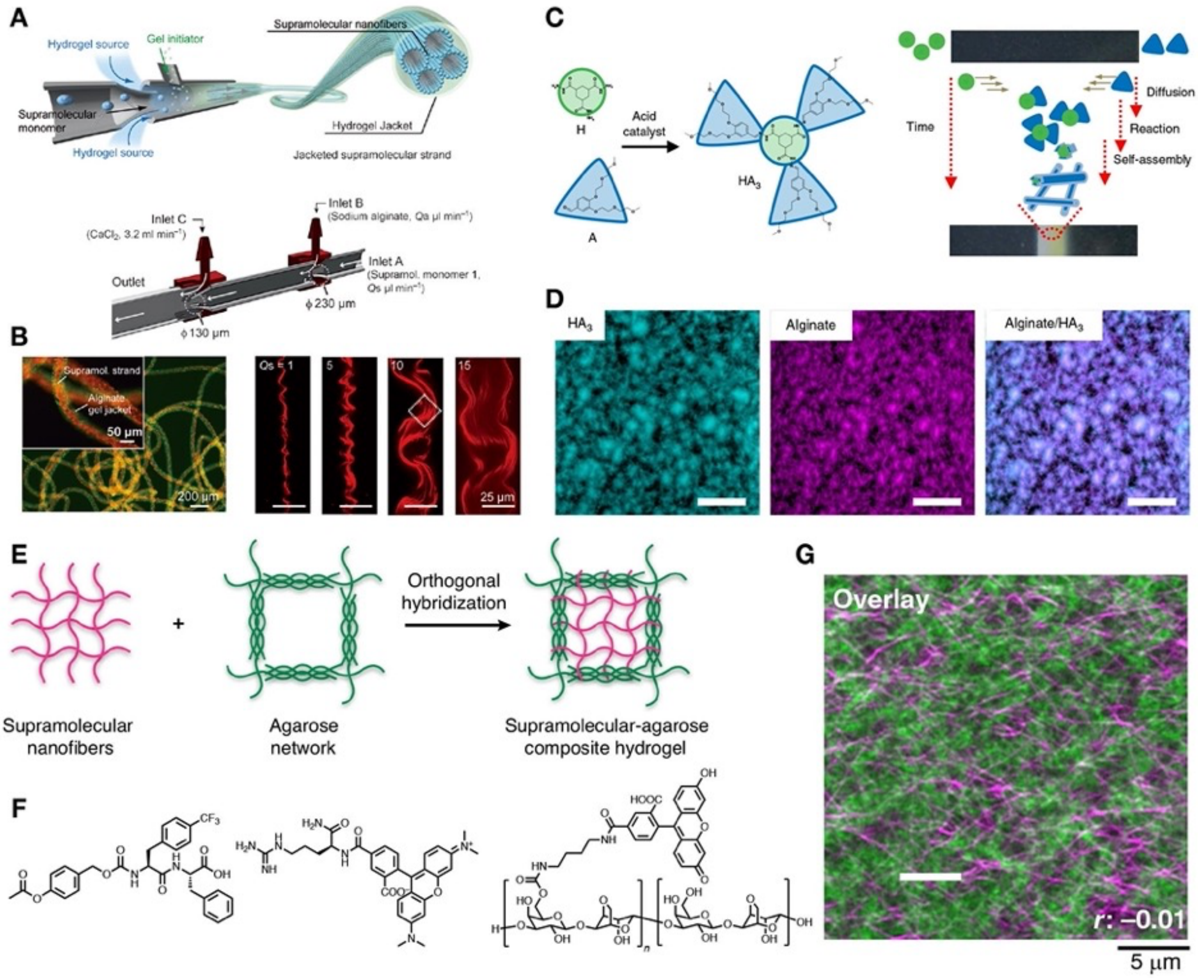

Figure 40. (**A**) Formation of jacketed strands composed of supramolecular nanofibers covered by Ca-alginate by the microfluidic method. (**B**) CLSM imaging of jacketed supramolecular strands. Red: supramolecular nanofibers, green: Ca-alginate. Reproduced with permission from ref 203. Copyright 2012 Wiley-VCH. (**C**) Self-assembly of supmolecular fibers in Ca-alginate matrix by use of reaction-diffusion. (**D**) CLSM imaging of

the hybrid hydrogel. Cyan: supramolecular fibers, magenta: Ca-alginate. Scale bar: 50 µm. Reproduced with permission from ref 207. Copyright 2017 Springer Nature. (**E**) Orthogonal hybridization of supramolecular nanofibers and agarose. (**F**) Chemical structures of a peptide-type hydrogelator, its fluorescent probe, and fluorescein-modified agarose. (**G**) Airyscan CLSM image of the composite hydrogel. Green: agarose, magenta: supramolecular nanofibers. Reproduced with permission from ref 208. Copyright 2020 Springer Nature.

CLSM imaging enables to visualize larger structural heterogeneity of micrometer- or submilimeter-scale phase-separated hydrogels.[269,295,296] In 2019, Wang *et al.* reported a hierarchical compartmentalized supramolecular hydrogel through multilevel self-sorting events.[296] They used a modular gel system with tunable properties based on *in situ* formation of hydrazone hydrogelators from a tris-hydrazide core and benzaldehyde derivatives (Figure 41A). A turbid hydrogel was formed through mixing a tris-hydrazide core (H) with neutral (ethyleneglycol) and anionic (sulfonate) benzaldehydes (A and A^-, respectively). CLSM imaging revealed a worm-like microstructure with a width of *ca.* 10 µm, which was preferentially stained with fluorescein-tethered anionic benzaldehyde (Figure 41B). In magnified views, fibrous structures with a width of *ca.* 200 nm could be observed at interstitial space between the worm-like structure but no significant object was detected in the worm-like structure probably due to thinner nanofibers that cannot be resolved by CLSM. The cationic fluorescent dye, Hoechst33342, selectively stained the worm-like structure, implying that the worm-like structure should be composed of anionic-charged nanofibers whereas the interstitial space could be filled with neutral nanofibers. Time-lapse imaging clarified a formation process of the worm-like structure: a homogenous Hoechst33342 fluorescence initially appeared, and, after 5 h this fluorescence started to become inhomogenous, followed by the sheet worm-like structure could be observed after 5.6 h. This phase-separation phenomenon is similar to an aqueous two-phase system of PEG polymers and anionic polyelectrotes.

Inspired by self-sorting supramolecular hydrogels, Sun *et al.* synthesized micrometer-sized compartmentalized hydrogels by mixing of diblock copolypeptides that self-assemble through hydrophobic interaction or polyion complexation.[492,497] They employed amphiphilic diblock copolypeptides bearing hydrophobic L-leucine residues as a self-assembling moiety and nonionic, hydrophilic L-methionine sulfoxide chain $(\mathrm{M^{O}A})_{200}\mathrm{L}_{30}$ (Figure 41C). For polyion complexation, two types of dual hydrophilic copolypeptide consisting of poly(L-glutamate) or poly(L-lysine) residues as charged segments and L-methionine sulfoxide $[(\mathrm{M^{O}A}_{155})\mathrm{K}_{55}$ and $(\mathrm{M^{O}A})_{155}\mathrm{E}_{55}]$ were employed. CLSM imaging of a hydrogel formed through mixing fluorescently-labeled $(\mathrm{M^{O}A})_{200}\mathrm{L}_{30}$, $(\mathrm{M^{O}A}_{155})\mathrm{K}_{55}$, and $(\mathrm{M^{O}A})_{155}\mathrm{E}_{55}$ visualized a mutually-exclusive, segregated structure in microscale dimensions, which support the formation of self-sorted compartmentalized networks (Figure 40D, top). Furthermore, the *z*-stack imaging showed the segregated structure was also formed three-dimensionally (Figure 41D, bottom).

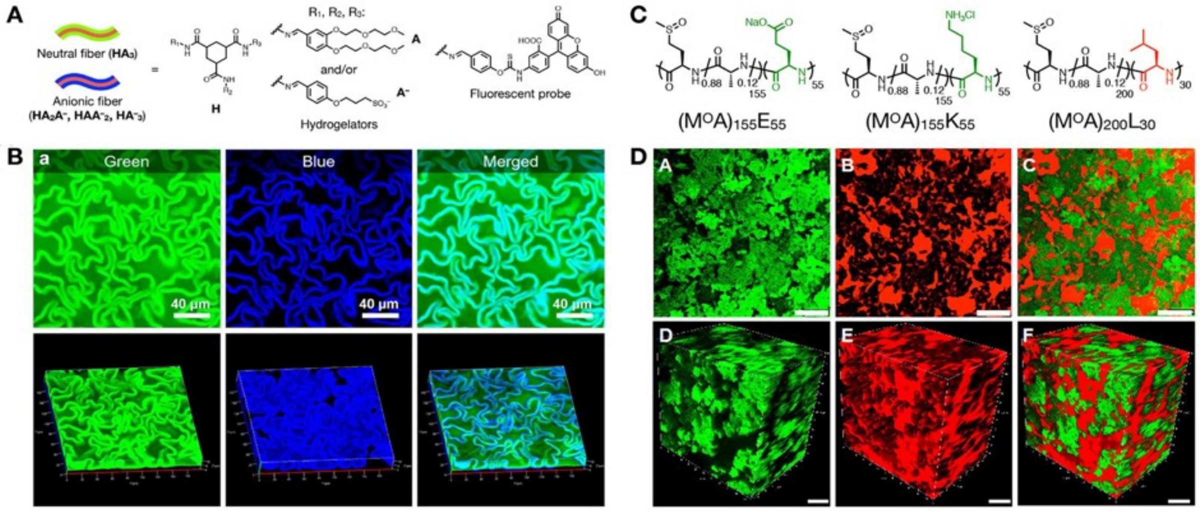

Figure 41. (**A**) Chemical structures of hydrogelators and a fluorescent probe. (**B**) CLSM imaging of a phase-separated supramolecular hydrogel. Green: fluorescein, blue: Hoechst33342. Reproduced with permission from ref 296. Copyright 2019 American Chemical Society. (**C**) Chemical structures of self-assembling polymers. (**D**) 2D and 3D CLSM images of a phase-separated polymer hydrogel. Green: Alexa fluor 488-labled $(\mathrm{M^{O}A})_{155}\mathrm{E}_{55}$, red: Alexa Fluor 633-labeled $(\mathrm{M^{O}A})_{200}\mathrm{E}_{30}$. Scale bar: 10 µm. Reproduced with permission from ref 497. Copyright 2019 American Chemical Society.

CLSM imaging is also powerful to clarify the structure of multicomponent protocells.[340,349,353,395,396,399,401,423,433,436,437,440–445,493–496,498] In 2014, Dora Tang *et al.* developed a hybrid protocell model based on the self-assembly of fatty-acid membrane at the surface of preorganized complex coacervate microdroplets.[407] The authors demonstrated the spontaneous formation of membrane-coated coacervate microdroplets upon addition of sodium oleate at concentration below critical micelle concentration to a solution of PDDA (polydiallyldimethylammonium chloride)/ATP and oligolysine/RNA coacervate microdroplets as confirmed dynamic light scattering (DLS) and small angle X-ray scattering measurements. CLSM imaging showed that a lipid-soluble BODIPY FL-C_{16} dye was located on the surface of the droplets in the presence of oleate, whereas homogeneous fluorescence could be observed throughout the interior in the absence of oleate (Figure 42). Fluorescence lifetime imaging microscopy (FLIM) with BODIPY C_{10}, a probe for the viscosity of the fatty-acid membrane, showed that the viscosity in the oleate surface layer is comparable to that of a control oleate/oleic acid vesicles (η = 20–40 cP). In contrast, the viscosity of the PDDA/ATP matrix was not significantly changed by the amount of oleate (1–4 cP). These data suggested that the lipid membrane did not influence the local structure of the phase-separated compartment. Furthermore, CLSM imaging clarified the remarkable changes in the uptake of fluorescent dyes. In the presence of negatively-charged oleate membrane, anionic dyes such as calcein or fluorescein were excluded from the droplet interior.

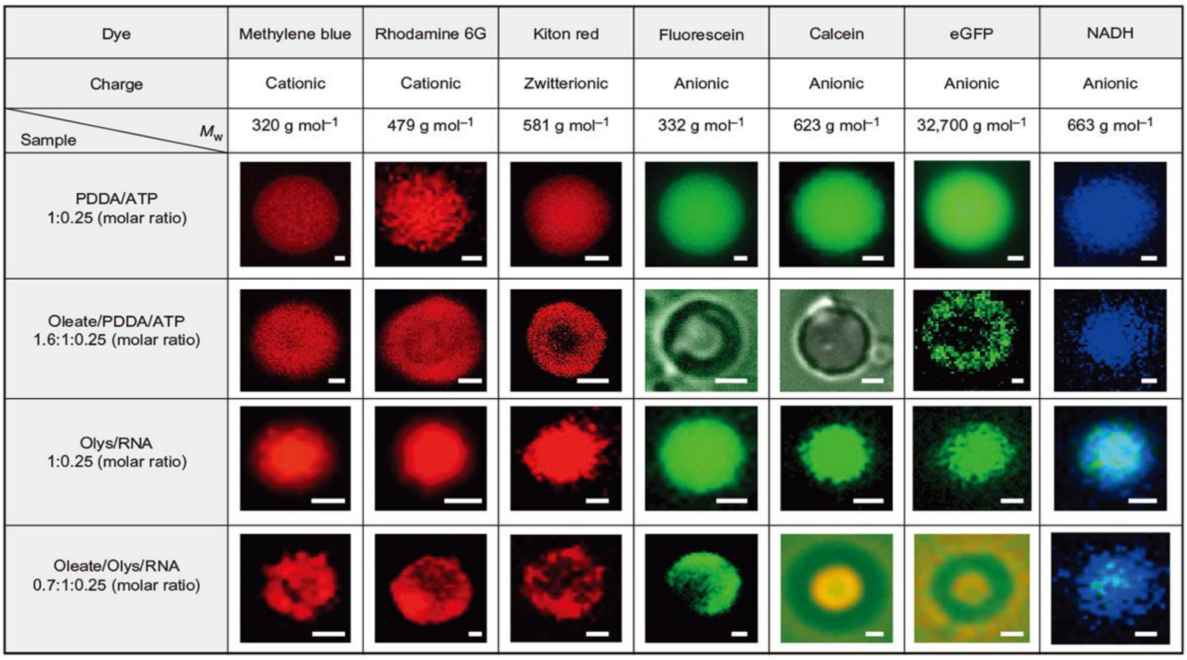

Dye	Methylene blue	Rhodamine 6G	Kiton red	Fluorescein	Calcein	eGFP	NADH
Charge	Cationic	Cationic	Zwitterionic	Anionic	Anionic	Anionic	Anionic
Sample M_w	320 g mol^{-1}	479 g mol^{-1}	581 g mol^{-1}	332 g mol^{-1}	623 g mol^{-1}	32,700 g mol^{-1}	663 g mol^{-1}
PDDA/ATP 1:0.25 (molar ratio)							
Oleate/PDDA/ATP 1.6:1:0.25 (molar ratio)							
Olys/RNA 1:0.25 (molar ratio)							
Oleate/Olys/RNA 0.7:1:0.25 (molar ratio)							

Figure 42. CLSM images of coacervate microdroplets in the absence/presence of fatty acids. Scale bar: 1 µm. Reproduced with permission from ref 407. Copyright 2014 Springer Nature.

CLSM imaging can be applied to examine the structures and functions of multiple droplet assemblies of hydrogels, polymer conjugates, water-in-oil emulsions.[350,439,499–510] In 2008, Matsumoto *et al.* reported photo-triggered mass transport and the subsequent enzymatic reactions in supramolecular gel droplets.[223] A hydrogel composed of a lipid-type supramolecular hydrogelator bearing fumaric amide as a *trans*-*cis* photo-switching module showed the macroscopic gel–sol transition upon light irradiation. The gel droplets were formed by injection of a hot solution of the gelator into hexadecane followed by vortex mixing (Figure 43A, top). CLSM imaging revealed that a diameter of the gel droplets was determined to be 50–100 µm (60 pL–0.5 nL) and visualized well-developed fibrous networks of the gelator within the droplet (Figure 43A, bottom). The authors then tried a photo-triggered enzymatic reaction through molecular diffusion between the droplets. Two distinct droplets containing alkaline phosphatase or a corresponding fluorogenic substrate were placed in contact. Without photo irradiation, the enzymatic reaction did not take place. However, upon photo-induced partial fusion of the two droplets, the fluorescence emission by phosphatase-catalyzed reaction product immediately appeared at the interface, indicating that mass transport between the gel droplets was well controlled by light (Figure 43B).

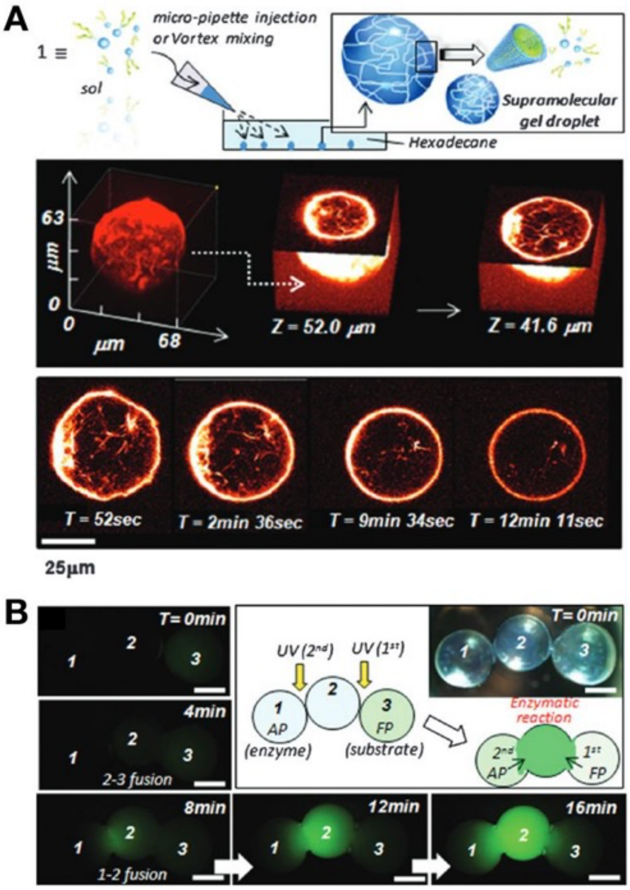

Figure 43. (**A**) (Top) Schematic illustration of formation of supramolecular gel droplets. (Bottom) 3D CLSM images of the gel droplet. (**B**) The photo-induced stepwise fusion between three gel droplets. Scale bar: 500 μm. Reproduced with permission from ref 223. Copyright 2008 Royal Society of Chemistry.

Gobbo *et al.* reported the programmed assembly of proteinosomes made from BSA covalently conjugated with PNIPAM-*co*-MAA (MAA: methacrylic acid) through strain-promoted azide-alkyne cycloaddition (SPAAC) reactions (Figure 44A).[508] To obtain synthetic prototissues, BSA/polymer nanoconjugates modified with azide or strained alkyne were mixed within w/o/w Pickering emulsions. After removal of the encapsulated oil, CLSM imaging visualized spatially-integrated spheroid-like structures (mean size: ~70 μm, volume: 180 ± 80 μL) (Figure 44B). Owing to thermo-responsive property of PNIPAM, the resultant synthetic spheroids showed a reversible swelling/shrinking behavior with the maximum shrinkage of ~40% (Figure 44C). Amplitude of contraction properties of the spheroids could be modulated by the inner pH change by enzymatic reaction proceeded in the spheroids.

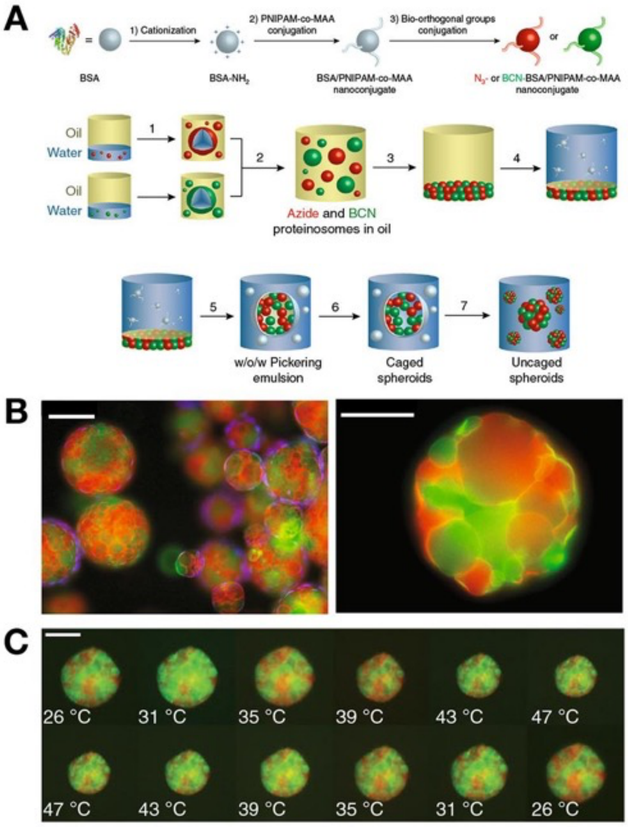

Figure 44. (**A**) Preparation of proteinosome spheroids. (**B**) Fluorescent microscopic images of caged spheroids composed of (red) RITC-labeled azide-, (green) FITC-modified alkyne-functionalized proteinosomes covered by (blue) a DyLight 405-labeled host proteinosome membrane. CLSM images of coacervate microdroplets in the absence/presence of fatty acids. Scale bar: 100 µm (left), 50 µm (right). (**C**) Temperature-responsive reversible volume changes of uncaged proteinosome spheroid. Scale bar: 50 µm. Reproduced with permission from ref 508. Copyright 2018 Springer Nature.

In 2020, Downs *et al.* reported a new strategy for making the gel droplet network composed of patterned multi-responsive hydrogels.[511] The gel network was prepared by photo-polymerization of manually-assembled pre-gel droplets of a mixture of NIPAM monomer, methylene bis(acrylamide) (MBA) crosslinker and α-ketoglutaric acid photoinitiator coated with lipid monolayer in lipid-containing oil. Photopolymerization resulted in rupture of the lipid bilayers to form a continuous PNIPAM gel network. By this gel droplet techniques, patterned domains containing temperature-responsive, magnetic-field responsive hydrogels upon incorporation of gold nanoparticles and magnetic beads, respectively, into the pre-gel solution. Optical microscopy visualized that the patterned gel network containing gold nanoparticles showed light-activated reversible shape change such as curling and domains carrying magnetic beads allowed movement in a magnetic field. Such multi-responsive hydrogel structures should give new potential for the design of miniaturized soft robotics and biomedical devices.

5.4.3. Manipulation of molecular assemblies

Confocal microscopy allows not only the observation but also the manipulation of specimens containing photo-reactive functional moieties, such as caged groups, at the micrometer resolution by combination with multi-photon excitation techniques.[223,234,248,352,357,512–536] In this section, representative examples about functionalization/manipulation of molecular assemblies are highlighted.

In 2009, Kloxin *et al.* firstly achieved 3D patterning of chemical PEG-based polymer gels with photodegradable nitrobenzyl linkers by a two-photon laser scanning microscope.[515] Using two-photon excitation, 3D patterns could be generated within a hydrogel by local photodegradation, which was confirmed by 3D CLSM imaging. The same group also demonstrated photo-induced 3D post-fabrication of tetra-arm PEG gels using combination of photo-induced thiol-ene reaction and photodegradation of nitrobenzyl groups (Figure 45A).[521] A di-functionalized linker possesses two photo-reactive functional groups: (i) a vinyl functionality at the side chain that is readily reacted to thiol-containing compounds through the radical-mediated thiol-ene addition under visible light irradiation, (ii) the photodegradable nitrobenzyl ester moiety embedded in the backbone that decomposes for cleavage of the crosslinks upon UV light irradiation. Multiphoton excitation techniques allowed to create elaborate, three-dimensional biochemical patterns within a hydrogel modified with these photo-reactive groups (Figure 45B, C). To demonstrate the potential utility of such a hydrogel, the authors showed functionalization of the gel with RGD peptides, which can be used to manipulate cellular functions in a spatiotemporally regulated manner. In 2019, Shadish *et al.* reported post-functionalization of chemical polymer gels by release and immobilization of multiple proteins, such as fluorescent proteins and growth factors, functionalized through sortase-tag based protein ligation.[533] Such photoreversible immobilization of epidermal growth factor (EGF) within the hydrogel enabled dynamic regulation of cellular proliferation and intracellular epidermal growth factor receptor (EGFR) signaling pathway.

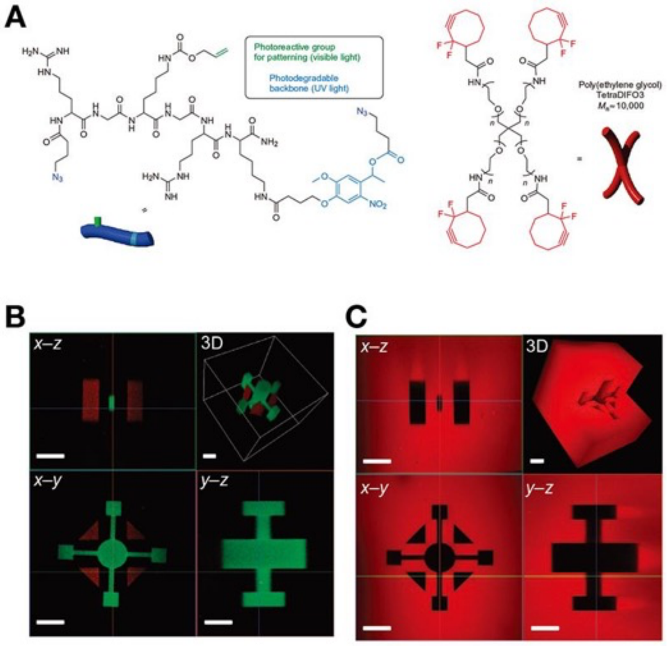

Figure 45. (**A**) Chemical structures of monomers of a photo-responsive tetra-armed PEG gel. (**B**) 3D patterning of the tetra-armed PEG gel by multiphoton laser light (860 nm) with an Alexa Fluor 488-modified RGD peptide. (**C**) Photodegradation by a multiphoton laser light (740 nm). Scale bar: 100 µm. Reproduced with permission from ref 521. Copyright 2011 Springer Nature.

In 2014, Yoshii *et al.* demonstrated 3D patterning of supramolecular hydrogels composed of a photodegradable peptide hydrogelator tethering dimethylaminocoumarin at the N-terminus (Figure 46A, B).[248] Upon two-photon excitation at 740 nm, the entangled nanofibers disappeared in the irradiated area, leading to a dramatic change of the fluidity with high spatial resolution (10 μm × 10 μm × 10 μm) (Figure 46C). The off-on switching of the Brownian motion of nanoparticles and proteins and of swimming of *E. Coli* inside the hydrogels were also observed.

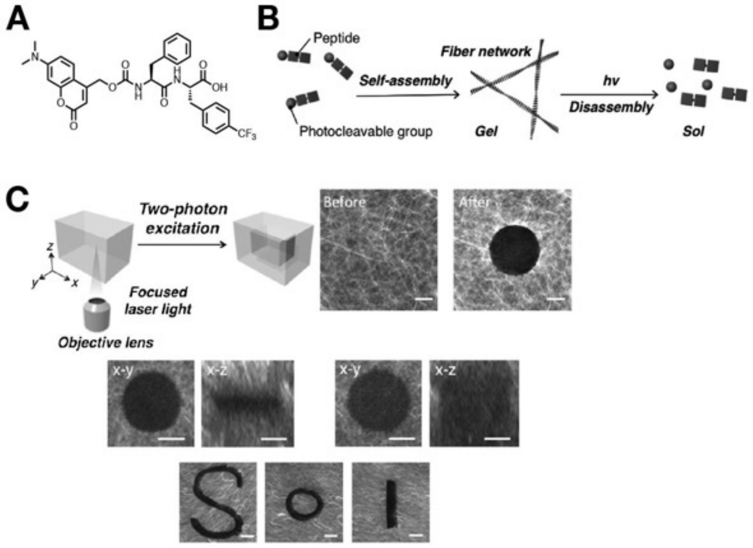

Figure 46. (**A**) Chemical structure of a photo-responsive supramolecular hydrogelator. (**B**) Schematic illustration of photo-responsive nanofiber degradation. (**C**) 3D patterning of the supramolecular hydrogel by the two-photon laser light. Scale bar: 10 μm (top, middle), 20 μm (bottom). Reproduced with permission from ref 248. Copyright 2014 Wiley-VCH.

In 2018, Oran *et al.* demonstrated a 3D nanofabrication technique by isotropic shrinkage of photo-patterned hydrogels.[531] A polyacrylate hydrogel was used for a scaffold, as this hydrogel is well known to expand and shrink by 10–20-fold in linear dimension. The 3D nanofabrication process was conducted by two-photon CLSM in the following three phases. First, two-photon excitation of fluorescein derivatives carrying a further modification handle causes the fluorescein to react with the hydrogel. Second, after removal of the fluorescein solution, functional molecules/materials such as fluorescent dyes, DNAs, and AuNP, are deposited through the modification handles on the hydrogel framework. Third, the patterned hydrogel was shrunken by 10–20-fold upon treatment of acid or divalent cations, resulting in creation of the desired nanoscale-level fabrication. The minimal feature size of this technique was estimated to be 59.6 ± 3.8 nm by measuring a line width of AuNP deposited from a single-voxel-wide pattern. This method can directly write conductive 3D silver nanostructures within a hydrogel scaffold.

Optical tweezers have emerged as a manipulation tool for microscopic objects such as nanoparticles and are frequently used to study behaviors of single molecules (such as molecular motors) modified with micrometer-sized beads. Optical tweezers can also be applied to artificial molecular assemblies. In 2003, Frusawa *et al.* measured the Young's modulus of a single-lipid nanotube consisting of synthetic glycolipids, cardanyl-β-D-glucopyranoside, by using optical tweezers.[213] A solution of the nanotubes was placed on a glass slide for optical trap, and the nanotube that attached well at only one end was bent by optical tweezers. The flexural rigidity K was estimated from the relaxation time τ (transition from bow-shaped to initial straight form) to be 2.2×10^{-22} Nm^2, which corresponds with the Young's modulus, $E \sim 720$ MPa. This value was similar to the Young's modulus of microtubules, $E \sim 1000$ MPa.

In 2015, Gould *et al.* reported manipulation of block copolymer micelles to allow the creation of arrays of functional soft-matter objects.[537,538] They employed B-A-B block polymer micelles bearing a crystalline PFS core and amorphous coronas of hydrophilic P2VP or hydrophobic PMVS. Through living crystallization-driven self-assembly, a spherical supermicelle with different core diameters (from 100 to 500 nm) was prepared upon addition of PFS-*b*-P2VP block copolymer unimers to short cylindrical PFS-*b*-PMVS seed micelles. The resultant micelles could be trapped and manipulated by optical tweezers as confirmed by optical microscopy (Figure 47A, B). They demonstrated the photoinitiated crosslinking of supermicelles held in contact by optical tweezers through vinyl groups under photoirradiation in the presence of photoinitiators. This dynamic holographic assembly enabled the patterning of supermicelles into arrays and growth of supermicelles under the flow condition (Figure 47C, D).

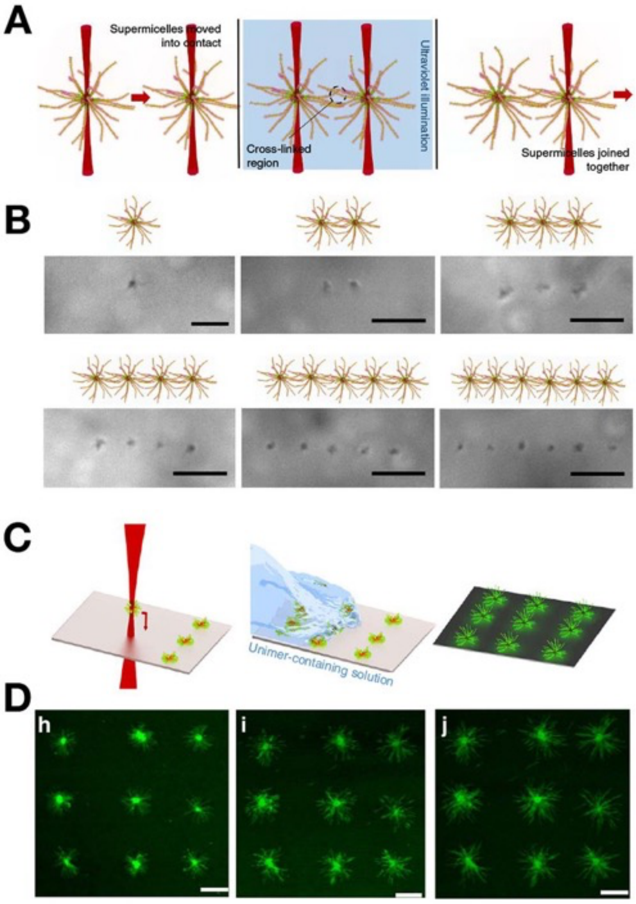

Figure 47. (**A**) Intermicelle crosslinking upon UV irradiation by use of optical tweezers. (**B**) Optical microscopic images of a chain-like linear super-structure containing up to six polymer micelles. (**C**) Patterned deposition and subsequent growth of supermicelles. (**D**) CLSM images of an array of supermicelles after addition and washing of 1, 2, and 3 aliquots of a polymer micelle solution. Scale bar: 5 μm. Reproduced with permission from ref 537. Copyright 2015 Springer Nature.

5.4.4. Observation of self-assembly/disassembly in cellular milieu

One of the current challenging issues in supramolecular chemistry is the controlled formation of molecular assemblies in complex biological environments such as live cells, tissues, and animals. Such molecular assemblies are expected to enable evaluation and manipulation of biomolecules activities and the consequent cell fate. CLSM is one of promising tools to examine molecular self-assembly in living cells/tissues/animals, which contains a myriad of biomolecules.

The Hamachi group developed magnetic resonance imaging- and fluorescent-based protein sensing relied on recognition-driven disassembly of self-assembling probes (Figure 48A).[539–543] The fluorescent-based probes consist of three modules: (i) a hydrophilic ligand specific to target proteins [*e.g.* methotrexate (MTX) for folate receptor, benzenesulfonamide for carbonic anhydrase], (ii) a fluorescent dye as a detection modality (*e.g.* TMR or FL), (iii) a relatively hydrophobic linker to connect the ligand and the fluorescent dye (Figure 48B).[542] The emission of the MTX-tethered probe [for dihydrofolate reductase (DHFR) and folate receptor] was weak ($\Phi = 0.03$), and significantly increased by addition of DHFR ($\Phi = 0.25$). AFM imaging revealed that the probe self-assembled into spherical aggregates with a diameter of 10–50 nm. This turn-on probe allowed to image membrane-bound receptor protein, folate receptors, on live cells, while the background signal from the extracellular region was negligible (Figure 48C). This disassembly-based sensing system can be applied to overexpressed and endogenous intracellular proteins, including carbonic anhydrase and heat shock protein 90, which process was clearly followed by CLSM imaging in live cells (Figure 48D, E).[543] The reversible assembly-disassembly in living cells enabled imaging-based inhibitor assay, providing affinity values toward active endogenous proteins in living cells (Figure 48F, G). This methodology would be helpful for direct drug discovery screening. In 2017, Li *et al.* successfully demonstrated that the recognition-driven disassembly concept is applicable to tumor-xenograft bearing mice.[544] The authors prepared self-assembled nanomaterials from a Zn^{2+} phthalocyanine derivative bearing targeting ligands (biotin) linked through triethylene glycol linkers (Pc-TEG-B). Fluorescent spectroscopy showed the fluorescence of Pc-TEG-B was completely quenched upon self-assembly, whereas the fluorescent intensity increased by *ca.* 250-fold on treatment of avidin. The authors succeeded in application of this probe to in vivo fluorescence imaging and photoacoustic tomography. After intravenous injection of the self-assembled Pc-TEG-B particles into mice bearing A549 tumors (avidin positive), the fluorescence with high S/N ratio could be observed from the tumor probably through enhanced permeation and retention (EPR) effect and receptor-mediated endocytosis. Interestingly, photoacoustic tomography, an emerging and noninvasive imaging modality, revealed that a photoacoustic signal of the self-assembled Pc-TEG-B could be detected from the tumor. These results indicated that the disassembly-based sensing system would be suitable for multimodal imaging techniques *in vivo*.

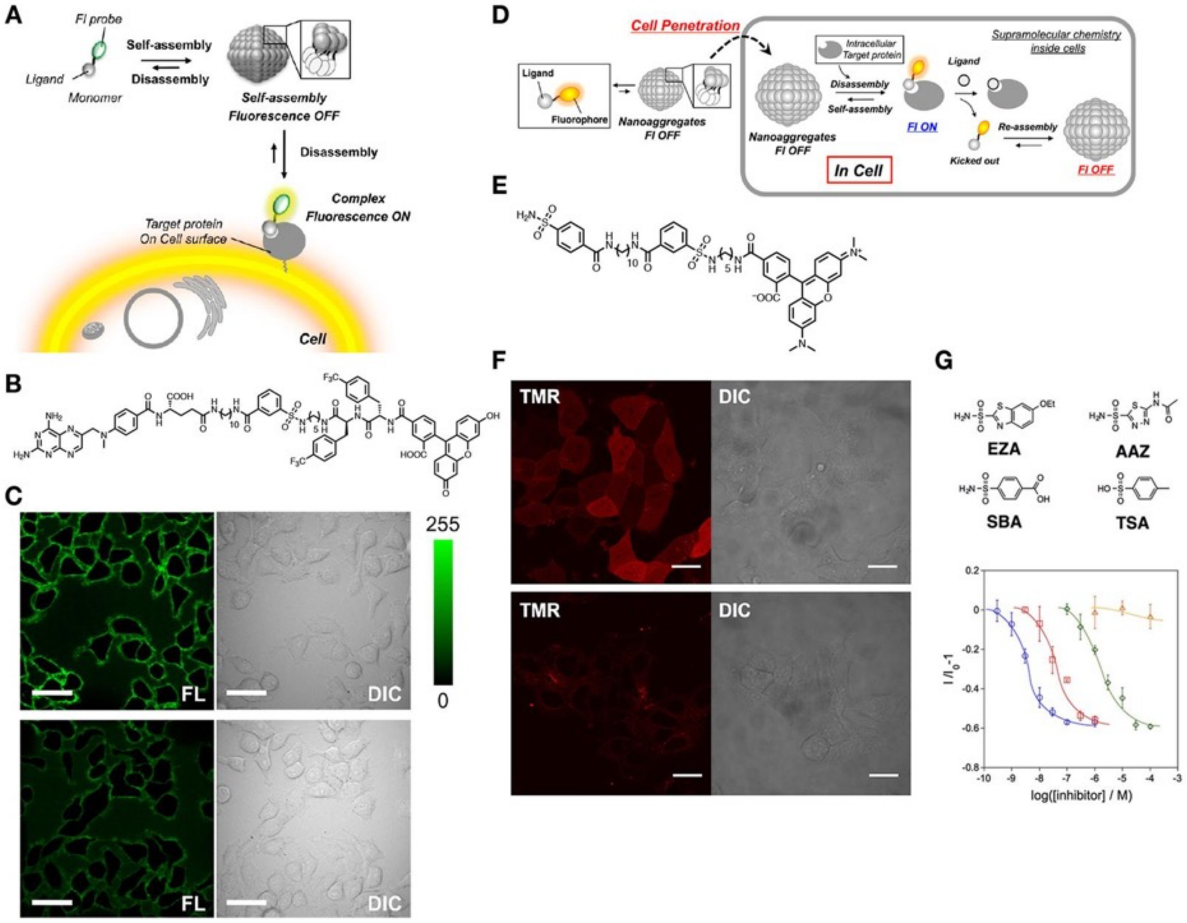

Figure 48. (**A**) Disassembly-induced turn-on detection of membrane-bound receptors. (**B**) Chemical structure of a self-assembling probe for folate receptor. (**C**) CLSM image of KB cells treated with the self-assembled probe in the (top) absence or (bottom) presence of folate, a competitive inhibitor. Scale bar: 40 μm. Reproduced with permission from ref 542. Copyright 2012 American Chemical Society. (**D**) Disassembly-induced turn-on detection of soluble proteins inside living cells. (**E**) Chemical structure of a self-assembling probe for carbonic anhydrase. (**F**) CLSM imaging of MCF-7 cells treated with the probe in the (top) absence or (bottom) presence of ethoxzolamide (EZA), a competitive inhibitor. Scale bar: 20

μm. (**G**) Fluorescence titration profile of the relative change in fluorescent intensity ($I/I_0 - 1$). Reproduced with permission from ref 543. Copyright 2014 American Chemical Society.

In 2012, Xu and coworkers reported CLSM imaging of enzyme-triggered self-assembly of peptide-based monomers in living cells.[545] To achieve this, they designed a hydrogelator precursor, NapFFK(NBD)Yp, which possesses NBD as an environmentally-sensitive fluorophore showing higher quantum yield in a hydrophobic environment (Figure 49A). Dephosphorylation of the precursor catalyzed by alkaline phosphatase produces the corresponding hydrogelator, resulting in self-assembly into a nanofibrous structure. CLSM imaging of HeLa cells after treatment of 500 μM of the precursor showed the accumulation of the fluorophore inside living cells (Figure 49B). The spatial distribution and morphology of the fluorescence was quite similar to that of endoplasmic reticulum (ER). In the presence of an inhibitor of PTP1B, a phosphatase localized on the surface of ER, increment of intracellular fluorescence became rather slow, suggesting PTP1B would contribute to dephosphorylation of the precursor. The concept of enzyme-triggered self-assembly has recently been extended to intracellular self-assembly targeting to other organelles including mitochondria, nuclei, etc.[338,546–554]

In 2014, Ye *et al.* reported bioorthogonal cyclization-mediated self-assembly *in vivo* through biocompatible reaction between free cysteine and cyanobenzothiazole with a second-order reaction of 9.1 $M^{-1}s^{-1}$.[555,556] To detect the activity of caspase-3/7, they elaborately designed a caspase-sensitive nanoaggregation probe, which possess D-cysteine and 2-cyano-6-hydroquinoline linked to an amino luciferin scaffold (Figure 49C). Amino and thiol groups of D-cysteine were capped with L-DEVD peptide and a disulfide bond, respectively, for two-step activation that was involved with caspase-3/7-catalyzed cleavage and intracellular thiol-mediated reduction. The two-step activation induces intramolecular condensation to produce a hydrophobic macrocycle, which spontaneously self-assemble into spherical aggregates *in situ*. 3D-SIM imaging of apoptotic HeLa cells treated with the Alexa Fluor 488-labeled probe revealed that strongly fluorescent puncta distributed throughout the cytosol and their average size was determined to be 148 ± 36 nm, which correlates well with *in vitro* DLS and TEM results (Figure 49D). The similar nanoparticle could be detected within an apoptotic tumor tissue slice after intravenous administration of the probe into doxorubicin-treated tumor-bearing mice.

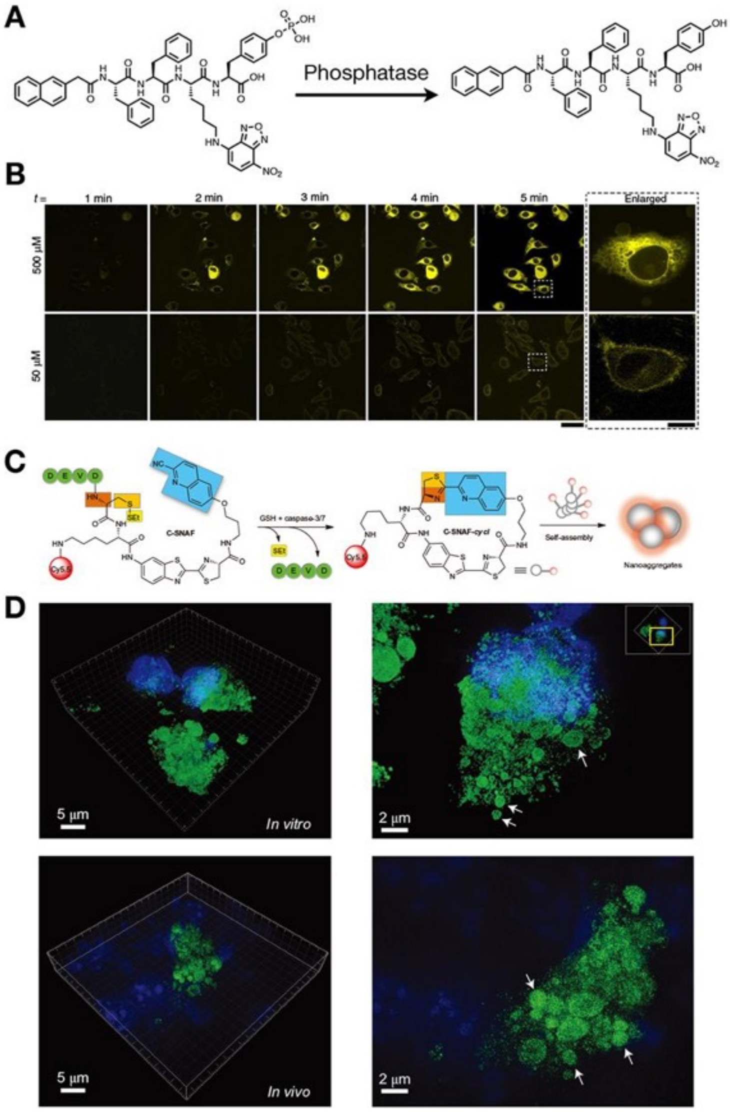

Figure 49. (**A**) Phosphatase-induced formation of a fluorescent hydrogelator. (**B**) Time-dependent CLSM images of HeLa cells treated with the gelator precursor. Scale bar: 50 μm. Reproduced with permission from ref 545. Copyright 2012 Springer Nature. (**C**) Glutathione- and caspase-induced self-assembly. (**D**) 3D-SIM images of self-assembled fluorescent nanoaggregates in (top) apoptotic cells and (bottom) apoptotic tumor tissues. Reproduced with permission from ref 556. Copyright 2014 Springer Nature.

Synthetic biology approach recently allows the construction of artificial molecular assemblies, such as hydrogels and coacervate droplets, from designed synthetic proteins in living cells, as confirmed by *in situ* CLSM imaging.[341,557–565]

In 2018, Nakamura *et al.* reported a strategy for a rapid production of protein-based hydrogels inside living cells, named iPOLYMER, that rely on a chemically-induced dimerization (CID) technique (Figure 50A).[341] They designed two types of polypeptides: a yellow fluorescent protein (YFP) tethering tandem repeats of FKBP, and a cyan fluorescent protein (CFP) carrying tandem repeats of FRB. These two polypeptides are expected to self-assemble into a hydrogel-like network upon treatment of rapamycin, a dimerizer of FKBP and FRB. Indeed, puncta could be observed immediately after addition of rapamycin to COS-7 cells expressing both polypeptides (Figure 50B). FRET measurement between CFP and YFP showed that higher FRET signals were detected by CLSM at the puncta within 5 min of rapamycin addition. Moreover, FRAP analysis of the puncta showed little fluorescent recovery, suggesting the irreversible nature of rapamycin-induced CID. Furthermore, the author succeeded in functionalization of iPOLYMER gels by fusing an RNA recognition motif to CR to produce RNA granule mimics inside living cells.

Very recently, Dzuricky *et al.* demonstrated engineering of liquid condensates of artificial disordered proteins in living cells.[564] They designed a polypeptide sequence, (GRGDSPYS)$_{XX}$ (XX: number of repeats, 20–80) (A-IDP), that was inspired by Rec-1 resilin. Fluorescent microscopic imaging showed formation of densely fluorescent small puncta in *E. Coli* expressing sfGFP-fused A-IDP (Figure 50C, D). The puncta grew in time and coalesce to become a single coacervate droplet per cell. In addition, the authors succeeded to carry out SPAAC and enzymatic reaction using a split β-galactosidase system inside the A-IDP condensates as confirmed by CLSM imaging.

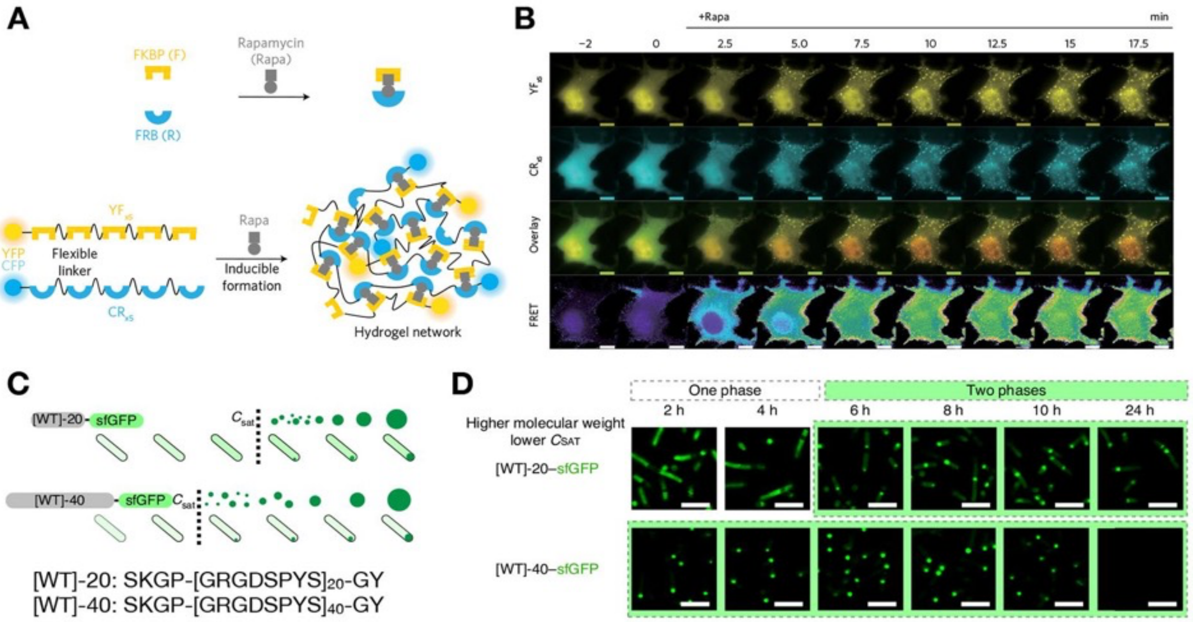

Figure 50. (**A**) iPOLYMER strategy for formation of the hydrogel network consisting of the YFP-tagged five tandem repeat of FKBP and the CFP-tagged five tandem repeat of FRB induced by rapamycin treatment. (**B**) Time-lapse CLSM imaging of fluorescent puncta formation in COS-7 cells. Scale bar: 10 μm. Reproduced with permission from ref 341. Copyright 2018 Springer Nature. (**C**) Intracellular droplet formation of sfGFP-tagged artificial intrinstically-disordered proteins in living *E. Coli*. (**D**) CLSM imaging of sfGFP-tagged artificial intrinstically-disordered proteins as a function of induction time. Scale bar: 5 μm. Reproduced with permission from ref 564. Copyright 2020 Springer Nature.

6. Conclusion and outlook

In conclusion, microscopic imaging techniques including EM, AFM, CLSM, and SR imaging allows the visualization of not only static structures of individual molecular assemblies at distinct length scale (sub nanometer to millimeter), but also their dynamic aspects over a wide range of time scale (ms–hours). As shown in Figure 51, these recently-developed imaging modalities allow to cover a wide range of components, sizes, and shapes of supramolecular assemblies. Besides, force microscopy by AFM and optical tweezers and fluorescence spectral/lifetime imaging by CLSM can evaluate physicochemical properties of supramolecules including stiffness, viscosity, dielectric constant, etc. Very recently, correlative microscopy has emerged as a promising approach, which allows us to provide more detailed structural information of the specimen using two distinct microscopic techniques in a relatively large scale.[566–568] Such correlative microscopy combines the advantages of distinct imaging modalities. For example, correlative light-electron microscopy provides both the specificity and real-time observation of confocal/super-resolution imaging and the better structural resolution of EM. Xu and coworkers reported correlative light and electron microscopy of self-assembled synthetic nanofibers formed on cell surfaces (Figure 52A–I).[569] Nakamura *et al*. investigated the ultrastructure of iPOLYMER puncta by correlative fluorescent and electron microscopy (Figure 52J).[341] Such rapidly evolving microscopic imaging technologies could open up new opportunities for deeper understanding and further development of synthetic molecular assemblies as well as natural ones, which leads to rational design of novel supramolecular assembled materials.

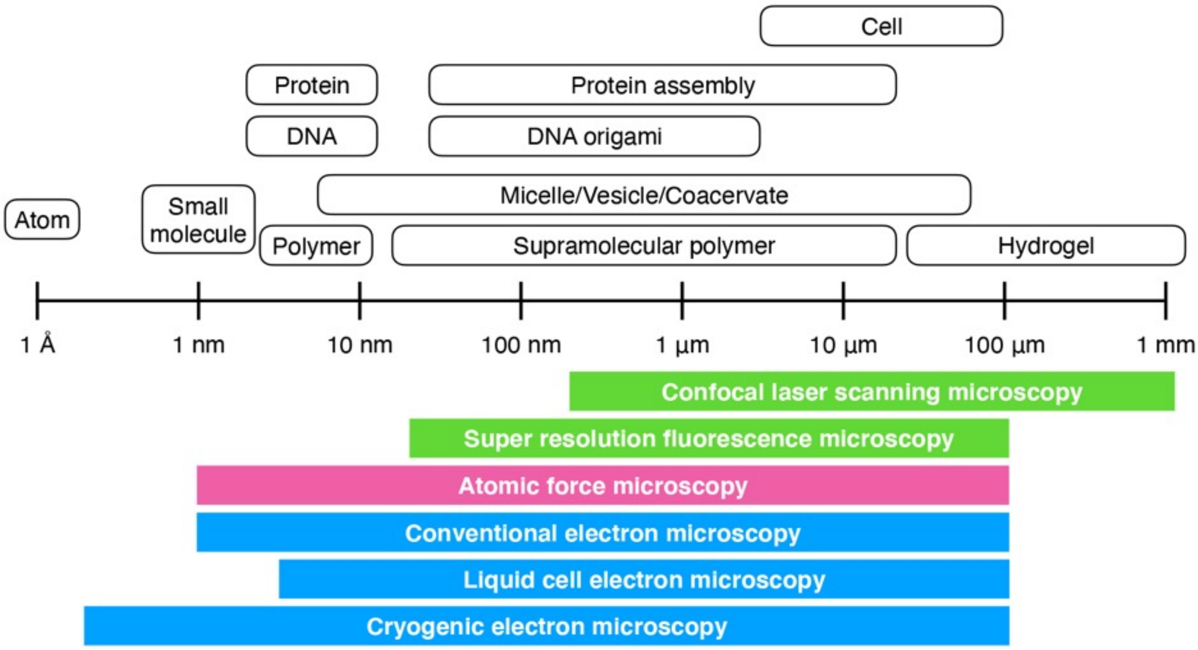

Figure 51. Spatial resolution of imaging techniques and size of organic molecules and their assemblies.

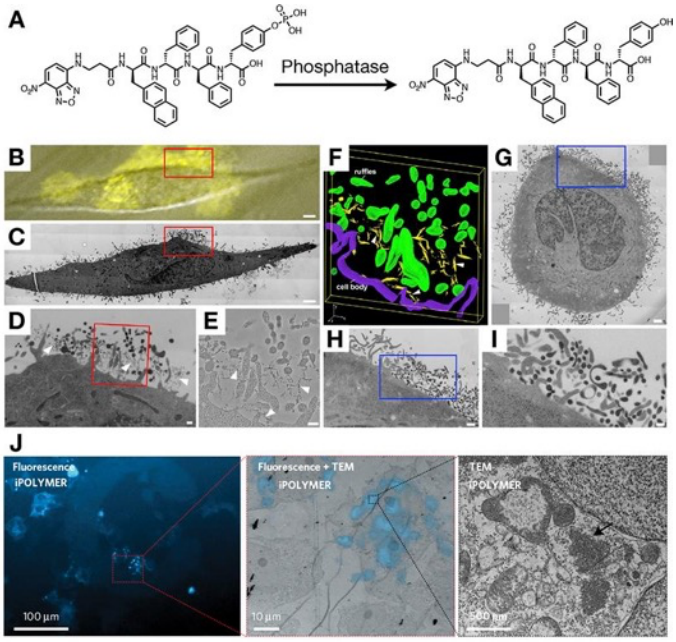

Figure 52. (**A**) Phosphatase-induced formation of a fluorescent hydrogelator. (**B**) Overlay image of fluorescent and differential interference contrast images of HeLa cells treated with the hydrogel precursor. (**C**) TEM image of the same cell shown in (**B**). (**D**, **E**) Higher-magnification TEM images of the red boxed areas shown in (**B**) and (**C**), respectively. (**F**) 3D rendered model of the 3D tomographic reconstruction. (**G–I**) TEM images of untreated cells. Scale bars: (**B**, **C**, **G**) 2000 nm, (**D**, **E**, **I**) 200 nm, (**H**) 500 nm. (**H**, **I**) Higher-magnification TEM images of the blue boxed areas shown in (**G**) and (**H**), respectively. Reproduced with permission from ref 569. Copyright 2016 Elsevier. (**J**) Correlative EM/CLSM images of iPOLYMER gels. Reproduced with permission from ref 341. Copyright 2018 Springer Nature.

Author information

Corresponding author

*E-mail: ihamachi@sbchem.kyoto-u.ac.jp

ORCID

Ryou Kubota: 0000-0001-8112-8169

Itaru Hamachi: 0000-0002-3327-3916

Notes

The authors declare no competing financial interest.

Biographies

Ryou Kubota received B.S., M.S., Ph.D. degrees from the University of Tokyo in Chemistry in 2008, 2010, 2013, respectively, under supervision of Prof. Mitsuhiko Shionoya. He became a postdoctoral researcher in Kyoto University and was promoted as an assistant professor at the same university in 2015. His research interests are development of cell-inspired supramolecular materials and regulation of cellular functions with supramolecular chemistry.

Wataru Tanaka obtained M.S. and Ph.D. from Kyoto University in 2017 and 2021, respectively, under the supervision of Prof. Itaru Hamachi. In 2021, He started his academic carrier as an assistant professor in Prof. Takeshi Yanagida’s group at the University of Tokyo. His research interests include multi-component supramolecular materials.

Itaru Hamachi obtained Ph.D. at Department of Synthetic Chemistry of Kyoto University in 1988 under the supervision of Prof. Iwao Tabushi. He started his academic career as an assistant professor in Prof. Toyoki Kunitake’s group at Kyushu University in 1988, and then moved to Seiji Shinkai’s lab in the same department as an associate professor In 2001, he became a full professor at Kyushu University and then moved to Department of Synthetic Chemistry and Biological Chemistry of Kyoto University in 2005. Currently, he is also a research director of JST ERATO project termed Innovative Molecular Technology for

Neuroscience. His interest has now been extended to chemical biology and organic chemistry in living supramolecular biomaterials.

Acknowledgements

This work was supported by a Grant-in-Aid for Scientific Research on Innovative Areas “Chemistry for Multimolecular Crowding Biosystems” (JSPS KAKENHI Grant JP17H06348), JST ERATO Grant Number JPMJER1802 to I.H., by a Grant-in-Aid for Young Scientists (JSPS KAKENHI Grant JP20K15400) to R.K., and by a Research Fellowship from the Japan Society for the Promotion of Science (JSPS) for Young Scientists to W.T. (JSPS KAKENHI Grant JP19J14474).

A list of abbreviations

AFM	atomic force microscopy
AMP	adenosine monophosphate
ATP	adenosine triphosphate
BSA	bovine serum albumin
BTA	1,3,5-benzenetricarboxamide
CD	circular dichroism
CDSA	crystallization-driven self-assembly
CLSM	confocal laser scanning microscopy
Cryo-EM	cryogenic electron microscopy
CuAAC	Cu^+-catalyzed azide-alkyne cycloaddition
DHPE	1,2-dihexadecanoyl-*sn*-glycero-3-phosphoethanolamine
DHFR	dihydroforate reductase
DIC	differential interference contrast
DLS	dynamic light scattering
DMS	dimethyl sulfate
DOPC	1,2-dioleoyl-*sn*-glycero-3-phosphocholine
DOPS	1,2-dioleoyl-*sn*-glycero-3-phospho-L-serine
DPPE	1,2-dipalmitoyl-*sn*-glycero-3-phosphoethanolamine
DTT	dithiothreitol
EDC	1-ethyl-3-(3-dimethylaminopropyl)carbodiimide
EDTA	ethylenediaminetetraacetic acid
EDX	energy dispersive X-ray spectroscopy
EGF	epidermal growth factor
EGFR	epidermal growth factor receptor
EM	electron microscopy
EPR	enhanced permeation and retention
FD	force distance curve
FITC	fluorescein isothiocyanate

FLIM	fluorescence lifetime imaging microscopy
FRAP	fluorescence recovery after photobleaching
GDP	guanosine diphosphate
GFP	green fluorescent protein
GTP	guanosine triphosphate
HMW	high molecular weight
HOPG	highly ordered pyrolytic graphite
HS-AFM	high speed-atomic force microscopy
IMS	imaging mass spectroscopy
iPAINT	interfacial point accumulation for imaging in nanoscale topography
LC-EM	liquid cell electron microscopy
LCST	lower critical solution temperature
LMW	low molecular weight
LPP	lambda protein phosphatase
MAA	methacrylic acid
MALDI	matrix assisted laser desorption ionization
MBA	methylene bis(acrylamide)
MCH	methylcyclohexane
MD	molecular dynamics
MF	melamine formaldehyde
MOF	metal-organic framework
MMT	montmorillonite
MTX	methotrexate
NBD	nitrobenzofurazan
NHS	*N*-hydroxysuccinimide
OPV	oligo(*p*-phenylenevinylene)
P2VP	poly(2-vinylpyridine)
PA	peptide amphiphile
PAAm	polyacrylamide

PAH	poly(allylamine hydrochloride)
PAINT	point accumulation for imaging in nanoscale topography
PALM	photoactivated localization microscopy
PBI	perylene bisimide
PBO	poly(butylene oxide)
PBS	phosphate buffered saline
PCL	poly(caprolactone)
PDDA	polydiallyldimethylammonium chloride
PDI	perylene diimide
PDMS	polydimethylsiloxane
PEG	polyethylene glycol
PEO	poly(ethylene oxide)
PeP	peptide-grafted polymer
PFS	poly(ferrocenyldimethylsilane)
PIC	polyisocyanide
PMVS	poly(methylvinylsiloxane)
PNIPAM	poly(*N*-isopropylacrylamide)
PS	phosphatidylserine
PSS	poly(sodium styrenesulfonate)
RITC	rhodamine isothiocyanate
SEM	scanning electron microscopy
SIM	structured illumination microscopy
SMLM	single molecule localization microscopy
SPAAC	strain-promoted azide-alkyne cycloaddition
STED	stimulated emission depletion
STEM	scanning transmission electron microscopy
STORM	stochastic optical reconstruction microscopy
TACN	1,4,7-triazacyclononane
TEM	transmission electron microscopy

TIRFM	total internal reflection fluorescence microscope
TMR	tetramethylrhodamine
UPLC	ultra-performance liquid chromatography
ZIF	zeolite imidazolate framework

References

(1) Dufrêne, Y. F.; Ando, T.; Garcia, R.; Alsteens, D.; Martinez-Martin, D.; Engel, A.; Gerber, C.; Müller, D. J. Imaging Modes of Atomic Force Microscopy for Application in Molecular and Cell Biology. *Nat. Nanotechnol.* **2017**, *12*, 295–307.

(2) Kühlbrandt, W. Biochemistry. The Resolution Revolution. *Science* **2014**, *343*, 1443–1444.

(3) Alushin, G. M.; Lander, G. C.; Kellogg, E. H.; Zhang, R.; Baker, D.; Nogales, E. High-Resolution Microtubule Structures Reveal the Structural Transitions in Aβ-Tubulin upon GTP Hydrolysis. *Cell* **2014**, *157*, 1117–1129.

(4) Yang, G.; Zhang, X.; Kochovski, Z.; Zhang, Y.; Dai, B.; Sakai, F.; Jiang, L.; Lu, Y.; Ballauff, M.; Li, X. *et al.* Precise and Reversible Protein-Microtubule-Like Structure with Helicity Driven by Dual Supramolecular Interactions. *J. Am. Chem. Soc.* **2016**, *138*, 1932–1937.

(5) Guenther, E. L.; Ge, P.; Trinh, H.; Sawaya, M. R.; Cascio, D.; Boyer, D. R.; Gonen, T.; Zhou, Z. H.; Eisenberg, D. S. Atomic-Level Evidence for Packing and Positional Amyloid Polymorphism by Segment from TDP-43 RRM2. *Nat. Struct. Mol. Biol.* **2018**, *25*, 311–319.

(6) Li, Z.; Chen, S.; Gao, C.; Yang, Z.; Shih, K.-C.; Kochovski, Z.; Yang, G.; Gou, L.; Nieh, M.-P.; Jiang, M. *et al.* Chemically Controlled Helical Polymorphism in Protein Tubes by Selective Modulation of Supramolecular Interactions. *J. Am. Chem. Soc.* **2019**, *141*, 19448–19457.

(7) de Jonge, N.; Ross, F. M. Electron Microscopy of Specimens in Liquid. *Nat. Nanotechnol.* **2011**, *6*, 695–704.

(8) Smith, J. W.; Chen, Q. Liquid-Phase Electron Microscopy Imaging of Cellular and Biomolecular Systems. *J. Mater. Chem. B Mater. Biol. Med.* **2020**, *8*, 8490–8506.

(9) Wu, H.; Friedrich, H.; Patterson, J. P.; Sommerdijk, N. A. J. M.; de Jonge, N. Liquid-Phase Electron Microscopy for Soft Matter Science and Biology. *Adv. Mater.* **2020**, *32*, e2001582.

(10) Ando, T.; Uchihashi, T.; Scheuring, S. Filming Biomolecular Processes by High-Speed Atomic Force Microscopy. *Chem. Rev.* **2014**, *114*, 3120–3188.

(11) Heath, G. R.; Scheuring, S. Advances in High-Speed Atomic Force Microscopy (HS-AFM) Reveal Dynamics of Transmembrane Channels and Transporters. *Curr. Opin. Struct. Biol.* **2019**, *57*, 93–102.

(12) Uchihashi, T.; Ganser, C. Recent Advances in Bioimaging with High-Speed Atomic Force Microscopy. *Biophys. Rev.* **2020**, *12*, 363–369.

(13) Mears, L. L. E.; Draper, E. R.; Castilla, A. M.; Su, H.; Zhuola; Dietrich, B.; Nolan, M. C.; Smith, G. N.; Doutch, J.; Rogers, S. *et al.* Drying Affects the Fiber Network in Low Molecular Weight Hydrogels. *Biomacromolecules* **2017**, *18*, 3531–3540.

(14) Newcomb, C. J.; Moyer, T. J.; Lee, S. S.; Stupp, S. I. Advances in Cryogenic Transmission Electron Microscopy for the Characterization of Dynamic Self-Assembling Nanostructures. *Curr. Opin. Colloid Interface Sci.* **2012**, *17*, 350–359.

(15) Danino, D. Cryo-TEM of Soft Molecular Assemblies. *Curr. Opin. Colloid Interface Sci.* **2012**, *17*, 316–329.

(16) Halberstadt, E. S.; Henisch, H. K.; Nickl, J.; White, E. W. Gel Structure and Crystal Nucleation. *J. Colloid Interface Sci.* **1969**, *29*, 469–471.

(17) Lewin, M.; Roldan, L. G. The Effect of Liquid Anhydrous Ammonia in the Structure and Morphology of Cotton Cellulose. *J. Polym. Sci. C Polym. Symp.* **1971**, *36*, 213–229.

(18) Trelstad, R. L.; Hayashi, K.; Gross, J. Collagen Fibrillogenesis: Intermediate Aggregates and Suprafibrillar Order. *Proc. Natl. Acad. Sci. U. S. A.* **1976**, *73*, 4027–4031.

(19) Hirano, S.; Yamaguchi, R.; Matsuda, N. Architecture of Chitin Gel as Examined by Scanning Electron Microscopy. *Biopolymers* **1977**, *16*, 1987–1992.

(20) Margolis, R. L.; Wilson, L. Opposite End Assembly and Disassembly of Microtubules at Steady State in Vitro. *Cell* **1978**, *13*, 1–8.

(21) Engel, A. Molecular Weight Determination by Scanning Transmission Electron Microscopy. *Ultramicroscopy* **1978**, *3*, 273–281.

(22) Pollard, T. D.; Mooseker, M. S. Direct Measurement of Actin Polymerization Rate Constants by Electron Microscopy of Actin Filaments Nucleated by Isolated Microvillus Cores. *J. Cell Biol.* **1981**, *88*, 654–659.

(23) Blank, Z.; Reimschuessel, A. C. Structural Studies of Organic Gels by SEM. *J. Mater. Sci.* **1974**, *9*, 1815–1822.

(24) Canham, P. A.; Lally, T. P.; Price, C.; Stubbersfield, R. B. Formation of Worm-like Micelles from a Polystyrene–Polybutadiene–Polystyrene Block Copolymer in Ethyl Acetate. *J. Chem. Soc. Lond. Faraday Trans. 1* **1980**, *76*, 1857–1867.

(25) Price, C. Micelle Formation by Block Copolymers in Organic Solvents. *J. Macromol. Sci. Part A Pure Appl. Chem.* **1983**, *55*, 1563–1572.

(26) Gulik-Krzywicki, T.; Fouquey, C.; Lehn, J. Electron Microscopic Study of Supramolecular Liquid Crystalline Polymers Formed by Molecular-Recognition-Directed Self-Assembly from Complementary Chiral Components. *Proc. Natl. Acad. Sci. U. S. A.* **1993**, *90*, 163–167.

(27) Zhang, L.; Eisenberg, A. Multiple Morphologies of “Crew-Cut” Aggregates of Polystyrene-*b*-Poly(Acrylic Acid) Block Copolymers. *Science* **1995**, *268*, 1728–1731.

(28) Massey, J.; Power, K. N.; Manners, I.; Winnik, M. A. Self-Assembly of a Novel Organometallic─Inorganic Block Copolymer in Solution and the Solid State: Nonintrusive Observation of Novel Wormlike Poly(Ferrocenyldimethylsilane)-*b*-Poly(Dimethylsiloxane) Micelles. *J. Am. Chem. Soc.* **1998**, *120*, 9533–9540.

(29) Engelkamp, H.; Middelbeek, S.; Nolte, R. J. Self-Assembly of Disk-Shaped Molecules to Coiled-Coil Aggregates with Tunable Helicity. *Science* **1999**, *284*, 785–788.

(30) Wang, Q.; Yang, Z.; Zhang, X.; Xiao, X.; Chang, C. K.; Xu, B. A Supramolecular-Hydrogel-Encapsulated Hemin as an Artificial Enzyme to Mimic Peroxidase. *Angew. Chem. Int. Ed.* **2007**, *46*, 4285–4289.

(31) Komatsu, H.; Matsumoto, S.; Tamaru, S.-I.; Kaneko, K.; Ikeda, M.; Hamachi, I. Supramolecular Hydrogel Exhibiting Four Basic Logic Gate Functions to Fine-Tune Substance Release. *J. Am. Chem. Soc.* **2009**, *131*, 5580–5585.

(32) Wyroba, E.; Suski, S.; Miller, K.; Bartosiewicz, R. Biomedical and Agricultural Applications of Energy Dispersive X-Ray Spectroscopy in Electron Microscopy. *Cell. Mol. Biol. Lett.* **2015**, *20*, 488–509.

(33) Gädt, T.; Ieong, N. S.; Cambridge, G.; Winnik, M. A.; Manners, I. Complex and Hierarchical Micelle Architectures from Diblock Copolymers Using Living, Crystallization-Driven Polymerizations. *Nat. Mater.* **2009**, *8*, 144–150.

(34) Zhang, W.; Jin, W.; Fukushima, T.; Saeki, A.; Seki, S.; Aida, T. Supramolecular Linear Heterojunction Composed of Graphite-like Semiconducting Nanotubular Segments. *Science* **2011**, *334*, 340–343.

(35) Talmon, Y. Staining and Drying-Induced Artifacts in Electron Microscopy of Surfactant Dispersions. *J. Colloid Interface Sci.* **1983**, *93*, 366–382.

(36) Taylor, K. A.; Glaeser, R. M. Electron Diffraction of Frozen, Hydrated Protein Crystals. *Science* **1974**, *186*, 1036–1037.

(37) Dubochet, J.; Lepault, J.; Freeman, R.; Berriman, J. A.; Homo, J.-C. Electron Microscopy of Frozen Water and Aqueous Solutions. *J. Microsc.* **1982**, *128*, 219–237.

(38) Cui, H.; Hodgdon, T. K.; Kaler, E. W.; Abezgauz, L.; Danino, D.; Lubovsky, M.; Talmon, Y.; Pochan, D. J. Elucidating the Assembled Structure of Amphiphiles in Solution via Cryogenic Transmission Electron Microscopy. *Soft Matter* **2007**, *3*, 945–955.

(39) Friedrich, H.; Frederik, P. M.; de With, G.; Sommerdijk, N. A. J. M. Imaging of Self-Assembled Structures: Interpretation of TEM and Cryo-TEM Images. *Angew. Chem. Int. Ed.* **2010**, *49*, 7850–7858.

(40) Franken, L. E.; Boekema, E. J.; Stuart, M. C. A. Transmission Electron Microscopy as a Tool for the Characterization of Soft Materials: Application and Interpretation. *Adv. Sci.* **2017**, *4*, 1600476.

(41) Won, Y. Y.; Davis, H. T.; Bates, F. S. Giant Wormlike Rubber Micelles. *Science* **1999**, *283*, 960–963.

(42) Brizard, A.; Stuart, M.; van Bommel, K.; Friggeri, A.; de Jong, M.; van Esch, J. Preparation of Nanostructures by Orthogonal Self-Assembly of Hydrogelators and Surfactants. *Angew. Chem. Int. Ed.* **2008**, *47*, 2063–2066.

(43) Boekhoven, J.; Brizard, A. M.; Stuart, M. C. A.; Florusse, L.; Raffy, G.; Del Guerzo, A.; van Esch, J. H. Bio-Inspired Supramolecular Materials by Orthogonal Self-Assembly of Hydrogelators and Phospholipids. *Chem. Sci.* **2016**, *7*, 6021–6031.

(44) Majumder, P.; Baxa, U.; Walsh, S. T. R.; Schneider, J. P. Design of a Multicompartment Hydrogel That Facilitates Time-Resolved Delivery of Combination Therapy and Synergized Killing of Glioblastoma. *Angew. Chem. Int. Ed.* **2018**, *57*, 15040–15044.

(45) Danino, D.; Moon, K.-H.; Hinshaw, J. E. Rapid Constriction of Lipid Bilayers by the Mechanochemical Enzyme Dynamin. *J. Struct. Biol.* **2004**, *147*, 259–267.

(46) Hinshaw, J. E. Dynamin and Its Role in Membrane Fission. *Annu. Rev. Cell Dev. Biol.* **2000**, *16*, 483–519.

(47) Pashuck, E. T.; Stupp, S. I. Direct Observation of Morphological Tranformation from Twisted Ribbons into Helical Ribbons. *J. Am. Chem. Soc.* **2010**, *132*, 8819–8821.

(48) Ziserman, L.; Lee, H.-Y.; Raghavan, S. R.; Mor, A.; Danino, D. Unraveling the Mechanism of Nanotube Formation by Chiral Self-Assembly of Amphiphiles. *J. Am. Chem. Soc.* **2011**, *133*, 2511–2517.

(49) Rubinov, B.; Wagner, N.; Matmor, M.; Regev, O.; Ashkenasy, N.; Ashkenasy, G. Transient Fibril Structures Facilitating Nonenzymatic Self-Replication. *ACS Nano* **2012**, *6*, 7893–7901.

(50) Fichman, G.; Guterman, T.; Damron, J.; Adler-Abramovich, L.; Schmidt, J.; Kesselman, E.; Shimon, L. J. W.; Ramamoorthy, A.; Talmon, Y.; Gazit, E. Spontaneous Structural Transition and Crystal Formation in Minimal Supramolecular Polymer Model. *Sci. Adv.* **2016**, *2*, e1500827.

(51) Yuan, C.; Levin, A.; Chen, W.; Xing, R.; Zou, Q.; Herling, T. W.; Challa, P. K.; Knowles, T. P. J.; Yan, X. Nucleation and Growth of Amino Acid and Peptide Supramolecular Polymers through Liquid-Liquid Phase Separation. *Angew. Chem. Int. Ed.* **2019**, *58*, 18116–18123.

(52) Li, Y.; Wang, K.; Zhou, W.; Li, Y.; Vila, R.; Huang, W.; Wang, H.; Chen, G.; Wu, G.-H.; Tsao, Y. *et al.* Cryo-EM Structures of Atomic Surfaces and Host-Guest Chemistry in Metal-Organic Frameworks. *Matter* **2019**, *1*, 428–438.

(53) Nogales, E. The Development of Cryo-EM into a Mainstream Structural Biology Technique. *Nat. Methods* **2016**, *13*, 24–27.

(54) Wrapp, D.; Wang, N.; Corbett, K. S.; Goldsmith, J. A.; Hsieh, C.-L.; Abiona, O.; Graham, B. S.; McLellan, J. S. Cryo-EM Structure of the 2019-NCoV Spike in the Prefusion Conformation. *Science* **2020**, *367*, 1260–1263.

(55) Yip, K. M.; Fischer, N.; Paknia, E.; Chari, A.; Stark, H. Atomic-Resolution Protein Structure Determination by Cryo-EM. *Nature* **2020**, *587*, 157–161.

(56) Nakane, T.; Kotecha, A.; Sente, A.; McMullan, G.; Masiulis, S.; Brown, P. M. G. E.; Grigoras, I. T.; Malinauskaite, L.; Malinauskas, T.; Miehling, J. *et al.* Single-Particle Cryo-EM at Atomic Resolution. *Nature* **2020**, *587*, 152–156.

(57) Beck, M.; Baumeister, W. Cryo-Electron Tomography: Can It Reveal the Molecular Sociology of Cells in Atomic Detail? *Trends Cell Biol.* **2016**, *26*, 825−837.

(58) Doerr, A. Cryo-Electron Tomography. *Nat. Methods* **2017**, *14*, 34–34.

(59) Harapin, J.; Eibauer, M.; Medalia, O. Structural Analysis of Supramolecular Assemblies by Cryo-Electron Tomography. *Structure* **2013**, *21*, 1522–1530.

(60) Manka, S. W.; Moores, C. A. Microtubule Structure by Cryo-EM: Snapshots of Dynamic Instability. *Essays Biochem.* **2018**, *62*, 737–751.

(61) Desai, A.; Mitchison, T. J. Microtubule Polymerization Dynamics. *Annu. Rev. Cell Dev. Biol.* **1997**, *13*, 83–117.

(62) Liu, T.; Dai, A.; Cao, Y.; Zhang, R.; Dong, M.-Q.; Wang, H.-W. Structural Insights of WHAMM's Interaction with Microtubules by Cryo-EM. *J. Mol. Biol.* **2017**, *429*, 1352–1363.

(63) Kellogg, E. H.; Hejab, N. M. A.; Poepsel, S.; Downing, K. H.; DiMaio, F.; Nogales, E. Near-Atomic Model of Microtubule-Tau Interactions. *Science* **2018**, *360*, 1242–1246.

(64) Manka, S. W.; Moores, C. A. The Role of Tubulin-Tubulin Lattice Contacts in the Mechanism of Microtubule Dynamic Instability. *Nat. Struct. Mol. Biol.* **2018**, *25*, 607–615.

(65) Ichikawa, M.; Khalifa, A. A. Z.; Kubo, S.; Dai, D.; Basu, K.; Maghrebi, M. A. F.; Vargas, J.; Bui, K. H. Tubulin Lattice in Cilia Is in a Stressed Form Regulated by Microtubule Inner Proteins. *Proc. Natl. Acad. Sci. U. S. A.* **2019**, *116*, 19930–19938.

(66) Zhang, W.; Kochovski, Z.; Lu, Y.; Schmidt, B. V. K. J.; Antonietti, M.; Yuan, J. Internal Morphology-Controllable Self-Assembly in Poly(Ionic Liquid) Nanoparticles. *ACS Nano* **2016**, *10*, 7731–7737.

(67) Rodriguez, J. A.; Ivanova, M. I.; Sawaya, M. R.; Cascio, D.; Reyes, F. E.; Shi, D.; Sangwan, S.; Guenther, E. L.; Johnson, L. M.; Zhang, M. *et al.* Structure of the Toxic Core of α-Synuclein from Invisible Crystals. *Nature* **2015**, *525*, 486–490.

(68) Nannenga, B. L.; Gonen, T. The Cryo-EM Method Microcrystal Electron Diffraction (MicroED). *Nat. Methods* **2019**, *16*, 369−379.

(69) Gim, S.; Fittolani, G.; Nishiyama, Y.; Seeberger, P. H.; Ogawa, Y.; Delbianco, M. Supramolecular Assembly and Chirality of Synthetic Carbohydrate Materials. *Angew. Chem. Int. Ed.* **2020**. 59, 22577–22583.

(70) Hamada, H.; Nakamuro, T.; Yamashita, K.; Yanagisawa, H.; Nureki, O.; Kikkawa, M.; Harano, K.; Shang, R.; Nakamura, E. Spiro-Conjugated Carbon/Heteroatom-Bridgedp-Phenylenevinylenes: Synthesis, Properties, and Microcrystal Electron Crystallographic Analysis of Racemic Solid Solutions. *Bull. Chem. Soc. Jpn.* **2020**, *93*, 776–782.

(71) Ueda, M.; Aoki, T.; Akiyama, T.; Nakamuro, T.; Yamashita, K.; Yanagisawa, H.; Nureki, O.; Kikkawa, M.; Nakamura, E.; Aida, T. *et al.* Alternating Heterochiral

Supramolecular Copolymerization. *J. Am. Chem. Soc.* **2021**, https://doi.org/10.1021/jacs.1c00823.

(72) Kato, K.; Takaba, K.; Maki-Yonekura, S.; Mitoma, N.; Nakanishi, Y.; Nishihara, T.; Hatakeyama, T.; Kawada, T.; Hijikata, Y.; Pirillo, J. *et al.* Double-Helix Supramolecular Nanofibers Assembled from Negatively Curved Nanographenes. *J. Am. Chem. Soc.* **2021**, https://doi.org/10.1021/jacs.1c00863.

(73) Ross, F. M. Opportunities and Challenges in Liquid Cell Electron Microscopy. *Science* **2015**, *350*, aaa9886.

(74) de Jonge, N. Theory of the Spatial Resolution of (Scanning) Transmission Electron Microscopy in Liquid Water or Ice Layers. *Ultramicroscopy* **2018**, *187*, 113–125.

(75) de Jonge, N.; Houben, L.; Dunin-Borkowski, R. E.; Ross, F. M. Resolution and Aberration Correction in Liquid Cell Transmission Electron Microscopy. *Nat. Rev. Mater.* **2019**, *4*, 61–78.

(76) Williamson, M. J.; Tromp, R. M.; Vereecken, P. M.; Hull, R.; Ross, F. M. Dynamic Microscopy of Nanoscale Cluster Growth at the Solid–Liquid Interface. *Nat. Mater.* **2003**, *2*, 532–536.

(77) Zheng, H.; Smith, R. K.; Jun, Y.-W.; Kisielowski, C.; Dahmen, U.; Paul Alivisatos, A. Observation of Single Colloidal Platinum Nanocrystal Growth Trajectories. *Science* **2009**, *324*, 1309–1312.

(78) Huang, J. Y.; Zhong, L.; Wang, C. M.; Sullivan, J. P.; Xu, W.; Zhang, L. Q.; Mao, S. X.; Hudak, N. S.; Liu, X. H.; Subramanian, A. *et al.* In Situ Observation of the Electrochemical Lithiation of a Single SnO_2 Nanowire Electrode. *Science* **2010**, *330*, 1515–1520.

(79) Ross, F. M. Controlling Nanowire Structures through Real Time Growth Studies. *Rep. Prog. Phys.* **2010**, *73*, 114501.

(80) de Jonge, N.; Peckys, D. B.; Kremers, G. J.; Piston, D. W. Electron Microscopy of Whole Cells in Liquid with Nanometer Resolution. *Proc. Natl. Acad. Sci. U. S. A.* **2009**, *106*, 2159–2164.

(81) Peckys, D. B.; Korf, U.; de Jonge, N. Local Variations of HER2 Dimerization in Breast Cancer Cells Discovered by Correlative Fluorescence and Liquid Electron Microscopy. *Sci. Adv.* **2015**, *1*, e1500165.

(82) Proetto, M. T.; Rush, A. M.; Chien, M.-P.; Abellan Baeza, P.; Patterson, J. P.; Thompson, M. P.; Olson, N. H.; Moore, C. E.; Rheingold, A. L.; Andolina, C. *et al.* Dynamics of Soft Nanomaterials Captured by Transmission Electron Microscopy in Liquid Water. *J. Am. Chem. Soc.* **2014**, *136*, 1162–1165.

(83) Parent, L. R.; Bakalis, E.; Ramírez-Hernández, A.; Kammeyer, J. K.; Park, C.; de Pablo, J.; Zerbetto, F.; Patterson, J. P.; Gianneschi, N. C. Directly Observing Micelle Fusion and Growth in Solution by Liquid-Cell Transmission Electron Microscopy. *J. Am. Chem. Soc.* **2017**, *139*, 17140–17151.

(84) Ianiro, A.; Wu, H.; van Rijt, M. M. J.; Vena, M. P.; Keizer, A. D. A.; Esteves, A. C. C.; Tuinier, R.; Friedrich, H.; Sommerdijk, N. A. J. M.; Patterson, J. P. Liquid-Liquid Phase Separation during Amphiphilic Self-Assembly. *Nat. Chem.* **2019**, *11*, 320–328.

(85) Le Ferrand, H.; Duchamp, M.; Gabryelczyk, B.; Cai, H.; Miserez, A. Time-Resolved Observations of Liquid-Liquid Phase Separation at the Nanoscale Using in Situ Liquid Transmission Electron Microscopy. *J. Am. Chem. Soc.* **2019**, *141*, 7202–7210.

(86) Touve, M. A.; Carlini, A. S.; Gianneschi, N. C. Self-Assembling Peptides Imaged by Correlated Liquid Cell Transmission Electron Microscopy and MALDI-Imaging Mass Spectrometry. *Nat. Commun.* **2019**, *10*, 4837.

(87) Hoppe, S. M.; Sasaki, D. Y.; Kinghorn, A. N.; Hattar, K. In-Situ Transmission Electron Microscopy of Liposomes in an Aqueous Environment. *Langmuir* **2013**, *29*, 9958–9961.

(88) Wang, C.; Qiao, Q.; Shokuhfar, T.; Klie, R. F. High-Resolution Electron Microscopy and Spectroscopy of Ferritin in Biocompatible Graphene Liquid Cells and Graphene Sandwiches. *Adv. Mater.* **2014**, *26*, 3410–3414.

(89) DiMemmo, L. M.; Cameron Varano, A.; Haulenbeek, J.; Liang, Y.; Patel, K.; Dukes, M. J.; Zheng, S.; Hubert, M.; Piccoli, S. P.; Kelly, D. F. Real-Time Observation of

Protein Aggregates in Pharmaceutical Formulations Using Liquid Cell Electron Microscopy. *Lab Chip* **2017**, *17*, 315–322.

(90) Wang, H.; Li, B.; Kim, Y.-J.; Kwon, O.-H.; Granick, S. Intermediate States of Molecular Self-Assembly from Liquid-Cell Electron Microscopy. *Proc. Natl. Acad. Sci. U. S. A.* **2020**, *117*, 1283–1292.

(91) Gong, X.; Gnanasekaran, K.; Chen, Z.; Robison, L.; Wasson, M. C.; Bentz, K. C.; Cohen, S. M.; Farha, O. K.; Gianneschi, N. C. Insights into the Structure and Dynamics of Metal-Organic Frameworks via Transmission Electron Microscopy. *J. Am. Chem. Soc.* **2020**, *142*, 17224–17235.

(92) Patterson, J. P.; Abellan, P.; Denny, M. S., Jr; Park, C.; Browning, N. D.; Cohen, S. M.; Evans, J. E.; Gianneschi, N. C. Observing the Growth of Metal-Organic Frameworks by in Situ Liquid Cell Transmission Electron Microscopy. *J. Am. Chem. Soc.* **2015**, *137*, 7322–7328.

(93) Binnig, G.; Quate, C. F.; Gerber, C. Atomic Force Microscope. *Phys. Rev. Lett.* **1986**, *56*, 930–933.

(94) Hansma, H. G.; Hoh, J. H. Biomolecular Imaging with the Atomic Force Microscope. *Annu. Rev. Biophys. Biomol. Struct.* **1994**, *23*, 115–139.

(95) Henderson, E.; Haydon, P. G.; Sakaguchi, D. S. Actin Filament Dynamics in Living Glial Cells Imaged by Atomic Force Microscopy. *Science* **1992**, *257*, 1944–1946.

(96) Hoh, J. H.; Schoenenberger, C. A. Surface Morphology and Mechanical Properties of MDCK Monolayers by Atomic Force Microscopy. *J. Cell Sci.* **1994**, *107*, 1105–1114.

(97) Yang, J.; Mou, J.; Shao, Z. Structure and Stability of Pertussis Toxin Studied by in Situ Atomic Force Microscopy. *FEBS Lett.* **1994**, *338*, 89–92.

(98) Schabert, F. A.; Henn, C.; Engel, A. Native Escherichia Coli OmpF Porin Surfaces Probed by Atomic Force Microscopy. *Science* **1995**, *268*, 92–94.

(99) Müller, D. J.; Janovjak, H.; Lehto, T.; Kuerschner, L.; Anderson, K. Observing Structure, Function and Assembly of Single Proteins by AFM. *Prog. Biophys. Mol. Biol.* **2002**, *79*, 1–43.

(100) Leclère, P.; Surin, M.; Viville, P.; Lazzaroni, R.; Kilbinger, A. F. M.; Henze, O.; Feast, W. J.; Cavallini, M.; Biscarini, F.; Schenning, A. P. H. J. *et al.* About Oligothiophene Self-Assembly: From Aggregation in Solution to Solid-State Nanostructures. *Chem. Mater.* **2004**, *16*, 4452–4466.

(101) Harper, J. D.; Lieber, C. M.; Lansbury, P. T. Atomic Force Microscopic Imaging of Seeded Fibril Formation and Fibril Branching by the Alzheimer's Disease Amyloid-β Protein. *Chem. Biol.* **1997**, *4*, 951–959.

(102) Dufrêne, Y. F.; Martínez-Martín, D.; Medalsy, I.; Alsteens, D.; Müller, D. J. Multiparametric Imaging of Biological Systems by Force-Distance Curve–Based AFM. *Nat. Methods* **2013**, *10*, 847–854.

(103) Alsteens, D.; Müller, D. J.; Dufrêne, Y. F. Multiparametric Atomic Force Microscopy Imaging of Biomolecular and Cellular Systems. *Acc. Chem. Res.* **2017**, *50*, 924–931.

(104) Fukui, T.; Uchihashi, T.; Sasaki, N.; Watanabe, H.; Takeuchi, M.; Sugiyasu, K. Direct Observation and Manipulation of Supramolecular Polymerization by High-Speed Atomic Force Microscopy. *Angew. Chem. Int. Ed.* **2018**, *57*, 15465–15470.

(105) Maity, S.; Ottelé, J.; Santiago, G. M.; Frederix, P. W. J. M.; Kroon, P.; Markovitch, O.; Stuart, M. C. A.; Marrink, S. J.; Otto, S.; Roos, W. H. Caught in the Act: Mechanistic Insight into Supramolecular Polymerization-Driven Self-Replication from Real-Time Visualization. *J. Am. Chem. Soc.* **2020**, *142*, 13709–13717.

(106) Hansma, P. K.; Elings, V. B.; Marti, O.; Bracker, C. E. Scanning Tunneling Microscopy and Atomic Force Microscopy: Application to Biology and Technology. *Science* **1988**, *242*, 209–216.

(107) Engel, A. Biological Applications of Scanning Probe Microscopes. *Annu. Rev. Biophys. Biophys. Chem.* **1991**, *20*, 79–108.

(108) Delain, E.; Fourcade, A.; Poulin, J.-C.; Barbin, A.; Coulaud, D.; Le Cam, E.; Paris, E. Comparative Observations of Biological Specimens, Especially DNA and Filamentous Actin Molecules in Atomic Force, Tunnelling and Electron Microscopes. *Microsc. Microanal. Microstruct.* **1992**, *3*, 457–470.

(109) Kohori, F.; Sakai, K.; Aoyagi, T.; Yokoyama, M.; Sakurai, Y.; Okano, T. Preparation and Characterization of Thermally Responsive Block Copolymer Micelles Comprising Poly(*N*-Isopropylacrylamide-*b*-DL-Lactide). *J. Control. Release* **1998**, *55*, 87–98.

(110) Heskins, M.; Guillet, J. E. Solution Properties of Poly(*N*-Isopropylacrylamide). *J. Macromol. Sci. Part A* **1968**, *2*, 1441–1455.

(111) Schenning, A. P. H. J.; v. Herrikhuyzen, J.; Jonkheijm, P.; Chen, Z.; Würthner, F.; Meijer, E. W. Photoinduced Electron Transfer in Hydrogen-Bonded Oligo(*p*-Phenylene Vinylene)─Perylene Bisimide Chiral Assemblies. *J. Am. Chem. Soc.* **2002**, *124*, 10252–10253.

(112) Schenning, A. P. H. J.; Kilbinger, A. F. M.; Biscarini, F.; Cavallini, M.; Cooper, H. J.; Derrick, P. J.; Feast, W. J.; Lazzaroni, R.; Leclère, P.; McDonell, L. A. *et al.* Supramolecular Organization of α,α‘-Disubstituted Sexithiophenes. *J. Am. Chem. Soc.* **2002**, *124*, 1269–1275.

(113) Würthner, F.; Chen, Z.; Hoeben, F. J. M.; Osswald, P.; You, C.-C.; Jonkheijm, P.; Herrikhuyzen, J. V.; Schenning, A. P. H. J.; van der Schoot, P. P. A. M.; Meijer, E. W. *et al.* Supramolecular p-n-Heterojunctions by Co-Self-Organization of Oligo(*p*-Phenylene Vinylene) and Perylene Bisimide Dyes. *J. Am. Chem. Soc.* **2004**, *126*, 10611–10618.

(114) Yagai, S.; Kitamoto, Y.; Datta, S.; Adhikari, B. Supramolecular Polymers Capable of Controlling Their Topology. *Acc. Chem. Res.* **2019**, *52*, 1325–1335.

(115) Datta, S.; Kato, Y.; Higashiharaguchi, S.; Aratsu, K.; Isobe, A.; Saito, T.; Prabhu, D. D.; Kitamoto, Y.; Hollamby, M. J.; Smith, A. J. *et al.* Self-Assembled Poly-Catenanes from Supramolecular Toroidal Building Blocks. *Nature* **2020**, *583*, 400–405.

(116) de Pablo, P. J.; Schaap, I. A. T.; MacKintosh, F. C.; Schmidt, C. F. Deformation and Collapse of Microtubules on the Nanometer Scale. *Phys. Rev. Lett.* **2003**, *91*, 098101.

(117) Kol, N.; Adler-Abramovich, L.; Barlam, D.; Shneck, R. Z.; Gazit, E.; Rousso, I. Self-Assembled Peptide Nanotubes Are Uniquely Rigid Bioinspired Supramolecular Structures. *Nano Lett.* **2005**, *5*, 1343–1346.

(118) Smith, J. F.; Knowles, T. P. J.; Dobson, C. M.; Macphee, C. E.; Welland, M. E. Characterization of the Nanoscale Properties of Individual Amyloid Fibrils. *Proc. Natl. Acad. Sci. U. S. A.* **2006**, *103*, 15806–15811.

(119) Zhao, Y.; Tamhane, K.; Zhang, X.; An, L.; Fang, J. Radial Elasticity of Self-Assembled Lipid Tubules. *ACS Nano* **2008**, *2*, 1466–1472.

(120) Knowles, T. P. J.; Buehler, M. J. Nanomechanics of Functional and Pathological Amyloid Materials. *Nat. Nanotechnol.* **2011**, *6*, 469–479.

(121) Bera, S.; Mondal, S.; Xue, B.; Shimon, L. J. W.; Cao, Y.; Gazit, E. Rigid Helical-like Assemblies from a Self-Aggregating Tripeptide. *Nat. Mater.* **2019**, *18*, 503–509.

(122) Frederix, P. W. J. M.; Scott, G. G.; Abul-Haija, Y. M.; Kalafatovic, D.; Pappas, C. G.; Javid, N.; Hunt, N. T.; Ulijn, R. V.; Tuttle, T. Exploring the Sequence Space for (Tri-)Peptide Self-Assembly to Design and Discover New Hydrogels. *Nat. Chem.* **2015**, *7*, 30–37.

(123) Manne, S.; Cleveland, J. P.; Gaub, H. E.; Stucky, G. D.; Hansma, P. K. Direct Visualization of Surfactant Hemimicelles by Force Microscopy of the Electrical Double Layer. *Langmuir* **1994**, *10*, 4409–4413.

(124) Manne, S.; Gaub, H. E. Molecular Organization of Surfactants at Solid-Liquid Interfaces. *Science* **1995**, *270*, 1480–1482.

(125) Manne, S.; Schäffer, T. E.; Huo, Q.; Hansma, P. K.; Morse, D. E.; Stucky, G. D.; Aksay, I. A. Gemini Surfactants at Solid─Liquid Interfaces: Control of Interfacial Aggregate Geometry. *Langmuir* **1997**, *13*, 6382–6387.

(126) Graveland-Bikker, J. F.; Schaap, I. A. T.; Schmidt, C. F.; de Kruif, C. G. Structural and Mechanical Study of a Self-Assembling Protein Nanotube. *Nano Lett.* **2006**, *6*, 616−621.

(127) Yang, H.; Fung, S.-Y.; Pritzker, M.; Chen, P. Mechanical-Force-Induced Nucleation and Growth of Peptide Nanofibers at Liquid/Solid Interfaces. *Angew. Chem. Int. Ed.* **2008**, *47*, 4397–4400.

(128) Zhang, F.-C.; Zhang, F.; Su, H.-N.; Li, H.; Zhang, Y.; Hu, J. Mechanical Manipulation Assisted Self-Assembly to Achieve Defect Repair and Guided Epitaxial Growth of Individual Peptide Nanofilaments. *ACS Nano* **2010**, *4*, 5791–5796.

(129) Jin, H.; Jiao, F.; Daily, M. D.; Chen, Y.; Yan, F.; Ding, Y.-H.; Zhang, X.; Robertson, E. J.; Baer, M. D.; Chen, C.-L. Highly Stable and Self-Repairing Membrane-Mimetic 2D Nanomaterials Assembled from Lipid-like Peptoids. *Nat. Commun.* **2016**, *7*, 12252.

(130) Ma, X.; Zhang, S.; Jiao, F.; Newcomb, C. J.; Zhang, Y.; Prakash, A.; Liao, Z.; Baer, M. D.; Mundy, C. J.; Pfaendtner, J. *et al.* Tuning Crystallization Pathways through Sequence Engineering of Biomimetic Polymers. *Nat. Mater.* **2017**, *16*, 767–774.

(131) Tørring, T.; Voigt, N. V.; Nangreave, J.; Yan, H.; Gothelf, K. V. DNA Origami: A Quantum Leap for Self-Assembly of Complex Structures. *Chem. Soc. Rev.* **2011**, *40*, 5636–5646.

(132) Saccà, B.; Niemeyer, C. M. DNA Origami: The Art of Folding DNA. *Angew. Chem. Int. Ed.* **2012**, *51*, 58–66.

(133) Hong, F.; Zhang, F.; Liu, Y.; Yan, H. DNA Origami: Scaffolds for Creating Higher Order Structures. *Chem. Rev.* **2017**, *117*, 12584–12640.

(134) Rothemund, P. W. K. Folding DNA to Create Nanoscale Shapes and Patterns. *Nature* **2006**, *440*, 297–302.

(135) Chhabra, R.; Sharma, J.; Ke, Y.; Liu, Y.; Rinker, S.; Lindsay, S.; Yan, H. Spatially Addressable Multiprotein Nanoarrays Templated by Aptamer-Tagged DNA Nanoarchitectures. *J. Am. Chem. Soc.* **2007**, *129*, 10304–10305.

(136) Aghebat Rafat, A.; Sagredo, S.; Thalhammer, M.; Simmel, F. C. Barcoded DNA Origami Structures for Multiplexed Optimization and Enrichment of DNA-Based Protein-Binding Cavities. *Nat. Chem.* **2020**, *12*, 852–859.

(137) Williams, B. A. R.; Lund, K.; Liu, Y.; Yan, H.; Chaput, J. C. Self-Assembled Peptide Nanoarrays: An Approach to Studying Protein–Protein Interactions. *Angew. Chem. Int. Ed.* **2007**, *46*, 3051–3054.

(138) Ke, Y.; Lindsay, S.; Chang, Y.; Liu, Y.; Yan, H. Self-Assembled Water-Soluble Nucleic Acid Probe Tiles for Label-Free RNA Hybridization Assays. *Science* **2008**, *319*, 180–183.

(139) Maune, H. T.; Han, S.-P.; Barish, R. D.; Bockrath, M.; Goddard, W. A., III; Rothemund, P. W. K.; Winfree, E. Self-Assembly of Carbon Nanotubes into Two-Dimensional Geometries Using DNA Origami Templates. *Nat. Nanotechnol.* **2010**, *5*, 61–66.

(140) Ke, G.; Liu, M.; Jiang, S.; Qi, X.; Yang, Y. R.; Wootten, S.; Zhang, F.; Zhu, Z.; Liu, Y.; Yang, C. J.; Yan, H. Directional Regulation of Enzyme Pathways through the Control of Substrate Channeling on a DNA Origami Scaffold. *Angew. Chem. Int. Ed.* **2016**, *128*, 7609–7612.

(141) Voigt, N. V.; Tørring, T.; Rotaru, A.; Jacobsen, M. F.; Ravnsbaek, J. B.; Subramani, R.; Mamdouh, W.; Kjems, J.; Mokhir, A.; Besenbacher, F. *et al.* Single-Molecule Chemical Reactions on DNA Origami. *Nat. Nanotechnol.* **2010**, *5*, 200–203.

(142) Shen, W.; Zhong, H.; Neff, D.; Norton, M. L. NTA Directed Protein Nanopatterning on DNA Origami Nanoconstructs. *J. Am. Chem. Soc.* **2009**, *131*, 6660–6661.

(143) Saccà, B.; Meyer, R.; Erkelenz, M.; Kiko, K.; Arndt, A.; Schroeder, H.; Rabe, K. S.; Niemeyer, C. M. Orthogonal Protein Decoration of DNA Origami. *Angew. Chem. Int. Ed.* **2010**, *49*, 9378–9383.

(144) Nguyen, T. M.; Nakata, E.; Saimura, M.; Dinh, H.; Morii, T. Design of Modular Protein Tags for Orthogonal Covalent Bond Formation at Specific DNA Sequences. *J. Am. Chem. Soc.* **2017**, *139*, 8487–8496.

(145) Song, J.; Arbona, J.-M.; Zhang, Z.; Liu, L.; Xie, E.; Elezgaray, J.; Aime, J.-P.; Gothelf, K. V.; Besenbacher, F.; Dong, M. Direct Visualization of Transient Thermal Response of a DNA Origami. *J. Am. Chem. Soc.* **2012**, *134*, 9844–9847.

(146) Suzuki, A.; Yamazaki, M.; Kobiki, Y. Direct Observation of Polymer Gel Surfaces by Atomic Force Microscopy. *J. Chem. Phys.* **1996**, *104*, 1751–1757.

(147) Pernodet, N.; Maaloum, M.; Tinland, B. Pore Size of Agarose Gels by Atomic Force Microscopy. *Electrophoresis* **1997**, *18*, 55–58.

(148) Wiedemair, J.; Serpe, M. J.; Kim, J.; Masson, J.-F.; Lyon, L. A.; Mizaikoff, B.; Kranz, C. In-Situ AFM Studies of the Phase-Transition Behavior of Single Thermoresponsive Hydrogel Particles. *Langmuir* **2007**, *23*, 130–137.

(149) de Almeida, P.; Jaspers, M.; Vaessen, S.; Tagit, O.; Portale, G.; Rowan, A. E.; Kouwer, P. H. J. Cytoskeletal Stiffening in Synthetic Hydrogels. *Nat. Commun.* **2019**, *10*, 609.

(150) Kim, S. H.; Opdahl, A.; Marmo, C.; Somorjai, G. A. AFM and SFG Studies of PHEMA-Based Hydrogel Contact Lens Surfaces in Saline Solution: Adhesion, Friction, and the Presence of Non-Crosslinked Polymer Chains at the Surface. *Biomaterials* **2002**, *23*, 1657–1666.

(151) Seidlits, S. K.; Khaing, Z. Z.; Petersen, R. R.; Nickels, J. D.; Vanscoy, J. E.; Shear, J. B.; Schmidt, C. E. The Effects of Hyaluronic Acid Hydrogels with Tunable Mechanical Properties on Neural Progenitor Cell Differentiation. *Biomaterials* **2010**, *31*, 3930–3940.

(152) Ouasti, S.; Donno, R.; Cellesi, F.; Sherratt, M. J.; Terenghi, G.; Tirelli, N. Network Connectivity, Mechanical Properties and Cell Adhesion for Hyaluronic Acid/PEG Hydrogels. *Biomaterials* **2011**, *32*, 6456–6470.

(153) Galluzzi, M.; Biswas, C. S.; Wu, Y.; Wang, Q.; Du, B.; Stadler, F. J. Space-Resolved Quantitative Mechanical Measurements of Soft and Supersoft Materials by Atomic Force Microscopy. *NPG Asia Mater.* **2016**, *8*, e327–e327.

(154) Aziz, A. H.; Wahlquist, J.; Sollner, A.; Ferguson, V.; DelRio, F. W.; Bryant, S. J. Mechanical Characterization of Sequentially Layered Photo-Clickable Thiol-Ene Hydrogels. *J. Mech. Behav. Biomed. Mater.* **2017**, *65*, 454–465.

(155) Rosales, A. M.; Vega, S. L.; DelRio, F. W.; Burdick, J. A.; Anseth, K. S. Hydrogels with Reversible Mechanics to Probe Dynamic Cell Microenvironments. *Angew. Chem. Int. Ed.* **2017**, *56*, 12132–12136.

(156) Garcia, R. Nanomechanical Mapping of Soft Materials with the Atomic Force Microscope: Methods, Theory and Applications. *Chem. Soc. Rev.* **2020**, *49*, 5850–5884.

(157) Ando, T.; Uchihashi, T.; Fukuma, T. High-Speed Atomic Force Microscopy for Nano-Visualization of Dynamic Biomolecular Processes. *Prog. Surf. Sci.* **2008**, *83*, 337–437.

(158) Ando, T.; Uchihashi, T.; Kodera, N.; Yamamoto, D.; Miyagi, A.; Taniguchi, M.; Yamashita, H. High-Speed AFM and Nano-Visualization of Biomolecular Processes. *Pflügers Arch. - Eur. J. Physiol.* **2008**, *456*, 211–225.

(159) Kodera, N.; Yamamoto, D.; Ishikawa, R.; Ando, T. Video Imaging of Walking Myosin V by High-Speed Atomic Force Microscopy. *Nature* **2010**, *468*, 72–76.

(160) Shibata, M.; Yamashita, H.; Uchihashi, T.; Kandori, H.; Ando, T. High-Speed Atomic Force Microscopy Shows Dynamic Molecular Processes in Photoactivated Bacteriorhodopsin. *Nat. Nanotechnol.* **2010**, *5*, 208–212.

(161) Fantner, G. E.; Barbero, R. J.; Gray, D. S.; Belcher, A. M. Kinetics of Antimicrobial Peptide Activity Measured on Individual Bacterial Cells Using High-Speed Atomic Force Microscopy. *Nat. Nanotechnol.* **2010**, *5*, 280–285.

(162) Uchihashi, T.; Iino, R.; Ando, T.; Noji, H. High-Speed Atomic Force Microscopy Reveals Rotary Catalysis of Rotorless F-ATPase. *Science* **2011**, *333*, 755–758.

(163) Suzuki, Y.; Sakai, N.; Yoshida, A.; Uekusa, Y.; Yagi, A.; Imaoka, Y.; Ito, S.; Karaki, K.; Takeyasu, K. High-Speed Atomic Force Microscopy Combined with Inverted Optical Microscopy for Studying Cellular Events. *Sci. Rep.* **2013**, *3*, 2131.

(164) Shibata, M.; Nishimasu, H.; Kodera, N.; Hirano, S.; Ando, T.; Uchihashi, T.; Nureki, O. Real-Space and Real-Time Dynamics of CRISPR-Cas9 Visualized by High-Speed Atomic Force Microscopy. *Nat. Commun.* **2017**, *8*, 1430.

(165) Miyagi, A.; Chipot, C.; Rangl, M.; Scheuring, S. High-Speed Atomic Force Microscopy Shows That Annexin V Stabilizes Membranes on the Second Timescale. *Nat. Nanotechnol.* **2016**, *11*, 783–790.

(166) Heath, G. R.; Scheuring, S. High-Speed AFM Height Spectroscopy Reveals Ms-Dynamics of Unlabeled Biomolecules. *Nat. Commun.* **2018**, *9*, 4983.

(167) Lin, Y.-C.; Chipot, C.; Scheuring, S. Annexin-V Stabilizes Membrane Defects by Inducing Lipid Phase Transition. *Nat. Commun.* **2020**, *11*, 1–13.

(168) Lizarbe, M. A.; Barrasa, J. I.; Olmo, N.; Gavilanes, F.; Turnay, J. Annexin-Phospholipid Interactions. Functional Implications. *Int. J. Mol. Sci.* **2013**, *14*, 2652–2683.

(169) Suzuki, Y.; Endo, M.; Yang, Y.; Sugiyama, H. Dynamic Assembly/Disassembly Processes of Photoresponsive DNA Origami Nanostructures Directly Visualized on a Lipid Membrane Surface. *J. Am. Chem. Soc.* **2014**, *136*, 1714–1717.

(170) Suzuki, Y.; Endo, M.; Sugiyama, H. Lipid-Bilayer-Assisted Two-Dimensional Self-Assembly of DNA Origami Nanostructures. *Nat. Commun.* **2015**, *6*, 8052.

(171) Ramakrishnan, S.; Shen, B.; Kostiainen, M. A.; Grundmeier, G.; Keller, A.; Linko, V. Real-Time Observation of Superstructure-Dependent DNA Origami Digestion by DNase I Using High-Speed Atomic Force Microscopy. *Chembiochem* **2019**, *20*, 2818–2823.

(172) Yamamoto, D.; Nagura, N.; Omote, S.; Taniguchi, M.; Ando, T. Streptavidin 2D Crystal Substrates for Visualizing Biomolecular Processes by Atomic Force Microscopy. *Biophys. J.* **2009**, *97*, 2358–2367.

(173) Milhiet, P.-E.; Yamamoto, D.; Berthoumieu, O.; Dosset, P.; Le Grimellec, C.; Verdier, J.-M.; Marchal, S.; Ando, T. Deciphering the Structure, Growth and Assembly of Amyloid-like Fibrils Using High-Speed Atomic Force Microscopy. *PLoS One* **2010**, *5*, e13240.

(174) Chiaruttini, N.; Redondo-Morata, L.; Colom, A.; Humbert, F.; Lenz, M.; Scheuring, S.; Roux, A. Relaxation of Loaded ESCRT-III Spiral Springs Drives Membrane Deformation. *Cell* **2015**, *163*, 866–879.

(175) Watanabe-Nakayama, T.; Ono, K.; Itami, M.; Takahashi, R.; Teplow, D. B.; Yamada, M. High-Speed Atomic Force Microscopy Reveals Structural Dynamics of Amyloid Β1-42 Aggregates. *Proc. Natl. Acad. Sci. U. S. A.* **2016**, *113*, 5835–5840.

(176) Tashiro, R.; Taguchi, H.; Hidaka, K.; Endo, M.; Sugiyama, H. Effects of Physical Damage in the Intermediate Phase on the Progression of Amyloid β Fibrillization. *Chem. Asian J.* **2019**, *14*, 4140–4145.

(177) Owa, M.; Uchihashi, T.; Yanagisawa, H.-A.; Yamano, T.; Iguchi, H.; Fukuzawa, H.; Wakabayashi, K.-I.; Ando, T.; Kikkawa, M. Inner Lumen Proteins Stabilize Doublet Microtubules in Cilia and Flagella. *Nat. Commun.* **2019**, *10*, 1143.

(178) Jiao, F.; Cannon, K. S.; Lin, Y.-C.; Gladfelter, A. S.; Scheuring, S. The Hierarchical Assembly of Septins Revealed by High-Speed AFM. *Nat. Commun.* **2020**, *11*, 5062.

(179) Pollard, T. D.; Borisy, G. G. Cellular Motility Driven by Assembly and Disassembly of Actin Filaments. *Cell* **2003**, *112*, 453–465.

(180) Fujiwara, I.; Takahashi, S.; Tadakuma, H.; Funatsu, T.; Ishiwata, S. Microscopic Analysis of Polymerization Dynamics with Individual Actin Filaments. *Nat. Cell Biol.* **2002**, *4*, 666–673.

(181) Kuhn, J. R.; Pollard, T. D. Real-Time Measurements of Actin Filament Polymerization by Total Internal Reflection Fluorescence Microscopy. *Biophys. J.* **2005**, *88*, 1387–1402.

(182) Czajkowsky, D. M.; Shao, Z. Inhibition of Protein Adsorption to Muscovite Mica by Monovalent Cations. *J. Microsc.* **2003**, *211*, 1–7.

(183) Ogi, S.; Sugiyasu, K.; Manna, S.; Samitsu, S.; Takeuchi, M. Living Supramolecular Polymerization Realized through a Biomimetic Approach. *Nat. Chem.* **2014**, *6*, 188–195.

(184) Carnall, J. M. A.; Waudby, C. A.; Belenguer, A. M.; Stuart, M. C. A.; Peyralans, J. J.-P.; Otto, S. Mechanosensitive Self-Replication Driven by Self-Organization. *Science* **2010**, *327*, 1502–1506.

(185) Colomb-Delsuc, M.; Mattia, E.; Sadownik, J. W.; Otto, S. Exponential Self-Replication Enabled through a Fibre Elongation/Breakage Mechanism. *Nat. Commun.* **2015**, *6*, 7427.

(186) Hell, S .W.; Wichmann, J. Breaking the Diffraction Resolution Limit by Stimulated Emission: Stimulated-Emission-Depletion Fluorescence Microscopy. *Opt. Lett.* **1994**, *19*, 780–782.

(187) Eggeling, C.; Willig, K. I.; Sahl, S. J.; Hell, S. W. Lens-Based Fluorescence Nanoscopy. *Q. Rev. Biophys.* **2015**, *48*, 178–243.

(188) Blom, H.; Widengren, J. Stimulated Emission Depletion Microscopy. *Chem. Rev.* **2017**, *117*, 7377–7427.

(189) Betzig, E.; Patterson, G. H.; Sougrat, R.; Lindwasser, O. W.; Olenych, S.; Bonifacino, J. S.; Davidson, M. W.; Lippincott-Schwartz, J.; Hess, H. F. Imaging Intracellular Fluorescent Proteins at Nanometer Resolution. *Science* **2006**, *313*, 1642–1645.

(190) Rust, M. J.; Bates, M.; Zhuang, X. Sub-Diffraction-Limit Imaging by Stochastic Optical Reconstruction Microscopy (STORM). *Nat. Methods* **2006**, *3*, 793–795.

(191) Sauer, M.; Heilemann, M. Single-Molecule Localization Microscopy in Eukaryotes. *Chem. Rev.* **2017**, *117*, 7478–7509.

(192) von Diezmann, A.; Shechtman, Y.; Moerner, W. E. Three-Dimensional Localization of Single Molecules for Super-Resolution Imaging and Single-Particle Tracking. *Chem. Rev.* **2017**, *117*, 7244–7275.

(193) Guerra, J. M. Super-resolution through Illumination by Diffraction-born Evanescent Waves. *Appl. Phys. Lett.* **1995**, *66*, 3555−3557.

(194) Heintzmann, R.; Huser, T. Super-Resolution Structured Illumination Microscopy. *Chem. Rev.* **2017**, *117*, 13890–13908.

(195) Wu, Y.; Shroff, H. Faster, Sharper, and Deeper: Structured Illumination Microscopy for Biological Imaging. *Nat. Methods* **2018**, *15*, 1011–1019.

(196) Pujals, S.; Feiner-Gracia, N.; Delcanale, P.; Voets, I.; Albertazzi, L. Super-Resolution Microscopy as a Powerful Tool to Study Complex Synthetic Materials. *Nat. Rev. Chem.* **2019**, *3*, 68–84.

(197) Schermelleh, L.; Ferrand, A.; Huser, T.; Eggeling, C.; Sauer, M.; Biehlmaier, O.; Drummen, G. P. C. Super-Resolution Microscopy Demystified. *Nat. Cell Biol.* **2019**, *21*, 72–84.

(198) Sahl, S. J.; Hell, S. W.; Jakobs, S. Fluorescence Nanoscopy in Cell Biology. *Nat. Rev. Mol. Cell Biol.* **2017**, *18*, 685–701.

(199) Donath, E.; Sukhorukov, G. B.; Caruso, F.; Davis, S. A.; Möhwald, H. Novel Hollow Polymer Shells by Colloid-Templated Assembly of Polyelectrolytes. *Angew. Chem. Int. Ed.* **1998**, *37*, 2202–2205.

(200) Ilhan, F.; Galow, T. H.; Gray, M.; Clavier, G.; Rotello, V. M. Giant Vesicle Formation through Self-Assembly of Complementary Random Copolymers. *J. Am. Chem. Soc.* **2000**, *122*, 5895–5896.

(201) Bellomo, E. G.; Wyrsta, M. D.; Pakstis, L.; Pochan, D. J.; Deming, T. J. Stimuli-Responsive Polypeptide Vesicles by Conformation-Specific Assembly. *Nat. Mater.* **2004**, *3*, 244–248.

(202) Hirokawa, Y.; Jinnai, H.; Nishikawa, Y.; Okamoto, T.; Hashimoto, T. Direct Observation of Internal Structures in Poly(*N*-Isopropylacrylamide) Chemical Gels. *Macromolecules* **1999**, *32*, 7093–7099.

(203) Kiriya, D.; Ikeda, M.; Onoe, H.; Takinoue, M.; Komatsu, H.; Shimoyama, Y.; Hamachi, I.; Takeuchi, S. Meter-Long and Robust Supramolecular Strands Encapsulated in Hydrogel Jackets. *Angew. Chem. Int. Ed.* **2012**, *51*, 1553–1557.

(204) Russ, N.; Zielbauer, B. I.; Koynov, K.; Vilgis, T. A. Influence of Nongelling Hydrocolloids on the Gelation of Agarose. *Biomacromolecules* **2013**, *14*, 4116–4124.

(205) Chaudhuri, O.; Koshy, S. T.; Branco da Cunha, C.; Shin, J.-W.; Verbeke, C. S.; Allison, K. H.; Mooney, D. J. Extracellular Matrix Stiffness and Composition Jointly Regulate the Induction of Malignant Phenotypes in Mammary Epithelium. *Nat. Mater.* **2014**, *13*, 970–978.

(206) Fan, J.; Zou, J.; He, X.; Zhang, F.; Zhang, S.; Raymond, J. E.; Wooley, K. L. Tunable Mechano-Responsive Organogels by Ring-Opening Copolymerizations of *N*-Carboxyanhydrides. *Chem. Sci.* **2014**, *5*, 141–150.

(207) Lovrak, M.; Hendriksen, W. E. J.; Maity, C.; Mytnyk, S.; van Steijn, V.; Eelkema, R.; van Esch, J. H. Free-Standing Supramolecular Hydrogel Objects by Reaction-Diffusion. *Nat. Commun.* **2017**, *8*, 15317.

(208) Shigemitsu, H.; Kubota, R.; Nakamura, K.; Matsuzaki, T.; Minami, S.; Aoyama, T.; Urayama, K.; Hamachi, I. Protein-Responsive Protein Release of Supramolecular/Polymer Hydrogel Composite Integrating Enzyme Activation Systems. *Nat. Commun.* **2020**, *11*, 3859.

(209) Nowak, A. P.; Breedveld, V.; Pakstis, L.; Ozbas, B.; Pine, D. J.; Pochan, D.; Deming, T. J. Rapidly Recovering Hydrogel Scaffolds from Self-Assembling Diblock Copolypeptide Amphiphiles. *Nature* **2002**, *417*, 424–428.

(210) Schneider, J. P.; Pochan, D. J.; Ozbas, B.; Rajagopal, K.; Pakstis, L.; Kretsinger, J. Responsive Hydrogels from the Intramolecular Folding and Self-Assembly of a Designed Peptide. *J. Am. Chem. Soc.* **2002**, *124*, 15030–15037.

(211) Kiyonaka, S.; Sugiyasu, K.; Shinkai, S.; Hamachi, I. First Thermally Responsive Supramolecular Polymer Based on Glycosylated Amino Acid. *J. Am. Chem. Soc.* **2002**, *124*, 10954–10955.

(212) Kazantsev, R. V.; Dannenhoffer, A. J.; Weingarten, A. S.; Phelan, B. T.; Harutyunyan, B.; Aytun, T.; Narayanan, A.; Fairfield, D. J.; Boekhoven, J.; Sai, H. *et al.* Crystal-Phase Transitions and Photocatalysis in SupramolecularScaffolds. *J. Am. Chem. Soc.* **2017**, *139*, 6120─6127.

(213) Frusawa, H.; Fukagawa, A.; Ikeda, Y.; Araki, J.; Ito, K.; John, G.; Shimizu, T. Aligning a Single-Lipid Nanotube with Moderate Stiffness. *Angew. Chem. Int. Ed.* **2003**, *42*, 72–74.

(214) Kiyonaka, S.; Sada, K.; Yoshimura, I.; Shinkai, S.; Kato, N.; Hamachi, I. Semi-Wet Peptide/Protein Array Using Supramolecular Hydrogel. *Nat. Mater.* **2004**, *3*, 58–64.

(215) Smith, A. M.; Acquah, S. F. A.; Bone, N.; Kroto, H. W.; Ryadnov, M. G.; Stevens, M. S. P.; Walton, D. R. M.; Woolfson, D. N. Polar Assembly in a Designed Protein Fiber. *Angew. Chem. Int. Ed.* **2004**, *44*, 325–328.

(216) Sugiyasu, K.; Fujita, N.; Shinkai, S. Visible-Light-Harvesting Organogel Composed of Cholesterol-Based Perylene Derivatives. *Angew. Chem. Int. Ed.* **2004**, *43*, 1229–1233.

(217) Zhou, S.-L.; Matsumoto, S.; Tian, H.-D.; Yamane, H.; Ojida, A.; Kiyonaka, S.; Hamachi, I. pH-Responsive Shrinkage/Swelling of a Supramolecular Hydrogel Composed of Two Small Amphiphilic Molecules. *Chem. Eur. J.* **2005**, *11*, 1130–1136.

(218) Yamaguchi, S.; Yoshimura, I.; Kohira, T.; Tamaru, S.-I.; Hamachi, I. Cooperation between Artificial Receptors and Supramolecular Hydrogels for Sensing and Discriminating Phosphate Derivatives. *J. Am. Chem. Soc.* **2005**, *127*, 11835–11841.

(219) Tamaru, S.-I.; Kiyonaka, S.; Hamachi, I. Three Distinct Read-out Modes for Enzyme Activity Can Operate in a Semi-Wet Supramolecular Hydrogel. *Chem. Eur. J* **2005**, *11*, 7294–7304.

(220) Del Guerzo, A.; Olive, A. G. L.; Reichwagen, J.; Hopf, H.; Desvergne, J.-P. Energy Transfer in Self-Assembled [N]-Acene Fibers Involving > or =100 Donors per Acceptor. *J. Am. Chem. Soc.* **2005**, *127*, 17984−17985.

(221) Koshi, Y.; Nakata, E.; Yamane, H.; Hamachi, I. A Fluorescent Lectin Array Using Supramolecular Hydrogel for Simple Detection and Pattern Profiling for Various Glycoconjugates. *J. Am. Chem. Soc.* **2006**, *128*, 10413–10422.

(222) Behanna, H. A.; Rajangam, K.; Stupp, S. I. Modulation of Fluorescence through Coassembly of Molecules in Organic Nanostructures. *J. Am. Chem. Soc.* **2007**, *129*, 321–327.

(223) Matsumoto, S.; Yamaguchi, S.; Wada, A.; Matsui, T.; Ikeda, M.; Hamachi, I. Photo-Responsive Gel Droplet as a Nano- or Pico-Litre Container Comprising a Supramolecular Hydrogel. *Chem. Commun.* **2008**, 1545–1547.

(224) Yuen, M.-Y.; Roy, V. A. L.; Lu, W.; Kui, S. C. F.; Tong, G. S. M.; So, M.-H.; Chui, S. S.-Y.; Muccini, M.; Ning, J. Q.; Xu, S. J. *et al.* Semiconducting and Electroluminescent

Nanowires Self-Assembled from Organoplatinum(II) Complexes. *Angew. Chem. Int. Ed.* **2008**, *47*, 9895–9899.

(225) Wang, C.; Yin, S.; Chen, S.; Xu, H.; Wang, Z.; Zhang, X. Controlled Self-Assembly Manipulated by Charge-Transfer Interactions: From Tubes to Vesicles. *Angew. Chem. Int. Ed.* **2008**, *47*, 9049–9052.

(226) Ikeda, M.; Ueno, S.; Matsumoto, S.; Shimizu, Y.; Komatsu, H.; Kusumoto, K.-I.; Hamachi, I. Three-Dimensional Encapsulation of Live Cells by Using a Hybrid Matrix of Nanoparticles in a Supramolecular Hydrogel. *Chem. Eur. J.* **2008**, *14*, 10808–10815.

(227) Wada, A.; Tamaru, S.-I.; Ikeda, M.; Hamachi, I. MCM-Enzyme-Supramolecular Hydrogel Hybrid as a Fluorescence Sensing Material for Polyanions of Biological Significance. *J. Am. Chem. Soc.* **2009**, *131*, 5321–5330.

(228) Diring, S.; Camerel, F.; Donnio, B.; Dintzer, T.; Toffanin, S.; Capelli, R.; Muccini, M.; Ziessel, R. Luminescent Ethynyl-Pyrene Liquid Crystals and Gels for Optoelectronic Devices. *J. Am. Chem. Soc.* **2009**, *131*, 18177–18185.

(229) Tamaru, S.-I.; Ikeda, M.; Shimidzu, Y.; Matsumoto, S.; Takeuchi, S.; Hamachi, I. Fluidic Supramolecular Nano- and Microfibres as Molecular Rails for Regulated Movement of Nanosubstances. *Nat. Commun.* **2010**, *1*, 20.

(230) Johnson, E. K.; Adams, D. J.; Cameron, P. J. Directed Self-Assembly of Dipeptides to Form Ultrathin Hydrogel Membranes. *J. Am. Chem. Soc.* **2010**, *132*, 5130–5136.

(231) Huang, M.; Schilde, U.; Kumke, M.; Antonietti, M.; Cölfen, H. Polymer-Induced Self-Assembly of Small Organic Molecules into Ultralong Microbelts with Electronic Conductivity. *J. Am. Chem. Soc.* **2010**, *132*, 3700–3707.

(232) Ikeda, M.; Tanida, T.; Yoshii, T.; Hamachi, I. Rational Molecular Design of Stimulus-Responsive Supramolecular Hydrogels Based on Dipeptides. *Adv. Mater.* **2011**, *23*, 2819–2822.

(233) Ikeda, M.; Yoshii, T.; Matsui, T.; Tanida, T.; Komatsu, H.; Hamachi, I. Montmorillonite-Supramolecular Hydrogel Hybrid for Fluorocolorimetric Sensing of Polyamines. *J. Am. Chem. Soc.* **2011**, *133*, 1670–1673.

(234) Komatsu, H.; Tsukiji, S.; Ikeda, M.; Hamachi, I. Stiff, Multistimuli-Responsive Supramolecular Hydrogels as Unique Molds for 2D/3D Microarchitectures of Live Cells. *Chem. Asian J.* **2011**, *6*, 2368–2375.

(235) Po, C.; Tam, A. Y.-Y.; Wong, K. M.-C.; Yam, V. W.-W. Supramolecular Self-Assembly of Amphiphilic Anionic Platinum(II) Complexes: A Correlation between Spectroscopic and Morphological Properties. *J. Am. Chem. Soc.* **2011**, *133*, 12136–12143.

(236) Coleman, A. C.; Beierle, J. M.; Stuart, M. C. A.; Maciá, B.; Caroli, G.; Mika, J. T.; van Dijken, D. J.; Chen, J.; Browne, W. R.; Feringa, B. L. Light-Induced Disassembly of Self-Assembled Vesicle-Capped Nanotubes Observed in Real Time. *Nat. Nanotechnol.* **2011**, *6*, 547–552.

(237) Strassert, C. A.; Chien, C.-H.; Galvez Lopez, M. D.; Kourkoulos, D.; Hertel, D.; Meerholz, K.; De Cola, L. Switching On Luminescence by the Self-Assembly of a Platinum(II) Complex into Gelating Nanofibers and Electroluminescent Films. *Angew. Chem. Int. Ed.* **2011**, *50*, 946–950.

(238) Giansante, C.; Raffy, G.; Schäfer, C.; Rahma, H.; Kao, M.-T.; Olive, A. G. L.; Del Guerzo, A. White-Light-Emitting Self-Assembled Nanofibers and Their Evidence by Microspectroscopy of Individual Objects. *J. Am. Chem. Soc.* **2011**, *133*, 316–325.

(239) Di Maria, F.; Olivelli, P.; Gazzano, M.; Zanelli, A.; Biasiucci, M.; Gigli, G.; Gentili, D.; D'Angelo, P.; Cavallini, M.; Barbarella, G. A Successful Chemical Strategy to Induce Oligothiophene Self-Assembly into Fibers with Tunable Shape and Function. *J. Am. Chem. Soc.* **2011**, *133*, 8654–8661.

(240) Boekhoven, J.; Koot, M.; Wezendonk, T. A.; Eelkema, R.; van Esch, J. H. A Self-Assembled Delivery Platform with Post-Production Tunable Release Rate. *J. Am. Chem. Soc.* **2012**, *134*, 12908–12911.

(241) Wang, M.; Mohebbi, A. R.; Sun, Y.; Wudl, F. Ribbons, Vesicles, and Baskets: Supramolecular Assembly of a Coil-Plate-Coil Emeraldicene Derivative. *Angew. Chem. Int. Ed.* **2012**, *51*, 6920–6924.

(242) Pati, D.; Kalva, N.; Das, S.; Kumaraswamy, G.; Sen Gupta, S.; Ambade, A. V. Multiple Topologies from Glycopolypeptide-Dendron Conjugate Self-Assembly: Nanorods, Micelles, and Organogels. *J. Am. Chem. Soc.* **2012**, *134*, 7796–7802.

(243) Ren, Y.; Kan, W. H.; Thangadurai, V.; Baumgartner, T. Bio-Inspired Phosphole-Lipids: From Highly Fluorescent Organogels to Mechanically Responsive FRET. *Angew. Chem. Int. Ed.* **2012**, *51*, 3964–3968.

(244) Kieltyka, R. E.; Pape, A. C. H.; Albertazzi, L.; Nakano, Y.; Bastings, M. M. C.; Voets, I. K.; Dankers, P. Y. W.; Meijer, E. W. Mesoscale Modulation of Supramolecular Ureidopyrimidinone-Based Poly(Ethylene Glycol) Transient Networks in Water. *J. Am. Chem. Soc.* **2013**, *135*, 11159–11164.

(245) Boekhoven, J.; Poolman, J. M.; Maity, C.; Li, F.; van der Mee, L.; Minkenberg, C. B.; Mendes, E.; van Esch, J. H.; Eelkema, R. Catalytic Control over Supramolecular Gel Formation. *Nat. Chem.* **2013**, *5*, 433–437.

(246) Lei, Y. L.; Liao, L. S.; Lee, S. T. Selective Growth of Dual-Color-Emitting Heterogeneous Microdumbbells Composed of Organic Charge-Transfer Complexes. *J. Am. Chem. Soc.* **2013**, *135*, 3744–3747.

(247) Albertazzi, L.; Martinez-Veracoechea, F. J.; Leenders, C. M. A.; Voets, I. K.; Frenkel, D.; Meijer, E. W. Spatiotemporal Control and Superselectivity in Supramolecular Polymers Using Multivalency. *Proc. Natl. Acad. Sci. U. S. A.* **2013**, *110*, 12203–12208.

(248) Yoshii, T.; Ikeda, M.; Hamachi, I. Two-Photon-Responsive Supramolecular Hydrogel for Controlling Materials Motion in Micrometer Space. *Angew. Chem. Int. Ed.* **2014**, *53*, 7264–7267.

(249) Ikeda, M.; Tanida, T.; Yoshii, T.; Kurotani, K.; Onogi, S.; Urayama, K.; Hamachi, I. Installing Logic-Gate Responses to a Variety of Biological Substances in Supramolecular Hydrogel-Enzyme Hybrids. *Nat. Chem.* **2014**, *6*, 511–518.

(250) Olive, A. G. L.; Abdullah, N. H.; Ziemecka, I.; Mendes, E.; Eelkema, R.; van Esch, J. H. Spatial and Directional Control over Self-Assembly Using Catalytic Micropatterned Surfaces. *Angew. Chem. Int. Ed.* **2014**, *126*, 4216–4220.

(251) Albertazzi, L.; van der Zwaag, D.; Leenders, C. M. A.; Fitzner, R.; van der Hofstad, R. W.; Meijer, E. W. Probing Exchange Pathways in One-Dimensional Aggregates with Super-Resolution Microscopy. *Science* **2014**, *344*, 491–495.

(252) Kong, Q.; Liao, Q.; Xu, Z.; Wang, X.; Yao, J.; Fu, H. Epitaxial Self-Assembly of Binary Molecular Components into Branched Nanowire Heterostructures for Photonic Applications. *J. Am. Chem. Soc.* **2014**, *136*, 2382–2388.

(253) Boekhoven, J.; Hendriksen, W. E.; Koper, G. J. M.; Eelkema, R.; van Esch, J. H. Transient Assembly of Active Materials Fueled by a Chemical Reaction. *Science* **2015**, *349*, 1075–1079.

(254) Maity, C.; Hendriksen, W. E.; van Esch, J. H.; Eelkema, R. Spatial Structuring of a Supramolecular Hydrogel by Using a Visible-Light Triggered Catalyst. *Angew. Chem. Int. Ed.* **2015**, *54*, 998–1001.

(255) Bertolani, A.; Pirrie, L.; Stefan, L.; Houbenov, N.; Haataja, J. S.; Catalano, L.; Terraneo, G.; Giancane, G.; Valli, L.; Milani, R. *et al.* Supramolecular Amplification of Amyloid Self-Assembly by Iodination. *Nat. Commun.* **2015**, *6*, 7574.

(256) Vigier-Carrière, C.; Garnier, T.; Wagner, D.; Lavalle, P.; Rabineau, M.; Hemmerlé, J.; Senger, B.; Schaaf, P.; Boulmedais, F.; Jierry, L. Bioactive Seed Layer for Surface-Confined Self-Assembly of Peptides. *Angew. Chem. Int. Ed.* **2015**, *54*, 10198–10201.

(257) Liu, K.; Xing, R.; Chen, C.; Shen, G.; Yan, L.; Zou, Q.; Ma, G.; Möhwald, H.; Yan, X. Peptide-Induced Hierarchical Long-Range Order and Photocatalytic Activity of Porphyrin Assemblies. *Angew. Chem. Int. Ed.* **2015**, *54*, 500–505.

(258) López-Andarias, J.; Rodriguez, M. J.; Atienza, C.; López, J. L.; Mikie, T.; Casado, S.; Seki, S.; Carrascosa, J. L.; Martín, N. Highly Ordered n/p-Co-Assembled Materials with Remarkable Charge Mobilities. *J. Am. Chem. Soc.* **2015**, *137*, 893–897.

(259) Baker, M. B.; Albertazzi, L.; Voets, I. K.; Leenders, C. M. A.; Palmans, A. R. A.; Pavan, G. M.; Meijer, E. W. Consequences of Chirality on the Dynamics of a Water-Soluble Supramolecular Polymer. *Nat. Commun.* **2015**, *6*, 6234.

(260) Onogi, S.; Shigemitsu, H.; Yoshii, T.; Tanida, T.; Ikeda, M.; Kubota, R.; Hamachi, I. In Situ Real-Time Imaging of Self-Sorted Supramolecular Nanofibres. *Nat. Chem.* **2016**, *8*, 743–752.

(261) da Silva, R. M. P.; van der Zwaag, D.; Albertazzi, L.; Lee, S. S.; Meijer, E. W.; Stupp, S. I. Super-Resolution Microscopy Reveals Structural Diversity in Molecular Exchange among Peptide Amphiphile Nanofibres. *Nat. Commun.* **2016**, *7*, 11561.

(262) Beuwer, M. A.; Knopper, M. F.; Albertazzi, L.; van der Zwaag, D.; Ellenbroek, W. G.; Meijer, E. W.; Prins, M. W. J.; Zijlstra, P. Mechanical Properties of Single Supramolecular Polymers from Correlative AFM and Fluorescence Microscopy. *Polym. Chem.* **2016**, *7*, 7260–7268.

(263) Aloi, A.; Vilanova, N.; Albertazzi, L.; Voets, I. K. iPAINT: A General Approach Tailored to Image the Topology of Interfaces with Nanometer Resolution. *Nanoscale* **2016**, *8*, 8712–8716.

(264) Guterman, T.; Kornreich, M.; Stern, A.; Adler-Abramovich, L.; Porath, D.; Beck, R.; Shimon, L. J. W.; Gazit, E. Formation of Bacterial Pilus-like Nanofibres by Designed Minimalistic Self-Assembling Peptides. *Nat. Commun.* **2016**, *7*, 13482.

(265) Aliprandi, A.; Mauro, M.; De Cola, L. Controlling and Imaging Biomimetic Self-Assembly. *Nat. Chem.* **2016**, *8*, 10–15.

(266) Baker, M. B.; Gosens, R. P. J.; Albertazzi, L.; Matsumoto, N. M.; Palmans, A. R. A.; Meijer, E. W. Exposing Differences in Monomer Exchange Rates of Multicomponent Supramolecular Polymers in Water. *Chembiochem* **2016**, *17*, 207–213.

(267) Singh, N.; Maity, C.; Zhang, K.; Angulo-Pachón, C. A.; van Esch, J. H.; Eelkema, R.; Escuder, B. Synthesis of a Double-Network Supramolecular Hydrogel by Having One Network Catalyse the Formation of the Second. *Chem. Eur. J.* **2017**, *23*, 2018–2021.

(268) Noteborn, W. E. M.; Zwagerman, D. N. H.; Talens, V. S.; Maity, C.; van der Mee, L.; Poolman, J. M.; Mytnyk, S.; van Esch, J. H.; Kros, A.; Eelkema, R. *et al.* Crosslinker-Induced Effects on the Gelation Pathway of a Low Molecular Weight Hydrogel. *Adv. Mater.* **2017**, *29*, 1603769.

(269) Mytnyk, S.; Olive, A. G. L.; Versluis, F.; Poolman, J. M.; Mendes, E.; Eelkema, R.; van Esch, J. H. Compartmentalizing Supramolecular Hydrogels Using Aqueous Multi-Phase Systems. *Angew. Chem. Int. Ed.* **2017**, *56*, 14923–14927.

(270) Tena-Solsona, M.; Rieß, B.; Grötsch, R. K.; Löhrer, F. C.; Wanzke, C.; Käsdorf, B.; Bausch, A. R.; Müller-Buschbaum, P.; Lieleg, O.; Boekhoven, J. Non-Equilibrium Dissipative Supramolecular Materials with a Tunable Lifetime. *Nat. Commun.* **2017**, *8*, 15895.

(271) Fukui, T.; Kawai, S.; Fujinuma, S.; Matsushita, Y.; Yasuda, T.; Sakurai, T.; Seki, S.; Takeuchi, M.; Sugiyasu, K. Control over Differentiation of a Metastable Supramolecular Assembly in One and Two Dimensions. *Nat. Chem.* **2017**, *9*, 493–499.

(272) Tsuzuki, T.; Kabumoto, M.; Arakawa, H.; Ikeda, M. The Effect of Carbohydrate Structures on the Hydrogelation Ability and Morphology of Self-Assembled Structures of Peptide-Carbohydrate Conjugates in Water. *Org. Biomol. Chem.* **2017**, *15*, 4595–4600.

(273) Hendrikse, S. I. S.; Wijnands, S. P. W.; Lafleur, R. P. M.; Pouderoijen, M. J.; Janssen, H. M.; Dankers, P. Y. W.; Meijer, E. W. Controlling and Tuning the Dynamic Nature of Supramolecular Polymers in Aqueous Solutions. *Chem. Commun.* **2017**, *53*, 2279–2282.

(274) Nishida, Y.; Tanaka, A.; Yamamoto, S.; Tominaga, Y.; Kunikata, N.; Mizuhata, M.; Maruyama, T. In Situ Synthesis of a Supramolecular Hydrogelator at an Oil/Water Interface for Stabilization and Stimuli-Induced Fusion of Microdroplets. *Angew. Chem. Int. Ed.* **2017**, *56*, 9410–9414.

(275) Liu, Y.; Peng, C.; Xiong, W.; Zhang, Y.; Gong, Y.; Che, Y.; Zhao, J. Two-Dimensional Seeded Self-Assembly of a Complex Hierarchical Perylene-Based Heterostructure. *Angew. Chem. Int. Ed.* **2017**, *56*, 11380–11384.

(276) Gorai, T.; Maitra, U. Luminescence Resonance Energy Transfer in a Multiple-Component, Self-Assembled Supramolecular Hydrogel. *Angew. Chem. Int. Ed.* **2017**, *56*, 10730–10734.

(277) Pujals, S.; Tao, K.; Terradellas, A.; Gazit, E.; Albertazzi, L. Studying Structure and Dynamics of Self-Assembled Peptide Nanostructures Using Fluorescence and Super Resolution Microscopy. *Chem. Commun.* **2017**, *53*, 7294–7297.

(278) Yang, S.; Shin, S.; Choi, I.; Lee, J.; Choi, T.-L. Direct Formation of Large-Area 2D Nanosheets from Fluorescent Semiconducting Homopolymer with Orthorhombic Crystalline Orientation. *J. Am. Chem. Soc.* **2017**, *139*, 3082–3088.

(279) Goto, T.; Okazaki, Y.; Ueki, M.; Kuwahara, Y.; Takafuji, M.; Oda, R.; Ihara, H. Induction of Strong and Tunable Circularly Polarized Luminescence of Nonchiral, Nonmetal, Low-Molecular-Weight Fluorophores Using Chiral Nanotemplates. *Angew. Chem. Int. Ed.* **2017**, *56*, 2989–2993.

(280) Kazantsev, R. V.; Dannenhoffer, A. J.; Weingarten, A. S.; Phelan, B. T.; Harutyunyan, B.; Aytun, T.; Narayanan, A.; Fairfield, D. J.; Boekhoven, J.; Sai, H. *et al.* Crystal-Phase Transitions and Photocatalysis in Supramolecular Scaffolds. *J. Am. Chem. Soc.* **2017**, *139*, 6120–6127.

(281) Yang, D.; Duan, P.; Zhang, L.; Liu, M. Chirality and Energy Transfer Amplified Circularly Polarized Luminescence in Composite Nanohelix. *Nat. Commun.* **2017**, *8*, 15727.

(282) Sarkar, A.; Dhiman, S.; Chalishazar, A.; George, S. J. Visualization of Stereoselective Supramolecular Polymers by Chirality-Controlled Energy Transfer. *Angew. Chem. Int. Ed.* **2017**, *56*, 13767–13771.

(283) Lee, S. S.; Fyrner, T.; Chen, F.; Álvarez, Z.; Sleep, E.; Chun, D. S.; Weiner, J. A.; Cook, R. W.; Freshman, R. D.; Schallmo, M. S. *et al.* Sulfated Glycopeptide Nanostructures for Multipotent Protein Activation. *Nat. Nanotechnol.* **2017**, *12*, 821–829.

(284) Shigemitsu, H.; Fujisaku, T.; Tanaka, W.; Kubota, R.; Minami, S.; Urayama, K.; Hamachi, I. An Adaptive Supramolecular Hydrogel Comprising Self-Sorting Double Nanofibre Networks. *Nat. Nanotechnol.* **2018**, *13*, 165–172.

(285) Kubota, R.; Liu, S.; Shigemitsu, H.; Nakamura, K.; Tanaka, W.; Ikeda, M.; Hamachi, I. Imaging-Based Study on Control Factors over Self-Sorting of Supramolecular Nanofibers Formed from Peptide- and Lipid-Type Hydrogelators. *Bioconjug. Chem.* **2018**, *29*, 2058–2067.

(286) Wang, Y.; Versluis, F.; Oldenhof, S.; Lakshminarayanan, V.; Zhang, K.; Wang, Y.; Wang, J.; Eelkema, R.; Guo, X.; van Esch, J. H. Directed Nanoscale Self-Assembly of Low Molecular Weight Hydrogelators Using Catalytic Nanoparticles. *Adv. Mater.* **2018**, *30*, e1707408.

(287) Panja, S.; Adams, D. J. Maintaining Homogeneity during a Sol-Gel Transition by an Autocatalytic Enzyme Reaction. *Chem. Commun.* **2018**, *55*, 47–50.

(288) Adelizzi, B.; Aloi, A.; Markvoort, A. J.; Ten Eikelder, H. M. M.; Voets, I. K.; Palmans, A. R. A.; Meijer, E. W. Supramolecular Block Copolymers under Thermodynamic Control. *J. Am. Chem. Soc.* **2018**, *140*, 7168–7175.

(289) Adelizzi, B.; Aloi, A.; Van Zee, N. J.; Palmans, A. R. A.; Meijer, E. W.; Voets, I. K. Painting Supramolecular Polymers in Organic Solvents by Super-Resolution Microscopy. *ACS Nano* **2018**, *12*, 4431–4439.

(290) Spitzer, D.; Marichez, V.; Formon, G. J. M.; Besenius, P.; Hermans, T. M. Surface-Assisted Self-Assembly of a Hydrogel by Proton Diffusion. *Angew. Chem. Int. Ed.* **2018**, *57*, 11349–11353.

(291) Chin, S. M.; Synatschke, C. V.; Liu, S.; Nap, R. J.; Sather, N. A.; Wang, Q.; Álvarez, Z.; Edelbrock, A. N.; Fyrner, T.; Palmer, L. C. *et al.* Covalent-Supramolecular Hybrid Polymers as Muscle-Inspired Anisotropic Actuators. *Nat. Commun.* **2018**, *9*, 2395.

(292) Kumar, M.; Ing, N. L.; Narang, V.; Wijerathne, N. K.; Hochbaum, A. I.; Ulijn, R. V. Amino-Acid-Encoded Biocatalytic Self-Assembly Enables the Formation of Transient Conducting Nanostructures. *Nat. Chem.* **2018**, *10*, 696–703.

(293) Wong, V. C.-H.; Po, C.; Leung, S. Y.-L.; Chan, A. K.-W.; Yang, S.; Zhu, B.; Cui, X.; Yam, V. W.-W. Formation of 1D Infinite Chains Directed by Metal-Metal and/or π-π Stacking Interactions of Water-Soluble Platinum(II) 2,6-Bis(Benzimidazol-2'-yl)Pyridine Double Complex Salts. *J. Am. Chem. Soc.* **2018**, *140*, 657–666.

(294) Tanaka, W.; Shigemitsu, H.; Fujisaku, T.; Kubota, R.; Minami, S.; Urayama, K.; Hamachi, I. Post-Assembly Fabrication of a Functional Multicomponent Supramolecular Hydrogel Based on a Self-Sorting Double Network. *J. Am. Chem. Soc.* **2019**, *141*, 4997–5004.

(295) Wang, Y.; de Kruijff, R. M.; Lovrak, M.; Guo, X.; Eelkema, R.; van Esch, J. H. Access to Metastable Gel States Using Seeded Self-Assembly of Low-Molecular-Weight Gelators. *Angew. Chem. Int. Ed.* **2019**, *58*, 3800–3803.

(296) Wang, Y.; Lovrak, M.; Liu, Q.; Maity, C.; le Sage, V. A. A.; Guo, X.; Eelkema, R.; van Esch, J. H. Hierarchically Compartmentalized Supramolecular Gels through Multilevel Self-Sorting. *J. Am. Chem. Soc.* **2019**, *141*, 2847–2851.

(297) Wang, Y.; Oldenhof, S.; Versluis, F.; Shah, M.; Zhang, K.; van Steijn, V.; Guo, X.; Eelkema, R.; van Esch, J. H. Controlled Fabrication of Micropatterned Supramolecular Gels by Directed Self-Assembly of Small Molecular Gelators. *Small* **2019**, *15*, e1804154.

(298) Okesola, B. O.; Wu, Y.; Derkus, B.; Gani, S.; Wu, D.; Knani, D.; Smith, D. K.; Adams, D. J.; Mata, A. Supramolecular Self-Assembly To Control Structural and Biological Properties of Multicomponent Hydrogels. *Chem. Mater.* **2019**, *31*, 7883–7897.

(299) Higashi, S. L.; Shibata, A.; Kitamura, Y.; Hirosawa, K. M.; Suzuki, K. G. N.; Matsuura, K.; Ikeda, M. Hybrid Soft Nanomaterials Composed of DNA Microspheres and Supramolecular Nanostructures of Semi-Artificial Glycopeptides. *Chem. Eur. J.* **2019**, *25*, 11955–11962.

(300) Draper, E. R.; Adams, D. J. Controlling the Assembly and Properties of Low-Molecular-Weight Hydrogelators. *Langmuir* **2019**, *35*, 6506–6521.

(301) Panja, S.; Adams, D. J. Gel to Gel Transitions by Dynamic Self-Assembly. *Chem. Commun.* **2019**, *55*, 10154−10157.

(302) Fuentes-Caparrós, A. M.; de Paula Gómez-Franco, F.; Dietrich, B.; Wilson, C.; Brasnett, C.; Seddon, A.; Adams, D. J. Annealing Multicomponent Supramolecular Gels. *Nanoscale* **2019**, *11*, 3275–3280.

(303) Wakabayashi, R.; Suehiro, A.; Goto, M.; Kamiya, N. Designer Aromatic Peptide Amphiphiles for Self-Assembly and Enzymatic Display of Proteins with Morphology Control. *Chem. Commun.* **2019**, *55*, 640–643.

(304) Dang, D.; Zhang, H.; Xu, Y.; Xu, R.; Wang, Z.; Kwok, R. T. K.; Lam, J. W. Y.; Zhang, L.; Meng, L.; Tang, B. Z. Super-Resolution Visualization of Self-Assembling Helical

Fibers Using Aggregation-Induced Emission Luminogens in Stimulated Emission Depletion Nanoscopy. *ACS Nano* **2019**, *13*, 11863–11873.

(305) Wakabayashi, R.; Obayashi, H.; Hashimoto, R.; Kamiya, N.; Goto, M. Complementary Interaction with Peptide Amphiphiles Guides Size-Controlled Assembly of Small Molecules for Intracellular Delivery. *Chem. Commun.* **2019**, *55*, 6997–7000.

(306) Kubota, R.; Nagao, K.; Tanaka, W.; Matsumura, R.; Aoyama, T.; Urayama, K.; Hamachi, I. Control of Seed Formation Allows Two Distinct Self-Sorting Patterns of Supramolecular Nanofibers. *Nat. Commun.* **2020**, *11*, 4100.

(307) Kubota, R.; Nakamura, K.; Torigoe, S.; Hamachi, I. The Power of Confocal Laser Scanning Microscopy in Supramolecular Chemistry: In Situ Real-Time Imaging of Stimuli-Responsive Multicomponent Supramolecular Hydrogels. *ChemistryOpen* **2020**, *9*, 67–79.

(308) Kubota, R.; Makuta, M.; Suzuki, R.; Ichikawa, M.; Tanaka, M.; Hamachi, I. Force Generation by a Propagating Wave of Supramolecular Nanofibers. *Nat. Commun.* **2020**, *11*, 3541.

(309) Wang, Y.; Xu, Z.; Lovrak, M.; le Sage, V. A. A.; Zhang, K.; Guo, X.; Eelkema, R.; Mendes, E.; van Esch, J. H. Biomimetic Strain-Stiffening Self-Assembled Hydrogels. *Angew. Chem. Int. Ed.* **2020**, *59*, 4830–4834.

(310) Wang, H.; Liu, L.; Bai, S.; Guo, X.; Eelkema, R.; van Esch, J. H.; Wang, Y. Transient Supramolecular Hydrogels Formed by Catalytic Control over Molecular Self-Assembly. *Soft Matter* **2020**, *16*, 9406–9409.

(311) Liu, Q.; Yuan, Z.; Zhao, M.; Huisman, M.; Drewes, G.; Piskorz, T.; Mytnyk, S.; Koper, G. J. M.; Mendes, E.; van Esch, J. H. Interfacial Microcompartmentalization by Kinetic Control of Selective Interfacial Accumulation. *Angew. Chem. Int. Ed.* **2020**, *59*, 23748–23754.

(312) Fuentes, E.; Boháčová, K.; Fuentes-Caparrós, A. M.; Schweins, R.; Draper, E. R.; Adams, D. J.; Pujals, S.; Albertazzi, L. PAINT-Ing Fluorenylmethoxycarbonyl (Fmoc)-Diphenylalanine Hydrogels. *Chem. Eur. J.* **2020**, *26*, 9869 –9873.

(313) Panja, S.; Dietrich, B.; Adams, D. J. Chemically Fuelled Self-Regulating Gel-to-Gel Transition. *ChemSystemsChem* **2020**, *2*, e1900038.

(314) Sugiura, T.; Kanada, T.; Mori, D.; Sakai, H.; Shibata, A.; Kitamura, Y.; Ikeda, M. Chemical Stimulus-Responsive Supramolecular Hydrogel Formation and Shrinkage of a Hydrazone-Containing Short Peptide Derivative. *Soft Matter* **2020**, *16*, 899–906.

(315) Arakawa, H.; Takeda, K.; Higashi, S. L.; Shibata, A.; Kitamura, Y.; Ikeda, M. Self-Assembly and Hydrogel Formation Ability of Fmoc-Dipeptides Comprising α-Methyl-L-Phenylalanine. *Polym. J.* **2020**, *52*, 923–930.

(316) Higashi, S. L.; Hirosawa, K. M.; Suzuki, K. G. N.; Matsuura, K.; Ikeda, M. One-Pot Construction of Multicomponent Supramolecular Materials Comprising Self-Sorted Supramolecular Architectures of DNA and Semi-Artificial Glycopeptides. *ACS Appl. Bio Mater.* **2020**. 3, 9082–9092.

(317) Dai, K.; Fores, J. R.; Wanzke, C.; Winkeljann, B.; Bergmann, A. M.; Lieleg, O.; Boekhoven, J. Regulating Chemically Fueled Peptide Assemblies by Molecular Design. *J. Am. Chem. Soc.* **2020**, *142*, 14142–14149.

(318) Kriebisch, B. A. K.; Jussupow, A.; Bergmann, A. M.; Kohler, F.; Dietz, H.; Kaila, V. R. I.; Boekhoven, J. Reciprocal Coupling in Chemically Fueled Assembly: A Reaction Cycle Regulates Self-Assembly and Vice Versa. *J. Am. Chem. Soc.* **2020**, *142*, 20837–20844.

(319) Sarkar, A.; Sasmal, R.; Empereur-Mot, C.; Bochicchio, D.; Kompella, S. V. K.; Sharma, K.; Dhiman, S.; Sundaram, B.; Agasti, S. S.; Pavan, G. M. *et al.* Self-Sorted, Random, and Block Supramolecular Copolymers via Sequence Controlled, Multicomponent Self-Assembly. *J. Am. Chem. Soc.* **2020**, *142*, 7606–7617.

(320) Sarkar, A.; Behera, T.; Sasmal, R.; Capelli, R.; Empereur-Mot, C.; Mahato, J.; Agasti, S. S.; Pavan, G. M.; Chowdhury, A.; George, S. J. Cooperative Supramolecular Block Copolymerization for the Synthesis of Functional Axial Organic Heterostructures. *J. Am. Chem. Soc.* **2020**, *142*, 11528–11539.

(321) Reja, A.; Afrose, S. P.; Das, D. Aldolase Cascade Facilitated by Self-Assembled Nanotubes from Short Peptide Amphiphiles. *Angew. Chem. Int. Ed.* **2020**, *59*, 4329–4334.

(322) Sarkhel, B.; Chatterjee, A.; Das, D. Covalent Catalysis by Cross β Amyloid Nanotubes. *J. Am. Chem. Soc.* **2020**, *142*, 4098–4103.

(323) Singh, N.; Lainer, B.; Formon, G. J. M.; De Piccoli, S.; Hermans, T. M. Re-Programming Hydrogel Properties Using a Fuel-Driven Reaction Cycle. *J. Am. Chem. Soc.* **2020**, *142*, 4083–4087.

(324) Huff, J. The Airyscan Detector from ZEISS: Confocal Imaging with Improved Signal-to-Noise Ratio and Super-Resolution. *Nat. Methods* **2015**, *12*, i–ii.

(325) Korobchevskaya, K.; Lagerholm, B. C.; Colin-York, H.; Fritzsche, M. Exploring the Potential of Airyscan Microscopy for Live Cell Imaging. *Photonics* **2017**, *4*, 41.

(326) Qiu, H.; Gao, Y.; Boott, C. E; Gould, O. E. C.; Harniman, R. L.; Miles, M. J.; Webb, S. E. D.; Winnik, M. A.; Manners, I. Uniform Patchy and Hollow Rectangular Platelet Micelles from Crystallizable Polymer Blends. *Science* **2016**, *352*, 697–701.

(327) Boott, C. E.; Laine, R. F.; Mahou, P.; Finnegan, J. R.; Leitao, E. M.; Webb, S. E. D.; Kaminski, C. F.; Manners, I. In Situ Visualization of Block Copolymer Self-Assembly in Organic Media by Super-Resolution Fluorescence Microscopy. *Chem. Eur. J.* **2015**, *21*, 18539–18542.

(328) Moerner, W. E. W. E. Single-Molecule Spectroscopy, Imaging, and Photocontrol: Foundations for Super-Resolution Microscopy (Nobel Lecture). *Angew. Chem. Int. Ed.* **2015**, *54*, 8067–8093.

(329) Hess, S. T.; Girirajan, T. P. K.; Mason, M. D. Ultra-High Resolution Imaging by Fluorescence Photoactivation Localization Microscopy. *Biophys. J.* **2006**, *91*, 4258–4272.

(330) Aoki, H.; Mori, K.; Ito, S. Conformational Analysis of Single Polymer Chains in Three Dimensions by Super-Resolution Fluorescence Microscopy. *Soft Matter* **2012**, *8*, 4390.

(331) Yan, J.; Zhao, L.-X.; Li, C.; Hu, Z.; Zhang, G.-F.; Chen, Z.-Q.; Chen, T.; Huang, Z.-L.; Zhu, J.; Zhu, M.-Q. Optical Nanoimaging for Block Copolymer Self-Assembly. *J. Am. Chem. Soc.* **2015**, *137*, 2436–2439.

(332) Nevskyi, O.; Sysoiev, D.; Oppermann, A.; Huhn, T.; Wöll, D. Nanoscopic Visualization of Soft Matter Using Fluorescent Diarylethene Photoswitches. *Angew. Chem. Int. Ed.* **2016**, *55*, 12698–12702.

(333) Gao, C.; Donath, E.; Möhwald, H.; Shen, J. Spontaneous Deposition of Water-Soluble Substances into Microcapsules: Phenomenon, Mechanism, and Application. *Angew. Chem. Int. Ed.* **2002**, *41*, 3789–3793.

(334) Artyukhin, A. B.; Shestakov, A.; Harper, J.; Bakajin, O.; Stroeve, P.; Noy, A. Functional One-Dimensional Lipid Bilayers on Carbon Nanotube Templates. *J. Am. Chem. Soc.* **2005**, *127*, 7538–7542.

(335) Robbins, G. P.; Jimbo, M.; Swift, J.; Therien, M. J.; Hammer, D. A.; Dmochowski, I. J. Photoinitiated Destruction of Composite Porphyrin-Protein Polymersomes. *J. Am. Chem. Soc.* **2009**, *131*, 3872–3874.

(336) Ge, X.; Conley, A. J.; Brandle, J. E.; Truant, R.; Filipe, C. D. M. In Vivo Formation of Protein Based Aqueous Microcompartments. *J. Am. Chem. Soc.* **2009**, *131*, 9094–9099.

(337) Christian, D. A.; Tian, A.; Ellenbroek, W. G.; Levental, I.; Rajagopal, K.; Janmey, P. A.; Liu, A. J.; Baumgart, T.; Discher, D. E. Spotted Vesicles, Striped Micelles and Janus Assemblies Induced by Ligand Binding. *Nat. Mater.* **2009**, *8*, 843–849.

(338) Tanaka, A.; Fukuoka, Y.; Morimoto, Y.; Honjo, T.; Koda, D.; Goto, M.; Maruyama, T. Cancer Cell Death Induced by the Intracellular Self-Assembly of an Enzyme-Responsive Supramolecular Gelator. *J. Am. Chem. Soc.* **2015**, *137*, 770–775.

(339) Rapp, P. B.; Omar, A. K.; Shen, J. J.; Buck, M. E.; Wang, Z.-G.; Tirrell, D. A. Analysis and Control of Chain Mobility in Protein Hydrogels. *J. Am. Chem. Soc.* **2017**, *139*, 3796–3804.

(340) Deng, N.-N.; Huck, W. T. S. Microfluidic Formation of Monodisperse Coacervate Organelles in Liposomes. *Angew. Chem. Int. Ed.* **2017**, *56*, 9736–9740.

(341) Nakamura, H.; Lee, A. A.; Afshar, A. S.; Watanabe, S.; Rho, E.; Razavi, S.; Suarez, A.; Lin, Y.-C.; Tanigawa, M.; Huang, B. *et al.* Intracellular Production of Hydrogels and

Synthetic RNA Granules by Multivalent Molecular Interactions. *Nat. Mater.* **2018**, *17*, 79–89.

(342) Roberts, S.; Harmon, T. S.; Schaal, J. L.; Miao, V.; Li, K. J.; Hunt, A.; Wen, Y.; Oas, T. G.; Collier, J. H.; Pappu, R. V. *et al.* Injectable Tissue Integrating Networks from Recombinant Polypeptides with Tunable Order. *Nat. Mater.* **2018**, *17*, 1154–1163.

(343) Alshareedah, I.; Kaur, T.; Ngo, J.; Seppala, H.; Kounatse, L.-A. D.; Wang, W.; Moosa, M. M.; Banerjee, P. R. Interplay between Short-Range Attraction and Long-Range Repulsion Controls Reentrant Liquid Condensation of Ribonucleoprotein-RNA Complexes. *J. Am. Chem. Soc.* **2019**, *141*, 14593–14602.

(344) Dogra, P.; Joshi, A.; Majumdar, A.; Mukhopadhyay, S. Intermolecular Charge-Transfer Modulates Liquid-Liquid Phase Separation and Liquid-to-Solid Maturation of an Intrinsically Disordered pH-Responsive Domain. *J. Am. Chem. Soc.* **2019**, *141*, 20380–20389.

(345) Ghosh, A.; Zhang, X.; Zhou, H.-X. Tug of War between Condensate Phases in a Minimal Macromolecular System. *J. Am. Chem. Soc.* **2020**, *142*, 8848–8861.

(346) Schulz, M.; Werner, S.; Bacia, K.; Binder, W. H. Controlling Molecular Recognition with Lipid/Polymer Domains in Vesicle Membranes. *Angew. Chem. Int. Ed.* **2013**, *52*, 1829–1833.

(347) Luo, Q.; Shi, Z.; Zhang, Y.; Chen, X.-J.; Han, S.-Y.; Baumgart, T.; Chenoweth, D. M.; Park, S.-J. DNA Island Formation on Binary Block Copolymer Vesicles. *J. Am. Chem. Soc.* **2016**, *138*, 10157–10162.

(348) Bhattacharya, A.; Niederholtmeyer, H.; Podolsky, K. A.; Bhattacharya, R.; Song, J.-J.; Brea, R. J.; Tsai, C.-H.; Sinha, S. K.; Devaraj, N. K. Lipid Sponge Droplets as Programmable Synthetic Organelles. *Proc. Natl. Acad. Sci. U. S. A.* **2020**, *117*, 18206–18215.

(349) Love, C.; Steinkühler, J.; Gonzales, D. T.; Yandrapalli, N.; Robinson, T.; Dimova, R.; Tang, T.-Y. D. Reversible pH-Responsive Coacervate Formation in Lipid Vesicles Activates Dormant Enzymatic Reactions. *Angew. Chem. Int. Ed.* **2020**, *59*, 5950–5957.

(350) Liu, J.; Tian, L.; Qiao, Y.; Zhou, S.; Patil, A. J.; Wang, K.; Li, M.; Mann, S. Hydrogel-Immobilized Coacervate Droplets as Modular Microreactor Assemblies. *Angew. Chem. Int. Ed.* **2020**, *59*, 6853–6859.

(351) Di Iorio, D.; Lu, Y.; Meulman, J.; Huskens, J. Recruitment of Receptors at Supported Lipid Bilayers Promoted by the Multivalent Binding of Ligand-Modified Unilamellar Vesicles. *Chem. Sci.* **2020**, *11*, 3307–3315.

(352) DeForest, C. A.; Tirrell, D. A. A Photoreversible Protein-Patterning Approach for Guiding Stem Cell Fate in Three-Dimensional Gels. *Nat. Mater.* **2015**, *14*, 523–531.

(353) Deng, N.-N.; Vibhute, M. A.; Zheng, L.; Zhao, H.; Yelleswarapu, M.; Huck, W. T. S. Macromolecularly Crowded Protocells from Reversibly Shrinking Monodisperse Liposomes. *J. Am. Chem. Soc.* **2018**, *140*, 7399–7402.

(354) Yamamoto, A.; Ichikawa, M. Direct Measurement of Single Soft Lipid Nanotubes: Nanoscale Information Extracted in a Noninvasive Manner. *Phys. Rev. E* **2012**, *86*, 061905.

(355) Averick, S.; Karácsony, O.; Mohin, J.; Yong, X.; Moellers, N. M.; Woodman, B. F.; Zhu, W.; Mehl, R. A.; Balazs, A. C.; Kowalewski, T. *et al.* Cooperative, Reversible Self-Assembly of Covalently Pre-Linked Proteins into Giant Fibrous Structures. *Angew. Chem. Int. Ed.* **2014**, *53*, 8050–8055.

(356) Gittes, F.; Mickey, B.; Nettleton, J.; Howard, J. Flexural Rigidity of Microtubules and Actin Filaments Measured from Thermal Fluctuations in Shape. *J. Cell Biol.* **1993**, *120*, 923–934.

(357) Matsumoto, S.; Yamaguchi, S.; Ueno, S.; Komatsu, H.; Ikeda, M.; Ishizuka, K.; Iko, Y.; Tabata, K. V.; Aoki, H.; Ito, S. *et al.* Photo Gel-Sol/Sol-Gel Transition and Its Patterning of a Supramolecular Hydrogel as Stimuli-Responsive Biomaterials. *Chem. Eur. J.* **2008**, *14*, 3977–3986.

(358) Kubota, R.; Torigoe, S.; Liu, S.; Hamachi, I. In Situ Real-Time Confocal Imaging of a Self-Assembling Peptide-Grafted Polymer Showing pH-Responsive Hydrogelation. *Chem. Lett.* **2020**, *49*, 1319–1323.

(359) Leira-Iglesias, J.; Tassoni, A.; Adachi, T.; Stich, M.; Hermans, T. M. Oscillations, Travelling Fronts and Patterns in a Supramolecular System. *Nat. Nanotechnol.* **2018**, *13*, 1021–1027.

(360) Takakura, K.; Toyota, T.; Sugawara, T. A Novel System of Self-Reproducing Giant Vesicles. *J. Am. Chem. Soc.* **2003**, *125*, 8134–8140.

(361) Hanczyc, M. M.; Fujikawa, S. M.; Szostak, J. W. Experimental Models of Primitive Cellular Compartments: Encapsulation, Growth, and Division. *Science* **2003**, *302*, 618–622.

(362) Takakura, K.; Sugawara, T. Membrane Dynamics of a Myelin-like Giant Multilamellar Vesicle Applicable to a Self-Reproducing System. *Langmuir* **2004**, *20*, 3832–3834.

(363) Zepik, H. H.; Walde, P.; Ishikawa, T. Vesicle Formation from Reactive Surfactants. *Angew. Chem. Int. Ed.* **2008**, *47*, 1323–1325.

(364) Howse, J. R.; Jones, R. A. L.; Battaglia, G.; Ducker, R. E.; Leggett, G. J.; Ryan, A. J. Templated Formation of Giant Polymer Vesicles with Controlled Size Distributions. *Nat. Mater.* **2009**, *8*, 507–511.

(365) Zhu, T. F.; Szostak, J. W. Coupled Growth and Division of Model Protocell Membranes. *J. Am. Chem. Soc.* **2009**, *131*, 5705–5713.

(366) Kurihara, K.; Tamura, M.; Shohda, K.-I.; Toyota, T.; Suzuki, K.; Sugawara, T. Self-Reproduction of Supramolecular Giant Vesicles Combined with the Amplification of Encapsulated DNA. *Nat. Chem.* **2011**, *3*, 775–781.

(367) Budin, I.; Devaraj, N. K. Membrane Assembly Driven by a Biomimetic Coupling Reaction. *J. Am. Chem. Soc.* **2012**, *134*, 751–753.

(368) Adamala, K.; Szostak, J. W. Competition between Model Protocells Driven by an Encapsulated Catalyst. *Nat. Chem.* **2013**, *5*, 495–501.

(369) Stano, P.; D'Aguanno, E.; Bolz, J.; Fahr, A.; Luisi, P. L. A Remarkable Self-Organization Process as the Origin of Primitive Functional Cells. *Angew. Chem. Int. Ed.* **2013**, *52*, 13397–13400.

(370) Bao, C.; Pähler, G.; Geil, B.; Janshoff, A. Optical Fusion Assay Based on Membrane-Coated Spheres in a 2D Assembly. *J. Am. Chem. Soc.* **2013**, *135*, 12176–12179.

(371) Sato, Y.; Yasuhara, K.; Kikuchi, J.-I.; Sato, T. N. Synthetic Cell Division System: Controlling Equal vs. Unequal Divisions by Design. *Sci. Rep.* **2013**, *3*, 3475.

(372) Takakura, K.; Yamamoto, T.; Kurihara, K.; Toyota, T.; Ohnuma, K.; Sugawara, T. Spontaneous Transformation from Micelles to Vesicles Associated with Sequential Conversions of Comprising Amphiphiles within Assemblies. *Chem. Commun.* **2014**, *50*, 2190–2192.

(373) Brea, R. J.; Cole, C. M.; Devaraj, N. K. In Situ Vesicle Formation by Native Chemical Ligation. *Angew. Chem. Int. Ed.* **2014**, *53*, 14102–14105.

(374) Hardy, M. D.; Yang, J.; Selimkhanov, J.; Cole, C. M.; Tsimring, L. S.; Devaraj, N. K. Self-Reproducing Catalyst Drives Repeated Phospholipid Synthesis and Membrane Growth. *Proc. Natl. Acad. Sci. U. S. A.* **2015**, *112*, 8187–8192.

(375) Kurihara, K.; Okura, Y.; Matsuo, M.; Toyota, T.; Suzuki, K.; Sugawara, T. A Recursive Vesicle-Based Model Protocell with a Primitive Model Cell Cycle. *Nat. Commun.* **2015**, *6*, 8352.

(376) Brea, R.; Bhattacharya, A.; Devaraj, N. Spontaneous Phospholipid Membrane Formation by Histidine Ligation. *Synlett* **2016**, *28*, 108–112.

(377) Wong, C. K.; Mason, A. F.; Stenzel, M. H.; Thordarson, P. Formation of Non-Spherical Polymersomes Driven by Hydrophobic Directional Aromatic Perylene Interactions. *Nat. Commun.* **2017**, *8*, 1240.

(378) Peyret, A.; Ibarboure, E.; Tron, A.; Beauté, L.; Rust, R.; Sandre, O.; McClenaghan, N. D.; Lecommandoux, S. Polymersome Popping by Light-Induced Osmotic Shock under Temporal, Spatial, and Spectral Control. *Angew. Chem. Int. Ed.* **2017**, *56*, 1566–1570.

(379) Fu, M.; Li, J. Spontaneous Membrane Generation and Extension in a Dipeptide Single Crystal and Phospholipid Mixed System. *Angew. Chem. Int. Ed.* **2018**, *57*, 11404–11407.

(380) Litschel, T.; Ramm, B.; Maas, R.; Heymann, M.; Schwille, P. Beating Vesicles: Encapsulated Protein Oscillations Cause Dynamic Membrane Deformations. *Angew. Chem. Int. Ed.* **2018**, *57*, 16286–16290.

(381) Bhattacharya, A.; Brea, R. J.; Niederholtmeyer, H.; Devaraj, N. K. A Minimal Biochemical Route towards de Novo Formation of Synthetic Phospholipid Membranes. *Nat. Commun.* **2019**, *10*, 300.

(382) Kurisu, M.; Aoki, H.; Jimbo, T.; Sakuma, Y.; Imai, M.; Serrano-Luginbühl, S.; Walde, P. Reproduction of Vesicles Coupled with a Vesicle Surface-Confined Enzymatic Polymerisation. *Commun. Chem.* **2019**, *2*, 117.

(383) Ishii, I.; Ominato, Y.; Karasawa, A.; Takahashi, T.; Matsuo, M.; Suzuki, K.; Sugawara, T. Morphological Changes of Kinetically Trapped Tubular Vesicles Driven by the Production of Synthetic Phospholipids in a Vesicular Membrane. *Chem. Lett.* **2019**, *48*, 932–935.

(384) Castro, J. M.; Sugiyama, H.; Toyota, T. Budding and Division of Giant Vesicles Linked to Phospholipid Production. *Sci. Rep.* **2019**, *9*, 165.

(385) Liu, L.; Zou, Y.; Bhattacharya, A.; Zhang, D.; Lang, S. Q.; Houk, K. N.; Devaraj, N. K. Enzyme-Free Synthesis of Natural Phospholipids in Water. *Nat. Chem.* **2020**, *12*, 1029–1034.

(386) Post, E. A. J.; Fletcher, S. P. Dissipative Self-Assembly, Competition and Inhibition in a Self-Reproducing Protocell Model. *Chem. Sci.* **2020**, *19*, 516.

(387) Miele, Y.; Medveczky, Z.; Holló, G.; Tegze, B.; Derényi, I.; Hórvölgyi, Z.; Altamura, E.; Lagzi, I.; Rossi, F. Self-Division of Giant Vesicles Driven by an Internal Enzymatic Reaction. *Chem. Sci.* **2020**, *11*, 3228–3235.

(388) Rikken, R. S. M.; Engelkamp, H.; Nolte, R. J. M.; Maan, J. C.; van Hest, J. C. M.; Wilson, D. A.; Christianen, P. C. M. Shaping Polymersomes into Predictable Morphologies via Out-of-Equilibrium Self-Assembly. *Nat. Commun.* **2016**, *7*, 12606.

(389) Buddingh’, B. C.; Llopis-Lorente, A.; Loai K E; van Hest, J. C. M. Dynamic Spatial and Structural Organization in Artificial Cells Regulates Signal Processing by Protein Scaffolding. *Chem. Sci.* **2020**, *11*, 12829–12834.

(390) Peresypkin, A. V.; Menger, F. M. Zwitterionic Geminis. Coacervate Formation from a Single Organic Compound. *Org. Lett.* **1999**, *1*, 1347–1350.

(391) Menger, F. M.; Peresypkin, A. V.; Caran, K. L.; Apkarian, R. P. A Sponge Morphology in an Elementary Coacervate. *Langmuir* **2000**, *16*, 9113–9116.

(392) Helfrich, M. R.; Mangeney-Slavin, L. K.; Long, M. S.; Djoko, K. Y.; Keating, C. D. Aqueous Phase Separation in Giant Vesicles. *J. Am. Chem. Soc.* **2002**, *124*, 13374–13375.

(393) Imura, T.; Yanagishita, H.; Kitamoto, D. Coacervate Formation from Natural Glycolipid: One Acetyl Group on the Headgroup Triggers Coacervate-to-Vesicle Transition. *J. Am. Chem. Soc.* **2004**, *126*, 10804–10805.

(394) Jaeger, D. A.; Zeng, X.; Apkarian, R. P. Shamrock Surfactants: Synthesis and Characterization. *Langmuir* **2004**, *20*, 10427–10432.

(395) Long, M. S.; Jones, C. D.; Helfrich, M. R.; Mangeney-Slavin, L. K.; Keating, C. D. Dynamic Microcompartmentation in Synthetic Cells. *Proc. Natl. Acad. Sci. U. S. A.* **2005**, *102*, 5920–5925.

(396) Long, M. S.; Cans, A.-S.; Keating, C. D. Budding and Asymmetric Protein Microcompartmentation in Giant Vesicles Containing Two Aqueous Phases. *J. Am. Chem. Soc.* **2008**, *130*, 756–762.

(397) Cans, A.-S.; Andes-Koback, M.; Keating, C. D. Positioning Lipid Membrane Domains in Giant Vesicles by Micro-Organization of Aqueous Cytoplasm Mimic. *J. Am. Chem. Soc.* **2008**, *130*, 7400–7406.

(398) Spruijt, E.; Westphal, A. H.; Borst, J. W.; Cohen Stuart, M. A.; van der Gucht, J. Binodal Compositions of Polyelectrolyte Complexes. *Macromolecules* **2010**, *43*, 6476–6484.

(399) Dominak, L. M.; Gundermann, E. L.; Keating, C. D. Microcompartmentation in Artificial Cells: pH-Induced Conformational Changes Alter Protein Localization. *Langmuir* **2010**, *26*, 5697–5705.

(400) Koga, S.; Williams, D. S.; Perriman, A. W.; Mann, S. Peptide-Nucleotide Microdroplets as a Step towards a Membrane-Free Protocell Model. *Nat. Chem.* **2011**, *3*, 720–724.

(401) Krishna Kumar, R.; Yu, X.; Patil, A. J.; Li, M.; Mann, S. Cytoskeletal-like Supramolecular Assembly and Nanoparticle-Based Motors in a Model Protocell. *Angew. Chem. Int. Ed.* **2011**, *50*, 9343–9347.

(402) Strulson, C. A.; Molden, R. C.; Keating, C. D.; Bevilacqua, P. C. RNA Catalysis through Compartmentalization. *Nat. Chem.* **2012**, *4*, 941–946.

(403) Priftis, D.; Tirrell, M. Phase Behaviour and Complex Coacervation of Aqueous Polypeptide Solutions. *Soft Matter* **2012**, *8*, 9396–9405.

(404) Crosby, J.; Treadwell, T.; Hammerton, M.; Vasilakis, K.; Crump, M. P.; Williams, D. S.; Mann, S. Stabilization and Enhanced Reactivity of Actinorhodin Polyketide Synthase Minimal Complex in Polymer–Nucleotide Coacervate Droplets. *Chem. Commun.* **2012**, *48*, 11832–11834.

(405) Tang, T.-Y. D.; Antognozzi, M.; Vicary, J. A.; Perriman, A. W.; Mann, S. Small-Molecule Uptake in Membrane-Free Peptide/Nucleotide Protocells. *Soft Matter* **2013**, *9*, 7647.

(406) Sokolova, E.; Spruijt, E.; Hansen, M. M. K.; Dubuc, E.; Groen, J.; Chokkalingam, V.; Piruska, A.; Heus, H. A.; Huck, W. T. S. Enhanced Transcription Rates in Membrane-Free Protocells Formed by Coacervation of Cell Lysate. *Proc. Natl. Acad. Sci. U. S. A.* **2013**, *110*, 11692–11697.

(407) Dora Tang, T.-Y.; Rohaida Che Hak, C.; Thompson, A. J.; Kuimova, M. K.; Williams, D. S.; Perriman, A. W.; Mann, S. Fatty Acid Membrane Assembly on Coacervate Microdroplets as a Step towards a Hybrid Protocell Model. *Nat. Chem.* **2014**, *6*, 527–533.

(408) Jia, T. Z.; Hentrich, C.; Szostak, J. W. Rapid RNA Exchange in Aqueous Two-Phase System and Coacervate Droplets. *Orig. Life Evol. Biosph.* **2014**, *44*, 1–12.

(409) Black, K. A.; Priftis, D.; Perry, S. L.; Yip, J.; Byun, W. Y.; Tirrell, M. Protein Encapsulation via Polypeptide Complex Coacervation. *ACS Macro Lett.* **2014**, *3*, 1088–1091.

(410) Aumiller, W. M., Jr; Keating, C. D. Phosphorylation-Mediated RNA/Peptide Complex Coacervation as a Model for Intracellular Liquid Organelles. *Nat. Chem.* **2016**, *8*, 129–137.

(411) Nott, T. J.; Craggs, T. D.; Baldwin, A. J. Membraneless Organelles Can Melt Nucleic Acid Duplexes and Act as Biomolecular Filters. *Nat. Chem.* **2016**, *8*, 569–575.

(412) van Swaay, D.; Tang, T.-Y. D.; Mann, S.; de Mello, A. Microfluidic Formation of Membrane-Free Aqueous Coacervate Droplets in Water. *Angew. Chem. Int. Ed.* **2015**, *54*, 8398–8401.

(413) Semenov, S. N.; Wong, A. S. Y.; van der Made, R. M.; Postma, S. G. J.; Groen, J.; van Roekel, H. W. H.; de Greef, T. F. A.; Huck, W. T. S. Rational Design of Functional and Tunable Oscillating Enzymatic Networks. *Nat. Chem.* **2015**, *7*, 160–165.

(414) Higashiguchi, K.; Taira, G.; Kitai, J.-I.; Hirose, T.; Matsuda, K. Photoinduced Macroscopic Morphological Transformation of an Amphiphilic Diarylethene Assembly: Reversible Dynamic Motion. *J. Am. Chem. Soc.* **2015**, *137*, 2722–2729.

(415) Krishna Kumar, R.; Harniman, R. L.; Patil, A. J.; Mann, S. Self-Transformation and Structural Reconfiguration in Coacervate-Based Protocells. *Chem. Sci.* **2016**, *7*, 5879–5887.

(416) Garenne, D.; Beven, L.; Navailles, L.; Nallet, F.; Dufourc, E. J.; Douliez, J.-P. Sequestration of Proteins by Fatty Acid Coacervates for Their Encapsulation within Vesicles. *Angew. Chem. Int. Ed.* **2016**, *55*, 13475–13479.

(417) Yin, Y.; Niu, L.; Zhu, X.; Zhao, M.; Zhang, Z.; Mann, S.; Liang, D. Non-Equilibrium Behaviour in Coacervate-Based Protocells under Electric-Field-Induced Excitation. *Nat. Commun.* **2016**, *7*, 10658.

(418) Aumiller, W. M., Jr; Pir Cakmak, F.; Davis, B. W.; Keating, C. D. RNA-Based Coacervates as a Model for Membraneless Organelles: Formation, Properties, and Interfacial Liposome Assembly. *Langmuir* **2016**, *32*, 10042–10053.

(419) Martin, N.; Li, M.; Mann, S. Selective Uptake and Refolding of Globular Proteins in Coacervate Microdroplets. *Langmuir* **2016**, *32*, 5881–5889.

(420) Monterroso, B.; Zorrilla, S.; Sobrinos-Sanguino, M.; Keating, C. D.; Rivas, G. Microenvironments Created by Liquid-Liquid Phase Transition Control the Dynamic Distribution of Bacterial Division FtsZ Protein. *Sci. Rep.* **2016**, *6*, 35140.

(421) Tian, L.; Martin, N.; Bassindale, P. G.; Patil, A. J.; Li, M.; Barnes, A.; Drinkwater, B. W.; Mann, S. Spontaneous Assembly of Chemically Encoded Two-Dimensional Coacervate Droplet Arrays by Acoustic Wave Patterning. *Nat. Commun.* **2016**, *7*, 13068.

(422) Douliez, J.-P.; Martin, N.; Gaillard, C.; Beneyton, T.; Baret, J.-C.; Mann, S.; Beven, L. Catanionic Coacervate Droplets as a Surfactant-Based Membrane-Free Protocell Model. *Angew. Chem. Int. Ed.* **2017**, *56*, 13689–13693.

(423) Simon, J. R.; Carroll, N. J.; Rubinstein, M.; Chilkoti, A.; López, G. P. Programming Molecular Self-Assembly of Intrinsically Disordered Proteins Containing Sequences of Low Complexity. *Nat. Chem.* **2017**, *9*, 509–515.

(424) Wei, M.-T.; Elbaum-Garfinkle, S.; Holehouse, A. S.; Chen, C. C.-H.; Feric, M.; Arnold, C. B.; Priestley, R. D.; Pappu, R. V.; Brangwynne, C. P. Phase Behaviour of Disordered Proteins Underlying Low Density and High Permeability of Liquid Organelles. *Nat. Chem.* **2017**, *9*, 1118–1125.

(425) Vieregg, J. R.; Lueckheide, M.; Marciel, A. B.; Leon, L.; Bologna, A. J.; J Rivera, J. R.; Tirrell, M. V. Oligonucleotide─Peptide Complexes: Phase Control by Hybridization. *J. Am. Chem. Soc.* **2018**, *140*, 1632─1638.

(426) Banerjee, P. R.; Milin, A. N.; Moosa, M. M.; Onuchic, P. L.; Deniz, A. A. Reentrant Phase Transition Drives Dynamic Substructure Formation in Ribonucleoprotein Droplets. *Angew. Chem. Int. Ed.* **2017**, *56*, 11354–11359.

(427) Marianelli, A. M.; Miller, B. M.; Keating, C. D. Impact of Macromolecular Crowding on RNA/Spermine Complex Coacervation and Oligonucleotide Compartmentalization. *Soft Matter* **2018**, *14*, 368–378.

(428) Drobot, B.; Iglesias-Artola, J. M.; Le Vay, K.; Mayr, V.; Kar, M.; Kreysing, M.; Mutschler, H.; Tang, T.-Y. D. Compartmentalised RNA Catalysis in Membrane-Free Coacervate Protocells. *Nat. Commun.* **2018**, *9*, 3643.

(429) Mozhdehi, D.; Luginbuhl, K. M.; Simon, J. R.; Dzuricky, M.; Berger, R.; Varol, H. S.; Huang, F. C.; Buehne, K. L.; Mayne, N. R.; Weitzhandler, I. *et al.* Genetically Encoded Lipid-Polypeptide Hybrid Biomaterials That Exhibit Temperature-Triggered Hierarchical Self-Assembly. *Nat. Chem.* **2018**, *10*, 496–505.

(430) Pavan, B. V. V.; Fothergill, J.; Bretherton, J.; Tian, L.; Patil, A. J.; Davis, S. A.; Mann, S. Chloroplast-Containing Coacervate Micro-Droplets as a Step towards Photosynthetically Active Membrane-Free Protocells. *Chem. Commun.* **2018**, *54*, 3594–3597.

(431) Schuster, B. S.; Reed, E. H.; Parthasarathy, R.; Jahnke, C. N.; Caldwell, R. M.; Bermudez, J. G.; Ramage, H.; Good, M. C.; Hammer, D. A. Controllable Protein Phase Separation and Modular Recruitment to Form Responsive Membraneless Organelles. *Nat. Commun.* **2018**, *9*, 2985.

(432) Poudyal, R. R.; Guth-Metzler, R. M.; Veenis, A. J.; Frankel, E. A.; Keating, C. D.; Bevilacqua, P. C. Template-Directed RNA Polymerization and Enhanced Ribozyme Catalysis inside Membraneless Compartments Formed by Coacervates. *Nat. Commun.* **2019**, *10*, 490.

(433) Pir Cakmak, F.; Grigas, A. T.; Keating, C. D. Lipid Vesicle-Coated Complex Coacervates. *Langmuir* **2019**, *35*, 7830–7840.

(434) Poudyal, R. R.; Keating, C. D.; Bevilacqua, P. C. Polyanion-Assisted Ribozyme Catalysis Inside Complex Coacervates. *ACS Chem. Biol.* **2019**, *14*, 1243–1248.

(435) Yewdall, N. A.; Buddingh, B. C.; Altenburg, W. J.; Timmermans, S. B. P. E.; Vervoort, D. F. M.; Abdelmohsen, L. K. E. A.; Mason, A. F.; van Hest, J. C. M. Physicochemical Characterization of Polymer-Stabilized Coacervate Protocells. *Chembiochem* **2019**, *20*, 2643–2652.

(436) Wang, L.; Lin, Y.; Zhou, Y.; Xie, H.; Song, J.; Li, M.; Huang, Y.; Huang, X.; Mann, S. Autonomic Behaviors in Lipase-Active Oil Droplets. *Angew. Chem. Int. Ed.* **2019**, *58*, 1067–1071.

(437) Booth, R.; Qiao, Y.; Li, M.; Mann, S. Spatial Positioning and Chemical Coupling in Coacervate-in-Proteinosome Protocells. *Angew. Chem. Int. Ed.* **2019**, *58*, 9120–9124.

(438) Martin, N.; Tian, L.; Spencer, D.; Coutable-Pennarun, A.; Anderson, J. L. R.; Mann, S. Photoswitchable Phase Separation and Oligonucleotide Trafficking in DNA Coacervate Microdroplets. *Angew. Chem. Int. Ed.* **2019**, *58*, 14594–14598.

(439) Tian, L.; Li, M.; Patil, A. J.; Drinkwater, B. W.; Mann, S. Artificial Morphogen-Mediated Differentiation in Synthetic Protocells. *Nat. Commun.* **2019**, *10*, 3321.

(440) Mason, A. F.; Yewdall, N. A.; Welzen, P. L. W.; Shao, J.; van Stevendaal, M.; van Hest, J. C. M.; Williams, D. S.; Abdelmohsen, L. K. E. A. Mimicking Cellular Compartmentalization in a Hierarchical Protocell through Spontaneous Spatial Organization. *ACS Cent. Sci.* **2019**, *5*, 1360–1365.

(441) Lu, T.; Spruijt, E. Multiphase Complex Coacervate Droplets. *J. Am. Chem. Soc.* **2020**, *142*, 2905–2914.

(442) Magdalena Estirado, E.; Mason, A. F.; Alemán García, M. Á.; van Hest, J. C. M.; Brunsveld, L. Supramolecular Nanoscaffolds within Cytomimetic Protocells as Signal Localization Hubs. *J. Am. Chem. Soc.* **2020**, *142*, 9106–9111.

(443) Mountain, G. A.; Keating, C. D. Formation of Multiphase Complex Coacervates and Partitioning of Biomolecules within Them. *Biomacromolecules* **2020**, *21*, 630–640.

(444) Altenburg, W. J.; Yewdall, N. A.; Vervoort, D. F. M.; van Stevendaal, M. H. M. E.; Mason, A. F.; van Hest, J. C. M. Programmed Spatial Organization of Biomacromolecules into Discrete, Coacervate-Based Protocells. *Nat. Commun.* **2020**, *11*, 6282.

(445) Liu, S.; Zhang, Y.; Li, M.; Xiong, L.; Zhang, Z.; Yang, X.; He, X.; Wang, K.; Liu, J.; Mann, S. Enzyme-Mediated Nitric Oxide Production in Vasoactive Erythrocyte Membrane-Enclosed Coacervate Protocells. *Nat. Chem.* **2020**, *12*, 1165–1173.

(446) Gobbo, P.; Tian, L.; Pavan Kumar, B. V. V. S.; Turvey, S.; Cattelan, M.; Patil, A. J.; Carraro, M.; Bonchio, M.; Mann, S. Catalytic Processing in Ruthenium-Based Polyoxometalate Coacervate Protocells. *Nat. Commun.* **2020**, *11*, 41.

(447) Moreau, N. G.; Martin, N.; Gobbo, P.; Tang, T.-Y. D.; Mann, S. Spontaneous Membrane-Less Multi-Compartmentalization via Aqueous Two-Phase Separation in Complex Coacervate Micro-Droplets. *Chem. Commun.* **2020**, *56*, 12717–12720.

(448) Sato, Y.; Sakamoto, T.; Takinoue, M. Sequence-Based Engineering of Dynamic Functions of Micrometer-Sized DNA Droplets. *Sci. Adv.* **2020**, *6*, eaba3471.

(449) Maiti, S.; Fortunati, I.; Ferrante, C.; Scrimin, P.; Prins, L. J. Dissipative Self-Assembly of Vesicular Nanoreactors. *Nat. Chem.* **2016**, *8*, 725–731.

(450) Sorrenti, A.; Leira-Iglesias, J.; Sato, A.; Hermans, T. M. Non-Equilibrium Steady States in Supramolecular Polymerization. *Nat. Commun.* **2017**, *8*, 15899.

(451) Tena-Solsona, M.; Wanzke, C.; Riess, B.; Bausch, A. R.; Boekhoven, J. Self-Selection of Dissipative Assemblies Driven by Primitive Chemical Reaction Networks. *Nat. Commun.* **2018**, *9*, 2044.

(452) Te Brinke, E.; Groen, J.; Herrmann, A.; Heus, H. A.; Rivas, G.; Spruijt, E.; Huck, W. T. S. Dissipative Adaptation in Driven Self-Assembly Leading to Self-Dividing Fibrils. *Nat. Nanotechnol.* **2018**, *13*, 849–855.

(453) Solís Muñana, P.; Ragazzon, G.; Dupont, J.; Ren, C. Z.-J.; Prins, L. J.; Chen, J. L.-Y. Substrate-Induced Self-Assembly of Cooperative Catalysts. *Angew. Chem. Int. Ed.* **2018**, *57*, 16469–16474.

(454) Rieß, B.; Wanzke, C.; Tena-Solsona, M.; Grötsch, R. K.; Maity, C.; Boekhoven, J. Dissipative Assemblies That Inhibit Their Deactivation. *Soft Matter* **2018**, *14*, 4852–4859.

(455) Cardona, M. A.; Prins, L. J. ATP-Fuelled Self-Assembly to Regulate Chemical Reactivity in the Time Domain. *Chem. Sci.* **2020**, *11*, 1518–1522.

(456) Chandrabhas, S.; Maiti, S.; Fortunati, I.; Ferrante, C.; Gabrielli, L.; Prins, L. J. Nucleotide-Selective Templated Self-Assembly of Nanoreactors under Dissipative Conditions. *Angew. Chem. Int. Ed.* **2020**, *59*, 22223–22229.

(457) Wanzke, C.; Jussupow, A.; Kohler, F.; Dietz, H.; Kaila, V. R. I.; Boekhoven, J. Dynamic Vesicles Formed By Dissipative Self-Assembly. *ChemSystemsChem* **2020**, *2*, e1900044.

(458) Donau, C.; Späth, F.; Sosson, M.; Kriebisch, B. A. K.; Schnitter, F.; Tena-Solsona, M.; Kang, H.-S.; Salibi, E.; Sattler, M.; Mutschler, H. *et al.* Active Coacervate Droplets as a Model for Membraneless Organelles and Protocells. *Nat. Commun.* **2020**, *11*, 5167.

(459) Del Grosso, E.; Prins, L. J.; Ricci, F. Transient DNA-Based Nanostructures Controlled by Redox Inputs. *Angew. Chem. Int. Ed.* **2020**, *59*, 13238–13245.

(460) Wanzke, C.; Tena-Solsona, M.; Rieß, B.; Tebcharani, L.; Boekhoven, J. Active Droplets in a Hydrogel Release Drugs with a Constant and Tunable Rate. *Mater. Horiz.* **2020**, *7*, 1397–1403.

(461) He, F.; Gädt, T.; Manners, I.; Winnik, M. A. Fluorescent "Barcode" Multiblock Co-Micelles via the Living Self-Assembly of Di- and Triblock Copolymers with a Crystalline Core-Forming Metalloblock. *J. Am. Chem. Soc.* **2011**, *133*, 9095–9103.

(462) Hudson, Z. M.; Lunn, D. J.; Winnik, M. A.; Manners, I. Colour-Tunable Fluorescent Multiblock Micelles. *Nat. Commun.* **2014**, *5*, 3372.

(463) Hudson, Z. M.; Boott, C. E.; Robinson, M. E.; Rupar, P. A.; Winnik, M. A.; Manners, I. Tailored Hierarchical Micelle Architectures Using Living Crystallization-Driven Self-Assembly in Two Dimensions. *Nat. Chem.* **2014**, *6*, 893–898.

(464) Li, X.; Gao, Y.; Boott, C. E.; Winnik, M. A.; Manners, I. Non-Covalent Synthesis of Supermicelles with Complex Architectures Using Spatially Confined Hydrogen-Bonding Interactions. *Nat. Commun.* **2015**, *6*, 8127.

(465) Qiu, H.; Hudson, Z. M.; Winnik, M. A.; Manners, I. Multidimensional Hierarchical Self-Assembly of Amphiphilic Cylindrical Block Comicelles. *Science* **2015**, *347*, 1329–1332.

(466) Li, X.; Gao, Y.; Harniman, R.; Winnik, M.; Manners, I. Hierarchical Assembly of Cylindrical Block Comicelles Mediated by Spatially Confined Hydrogen-Bonding Interactions. *J. Am. Chem. Soc.* **2016**, *138*, 12902–12912.

(467) Li, X.; Gao, Y.; Boott, C. E.; Hayward, D. W.; Harniman, R.; Whittell, G. R.; Richardson, R. M.; Winnik, M. A.; Manners, I. "Cross" Supermicelles via the Hierarchical Assembly of Amphiphilic Cylindrical Triblock Comicelles. *J. Am. Chem. Soc.* **2016**, *138*, 4087–4095.

(468) Li, X.; Jin, B.; Gao, Y.; Hayward, D. W.; Winnik, M. A.; Luo, Y.; Manners, I. Monodisperse Cylindrical Micelles of Controlled Length with a Liquid-Crystalline Perfluorinated Core by 1D "Self-Seeding." *Angew. Chem. Int. Ed.* **2016**, *55*, 11392–11396.

(469) He, X.; Hsiao, M.-S.; Boott, C. E.; Harniman, R. L.; Nazemi, A.; Li, X.; Winnik, M. A.; Manners, I. Two-Dimensional Assemblies from Crystallizable Homopolymers with Charged Termini. *Nat. Mater.* **2017**, *16*, 481–488.

(470) Jin, X.-H.; Price, M. B.; Finnegan, J. R.; Boott, C. E.; Richter, J. M.; Rao, A.; Menke, S. M.; Friend, R. H.; Whittell, G. R.; Manners, I. Long-Range Exciton Transport in Conjugated Polymer Nanofibers Prepared by Seeded Growth. *Science* **2018**, *360*, 897–900.

(471) Pearce, S.; He, X.; Hsiao, M.-S.; Harniman, R. L.; MacFarlane, L. R.; Manners, I. Uniform, High-Aspect-Ratio, and Patchy 2D Platelets by Living Crystallization-Driven Self-Assembly of Crystallizable Poly(Ferrocenyldimethylsilane)-Based Homopolymers with Hydrophilic Charged Termini. *Macromolecules* **2019**, *52*, 6068–6079.

(472) Liu, Y.; Gong, Y.; Guo, Y.; Xiong, W.; Zhang, Y.; Zhao, J.; Che, Y.; Manners, I. Emergent Self-Assembly Pathways to Multidimensional Hierarchical Assemblies Using a Hetero-Seeding Approach. *Chem. Eur. J.* **2019**, *25*, 13484–13490.

(473) Shaikh, H.; Jin, X.-H.; Harniman, R. L.; Richardson, R. M.; Whittell, G. R.; Manners, I. Solid-State Donor-Acceptor Coaxial Heterojunction Nanowires via Living Crystallization-Driven Self-Assembly. *J. Am. Chem. Soc.* **2020**, *142*, 13469–13480.

(474) Fukui, T.; Garcia-Hernandez, J. D.; MacFarlane, L. R.; Lei, S.; Whittell, G. R.; Manners, I. Seeded Self-Assembly of Charge-Terminated Poly(3-Hexylthiophene) Amphiphiles Based on the Energy Landscape. *J. Am. Chem. Soc.* **2020**, *142*, 15038–15048.

(475) Tian, J.; Zhang, Y.; Du, L.; He, Y.; Jin, X.-H.; Pearce, S.; Eloi, J.-C.; Harniman, R. L.; Alibhai, D.; Ye, R. *et al.* Tailored Self-Assembled Photocatalytic Nanofibres for Visible-Light-Driven Hydrogen Production. *Nat. Chem.* **2020**, *12*, 1150–1156.

(476) Rho, J. Y.; Cox, H.; Mansfield, E. D. H.; Ellacott, S. H.; Peltier, R.; Brendel, J. C.; Hartlieb, M.; Waigh, T. A.; Perrier, S. Dual Self-Assembly of Supramolecular Peptide Nanotubes to Provide Stabilisation in Water. *Nat. Commun.* **2019**, *10*, 4708.

(477) Korlach, J.; Schwille, P.; Webb, W. W.; Feigenson, G. W. Characterization of Lipid Bilayer Phases by Confocal Microscopy and Fluorescence Correlation Spectroscopy. *Proc. Natl. Acad. Sci. U. S. A.* **1999**, *96*, 8461–8466.

(478) Dietrich, C.; Bagatolli, L. A.; Volovyk, Z. N.; Thompson, N. L.; Levi, M.; Jacobson, K.; Gratton, E. Lipid Rafts Reconstituted in Model Membranes. *Biophys. J.* **2001**, *80*, 1417–1428.

(479) Janosch, S.; Nicolini, C.; Ludolph, B.; Peters, C.; Völkert, M.; Hazlet, T. L.; Gratton, E.; Waldmann, H.; Winter, R. Partitioning of Dual-Lipidated Peptides into Membrane Microdomains: Lipid Sorting vs Peptide Aggregation. *J. Am. Chem. Soc.* **2004**, *126*, 7496–7503.

(480) Battaglia, G.; Ryan, A. J. Neuron-like Tubular Membranes Made of Diblock Copolymer Amphiphiles. *Angew. Chem. Int. Ed.* **2006**, *45*, 2052–2056.

(481) Loew, M.; Springer, R.; Scolari, S.; Altenbrunn, F.; Seitz, O.; Liebscher, J.; Huster, D.; Herrmann, A.; Arbuzova, A. Lipid Domain Specific Recruitment of Lipophilic Nucleic Acids: A Key for Switchable Functionalization of Membranes. *J. Am. Chem. Soc.* **2010**, *132*, 16066–16072.

(482) Yu, Y.; Vroman, J. A.; Bae, S. C.; Granick, S. Vesicle Budding Induced by a Pore-Forming Peptide. *J. Am. Chem. Soc.* **2010**, *132*, 195–201.

(483) Tayebi, L.; Ma, Y.; Vashaee, D.; Chen, G.; Sinha, S. K.; Parikh, A. N. Long-Range Interlayer Alignment of Intralayer Domains in Stacked Lipid Bilayers. *Nat. Mater.* **2012**, *11*, 1074–1080.

(484) Scheve, C. S.; Gonzales, P. A.; Momin, N.; Stachowiak, J. C. Steric Pressure between Membrane-Bound Proteins Opposes Lipid Phase Separation. *J. Am. Chem. Soc.* **2013**, *135*, 1185–1188.

(485) Moiset, G.; López, C. A.; Bartelds, R.; Syga, L.; Rijpkema, E.; Cukkemane, A.; Baldus, M.; Poolman, B.; Marrink, S. J. Disaccharides Impact the Lateral Organization of Lipid Membranes. *J. Am. Chem. Soc.* **2014**, *136*, 16167–16175.

(486) Fleming, S.; Debnath, S.; Frederix, P. W. J. M.; Hunt, N. T.; Ulijn, R. V. Insights into the Coassembly of Hydrogelators and Surfactants Based on Aromatic Peptide Amphiphiles. *Biomacromolecules* **2014**, *15*, 1171–1184.

(487) Gutierrez, M. G.; Malmstadt, N. Human Serotonin Receptor 5-HT 1A Preferentially Segregates to the Liquid Disordered Phase in Synthetic Lipid Bilayers. *J. Am. Chem. Soc.* **2014**, *136*, 13530–13533.

(488) Brea, R. J.; Rudd, A. K.; Devaraj, N. K. Nonenzymatic Biomimetic Remodeling of Phospholipids in Synthetic Liposomes. *Proc. Natl. Acad. Sci. U. S. A.* **2016**, *113*, 8589–8594.

(489) Franquelim, H. G.; Khmelinskaia, A.; Sobczak, J.-P.; Dietz, H.; Schwille, P. Membrane Sculpting by Curved DNA Origami Scaffolds. *Nat. Commun.* **2018**, *9*, 811.

(490) Sibold, J.; Kettelhoit, K.; Vuong, L.; Liu, F.; Werz, D. B.; Steinem, C. Synthesis of Gb3 Glycosphingolipids with Labeled Head Groups: Distribution in Phase-Separated Giant Unilamellar Vesicles. *Angew. Chem. Int. Ed.* **2019**, *58*, 17805–17813.

(491) Kamiya, K.; Kawano, R.; Osaki, T.; Akiyoshi, K.; Takeuchi, S. Cell-Sized Asymmetric Lipid Vesicles Facilitate the Investigation of Asymmetric Membranes. *Nat. Chem.* **2016**, *8*, 881–889.

(492) Sun, Y.; Wollenberg, A. L.; O'Shea, T. M.; Cui, Y.; Zhou, Z. H.; Sofroniew, M. V.; Deming, T. J. Conformation-Directed Formation of Self-Healing Diblock Copolypeptide Hydrogels via Polyion Complexation. *J. Am. Chem. Soc.* **2017**, *139*, 15114–15121.

(493) Dou, H.; Li, M.; Qiao, Y.; Harniman, R.; Li, X.; Boott, C. E.; Mann, S.; Manners, I. Higher-Order Assembly of Crystalline Cylindrical Micelles into Membrane-Extendable Colloidosomes. *Nat. Commun.* **2017**, *8*, 426.

(494) Mason, A. F.; Buddingh', B. C.; Williams, D. S.; van Hest, J. C. M. Hierarchical Self-Assembly of a Copolymer-Stabilized Coacervate Protocell. *J. Am. Chem. Soc.* **2017**, *139*, 17309–17312.

(495) Wang, L.; Wen, P.; Liu, X.; Zhou, Y.; Li, M.; Huang, Y.; Geng, L.; Mann, S.; Huang, X. Single-Step Fabrication of Multi-Compartmentalized Biphasic Proteinosomes. *Chem. Commun.* **2017**, *53*, 8537–8540.

(496) Gibard, C.; Bhowmik, S.; Karki, M.; Kim, E.-K.; Krishnamurthy, R. Phosphorylation, Oligomerization and Self-Assembly in Water under Potential Prebiotic Conditions. *Nat. Chem.* **2018**, *10*, 212–217.

(497) Sun, Y.; Bentolila, L. A.; Deming, T. J. Self-Sorting Microscale Compartmentalized Block Copolypeptide Hydrogels. *ACS Macro Letters*. **2019**, *8*, 1275–1279.

(498) Liu, X.; Formanek, P.; Voit, B.; Appelhans, D. Functional Cellular Mimics for the Spatiotemporal Control of Multiple Enzymatic Cascade Reactions. *Angew. Chem. Int. Ed.* **2017**, *56*, 16233–16238.

(499) Marguet, M.; Edembe, L.; Lecommandoux, S. Polymersomes in Polymersomes: Multiple Loading and Permeability Control. *Angew. Chem. Int. Ed.* **2012**, *51*, 1173–1176.

(500) Huang, X.; Li, M.; Green, D. C.; Williams, D. S.; Patil, A. J.; Mann, S. Interfacial Assembly of Protein-Polymer Nano-Conjugates into Stimulus-Responsive Biomimetic Protocells. *Nat. Commun.* **2013**, *4*, 2239.

(501) Peters, R. J. R. W.; Marguet, M.; Marais, S.; Fraaije, M. W.; van Hest, J. C. M.; Lecommandoux, S. Cascade Reactions in Multicompartmentalized Polymersomes. *Angew. Chem. Int. Ed.* **2014**, *53*, 146–150.

(502) Deng, N.-N.; Yelleswarapu, M.; Huck, W. T. S. Monodisperse Uni- and Multicompartment Liposomes. *J. Am. Chem. Soc.* **2016**, *138*, 7584–7591.

(503) Liu, X.; Zhou, P.; Huang, Y.; Li, M.; Huang, X.; Mann, S. Hierarchical Proteinosomes for Programmed Release of Multiple Components. *Angew. Chem. Int. Ed.* **2016**, *55*, 7095–7100.

(504) Deng, N.-N.; Yelleswarapu, M.; Zheng, L.; Huck, W. T. S. Microfluidic Assembly of Monodisperse Vesosomes as Artificial Cell Models. *J. Am. Chem. Soc.* **2017**, *139*, 587–590.

(505) Qiao, Y.; Li, M.; Booth, R.; Mann, S. Predatory Behaviour in Synthetic Protocell Communities. *Nat. Chem.* **2017**, *9*, 110–119.

(506) Martin, N.; Douliez, J.-P.; Qiao, Y.; Booth, R.; Li, M.; Mann, S. Antagonistic Chemical Coupling in Self-Reconfigurable Host-Guest Protocells. *Nat. Commun.* **2018**, *9*, 3652.

(507) Niederholtmeyer, H.; Chaggan, C.; Devaraj, N. K. Communication and Quorum Sensing in Non-Living Mimics of Eukaryotic Cells. *Nat. Commun.* **2018**, *9*, 5027.

(508) Gobbo, P.; Patil, A. J.; Li, M.; Harniman, R.; Briscoe, W. H.; Mann, S. Programmed Assembly of Synthetic Protocells into Thermoresponsive Prototissues. *Nat. Mater.* **2018**, *17*, 1145–1153.

(509) Joesaar, A.; Yang, S.; Bögels, B.; van der Linden, A.; Pieters, P.; Kumar, B. V. V. S. P.; Dalchau, N.; Phillips, A.; Mann, S.; de Greef, T. F. A. DNA-Based Communication in Populations of Synthetic Protocells. *Nat. Nanotechnol.* **2019**, *14*, 369–378.

(510) Buddingh', B. C.; Elzinga, J.; van Hest, J. C. M. Intercellular Communication between Artificial Cells by Allosteric Amplification of a Molecular Signal. *Nat. Commun.* **2020**, *11*, 1652.

(511) Downs, F. G.; Lunn, D. J.; Booth, M. J.; Sauer, J. B.; Ramsay, W. J.; Klemperer, R. G.; Hawker, C. J.; Bayley, H. Multi-Responsive Hydrogel Structures from Patterned Droplet Networks. *Nat. Chem.* **2020**, *12*, 363–371.

(512) Luo, Y.; Shoichet, M. S. A Photolabile Hydrogel for Guided Three-Dimensional Cell Growth and Migration. *Nat. Mater.* **2004**, *3*, 249–253.

(513) Hahn, M. S.; Miller, J. S.; West, J. L. Three-Dimensional Biochemical and Biomechanical Patterning of Hydrogels for Guiding Cell Behavior. *Adv. Mater.* **2006**, *18*, 2679–2684.

(514) Kaehr, B.; Shear, J. B. Mask-Directed Multiphoton Lithography. *J. Am. Chem. Soc.* **2007**, *129*, 1904–1905.

(515) Kloxin, A. M.; Kasko, A. M.; Salinas, C. N.; Anseth, K. S. Photodegradable Hydrogels for Dynamic Tuning of Physical and Chemical Properties. *Science* **2009**, *324*, 59–63.

(516) Lee, J.-T.; George, M. C.; Moore, J. S.; Braun, P. V. Multiphoton Writing of Three-Dimensional Fluidic Channels within a Porous Matrix. *J. Am. Chem. Soc.* **2009**, *131*, 11294–11295.

(517) DeForest, C. A.; Polizzotti, B. D.; Anseth, K. S. Sequential Click Reactions for Synthesizing and Patterning Three-Dimensional Cell Microenvironments. *Nat. Mater.* **2009**, *8*, 659–664.

(518) Muraoka, T.; Koh, C.-Y.; Cui, H.; Stupp, S. I. Light-Triggered Bioactivity in Three Dimensions. *Angew. Chem. Int. Ed.* **2009**, *48*, 5946–5949.

(519) Li, X.; Gao, Y.; Kuang, Y.; Xu, B. Enzymatic Formation of a Photoresponsive Supramolecular Hydrogel. *Chem. Commun.* **2010**, *46*, 5364–5366.

(520) Deforest, C. A.; Sims, E. A.; Anseth, K. S. Peptide-Functionalized Click Hydrogels with Independently Tunable Mechanics and Chemical Functionality for 3D Cell Culture. *Chem. Mater.* **2010**, *22*, 4783–4790.

(521) DeForest, C. A.; Anseth, K. S. Cytocompatible Click-Based Hydrogels with Dynamically Tunable Properties through Orthogonal Photoconjugation and Photocleavage Reactions. *Nat. Chem.* **2011**, *3*, 925–931.

(522) Wylie, R. G.; Ahsan, S.; Aizawa, Y.; Maxwell, K. L.; Morshead, C. M.; Shoichet, M. S. Spatially Controlled Simultaneous Patterning of Multiple Growth Factors in Three-Dimensional Hydrogels. *Nat. Mater.* **2011**, *10*, 799–806.

(523) DeForest, C. A.; Anseth, K. S. Photoreversible Patterning of Biomolecules within Click-Based Hydrogels. *Angew. Chem. Int. Ed.* **2012**, *51*, 1816–1819.

(524) Yoon, J.; Bian, P.; Kim, J.; McCarthy, T. J.; Hayward, R. C. Local Switching of Chemical Patterns through Light-Triggered Unfolding of Creased Hydrogel Surfaces. *Angew. Chem. Int. Ed.* **2012**, *51*, 7146–7149.

(525) Mosiewicz, K. A.; Kolb, L.; van der Vlies, A. J.; Martino, M. M.; Lienemann, P. S.; Hubbell, J. A.; Ehrbar, M.; Lutolf, M. P. In Situ Cell Manipulation through Enzymatic Hydrogel Photopatterning. *Nat. Mater.* **2013**, *12*, 1072–1078.

(526) He, M.; Li, J.; Tan, S.; Wang, R.; Zhang, Y. Photodegradable Supramolecular Hydrogels with Fluorescence Turn-on Reporter for Photomodulation of Cellular Microenvironments. *J. Am. Chem. Soc.* **2013**, *135*, 18718–18721.

(527) Siltanen, C.; Shin, D.-S.; Sutcliffe, J.; Revzin, A. Micropatterned Photodegradable Hydrogels for the Sorting of Microbeads and Cells. *Angew. Chem. Int. Ed.* **2013**, *52*, 9224–9228.

(528) Liu, Z.; Liu, T.; Lin, Q.; Bao, C.; Zhu, L. Sequential Control over Thiol Click Chemistry by a Reversibly Photoactivated Thiol Mechanism of Spirothiopyran. *Angew. Chem. Int. Ed.* **2015**, *54*, 174–178.

(529) Theis, S.; Iturmendi, A.; Gorsche, C.; Orthofer, M.; Lunzer, M.; Baudis, S.; Ovsianikov, A.; Liska, R.; Monkowius, U.; Teasdale, I. Metallo-Supramolecular Gels That Are Photocleavable with Visible and Near-Infrared Irradiation. *Angew. Chem. Int. Ed.* **2017**, *56*, 15857–15860.

(530) Lunzer, M.; Shi, L.; Andriotis, O. G.; Gruber, P.; Markovic, M.; Thurner, P. J.; Ossipov, D.; Liska, R.; Ovsianikov, A. A Modular Approach to Sensitized Two-Photon Patterning of Photodegradable Hydrogels. *Angew. Chem. Int. Ed.* **2018**, *57*, 15122–15127.

(531) Oran, D.; Rodriques, S. G.; Gao, R.; Asano, S.; Skylar-Scott, M. A.; Chen, F.; Tillberg, P. W.; Marblestone, A. H.; Boyden, E. S. 3D Nanofabrication by Volumetric Deposition and Controlled Shrinkage of Patterned Scaffolds. *Science* **2018**, *362*, 1281–1285.

(532) Badeau, B. A.; Comerford, M. P.; Arakawa, C. K.; Shadish, J. A.; DeForest, C. A. Engineered Modular Biomaterial Logic Gates for Environmentally Triggered Therapeutic Delivery. *Nat. Chem.* **2018**, *10*, 251–258.

(533) Shadish, J. A.; Benuska, G. M.; DeForest, C. A. Bioactive Site-Specifically Modified Proteins for 4D Patterning of Gel Biomaterials. *Nat. Mater.* **2019**, *18*, 1005–1014.

(534) Shadish, J. A.; Strange, A. C.; DeForest, C. A. Genetically Encoded Photocleavable Linkers for Patterned Protein Release from Biomaterials. *J. Am. Chem. Soc.* **2019**, *141*, 15619–15625.

(535) LeValley, P. J.; Neelarapu, R.; Sutherland, B. P.; Dasgupta, S.; Kloxin, C. J.; Kloxin, A. M. Photolabile Linkers: Exploiting Labile Bond Chemistry to Control Mode and Rate of Hydrogel Degradation and Protein Release. *J. Am. Chem. Soc.* **2020**, *142*, 4671–4679.

(536) Zhang, K.; Oldenhof, S.; Wang, Y.; van Esch, J. H.; Mendes, E. Spatial Manipulation and Integration of Supramolecular Filaments on Hydrogel Substrates towards Advanced Soft Devices. *Angew. Chem. Int. Ed.* **2020**, *59*, 8601–8607.

(537) Gould, O. E. C.; Qiu, H.; Lunn, D. J.; Rowden, J.; Harniman, R. L.; Hudson, Z. M.; Winnik, M. A.; Miles, M. J.; Manners, I. Transformation and Patterning of Supermicelles Using Dynamic Holographic Assembly. *Nat. Commun.* **2015**, *6*, 10009.

(538) Gould, O. E. C.; Box, S. J.; Boott, C. E.; Ward, A. D.; Winnik, M. A.; Miles, M. J.; Manners, I. Manipulation and Deposition of Complex, Functional Block Copolymer Nanostructures Using Optical Tweezers. *ACS Nano* **2019**, *13*, 3858–3866.

(539) Takaoka, Y.; Sakamoto, T.; Tsukiji, S.; Narazaki, M.; Matsuda, T.; Tochio, H.; Shirakawa, M.; Hamachi, I. Self-Assembling Nanoprobes That Display off/on ^{19}F Nuclear Magnetic Resonance Signals for Protein Detection and Imaging. *Nat. Chem.* **2009**, *1*, 557–561.

(540) Mizusawa, K.; Ishida, Y.; Takaoka, Y.; Miyagawa, M.; Tsukiji, S.; Hamachi, I. Disassembly-Driven Turn-on Fluorescent Nanoprobes for Selective Protein Detection. *J. Am. Chem. Soc.* **2010**, *132*, 7291–7293.

(541) Takaoka, Y.; Kiminami, K.; Mizusawa, K.; Matsuo, K.; Narazaki, M.; Matsuda, T.; Hamachi, I. Systematic Study of Protein Detection Mechanism of Self-Assembling ^{19}F NMR/MRI Nanoprobes toward Rational Design and Improved Sensitivity. *J. Am. Chem. Soc.* **2011**, *133*, 11725–11731.

(542) Mizusawa, K.; Takaoka, Y.; Hamachi, I. Specific Cell Surface Protein Imaging by Extended Self-Assembling Fluorescent Turn-on Nanoprobes. *J. Am. Chem. Soc.* **2012**, *134*, 13386–13395.

(543) Yoshii, T.; Mizusawa, K.; Takaoka, Y.; Hamachi, I. Intracellular Protein-Responsive Supramolecules: Protein Sensing and in-Cell Construction of Inhibitor Assay System. *J. Am. Chem. Soc.* **2014**, *136*, 16635–16642.

(544) Li, X.; Kim, C.-Y.; Lee, S.; Lee, D.; Chung, H.-M.; Kim, G.; Heo, S.-H.; Kim, C.; Hong, K.-S.; Yoon, J. Nanostructured Phthalocyanine Assemblies with Protein-Driven

Switchable Photoactivities for Biophotonic Imaging and Therapy. *J. Am. Chem. Soc.* **2017**, *139*, 10880–10886.

(545) Gao, Y.; Shi, J.; Yuan, D.; Xu, B. Imaging Enzyme-Triggered Self-Assembly of Small Molecules inside Live Cells. *Nat. Commun.* **2012**, *3*, 1033.

(546) Li, J.; Gao, Y.; Kuang, Y.; Shi, J.; Du, X.; Zhou, J.; Wang, H.; Yang, Z.; Xu, B. Dephosphorylation of D-Peptide Derivatives to Form Biofunctional, Supramolecular Nanofibers/Hydrogels and Their Potential Applications for Intracellular Imaging and Intratumoral Chemotherapy. *J. Am. Chem. Soc.* **2013**, *135*, 9907–9914.

(547) Zhou, J.; Du, X.; Li, J.; Yamagata, N.; Xu, B. Taurine Boosts Cellular Uptake of Small D-Peptides for Enzyme-Instructed Intracellular Molecular Self-Assembly. *J. Am. Chem. Soc.* **2015**, *137*, 10040–10043.

(548) Wang, H.; Feng, Z.; Wang, Y.; Zhou, R.; Yang, Z.; Xu, B. Integrating Enzymatic Self-Assembly and Mitochondria Targeting for Selectively Killing Cancer Cells without Acquired Drug Resistance. *J. Am. Chem. Soc.* **2016**, *138*, 16046–16055.

(549) Versluis, F.; van Elsland, D. M.; Mytnyk, S.; Perrier, D. L.; Trausel, F.; Poolman, J. M.; Maity, C.; le Sage, V. A. A.; van Kasteren, S. I.; van Esch, J. H.; Eelkema, R. Negatively Charged Lipid Membranes Catalyze Supramolecular Hydrogel Formation. *J. Am. Chem. Soc.* **2016**, *138*, 8670–8673.

(550) Zhou, J.; Du, X.; Yamagata, N.; Xu, B. Enzyme-Instructed Self-Assembly of Small D-Peptides as a Multiple-Step Process for Selectively Killing Cancer Cells. *J. Am. Chem. Soc.* **2016**, *138*, 3813–3823.

(551) He, H.; Wang, J.; Wang, H.; Zhou, N.; Yang, D.; Green, D. R.; Xu, B. Enzymatic Cleavage of Branched Peptides for Targeting Mitochondria. *J. Am. Chem. Soc.* **2018**, *140*, 1215–1218.

(552) Feng, Z.; Wang, H.; Wang, S.; Zhang, Q.; Zhang, X.; Rodal, A. A.; Xu, B. Enzymatic Assemblies Disrupt the Membrane and Target Endoplasmic Reticulum for Selective Cancer Cell Death. *J. Am. Chem. Soc.* **2018**, *140*, 9566–9573.

(553) Feng, Z.; Wang, H.; Xu, B. Instructed Assembly of Peptides for Intracellular Enzyme Sequestration. *J. Am. Chem. Soc.* **2018**, *140*, 16433–16437.

(554) Pieszka, M.; Han, S.; Volkmann, C.; Graf, R.; Lieberwirth, I.; Landfester, K.; Ng, D. Y. W.; Weil, T. Controlled Supramolecular Assembly Inside Living Cells by Sequential Multistaged Chemical Reactions. *J. Am. Chem. Soc.* **2020**, *142*, 15780–15789.

(555) Ye, D.; Liang, G.; Ma, M. L.; Rao, J. Controlling Intracellular Macrocyclization for the Imaging of Protease Activity. *Angew. Chem. Int. Ed.* **2011**, *50*, 2275–2279.

(556) Ye, D.; Shuhendler, A. J.; Cui, L.; Tong, L.; Tee, S. S.; Tikhomirov, G.; Felsher, D. W.; Rao, J. Bioorthogonal Cyclization-Mediated in Situ Self-Assembly of Small-Molecule Probes for Imaging Caspase Activity in Vivo. *Nat. Chem.* **2014**, *6*, 519–526.

(557) Lee, S.; Park, H.; Kyung, T.; Kim, N. Y.; Kim, S.; Kim, J.; Heo, W. D. Reversible Protein Inactivation by Optogenetic Trapping in Cells. *Nat. Methods* **2014**, *11*, 633–636.

(558) Nguyen, M. K.; Kim, C. Y.; Kim, J. M.; Park, B. O.; Lee, S.; Park, H.; Heo, W. D. Optogenetic Oligomerization of Rab GTPases Regulates Intracellular Membrane Trafficking. *Nat. Chem. Biol.* **2016**, *12*, 431–436.

(559) Watanabe, T.; Seki, T.; Fukano, T.; Sakaue-Sawano, A.; Karasawa, S.; Kubota, M.; Kurokawa, H.; Inoue, K.; Akatsuka, J.; Miyawaki, A. Genetic Visualization of Protein Interactions Harnessing Liquid Phase Transitions. *Sci. Rep.* **2017**, *7*, 46380.

(560) Shin, Y.; Berry, J.; Pannucci, N.; Haataja, M. P.; Toettcher, J. E.; Brangwynne, C. P. Spatiotemporal Control of Intracellular Phase Transitions Using Light-Activated OptoDroplets. *Cell* **2017**, *168*, 159–171.e14.

(561) Dine, E.; Gil, A. A.; Uribe, G.; Brangwynne, C. P.; Toettcher, J. E. Protein Phase Separation Provides Long-Term Memory of Transient Spatial Stimuli. *Cell Syst* **2018**, *6*, 655-663.e5.

(562) Zhang, Q.; Huang, H.; Zhang, L.; Wu, R.; Chung, C.-I.; Zhang, S.-Q.; Torra, J.; Schepis, A.; Coughlin, S. R.; Kornberg, T. B.; Shu, X. Visualizing Dynamics of Cell Signaling In Vivo with a Phase Separation-Based Kinase Reporter. *Mol. Cell* **2018**, *69*, 334-346.e4.

(563) Reinkemeier, C. D.; Girona, G. E.; Lemke, E. A. Designer Membraneless Organelles Enable Codon Reassignment of Selected mRNAs in Eukaryotes. *Science* **2019**, *363*, eaaw2644.

(564) Dzuricky, M.; Rogers, B. A.; Shahid, A.; Cremer, P. S.; Chilkoti, A. De Novo Engineering of Intracellular Condensates Using Artificial Disordered Proteins. *Nat. Chem.* **2020**, *12*, 814–825.

(565) Kim, N. Y.; Lee, S.; Yu, J.; Kim, N.; Won, S. S.; Park, H.; Heo, W. D. Optogenetic Control of MRNA Localization and Translation in Live Cells. *Nat. Cell Biol.* **2020**, *22*, 341–352.

(566) Caplan, J.; Niethammer, M.; Taylor, R. M., 2nd; Czymmek, K. J. The Power of Correlative Microscopy: Multi-Modal, Multi-Scale, Multi-Dimensional. *Curr. Opin. Struct. Biol.* **2011**, *21*, 686–693.

(567) Karreman, M. A.; Hyenne, V.; Schwab, Y.; Goetz, J. G. Intravital Correlative Microscopy: Imaging Life at the Nanoscale. *Trends Cell Biol.* **2016**, *26*, 848–863.

(568) Hauser, M.; Wojcik, M.; Kim, D.; Mahmoudi, M.; Li, W.; Xu, K. Correlative Super-Resolution Microscopy: New Dimensions and New Opportunities. *Chem. Rev.* **2017**, *117*, 7428–7456.

(569) Zhou, J.; Du, X.; Berciu, C.; He, H.; Shi, J.; Nicastro, D.; Xu, B. Enzyme-Instructed Self-Assembly for Spatiotemporal Profiling of the Activities of Alkaline Phosphatases on Live Cells. *Chem* **2016**, *1*, 246–263.

TOC graphic